UNIVERSITY OF FLORENCE

Dept. Civil and Environmental Engineering

International Doctorate in Civil and Environmental Engineering

RUHR UNIVERSITÄT BOCHUM

Dept. Wind Engineering and Fluid Mechanics

International Doctorate in Civil and Environmental Engineering

Platform and moorings modelling and optimization procedures for large semisubmersible floating offshore wind turbines

DOCTORAL THESIS

Ph.D. Candidate

Giulio Ferri

Doctoral Thesis Tutors

Prof. Claudio Borri

Prof. Rüdiger Höffer

Dr. Enzo Marino

Table of contents

List of Figures

List of Tables

List of Abbreviations

FOWT: Floating Offshore Wind Turbine

OWT: Offshore Wind Turbine

WT   Wind Turbine

SWL   Sea Water Level

TL   Tension Leg

TLP   Tension Leg Platform

CoM   Centre of Mass

CoB   Centre of Buoyancy

IRM   Inverse Reliability Method

FD   Frequency Domain

DoF   Degree of Freedom

LCOE   Levelized Cost of Electricity

BEM   Boundary Element Method

BVP   Boundary value Problem

CFD   Computational Fluid Dynamic

PM   Pierson-Moscowitz

JONSWAP   Joint North Sea Wave Project

RAO   Response Amplitude Operator

PSD   Power Spectral Density

MBC	Multi-Blade-Coordinate
FA	Fore-Aft
SS	Side-to-Side
RNA	Rotor Nacelle Assembly
DLC	Design Load Case
NTM	Normal Turbulence Model
GA	Genetic Algorithm
FORM	First Order Reliability Method
ECS	Environmental Contour Surface
IFORMs	Inverse First Order Reliability Method
CDF	Cumulative Density Function
PDF	Probability Density Function
RCA	Rainflow cycle-Counting-Algorithm
EFL	Equivalent Fatigue Load
ULS	Ultimate Limit State
SLS	Serviceability Limit State

List of Symbols

Letters

ρ_{h_2o}:   water density, equal to 1025 kg/m³

g: gravity acceleration

W_{tot}:   total weight of the floating body

$\overline{GM}$:   distance between the centre of mass and the metacentre

$\overline{KB}$:   distance between the keel point and the centre of buoyancy

$\overline{BM}$:   distance between the centre of buoyancy and the metacentre

A_{WL}:   waterplane area at the Sea Water Level for hydrostatic stability

I_{xx}:   second moment of area of the waterplane area with respect to the equilibrium position of the body

V_0:   buoyancy volume at equilibrium

$F^{Res}{}_k$: k^{th} component of the hydrostatic restoring forces

q_j: j^{th} component of the 6x1 displacement vector of the floating body

z_B: draught of the centre of buoyancy with respect to the equilibrium position of the body

σ_η^2:   variance of the irregular wave

$S_{\eta\eta}(\omega)$:   One-sided irregular wave spectrum

ω: circular frequency

ζ_j: amplitude of the jth wave component

k_j: wave number of the jth wave component

ε_j: phase angle of the jth wave component

$S_{PM}(\omega)$:   Pierson-Moskowitz wave spectrum

H_s: wave height

T_P: peak spectral period

$S_J(\omega)$:   JONSWAP wave spectrum

γ: peak shape parameter of the JONSWAP spectrum

$\sigma(\omega)$:   Scaling factor of the JONSWAP spectrum

$\varphi(x,y,z,t)$:   fluid total velocity potential

p: fluid pressure

$\rho_{h_2o}gz$:   gravity potential

$\frac{\partial}{\partial n}$:   partial derivative with respect to the direction normal to the body surface

λ: wavelength of the selected sea wave

$\phi(x,y,z)$:   fluid spatial velocity potential

$\phi_D(x,y,z)$:   Diffraction velocity potential

$\phi_R(x,y,z)$:   Radiation velocity potential

$\phi_0(x,y,z)$:   Incident wave velocity potential

$\phi_7(x,y,z)$:   Scattering velocity potential, resulting from the permeability condition imposed at the wetted surface of the floating body

S_B: wetted surface of the floating body

S_F: Free surface of the volume of control

S_0:   Seabed surface of the volume of control

S_∞:   Lateral surface of the volume of control

$Q(\xi,\eta,\zeta)$:   Source density function of the Boundary Value Problem of Radiation and

Diffraction, at the point (ξ, η, ζ) on S_B

$G(x, y, z, \xi, \eta, \zeta)$:   Green's Function of the Boundary Value Problem of Radiation and Diffraction

α: slenderness of the element subjected to the incoming wave

D: characteristic length of the element subjected to the incoming wave

C_M: inertial coefficient of the inertial term in the Morison equation

C_A: added mass coefficient of the inertial term in the Morison equation

C_D: drag coefficient of the nonlinear viscous term in the Morison equation

$\sigma_{\mathbf{u}-\dot{\mathbf{q}}}$:   standard deviation of the relative velocity between the wave and the cylinder

$\sigma_{\dot{\mathbf{q}}}$:   standard deviation of the velocity of the moving cylinder in the fluid

A_α: floater surface A_α, projected on the plane with normal direction $\alpha = x, y, z$

S_{β, A_α}:   first moment of area A_α about the axis β; $\alpha, \beta = x, y, z$

I_{β, A_α}:   first moment of area A_α about the axis β; $\alpha, \beta = x, y, z$

C_{Az}:   added mass coefficient in the heave direction

V_R: volume of fluid moving with the oscillating heave plate

D_h: diameter of the heave plate

D_c: diameter of the upper column

C_{Dz}:   drag coefficient in the heave direction

$A_{33}(0)$:   heave-heave Added Mass coefficient calculated at $\omega = 0$

a: average of all the heave plates oscillation amplitudes

μ_c: mass of the cable per unit length

D_{cable}:   cable diameter

w: apparent weight in fluid of the cable per unit length

C_B: seabed cable friction coefficient

(x_F, z_F):   horizontal and vertical position of the Fairlead with respect to the cable reference

frame (x, z)

(H, V): horizontal and vertical components of the tension in the cable at the Fairlead

L: unstretched length of the cable

EA: axial stiffness of the cable

L_B: portion of the cable resting on the seabed

s: local coordinate of the cable, starting from the anchor to the Fairlead

T: cable tension

l: horizontal position of the Fairlead, namely x_F

h: vertical position of the Fairlead, namely z_F

K_I: cable elastic stiffness

ΔL: elongation of the cable

L': deformed length of the cable

α: inclination of the cable with respect to the horizontal direction

R: horizontal distance between the platform centreline and the cable Fairlead

β_i: angle between the position of the ith and the platform centreline with respect to the horizontal plane xy

D_r: draught of the Fairlead with respect to the platform centreline

n: number of the cables

z_{hub}: hub height with respect to the SWL

x_G: x-position of the centre of mass

x_B: x-position of the centre of buoyancy

ψ_b: azimuthal location of the bth blade with respect to the rotor hub

b: number of blades, in this case 3

q_0: non-rotating coning mode DoF of the combined rotor blades

q_c: non-rotating cosine cyclic mode DoF of the combined rotor blades

q_s: non-rotating sine cyclic mode DoF of the combined rotor blades

q_b: generic DoF of the bth blade

Ω: rotor angular velocity

$\dot{\Omega}$:   rotor angular acceleration

ω_i: eigenfrequency of the ith DoF of the WT tower

$\phi_i(z)$:   eigenvector of the ith eigenfrequency, evaluated at the tower height z

m_{RN}:   lumped mass of Rotor and Nacelle, rigidly connected to the tower top

I_{RN}:   lumped inertia of Rotor and Nacelle, rigidly connected to the tower top

$\tilde{\rho}_i h_i$: i[th] tower element mass

$\phi_{1,z}(z)$:   derivative of the First Fore-Aft eigenvector with respect to z, i.e., slope of the First fore-Aft eigenvector

$S_K(f)$:   Kaimal spectrum as a function of frequency, f, for the wind turbulence, $K = u, v, w$ stands for the wind velocity direction

L_K: turbulence length scale

σ_K: turbulence standard deviation

$\overline{u_{hub}}$:   average wind speed at hub height

σ_1:   IEC 61400-1 Normal Turbulence Model, representative value of the turbulence standard deviation

I_{ref}:   reference turbulence intensity

Λ_1:   turbulence scale parameter

$S_R(\omega)$:   generic response spectrum

$\text{RAO}_{V\_base}(\omega)$:   tower-base shear force RAO

$\text{RAO}_{M\_base}(\omega)$:   tower-base bending moment RAO

h_{TT}:   tower-top height above the SWL

S_f: scaling factor for upscaling design procedure of large FOWTs

d: side column diameter

r: platform radius

drf: platform draft

$q_{5,mean}$:   steady pitch rotation under rated wind speed

Δx_{offset}: steady surge offset of the system under rated wind speed

z_{depth}:   water depth

M_{tot}:   total structural mass, including floater, moorings, and the Wind Turbine

$M_{upscaled}$:   total structural mass, including floater, moorings, and the Wind Turbine of the upscaled 10MW FOWT

x_{anch}:   design variable for the mooring layout: horizontal distance between the anchor and the platform centreline

U_w: 10 min average wind speed at 10 m height

β_{REL}:   target reliability index for First Order Reliability Methods

T_R: return period

$\Phi(\cdot)$:   Cumulative Density Function of the standard Gaussian distribution

$F_{U_w}(u_w)$:   Cumulative Density Function of the wind speed

$F_{H_s|U_w}(h_s|u_w)$: Cumulative Density Function of the conditional distribution of the significant wave height for a give wind speed

$F_{T_P|H_s,U_w}(t_p|h_s,u_w)$: Cumulative Density Function of the conditional distribution of T_P for given H_S and U_w

$f_{T_P|H_s}(t_p|h_s)$: Cumulative Density Function of the conditional distribution of T_P for given H_S

$f_{U_w,H_s,T_p}(u_w,h_s,t_p)$: joint probability distributions of (u_w,h_s,t_p)

α_U: shape parameter of the Weibull distribution of U_w

β_U: scale parameter of the Weibull distribution of U_w

$\Gamma(\cdot)$:   Gamma function

γ_U: second shape parameter for the Exponentiated Weibull distribution of U_w

α_H: shape parameter of the Weibull distributions of H_s

β_H: scale parameter of the Weibull distributions of H_s

δ_H: shifting parameter of the three-parameter Weibull distribution of H_s

$\mu_{ln(T_P)}(h)$: mean value of the LogNormal distribution of T_P for given H_s

$\sigma_{ln(T_P)}(h)$: standard deviation of the LogNormal distribution of T_P for given H_s

$UHC[kN]$: Ultimate Holding Capacity of the anchor system adopted, expressed in kN

T_1: manufacturing time associated with the phase of preparation and tacking

C_1: coefficient depending on the welding technology

Θ_{dw}: difficulty factor

k: number of raw steel plates assembled

ρ_{steel}: steel density

V_s: volume of the steel structure to be assembled

T_2: actual welding time

N_w: Total number of welds

C_{2i}: parameter related to the welding technology

α_{wi}: welding width

m_w: parameter related to the welding technology

L_{wi}: welding length

MC: total manufacturing cost

$M_{Platform}$: steel mass of the platform

$M_{Ballast}$: ballast mass of the platform

$M_{Mooring}$: mass of the mooring lines

M_{Anchor}: mass of the anchors

A: Lateral surface of the platform

P_{steel}:   steel price

$P_{concrete}$:   concrete price

P_{labor}:   Labor price

P_{moor}:   Mooring price

P_{Anchor}:   Anchor price

P_{Paint}:   anti-corrosive paint price

D_{Fat}:   damage accumulated in T seconds for a given wind-wave loading

v: Mean cyclic rate

K: intercept of the SN curve with the logN axis

m: slope of the SN curve

k: thickness exponent

SCF: Stress Concentration Factor, which allows to account for misalignment between segments of the structure

$\bar{S}$:   equivalent nominal stress range

$E[S^m]$:   expected value of S^m

t_w: wall thickness

t_{ref}:   reference thickness, equal to 25 mm for welded connections

δ: misalignment between sections

D_w: section outer diameter

$p(s)$:   stress range Probability Density Function for the estimation of $E[S^m]$

D_1, D_2, D_3, Q and R_D Empirical weights for the Dirlik method

Z: normalized stress range

m_n: n^{th} spectral moment of the stress range Power Spectral Density function

$P_S(f)$:   stress range Power Spectral Density function

x_m: mean frequency factor for Dirlik method

γ: Regularity factor for the Dirlik method

S^{UP}:   stress range upper bounds, i.e., the cut-off stress range

$\bar{Z}$:   upper bound factor

σ_S: standard deviation of the stress process

EFL: equivalent fatigue load

D_F: damage fraction

N: number of stress cycles that have been rainflow-counted

D_{TOT}:   total fatigue damage

Vectors and Matrices

$\boldsymbol{C}^{Hydro}$:   hydrostatic stiffness matrix

$\boldsymbol{F}^{Res}$:   hydrostatic restoring force vector

$\mathbf{V}(x,y,z,t)$:   fluid velocity vector

$\boldsymbol{n}$:   Outward normal to the floating body surface, S_B

$\boldsymbol{r}$:   position vector of a point on the floating body surface, S_B

$\mathbf{X}(\boldsymbol{\omega})$:   frequency dependent, first-order wave exciting force

$\mathbf{A}(\omega)$:   frequency dependent, hydrodynamic added mass matrix

$\mathbf{B}_{rad}(\omega)$: frequency dependent, hydrodynamic radiation damping matrix

$\boldsymbol{F}^{Platform}(t)$:   total exciting force vector acting on the floating platform in the time domain

$\boldsymbol{A}$:   frequency-independent, impulsive hydrodynamic added mass matrix

$\boldsymbol{F}^{Hydrodyn}(t)$:   total hydrodynamic load vector acting on the floating platform

$\mathbf{F}^{Lines}(t)$:   mooring lines load vector

$q(t)$:	displacement vector
$K(t - \tau)$:	wave radiation retardation kernel, which depends on $\mathbf{B}(\omega)$
$F^{Waves}(t)$:	total incident wave excitation load vector acting on the floating body
$\hat{q}(\omega)$:	steady-state, complex amplitude of the displacement vector
$RAO(\omega)$:	Response Amplitude Operator of the 6 DoFs of the floating body
$\mathbf{dF}^{Morison}(t)$:	Morison force per unit-length for a moving cylinder immersed in a fluid flow
$\mathbf{u}(t)$:	wave velocity normal to the cylinder axis for the Morison equation
$\mathbf{dF_{Drag}}$:	linearized viscous drag force per unit-length for the Morison equation
F_{Drag}:	total linearized viscous drag force
M_{Drag}:	total linearized viscous drag moment
$\mathbf{B}_{visc}$:	linearized Morison viscous drag damping matrix
$\mathbf{dF_z^{Morison}}$:	Morison force per unit length on heave plates
$\mathbf{w}$:	vertical component of the wave velocity
$\mathbf{p_b}$:	dynamic fluid pressure at the bottom of the heave plate, projected in the heave direction
$\mathbf{p_t}$:	dynamic fluid pressure at the top of the heave plate, projected in the heave direction
$\mathbf{dF_{Drag,z}^{Morioson}}$:	linearized heave plates drag term
K^P:	2x2 stiffness matrix of the single cable with respect to the cable refence frame (x, z)
F^P:	2x2 flexibility matrix of the single cable with respect to the cable refence frame (x, z)
$F^{Lines,0}$:	Static mooring lines force vector
C^{Moor}:	6x6 mooring system stiffness matrix with respect to the motion of the floating platform

$F^{buoyancy}$:	buoyancy load vector
F^{Grav}:	gravity force vector
F^{Aero}:	aerodynamic force vector
M:	FAST Linearized simulation, mass matrix of the modelled system
B:	FAST Linearized simulation, damping matrix of the modelled system
C:	FAST Linearized simulation, stiffness matrix of the modelled system
F:	FAST Linearized simulation, control force matrix of the modelled system
F_d:	FAST Linearized simulation, disturbance matrix of the modelled system
u:	FAST Linearized simulation, control vector
w_d:	FAST Linearized simulation, disturbance vector
X:	physical vector, containing the DoFs of the system: nF expressed in the non-rotating frame and $3m$ expressed in the rotating frame
$\tilde{t}$:	rotating matrix which transforms the rotating blade DoFs in non-rotating DoFs
T_1:	topological matrix which transforms X into a non-rotating physical vector
X_{NR}:	non-rotating physical vector, where the DoFs of the blades are transported in the non-rotating reference frame
T_2:	first derivative with respect to the azimuth ψ of T_1, for the estimation of $\dot{X}_{NR}$
T_3:	second derivative with respect to the azimuth ψ of T_2, for the estimation of $\ddot{X}_{NR}$
$\tilde{t}_2$:	first derivative the azimuth ψ of $\tilde{t}$
$\tilde{t}_3$:	second derivative the azimuth ψ of $\tilde{t}$
M_{NR}:	MBC transformation, mass matrix of the modelled system expressed in the non-rotating frame
B_{NR}:	MBC transformation, damping matrix of the modelled system expressed in the non-rotating frame
C_{NR}:	MBC transformation, stiffness matrix of the modelled system expressed in the non-

rotating frame

F_{NR}: MBC transformation, control force matrix of the modelled system expressed in the non-rotating frame

u_{NR}: MBC transformation, control vector of the modelled system expressed in the non-rotating frame

w_d: MBC transformation, mass matrix of the modelled system expressed in the non-rotating frame

M_{TW}: discretized tower mass matrix with finite elements to perform modal analysis on the WT tower

C_{TW}: discretized tower stiffness matrix with finite elements to perform modal analysis on the WT tower

d: displacement vector of the tower nodes discretized with finite elements

ϕ_1: first Fore-Aft eigenvector

$M_{,FA}$: mass matrix associated with the First Fore-Aft eigenfrequency, it includes the modal mass, $M_{77,FA}$ and the cross-coupling contribution in Surge and Pitch

$C_{,FA}$: stiffness matrix associated with the First Fore-Aft eigenfrequency, it includes the modal stiffness, $C_{77,FA}$ and the cross-coupling contribution in Surge and Pitch

M^{Float}: floater structural mass matrix

M^{Turb}: Wind Turbine structural mass matrix

B^{Turb}: Wind Turbine damping matrix, which includes structural, aerodynamic, and gyroscopic damping

B^{Mor}: linearized viscous drag damping matrix, which includes the contribution on slender elements and heave plates,

C^{Turb}: Wind Turbine stiffness matrix

$S_R(\omega)$: Generic response spectrum

$RAO_{FairDisp}(\omega)$: Fairlead displacement RAO

$RAO_{FairF}(\omega)$: Fairlead forces RAO

$\mathbf{X}_{env}$:   design, physical space of environmental variables $\left[u_w, h_s, t_p\right]$

$\mathbf{U}$:   non-physical space of independence standard Gaussian variables $[u_1, u_2, u_3]$

Operators

$(\dot{\cdot})$:   first derivative with respect to time

$(\ddot{\cdot})$:   second derivative with respect to time

$(\cdot)^T$:   transpose of a matrix or a vector

∇:   differential operator

∇^2:   Laplacian operator

δ_{ij}:   Kronecker delta

$\lim\limits_{x\to\infty}(\cdot)$:   limit for x going to ∞

$\frac{\partial}{\partial s}(\cdot) \equiv (\cdot)_{,s}$:   partial derivative with respect to the generic variable s

$\iint_S (\cdot)\, dS$:   surface integral

$\iiint_V (\cdot)\, dV$:   volume integral

Acknowledgments

During this long journey lasted more than three years, I met new people from different countries which have become important beyond the research field.

Firstly, I would like to thank my supervisors, Prof. Claudio Borri, from the University of Florence, and Prof. Rüdiger Höffer, from the Ruhr Universität Bochum, for the unconditional trust they demonstrate not only during the doctorate. I also want to express my sincere gratitude to my second Italian Supervisor, Dr. Enzo Marino, who has been always a reference point for my research, providing fundamental suggestions and advices for the development of my work.

Moreover, I would like to thank my colleague Niccolò Bruschi, who has been very important for my research and has become a true friend.

A big thanks to my fellow travellers of the 34th cycle, in particular Lorenzo Baldi and Niccolò Barni, who have been with me since the beginning. We shared good moments before and after the Covid 19 Pandemic that I will always remember.

In the end, I would like to thank all my family. Those who are still here and those who have left, for the unconditional support during this travel.

Abstract

Floating Offshore Wind Turbines (FOWTs) are ground-breaking systems in the sector, capable to exploit wind energy in deep-water areas, where the resource is stronger and abundant with respect to onshore and near-cost sites. They are multi-body systems consisting in a Wind Turbine (WT) supported by a floating platform anchored to the sea bottom by means of mooring lines. Their dynamic behaviour depends on a complex interaction which involves flexible and rigid structures, such as rotor blades, turbine tower, the nacelle, and the platform, which interact with wind and waves. Together with the dimension of such systems, which makes experimental modeling extremely challenging, numerical tools are inevitable for the optimization of such structures.

Being time-domain simulations yet unaffordable when thousands of simulations need to be performed, a coupled Frequency-Domain model of the entire system is developed. The FOWT is modelled as a 7 DoFs dynamic system, consisting in the 6 rigid-body motions of the platform and the first Fore-Aft flexible mode of the turbine tower. These DoFs are sufficient to characterize the tension in the mooring lines and the shear and bending stresses on the turbine tower. The tool presents a complete, first order, characterization of the floating platform hydrodynamic problem. Linear hydrodynamic coefficients of Added mass, Radiation damping and Diffraction + Froude-Krilov Forces are calculated by means of ANSYS AQWA. Viscous drag forces, exerted on slender elements of the platform, are modelled with Morison's equation, and are linearized adopting the Borgman method. Mooring lines are modelled with a quasi-static approach. A linearized simulation, performed by means of FAST [1] around a steady-state operating point, allows to estimate the turbine contributions to the equation of motion in terms of mass, damping and stiffness matrices, as well as the rotor aerodynamic loads at the tower top.

The developed FD model is code-to-code validated against time-domain simulations performed in FAST. Firstly, Response Amplitude Operators (RAOs) are compared, then, the response under turbulent wind and irregular wave is validated. In both cases, Results show good agreement not only for the motion of the platform and the tower-top deflection, but also for the stresses on the mooring lines and the tower-base.

The FD model is implemented in optimization procedures based on a Genetic Algorithm (GA), aiming at finding the floating substructure (platform + mooring) which most effectively reduces the amplification of the response at the platform eigenfrequencies. Design variables related to the geometry of the platform

and the mooring lines are considered. Feasibility constraints related to the maximum admissible platform displacements under wind-wave loadings are enforced to ensure the turbine performances. Also, restrains to mooring cables tension and anchor loads are imposed.

In the end, site-specific optimization procedures, targeted at reducing the costs of the substructure without an uncontrolled penalization of the structural performances, are carried out. Two installations in the Mediterranean Sea are considered. The Metocean environment is characterized adopting a First Order Reliability Method (FORM), considering records of wind speed, significant wave height and peak spectral period of the wave. Results show that the optimization strategies give useful information about the influences of platform and mooring characteristics on the system response. Moreover, it is proved that the costs can be reduced of about the 45% with a moderated increase of the stresses on the tower.

Chapter 1.
Introduction

During the last decade, wind energy has become one of the most important resources in the renewable energy sector. Recent statistics on the installed capacity in Europe, highlight offshore wind as a growing sector, with an average annual installed capacity of 3 GW in the last five years and cumulative installed capacity of 25 GW dated 2020 (Figure 1).
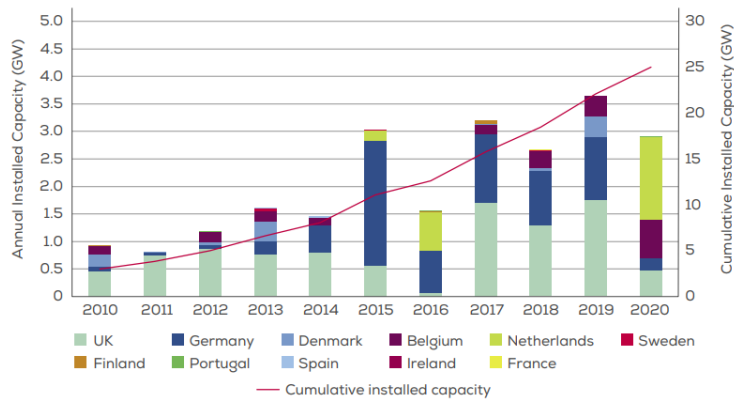
Figure 1: Annual offshore wind by country (left axis) and cumulative capacity (right axis) (GW) [2]

Of this offshore capacity, 63.7 MW are obtained from Floating Offshore wind Turbines (FOWTs), which is the 83% of the Global Floating wind fleet (Figure 2).
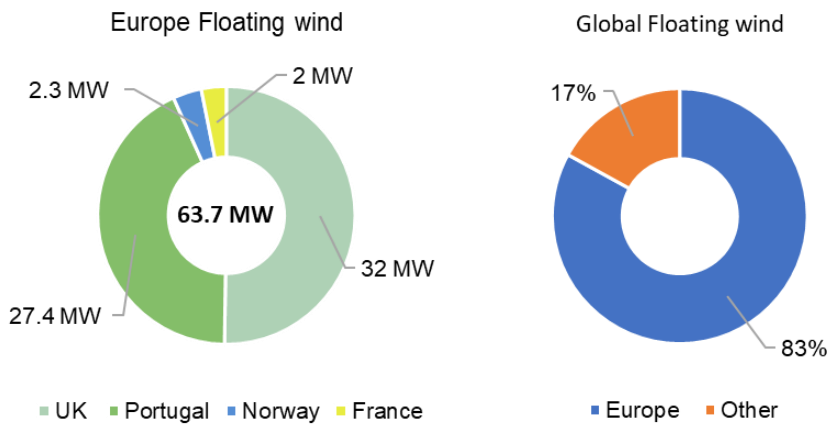
Figure 2: Annual offshore wind by country (left axis) and cumulative capacity (right axis) (GW) [2]

Higher wind speed, reduced turbulence, abundance of exploitable sites in deep water and almost absence of visual impact are some of the most important aspects which make FOWTs competitive with respect to fixed-bottom offshore and onshore technologies. On the other hand, construction and maintenance costs exponentially increase in open sea. Moreover, multiple fluid-structure interaction problems arise, involving simultaneously very slender and highly deformable bodies, such as rotor blades and mooring lines, and bluff bodies, such as the floating platform.

To properly reproduce the dynamic behaviour of such a structural system, physics-based engineering tools, accounting for coupled aero-hydro-servo-elastic modelling and nonlinear effects are needed. The large number of design variables involved, as well as the need for pursuing contrasting targets, such as reducing the overall cost and enhancing structural performances and reliability, raises the need for robust and sufficiently accurate optimization procedures. For these reasons, this research concerns the development of efficient strategies for the optimized design of platform and moorings supporting large Wind Turbines (WTs).

In the following, offshore wind turbines are introduced describing their main features, with particular attention on the support structures. In the end, the topic of the research is discussed.

1.1 Floating Offshore Wind Turbines

A horizontal-axis FOWT consists in four interacting structural systems: rotor and nacelle, tower, floating foundation, and the anchoring system (Figure 3).

The rotor and the nacelle are the part of the system where the kinetic energy of the rotating blades is converted in electric energy. They are both placed on the top of the turbine tower. All the electronic devices and the control system are placed inside the nacelle. The latter consist in a series of devices and algorithms which adjust blades positioning, rotor speed and orientation of the turbine in order to assure the correct production of energy at each wind speed, from the cut-in to the cut-out. When the wind speed exceeds the cut-out, the control system reduces loads on the tower and avoids faults.

The tower is usually a steel beam with a non-uniform circular cross-section. It keeps the rotor several meters above the Sea Water Level (SWL), where the wind speed is higher, and the effect of sea surface roughness is reduced. It holds the aerodynamic and servo-dynamic loads coming from rotor and nacelle.

The floating foundation transfers the loads from the tower-base to the sea bottom by means of two sub-systems: the platform and the mooring lines. The latter consist in a group of cables connected to the platform which provide the required horizontal stiffness to limit the displacements under admissible bounds. They are usually composed by steel chains or wires, but recently also polyester wires have been adopted. Slack catenary mooring systems are the most adopted due to their simplicity in the design and in the installation. They are very long (even more than 4 times the water depth) and with their dead weight,

they compensate the vertical loadings. The length of the cable can be designed in order to always maintain a portion of the line resting on the seabed. In this way, the anchors can be devised only for withstanding horizontal forces, allowing for simpler and more economic systems, such as drag embedded or gravity types. Slack catenaries marginally contribute to the rotational stability of the system.

Taut-line moorings are made of tensioned, inclined cables which contribute both to horizontal and rotational stability, allowing for lighter platforms and stiffer systems. They are significantly shorter than the catenary ones, and with a larger cross-section. The design of the anchor is crucial since they are inevitably stressed by vertical loadings. Usually, suction pile or driven pile systems are preferrable with respect to the gravity ones. Tension Leg (TL) moorings are a particular case of Taut-line with vertical cables. An hybrid system have been recently proposed for mooring a 10 MW WT [3]. The cable is composed of two segments. The first one, which starts from the anchor, is a catenary chain which, by dead weight, reduces the loads on the anchors. The second is an inclined, tensioned taut-line wire. Such system results in a combination of both the technologies.

Based on the way the buoyancy stability is achieved, different technologies can be identified (Figure 3):

- Ballast stabilized: the roll-pitch stability is achieved by means of ballast weights, which lowered the overall Centre of Mass (CoM) of the FOWT allowing for larger restoring moments. Displacements in surge-say and yaw have to be constrained by the mooring system. The most common concept of this typology is the spar [4] . It consists in a single cylinder with a very large draft. Due to its simplicity, it was one of the first developed concept and worldwide it is the most installed FOWT support platform. However, due its dimensions, which can be from 1 to 1.5 times the turbine tower height, it might be unfeasible for 10 MW WT and its field of applicability is restrained to a certain range of water depths.

- Buoyancy stabilized: The roll-pitch stability is almost totally achieved by the platform, thanks to the righting moment related to the inertia of the platform waterplane area. The mooring system must constrain the horizontal displacement and, marginally, the yaw rotation. In opposition with the ballast stabilized, they are characterized by reduced draft but very large footprint, resulting in lighter but stiffer systems. For this reason, attention should be paid on the dynamic response, in order to avoid large amplifications that can negatively affect the turbine behaviour [5].

- Mooring stabilized: the roll-pitch stability is achieved by means of a tensioned mooring system which is capable to provide a restoring moment. This allows to reduce the dimensions and the weight of the platform, and the length of the moorings. On the other hand, cables must withstand higher tensile stresses with respect to other concepts. Attention has to be paid on the anchoring system design, which must be capable to withstand vertical loadings, but also on the dynamic design. Such a concepts is very sensitive to roll-pitch motions, which can lead to tension losses in

the cables. For this reason, resonance in any wind-waves condition must be avoided. One of the most common example are the Tension Leg Platforms (TLPs) [6], but also hybrid concepts like taut-line or semi-taut-line platform have been developed [3].

Developing these three main concepts, hybrid solutions have been designed. The most common is the semisubmersible technology, which achieves stability both by ballast and buoyancy effects.
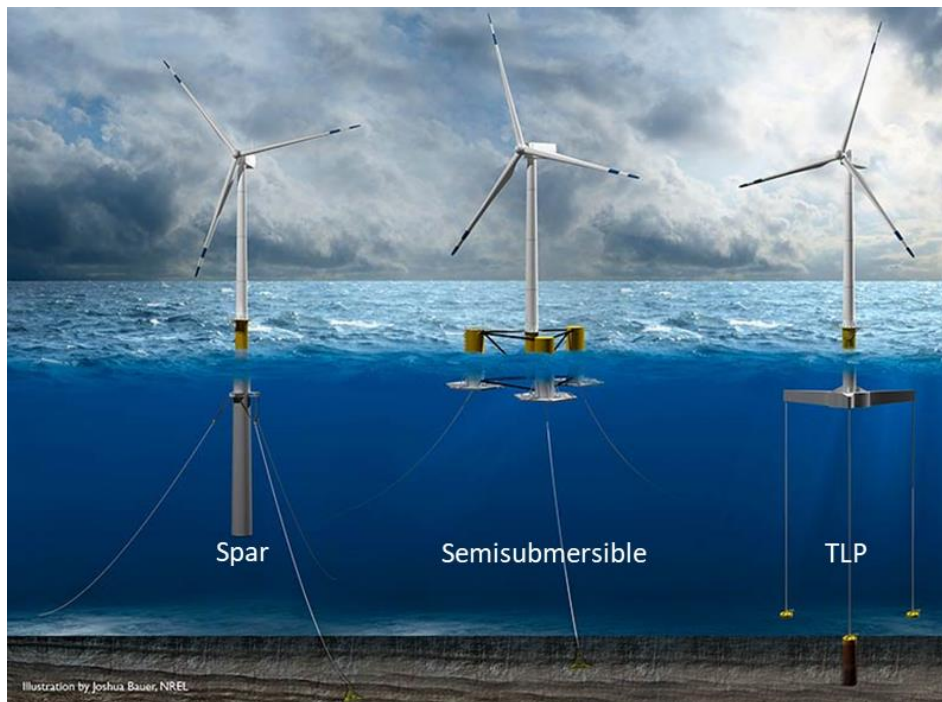
Figure 3: FOWT principal concepts, courtesy of [7].

1.2   Motivation

The dynamic modeling of the system is of primary importance to properly estimates the structural response and the wind-wave-structure interaction which arises. Two aspects must be considered for the analysis of a floating wind structure. On one hand, very accurate and computational expensive engineering tools are needed. On the other hand, design standards from IEC 61400 regulation require the simulation of a great number of load cases, to assess the long-term and short-term reliability of the structure. The numerical analysis of a FOWT can be performed by means of two different approaches: time-domain and Frequency-Domain (FD) analyses.

Time domain models are the most accurate tools for the FOWT simulation. They are capable to catch the nonlinear nature of the dynamic problem and to reproduce the aero-hydro-servo-elastic response of the system. The most common adopted codes in this engineering field are FAST [1], HAWC2 [8] and BLADED [9]. The structural system is modelled adopting a hybrid approach, namely employing a modal and multibody formulation, combining flexible, blades, tower, and mooring, and rigid, platform, bodies. They

have a high computational cost, but any load case can be reproduced, such as transients, turbine shut down, and faults.

In the past, several studies adopting time domain formulation have been carried out, concerning the proper estimation of the structural system behaviour and its interaction with wind and wave, both for fixed-bottom and floating OWTs [10] [11] [12]. The effects of nonlinear wave kinematics [13][14][15], as well as fatigue loads, resonance phenomena, and wind-wave misalignment [16][17][18] have been found to be of primary importance for reliably predictions of FOWTs response in harsh sea states. In particular, Bachynski and Moan [17] investigated the effect of ringing, a forcing load in the proximity of the resonance frequency, which is caused by higher order harmonics on Tension Leg Platform FOWTs. They found that such a nonlinear effect is determinant for a reliable estimation of short-term fatigue loads on tower and tendons.

Concerning wind and wave actions, the intrinsic stochastic nature of these two loads requires a statistical approach which considers, their correlation and their variability in time and space. The identification of the system response in terms of displacements and loads distributions requires lots of simulations which can lead to unaffordable computational costs.

On all considered, the identification of the nonlinear system response and its accurate statistical characterization call for high-fidelity computational expensive model and the simulation of lots of environmental conditions, both in normal and extreme condition. Reliability analysis performs this task of design loads extrapolation and reliability assurance. it can be carried on directly, by means of integration methods which estimate the probability of failure of the structure in its service life, or indirectly, by means of Inverse Reliability Methods (IRMs). The latter have a reduced computational cost since the probability of failure is set according to chosen return period. On the contrary, the high sensitivity to approximation of such procedures make accuracy the core task for not invalidating the design process.

However, when a very large number of simulations needs to be performed, e.g., in optimization procedures and reliability analysis, the computational cost of time-domain models may become unaffordable. The trade-off between accuracy and computational cost is therefore a basilar aspect of the design problem of a FOWT. Within this framework, FD models have become very popular in the research field. They adopt linearization for nonlinear terms, such as the drag force of the Morison's equation. Moreover, only steady load conditions can be treated. Despite these negative points, their extreme efficiency makes them very competitive when lots of simulations need to be performed. The first frequency-based parametric study was carried out by Sclavounus et al. [19]. They performed one of the first parametric design study of a FOWT and its mooring system based on a coupled FD model [20]. It was adopted a six-degree of freedom (DoF) platform model in which mooring lines and turbine contribution were modelled as added inertial, damping and stiffness matrices obtained from a linear analysis performed in FAST [1] around the steady state operating point of the system. Linear hydrodynamic contributions were calculated by the potential

flow solver WAMIT [21] at different frequencies. The optimization was performed with the intent of reducing significant quantities, such as nacelle acceleration and platform mass. Similar FD models were presented in [22] and [23]. Karimi et al. [24] performed a FD-based multi-objective optimization of a 5 MW FOWT aimed at controlling the construction costs. Dou et al. [25] proposed a FD-based optimization in which the nacelle displacement in the wind/wave direction and the platform motions were considered as DoFs. Recently, Tower-Platform FD models, have been successfully validated [26] [27] and proposed for the optimization of 10MW FOWTs [25] [28]. Optimization procedures were also focused on mooring lines. A FD model was used in [29] to reduce the cable length of a semisubmersible platform. More recently, Bruschi et al. [30] and Barbanti et al. [31] investigated the optimal amount of mass and position of clump weights in order to minimize the platform response. Also new mooring lines configurations [32] and platform shapes, suitable for larger WT, have been studied both numerically [33] and experimentally [3]. Although several critical aspects, such as short-term and long-term response [34], wind-wave misalignment [32] and extreme loads [35], of very large WTs have already been studied, the design of optimal supporting platform suitable for 10MW+ WTs is still an open problem. So far, design approaches based on power ratios rational upscaling [36], [34] have been proposed for the dimensioning of floating systems suitable for larger wind turbines. Such methods allows to obtain a platform suitable for a particular turbine by scaling a platform designed for a different turbine. The new floater is designed by scaling up all the geometry by the square root of the ratio between the powers of the two turbines. Although it is a very fast and simple procedure, it may lead to overdesigned systems, resulting in an uneconomic designs [28], [37]. Both these critical aspects are of primary importance for the power output and for the reduction of the price of electricity produced by a WT, i.e., the Levelized Cost of Electricity (LCOE), which, as acknowledged by both academic ([28], [38], [39]) and industrial sectors (https://www.naweawindtech2021.org/), is going to be the main goal for the next decade for the offshore renewable energy sector.

Since the substructure contributes for the 30% to the whole cost of a FOWT, new early-stage platform design strategies are needed. For this reason, the novelty of this research is the development and application of optimization procedures (including site-specific) able to manage contrasting targets, such as the enhancement of structural performances, also in a lifetime perspective, and the reduction on the manufacturing costs. While the latter is an evident instrument for the reduction of the LCOE, the former is beneficial as well to this objective since an optimized system from a structural point of view will suffer less failures and will require less maintenance.

Although the key task for WTs is the maximization of the production of energy, especially for floating systems undergoing very large displacements and rotations, this aspect is strongly influenced by the system dynamics. As highlighted by Robertson et al. [5], the floater concept can significantly alter the WT performances also in terms of power production. Moreover, Hegseth et al. [40], investigating the optimal

concept of a spar-like platform from a structural point of view, found that a shape which reduces rotation amplitudes was beneficial not only for the WT performances but also for the control system.

Recently, Chen et al. [41] studied the effects of the platform motions on aerodynamic performances of a FOWT, proving that the increase of motion amplitude and the combined surge-pitch action negatively affects the power generation. In this regard, Ali Shah et al. [38] addressed that for the reduction of the LCOE, new control strategies based not only on the maximization of the power output, but also on the minimization of platform motions and load mitigations are necessary. Both active and passive control methods have been recently studied for this purpose. Wakui et al. [42] developed a model predictive control system which stabilizes the power output and the platform motions based on preview of the incoming wind and wave. Verma et al. [43] developed an optimized Tuned Mass Damper (TMD) design for the mitigation of fatigue loads and the stabilization of the power generation. In the framework of platform control strategies, Yu et al. [44] proposed an active ballast system for the reduction of the motions for the OO-Star and the NAUTILUS floaters. Moreover, innovative platform concepts with a floating keel working as a stabilizing control system have been recently propose, such as the TetraSpar [45], [46].

Indeed, the mitigation of the pitch rotation, dominated mostly by the platform dynamics, strongly affects the nacelle accelerations [20], which has been widely adopted as an indicator of the rotor performances when the analyses were performed considering only the floater, [24], [19]. Thus, by optimizing the substructure from a structural point of view, especially on a lifetime perspective, it is possible to achieve also advantages to the lifetime power output.

Within this context, firstly, a coupled FD model is developed and validated. FD models have been successfully applied for optimizations of 10MW FOWTs supported by spar-like platforms [40], whose hydrodynamic model is simpler than semisubmersible concepts [47], which generally require the solution of the potential flow problem by means of a Boundary Element Method (BEM). This process requires the integration of the dynamic pressure arising by the velocity potential on the wetted surface of the platform, and can be generally done with any commercial code like WAMIT [21] or ANSYS AQWA [48]. Within an optimization framework, the solution of the potential flow problem at each objective function evaluation would require an unaffordable computational time. To circumvent this issue, in this thesis, the computation of the hydrodynamic coefficients is done in a new straightforward way by estimating outside the optimization procedures the coefficients of Added Mass, Radiation Damping and Hydrodynamic forces, over a grid of values, and interpolating them with multidimensional functions. In this way, the computational cost is drastically reduced. Also, procedures for the extrapolation of stresses on the WT and the mooring lines from the FD results are proposed and validated.

Concerning the optimization processes, they are focused on semisubmersible 10MW FOWTs in a Site-specific perspective for two installations in the Mediterranean Sea. Researches concerning installation sites

in the Italian waters have been carried out by Maienza et al [49]. They performed a sensitivity analysis of the main cost parameters for floating wind farms, such as the distance to the coast and the water depth. As far as it regards structural analyses, Ghigo et al. [39] performed platform optimization and cost analysis of a floating wind farm located near the island of Pantelleria. However, the work addressed on hydrostatic stability and very simplified modeling approaches.

Although dynamic analyses on FOWTs based on real records have been widely performed both in time-domain ([35], [34]) and FD ([28], [40]), there is still lack on research concerning coupled dynamic simulations of FOWTs for the Mediterranean Sea, which presents environmental conditions that are different with respect to installations in the northern Europe: large bathymetry (critical aspect for the design of mooring lines) and milder environmental conditions (reduced hydrodynamic loads and low wind resource).

Furthermore, even if the optimization procedures are carried on considering design variables only related to platform geometry and mooring layout, as a further innovative aspect, anchoring systems are also considered. This is done by employing early-stage design equations provided by international regulations and producers ([50], [51]), allowing to check also the feasibility of the anchors, which, especially for large WTs and very deep water, may become a crucial task in the design process. In conclusion, this work proposes Site-specific FD-based optimization procedures on the whole floating foundation (platform, moorings, and anchors) which consider as objective functions, both costs and structural performances under extreme and fatigue load conditions, aiming at finding the system characteristics which most effectively can minimize the LCOE of FOWTs.

1.3   Research outline

In this section, the dissertation structure is briefly described. Coupled FD modelling will be presented from Chapter 2 to Chapter 5. Consequently, optimization procedures will be illustrated, with particular attention to the characterizations of the wind-wave loading at a given site. Then, such loads will be considered in an optimization framework aiming at finding an optimal, site-specific, floating substructure.

Chapter 2 concerns the hydrodynamic modelling of the floating platform under the wave action. Firstly, the hydrodynamic modelling will be discussed, focusing the attention to the hydrostatic and hydrodynamic problems. In particular, hydrostatic stability and the potential flow theory will be deepened, providing practical example on two floater technologies. In the framework of linear hydrodynamics, only First-Order wave theory will be presented. Secondly, the derivation of the equation of motions of the platform will be illustrate, adopting both time-domain and FD representation. The nonlinear hydrodynamic of slender elements and of elements subjected to transverse flow will discussed, providing linearization procedures which allows to consider such elements also in a FD model.

Chapter 3 will be focused on mooring lines. The quasi-static model will be presented for both catenary (suspended or resting on the seabed) and taut (inclined and vertical) cables. Then, the formulation of the single cable stiffness matrix, i.e., with respect to the cable reference frame, will be derived and adopted to obtain the mooring system stiffness matrix, i.e., with respect to the platform reference frame. Appendix A will provide the expression of the generalized mooring stiffness matrix. In conclusion, the procedure for the estimation of the static displacement of a FOWT will be described and applied to two case-study: a semisubmersible platform with slack-catenary moorings and a TLP.

Chapter 4 illustrates the Wind Turbine modelling. At first, WT aerodynamics will be treated. Then, two possible procedures for the identification of the WT contributions to the equation of motion in FD will be presented. The first one involves linearized simulations in FAST and a Multi Blade Coordinate (MBC) transformation procedure to estimate the effects of the rotating rotor. The second one is a simplified method which allows to obtain the contributions from a Finite Element modal analysis and to calculate the aerodynamic damping from TD simulations of the isolated rotor under different wind speed. in conclusion, wind load modelling will be discussed according to the international regulations.

The validation of the coupled model is described in Chapter 5. The NREL 5MW OC4 DeepCwind semisubmersible FOWT [47] will be adopted as benchmark for the validation against the results obtained from TD simulation performed in FASTv8. Firstly, the validation concerns the Response Amplitude Operators (RAOs), secondly, the response under turbulent wind and irregular wave. In this Chapter, the procedure for tracing back stresses on the turbine and the mooring lines will also be presented.

Chapter 6 concerns the optimization 10 MW semisubmersible FOWT considering the peaks of the RAO at platform eigenfrequencies as target to be minimized. This procedure is focused on the dynamic properties of the substructure (platform +moorings) and on the calculation of the Response Amplitude Operators (RAOs). It gives very useful insight about the characteristics of the platform and the mooring system which most effectively influences the dynamic response in a particular DoF of a semisubmersible FOWT. Namely, it results in a sort of sensitivity analysis focused on the substructure geometry. Choice of the platform shape, identification of the design variables and hypothesis on the hydrodynamic contributions will be described. The procedure consists in two optimizations: the first one is carried out considering only design variable related to the platform geometry, while the second considering both platform and mooring geometry.

The design loads environment identification is presented in Chapter 7. The procedure for the extrapolation of the wind-wave characteristics is presented for three sites: one in shallow water from the North sea, and two in deep- water in the Mediterranean sea.

Chapter 8 is focused on the site-specific Reliability Based optimization of a 10 MW semisubmersible FOWT suitable for the two installations in deep water identified in Chapter 7. A procedure structured in 3 stages is

proposed to find the best solution in terms of platform and mooring system. The optimizations are targeted to enhancing structural performances, both under extreme and fatigue load conditions, but controlling the costs, and therefore reducing the LCOE.

Conclusion, remarks, and future development are presented in Chapter 9.

Chapter 2.
Floating platform

A FOWT is a complex multibody system, which is exposed to a multi-physics fluid-structure interaction involving wind and water (waves and currents). To properly reproduce the dynamic response of a FOWT, nonlinear aero-hydro-servo-elastic numerical simulations in the time-domain are usually necessary. The common approach is to combine modal- and multibody-dynamics formulations. As far as it regards the WT, both blades and tower are modelled as flexible elements adopting a linear modal representation, considering three DoFs for the blades (two flapwise and one edgewise bending-mode) and four DoFs for the tower (two fore-aft and two side-to-side bending mode). Nacelle and hub are modelled as rigid bodies, with appropriate lumped mass and inertia.

As far as it regards the floating platform, since it is supposed to be stiffer than blades and tower, hydro-elastic effects can be neglected. Therefore, the kinematics and kinetics can be well represented by a six-DOF-rigid-body model: three displacements, surge, sway, heave, and three rotations, roll, pitch, yaw. Also small-angle assumption is considered.

Different representations can be adopted for the mooring lines. The simplest is by means of a quasi-static model which, at each time step, iterates the catenary system of equation in order to change the stiffness of the mooring and the forces exerted at the platform fairleads. More sophisticated models divide the cable into elements characterized by lumped mass, connected to each other by springs and dampers. Moreover, applying Morison's equation, hydrodynamic loads due to sea waves and current can be distributed along the cables. Latest development allows also to consider localised rotational stiffness which arises when mooring chain rings rubbed together.

2.1   Hydrodynamic modelling

As already explained, when dealing with such complex structural systems under wind-waves dynamic loadings, Computational Fluid Dynamics (CFD) simulations are still unaffordable for the hydrodynamic modeling of the floater, due to the magnitude of the domain (order of kilometres). To overcome this issue, simplified approaches have been developed making use of the potential flow theory.

The modelling of a floating body under wave loading can be subdivided into two problems: static equilibrium and dynamic equilibrium, respectively hydrostatics and hydrodynamics.

2.1.1.   Hydrostatic problem

Hydrostatics solves the equilibrium (if it exists) of floating bodies in still water by applying the Archimedes principle. The platform is subjected to a static pressure exerted by the fluid on its wetted surface. The system is considered to be in equilibrium if the resultant fluid force, which is equal to the weight of the displaced volume of water, is equal to the total weight of the body [52]:

$$\rho_{h_2o} g \iiint_V dxdydz - W_{tot} = 0, \tag{2.1}$$

where ρ_{h_2o} is the water density, g is the gravity acceleration, $\iiint_V dxdydz$ is the volume of the body immersed in the fluid, i.e., the buoyancy volume, and W_{tot} is the total weight of the body. At the equilibrium position, a right-handed reference frame (x, y, z), fixed with respect to the mean position of the body, is established. The vertical z-axis is set positive upwards through the CoM of the body and the origin in the plane of the undisturbed free surface (Figure 4).

2.1.2.   Hydrostatic stability

Eq. 2.1 ensure the floatation of the system. The equilibrium configuration can be either neutral, unstable, or stable. In the case of horizontal displacements, surge and sway motions, and yaw motion, the equilibrium is neutral, unless horizontal forces due to wind (Rotor thrust) and waves (sea current) and/or wind-wave misaligned loads are applied. For the yaw case, the stability is guaranteed by the mooring system. Eq. 2.1 ensure the stability with respect to vertical displacement, heave motion. For pitch and roll, the equilibrium depends mostly by the characteristics of the floater. In particular, if holds [53]

$$\overline{GM} = \overline{KB} - \overline{KG} + \overline{BM} > 0, \tag{2.2}$$

the equilibrium with respect to roll and pitch motions is stable. Referring to Figure 4, $\overline{GM}$ is the distance between the body CoM, G, and the Metacentre, M; $\overline{KB} - \overline{KG}$ is the distance between the Centre of Buoyancy (CoB) and the CoM, while $\overline{BM}$ is the distance between the CoB and the Metacentre.
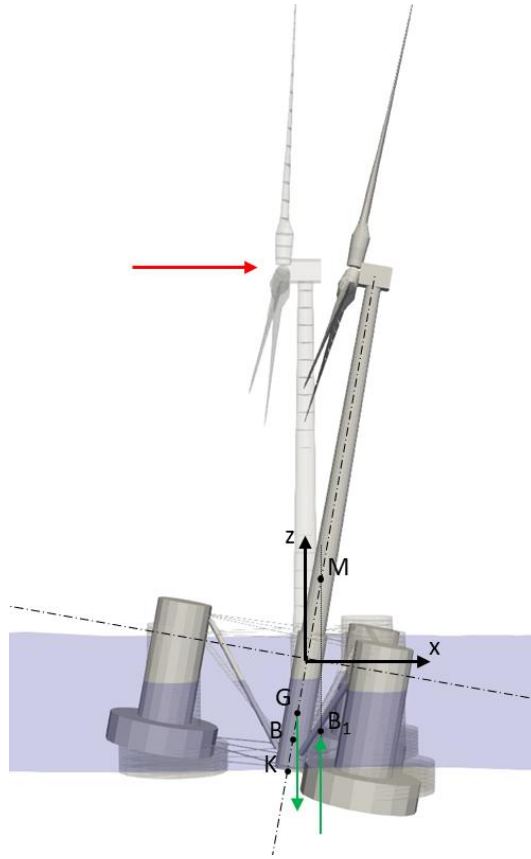
Figure 4: Reference frame for Hydrostatic stability analysis

The segment $\overline{\text{BM}}$ can be calculated considering the hull waterplane area, i.e. the intersection between hull and still-water level surface [53]:

$$\overline{\text{BM}} = \frac{I_{xx}}{V_0},$$

(2.3)

Where, I_{xx}, is the second moment of area of the waterplane area (A_{WL} in Figure 5) and V_0 is the buoyancy volume.
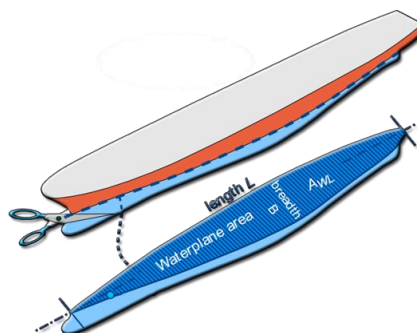
Figure 5: Waterplane area (https://www.mecaflux.com/en/Maitre_couple.htm).

Considering the inequality in Eq. 2.2, the larger is $\overline{GM}$, the *more* stable is the floater. This condition can be achieved either by increasing the waterplane area, maximizing $\overline{BM}$, which is the case of barge-like systems, or by maximizing $\overline{KB} - \overline{KG}$, therefore increasing the depth of the platform CoM, which is the case of spar-like solution.

2.1.3. Hydrostatic stiffness matrix

When a body is freely floating, restoring forces and moments arise from the effects of the water-plane area and the CoB. Such force and moment components can be written as [54]:

$$F^{Res}{}_k = -C^{Hydro}{}_{kj} q_j, \tag{2.4}$$

where q_j, $j = 1, 2, \dots, 6$ is the j-th component of the displacement vector, while $C^{Hydro}{}_{kj}, k = 1, 2, \dots, 6$, is the k-th, j-th component of the so-called hydrostatic stiffness matrix. When the floating body has x-z plane as a symmetry plane, the only non-zero components are [54]:

$$C^{Hydro}{}_{33} = \rho_{h_2o} g A_{WL}, \tag{2.5a}$$

$$C^{Hydro}{}_{44} = \rho_{h_2o} g V_0 z_B + \rho_{h_2o} g \iint_{A_{WP}} y^2 \, ds, \tag{2.5b}$$

$$C^{Hydro}{}_{55} = \rho_{h_2o} g V_0 z_B + \rho_{h_2o} g \iint_{A_{WP}} x^2 \, ds, \tag{2.5c}$$

where z_B is the CoB draft with respect to the reference frame previously described. Referring to Eqs. 2.5b-2.5c, roll and pitch restoring moments are computed relying only on system's CoB and water plane area moment of inertia contributions. For the complete estimation of such restoring moments, also the contribution related to the mass components should be considered, i.e., the static mass moment of the whole system (in the case of a FOWT: Rotor, Nacelle, Tower and Floater).

2.1.4. Hydrodynamic problem

The floating platform dynamic behaviour is deeply influenced by the characteristic of the incoming waves. These loadings are random processes that, from an engineering point of view, can be assumed stationary. Moreover, the attention is focused on wind-induced waves, propagating in only one direction, which is the case of long-crested irregular seas. In this case, the instantaneous wave elevation can be assumed a stationary, zero mean Gaussian process. Therefore, it can be characterized by the variance, σ_η^2 [53]:

$$\sigma_\eta^2 = \int_0^\infty S_{\eta\eta}(\omega) \, d\omega, \tag{2.6}$$

where $S_{\eta\eta}(\omega)$ is the one-sided wave spectrum. The irregular wave is assumed to be composed by a superimposition of regular waves (pure harmonic functions which propagate with only one circular frequency, ω) with wave amplitudes, ζ_i, equal to [53]:

$$\zeta_j = \sqrt{2S_{\eta\eta}(\omega_j)\Delta\omega_i}, \tag{2.7}$$

This way, the wave elevation of a long-crested irregular sea propagating along the x-axis can be written as the sum of a large number of wave components [53]:

$$\zeta(t) = \sum_{j=1}^{N} \zeta_j \sin(\omega_j t - k_j x + \varepsilon_j), \tag{2.8}$$

Here k_j and ε_j are respectively wave number and random phase angle of the j-th wave component. ε_j is normally distributed between 0 and 2π and constant with time. For deep water ω_j and k_j are related by the dispersion relation.

2.1.5. Wave spectra

As can be seen from Eq. 2.7, the wave spectrum relates the time domain solution of the waves (Eq. 2.8) to the FD representation. The common practice is to statistically determine $S_{\eta\eta}(\omega)$ from wave measurements, assuming the sea state as a stationary random process. For Offshore wind engineering purposes, two wave spectra are generally adopted: The Pierson-Moskowitz (PM) and the Joint North Sea Wave Project (JONSWAP) spectra. They both depend on two parameters: the significant wave height, H_s, and the peak spectral period, H_s. The Pierson-Moskowitz wave spectrum is used to describe the statistical properties of fully developed seas. The Power Spectral Density (PSD) function of the wave elevation is expressed as [54]:

$$S_{PM}(\omega) = \frac{1}{2\pi}\frac{5}{16} H_s^2 T_P \left(\frac{\omega T_P}{2\pi}\right)^{-5} \exp\left[-\frac{5}{4}\left(\frac{\omega T_P}{2\pi}\right)^{-4}\right], \tag{2.9}$$

Where H_s and T_P refer to the significant wave height and the peak spectral period of the incoming irregular wave; ω is the circular frequency. the JONSWAP wave spectrum is a modified PM spectrum, obtained introducing of a peak shape parameter, γ, and a scaling factor, $\sigma(\omega)$:

$$S_J(\omega) = \frac{1}{2\pi}\frac{5}{16} H_s^2 T_P \left(\frac{\omega T_P}{2\pi}\right)^{-5} \exp\left[-\frac{5}{4}\left(\frac{\omega T_P}{2\pi}\right)^{-4}\right][1 - 0.287ln(\gamma)]\gamma^{\exp\left\{-0.5\left[\frac{\frac{\omega T_P}{2\pi}-1}{\sigma(\omega)}\right]^2\right\}}, \tag{2.10}$$

It is recommended that the scaling factor and the peak shape parameter be derived from the significant wave height and peak spectral period as follows:

$$\sigma(\omega) = \begin{cases} 0.07 & for\ \omega \leq \frac{2\pi}{T_P} \\ 0.09 & for\ \omega > \frac{2\pi'}{T_P} \end{cases} \tag{2.11}$$

$$\gamma = \begin{cases} 5 & for\ \dfrac{T_P}{\sqrt{H_s}} \leq 3.6 \\ \exp\left(5.75 - 1.15\dfrac{T_P}{\sqrt{H_s}}\right) & for\ 3.6 < \dfrac{T_P}{\sqrt{H_s}} \leq 5, \\ 1 & for\ \dfrac{T_P}{\sqrt{H_s}} > 5 \end{cases} \tag{2.12}$$

A comparison between PM and JONSWAP spectrum is presented in Figure 6. As it is possible to observe, the PM spectrum has a wider band of excited frequencies with respect to the JONSWAP. It presents also a smaller peak in the proximity of the spectral period. The first has been developed for fully developed sea, while the second one has been derived from the first one and adopted for limited fetch situations, where the sea condition is never fully developed due to the interaction between wind-generated waves.

(a) (b)
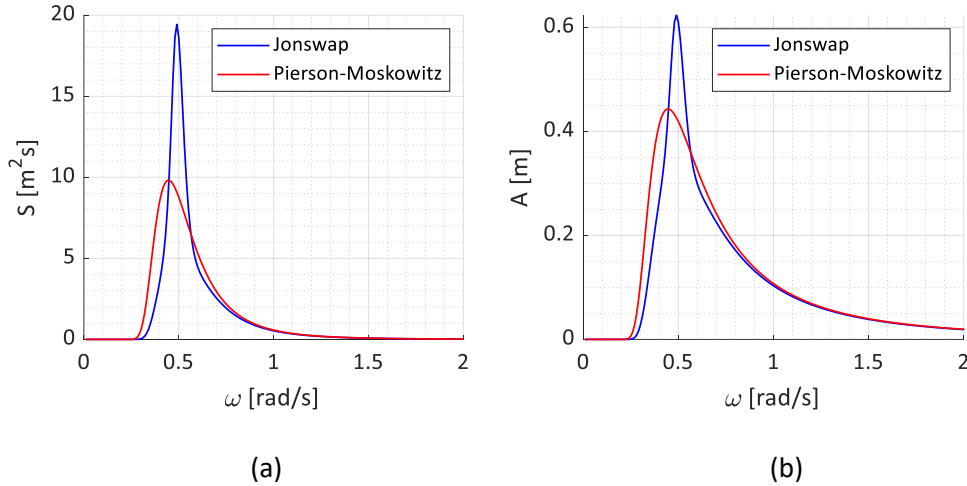
Figure 6: Comparison of JONSWAP and PM spectra (a) and wave amplitudes (b) for H_S=7 m and T_P=10 s.

2.1.6.   Linear wave theory

In this section, the linear wave theory is presented. The sea water is assumed incompressible and inviscid. The fluid motion is irrotational. Under such hypotheses, it exists a velocity potential, φ, which can be used to describe the fluid velocity, $\mathbf{V}(x,y,z,t)$, in a Cartesian coordinate system fixed in space [55]:

$$\mathbf{V}(x,y,z,t) = \nabla\varphi(x,y,z,t) = \frac{\partial\varphi(x,y,z,t)}{\partial x}\mathbf{i} + \frac{\partial\varphi(x,y,z,t)}{\partial y}\mathbf{j} + \frac{\partial\varphi(x,y,z,t)}{\partial z}\mathbf{k}, \tag{2.13}$$

where $(\mathbf{i}, \mathbf{j}, \mathbf{k})$ is the orthonormal base of the fixed cartesian coordinate system (x,y,z). Since the fluid is incompressible, it follows that the velocity potential satisfies the Laplace equation [52]:

$$\nabla^2 \varphi = \frac{\partial^2 \varphi}{\partial x^2} + \frac{\partial^2 \varphi}{\partial y^2} + \frac{\partial^2 \varphi}{\partial z^2} = 0, \tag{2.14}$$

From the hypotheses, the pressure distribution, p, follows the Bernoulli's equation:

$$p + \rho_{h_2 o} g z + \rho_{h_2 o} \frac{\partial \varphi}{\partial t} + \frac{1}{2} \rho_{h_2 o} \mathbf{V} \cdot \mathbf{V} = C, \tag{2.15}$$

Where $\rho_{h_2 o} g z$ is the gravity potential, assumed to be the only external force field, and C is an arbitrary constant.

2.1.6.1. Boundary conditions

The velocity potential φ can be found by solving Eq. 2.14 with relevant boundary conditions. When a body is fixed in a moving fluid, the velocity potential at the contact surface in the normal direction, $\frac{\partial \varphi}{\partial n}$, must be equal to zero due to impermeability principle:

$$\frac{\partial \varphi}{\partial n} = 0, \tag{2.16}$$

here $\frac{\partial}{\partial n}$ express the derivative in the normal to the body surface. If the body is moving with a certain velocity $\mathbf{U}$, Eq. 2.16 can be generalized into

$$\frac{\partial \varphi}{\partial n} = \mathbf{U} \cdot \mathbf{n}, \tag{2.17}$$

where $\mathbf{n}$ is the normal vector. Eqs. 16 and 17 are kinematic boundary conditions. In the particular case of the free-surface, $z = \zeta(x, y, t)$, assuming a fluid particle to remain of the free-surface, it is possible to write another kinematic boundary condition:

$$\frac{\partial \zeta}{\partial t} + \frac{\partial \varphi}{\partial x} \frac{\partial \zeta}{\partial x} + \frac{\partial \varphi}{\partial y} \frac{\partial \zeta}{\partial y} - \frac{\partial \varphi}{\partial z} = 0 \quad \text{on} \quad z = \zeta(x, y, t), \tag{2.18}$$

For the derivation of Eq. 2.18, the reader may refer to [52].

At the free surface, $z = \zeta(x, y, t)$, a condition on the pressure field can be imposed. Due to the equilibrium principle, the water pressure must be equal to the atmospheric pressure, p_0. Choosing C equal to p_0, Eq. 2.15 can be rewritten as follows:

$$g\zeta + \frac{\partial \varphi}{\partial t} + \frac{1}{2} \left(\left(\frac{\partial \varphi}{\partial x}\right)^2 + \left(\frac{\partial \varphi}{\partial y}\right)^2 + \left(\frac{\partial \varphi}{\partial z}\right)^2 \right) = 0 \quad \text{on} \quad z = \zeta(x, y, t), \tag{2.19}$$

Both Eqs. 2.18 and 2.19 are nonlinear. The problem can be simplified considering that the structure which interacts with the fluid has no forward speed and neglecting current effects. Then the free-surface conditions are linearized assuming the wave amplitude small compared to the wavelength. Firstly, the

conditions are transferred from the exact free-surface, $z = \zeta(x, y, t)$, to the mean free-surface, $z = 0$. Then, nonlinear terms in the wave amplitude are neglected, leading to:

$$\frac{\partial \zeta}{\partial t} = \frac{\partial \varphi}{\partial z} \quad \text{on} \quad z = 0, \tag{2.20}$$

$$g\zeta + \frac{\partial \varphi}{\partial t} = 0 \quad \text{on} \quad z = 0, \tag{2.21}$$

When the velocity potential, φ, is oscillating in time with circular frequency ω, and combining Eqs. 2.20 and 2.21, as single linearized dynamic free-surface can be rewritten:

$$-\omega^2 \varphi + g \frac{\partial \varphi}{\partial z} = 0 \quad \text{on} \quad z = 0, \tag{2.22}$$

2.1.6.2.   Velocity potential

Linear wave theory can be derived for propagating waves by assuming a horizontal sea bottom and a free-surface of infinite horizontal extent. Laplace equation (Eq. 2.14) is solved with the dynamic boundary condition (Eq. 2.22) and the sea bottom condition:

$$\frac{\partial \varphi}{\partial z} = 0 \quad \text{on} \quad z = -h, \tag{2.23}$$

where h is the water depth. The analytical solution for this problem can be derived adopting the separation of variables. Different expression for the linear wave velocity potential can be found whether the problem is in finite water depth or infinite water depth. In the equations below, the expressions of velocity potential are reported for both cases [52]:

$$\varphi = \frac{g\zeta}{\omega} e^{-kz} \cos(\omega t - kx) \quad \text{when} \quad h \to \infty, \tag{2.24}$$

$$\varphi = \frac{g\zeta}{\omega} \frac{cosh[k(z+h)]}{cosh(kh)} cos(\omega t - kx) \quad \text{otherwise}, \tag{2.25}$$

where ζ is the wave amplitude and k is the wave number, related to the wavelength, λ, by

$$\lambda = \frac{2\pi}{k}, \tag{2.26}$$

The wave number k is also related to the wave frequency ω by the dispersion relation

$$\frac{\omega^2}{g} = k \quad \text{when} \quad h \to \infty, \tag{2.27}$$

$$\frac{\omega^2}{g} = k \tanh(kh) \quad \text{otherwise}, \tag{2.28}$$

2.1.7. Diffraction and radiation problems

The potential flow theory can be applied to solve the hydrodynamic problem, i.e., to estimate the total velocity potential which arise around a freely floating body [52]. Assuming linear wave theory, under the hypothesis of small displacements, and steady state conditions, the total velocity potential, φ, can be rewritten isolating the dependency of time [55]

$$\varphi(x,y,z,t) = \phi(x,y,z)e^{-i\omega t}, \tag{2.29}$$

The spatial velocity potential $\phi(x,y,z)$ can be split into two different contributes:

$$\phi(x,y,z) = \phi_D(x,y,z) + \phi_R(x,y,z), \tag{2.30}$$

where $\phi_D(x,y,z)$ is the diffraction velocity potential and $\phi_R(x,y,z)$ is the radiation velocity potential. They are the solution of two different sub-problems:

1. Diffraction problem: the floating body is fixed in its reference position and is subjected to an incident wave. The solution of the potential flow results from the superimposition of the undisturbed incident wave velocity potential, $\phi_0(x,y,z)$ (which is given by Eq. 2.24 or 2.25) and the so-called scattering potential $\phi_7(x,y,z)$, which results from the application of a particular boundary condition which let $\phi_D(x,y,z)$ satisfies the impermeability principle in Eq. 2.16 at the wetted surface of the body:

$$\frac{\partial \phi_7}{\partial n} = -\frac{\partial \phi_o}{\partial n}, \tag{2.31}$$

2. Radiation problem: the fluid is in quiet; the floating body oscillates in its six DoFs separately with the same frequency of the incoming wave. $\phi_R(x,y,z)$ results from the superimposition of the six velocity potentials, $\phi_i(x,y,z)$ associated with each body motion. The the solution of the velocity potential is found by imposing at the wetted surface a moving boundary condition like Eq. 2.17.

$$\frac{\partial \phi_i}{\partial n} = n_i \quad i = 1,2,\ldots,6, \tag{2.32a}$$

where $\boldsymbol{n}$, is the outward normal to the body surface, n_i is defined by [55]

$$\boldsymbol{n} = \begin{bmatrix} n_1 \\ n_2 \\ n_3 \end{bmatrix}, \boldsymbol{r} \times \boldsymbol{n} = \begin{bmatrix} n_4 \\ n_5 \\ n_6 \end{bmatrix} \tag{2.32b}$$

Where $\boldsymbol{r}$, is the position vector.

These two Boundary Value Problems (BVPs) requires numerical methods for the discretization of the whole fluid domain (Figure 7 [52]) around the floating body and for the calculation of such potentials.
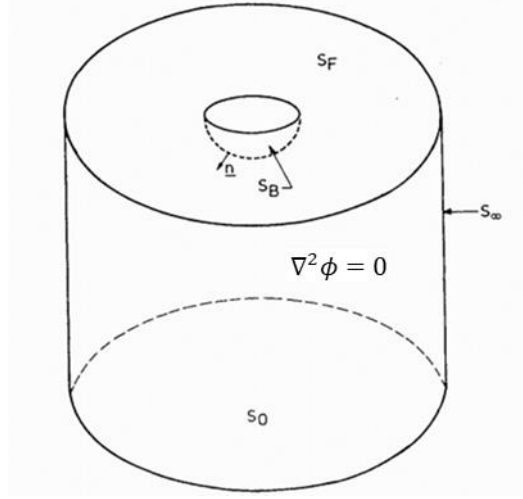
Figure 7: BVP of a floating body [52].

Referring to Figure 7, on the fluid surface SF, the dynamic boundary condition is applied, on the sea-bottom surface, the boundary condition in Eq. 2.22 is applied. Particular is the case of S_∞, where a radiation condition, which ensure that the wave propagates away from the body, has to be applied. On the floating body, whether scattering or moving boundary condition is applied, depending on Diffraction or Radiation problems, respectively. Once the boundary conditions are set, the boundary integral equation can be written as [52]

$$\iint_V \phi \cdot \nabla^2 (\phi) dV = \iint_S \phi \cdot \frac{\partial \phi}{\partial n} dS \qquad S = S_F \cup S_0 \cup S_\infty \cup S_B, \qquad (2.33)$$

Eq. 2.33 is rewritten invoking Green's second theorem, valid for any potential function. This procedure transforms a large volume-integral into a much easier to handle surface-integral. Considering two separate velocity potentials ϕ_j, ϕ_k, applying Green second theorem:

$$\iint_V (\phi_j \nabla^2 \phi_k - \phi_k \nabla^2 \phi_j) dV = \iint_S \left(\phi_j \cdot \frac{\partial \phi_k}{\partial n} - \phi_k \cdot \frac{\partial \phi_j}{\partial n} \right) dS \qquad S = S_F \cup S_0 \cup S_\infty \cup S_B, \quad (2.34)$$

Since the Laplace equation is valid for both ϕ_j, ϕ_k, left-hand side of Eq. 2.34 becomes zero, leading to the integral equation

$$\iint_S \left(\phi_j \cdot \frac{\partial \phi_k}{\partial n} \right) dS = \iint_S \left(\phi_k \cdot \frac{\partial \phi_j}{\partial n} \right) dS \qquad S = S_F \cup S_0 \cup S_\infty \cup S_B, \qquad (2.35)$$

As first shown by Lamb [55], the solution of $\phi_i(x, y, z)$, i= 1, 2,... 7, can be written as

$$\phi_i(x,y,z) = \iint_{S_B} Q_i(\xi,\eta,\zeta) G(x,y,z,\xi,\eta,\zeta)\, dS \qquad i = 1,2,\dots 7, \tag{2.36}$$

where $\phi_i(x,y,z)$, is the potential function in the point (x,y,z) at the mean wetted surface of the body, S_B; $Q(\xi,\eta,\zeta)$, is the unknown source density function in a point (ξ,η,ζ) at the mean wetted surface of the body, S_B; $G(x,y,z,\xi,\eta,\zeta)$ is the Green's function or the influence function of the pulsating source $Q_i(\xi,\eta,\zeta)$ located in (ξ,η,ζ), to the potential $\phi_i(x,y,z)$ in (x,y,z). This Green's function is chosen to automatically satisfy the Laplace equation, the linearized boundary conditions on the sea bottom and on the free surface, and the radiation boundary condition on S_∞. By doing that, the surface integral equation is reduced only on S_B. However, the expression of $G(x,y,z,\xi,\eta,\zeta)$ gets very complicated. The source densities $Q_i(\xi,\eta,\zeta)$ are found by satisfying the body boundary conditions of the scattering (Eq. 2.31) and radiation problems (Eq. 2.32b):

$$-2\pi Q_i(x,y,z) + \iint_{S_B} Q_i(\xi,\eta,\zeta) \frac{\partial}{\partial n} G(x,y,z,\xi,\eta,\zeta)\, dS = \begin{cases} n_i & when\ i = 1,\dots,6 \\ -\frac{\partial \phi_0}{n} & when\ i = 7 \end{cases}, \tag{2.37}$$

Eq. 2.37 is solved approximating the body surface with plane quadrilateral panels. Then, the potential, $\phi_i(x,y,z)$, is found by substituting the source density functions, $Q_i(x,y,z)$, in Eq. 2.36. Using Bernoulli equation (Eq. 2.15), the dynamic fluid pressure, per unit wave amplitude and unitary body motions, can be evaluated:

$$p(x,y,z,t) = -\rho \frac{\partial}{\partial t} \varphi(x,y,z,t) = \rho_{h_2o} i\omega\big(\phi_0(x,y,z) + \phi_7(x,y,z) + \sum_{i=1}^{6} \phi_i(x,y,z)\big) e^{-i\omega t}, \tag{2.38}$$

By integrating the pressure distribution over the wetted surface and projecting in the direction n_i of Eq. 2.32b, the first-order wave exciting forces $\boldsymbol{X}(\omega)$, the added mass $\boldsymbol{A}(\omega)$, and the radiation damping $\boldsymbol{B}(\omega)$, can be evaluated [55]:

$$X_k(\omega) = -i\omega \rho_{h_2o} \iint_{S_B} \big(\phi_0(x,y,z) + \phi_7(x,y,z)\big) n_k dS \quad k = 1,2,\dots,6, \tag{2.39a}$$

$$A_{ik}(\omega) = \frac{\rho_{h_2o}}{\omega} Im\left\{ \iint_{S_B} \phi_i(x,y,z) n_k dS \right\} \quad i,k = 1,2,\dots,6, \tag{2.39b}$$

$$B_{rad,ik}(\omega) = -\rho_{h_2o} Re\left\{ \iint_{S_B} \phi_i(x,y,z) n_k dS \right\} \quad i,k = 1,2,\dots,6 \tag{2.39c}$$

2.1.8. First-Order Hydrodynamic coefficients

These three are the so-called first-order hydrodynamic coefficients, which are dependent on the platform submerged geometry. To see how the hull shape influences the first-order dynamic response of a floating body, a comparison between two different platform is presented: the OC3 Hywind Spar and the ITI Energy

Barge (see Figure 8 and 9, Table). The first achieve stability by ballast draft, increasing $\overline{KB} - \overline{KG}$ (Eq. 2.3 and Figure 5), while the second one by water plane inertia, increasing $\overline{BM}$ (Eq. 2.3 and Figure 5).

Table 1: OC3 Hywind Spar platform structural properties [4].

Depth to platform base below SWL (draft)	[m]	120
Depth to top taper below SWL	[m]	4
Depth to bottom taper below SWL	[m]	12
Diameter above taper	[m]	6.5
Diameter below taper	[m]	9.4
Platform CM location below SWL	[m]	89.92
Platform mass, including ballast	[kg]	7.47E+06
Platform Roll inertia about CM	[kgm^2]	4.23E+09
Platform Pitch inertia about CM	[kgm^2]	4.23E+09
Platform Yaw inertia about CM	[kgm^2]	1.64E+08

Figure 8: OC3 Hywind Spar FOWT [4].

Table 2: ITI Energy Barge platform structural properties [54].

Depth to platform base below SWL (draft)	[m]	4
Elevation to platform top above SWL	[m]	6
Platform side	[m]	40
Platform CM location below SWL	[m]	0.28
Platform mass, including ballast	[kg]	5.45E+06
Platform Roll inertia about CM	[kgm^2]	7.27E+08
Platform Pitch inertia about CM	[kgm^2]	7.27E+08
Platform Yaw inertia about CM	[kgm^2]	1.45E+09

Figure 9: ITI Energy Barge [54].

A comparison between the Added mass coefficients of the two platforms is presented in Figure 10. ITI Energy presents a hull surface which is mostly developed in the plane xy, while OC3 Hywind in the sheaf of planes which contains the z-axis. For this reason, the two platforms present inverse trends in the Surge-Surge (Figure 10a) and Heave-Heave masses (Figure 10b). Similar trends can be noticed for the Pitch-Pitch (Figure 10c) and Yaw-Yaw (Figure 10d) masses. In particular, A_{66} of the spar platform is nearly zero since this coefficient increases with the distance of the hull surface from the axes origin.
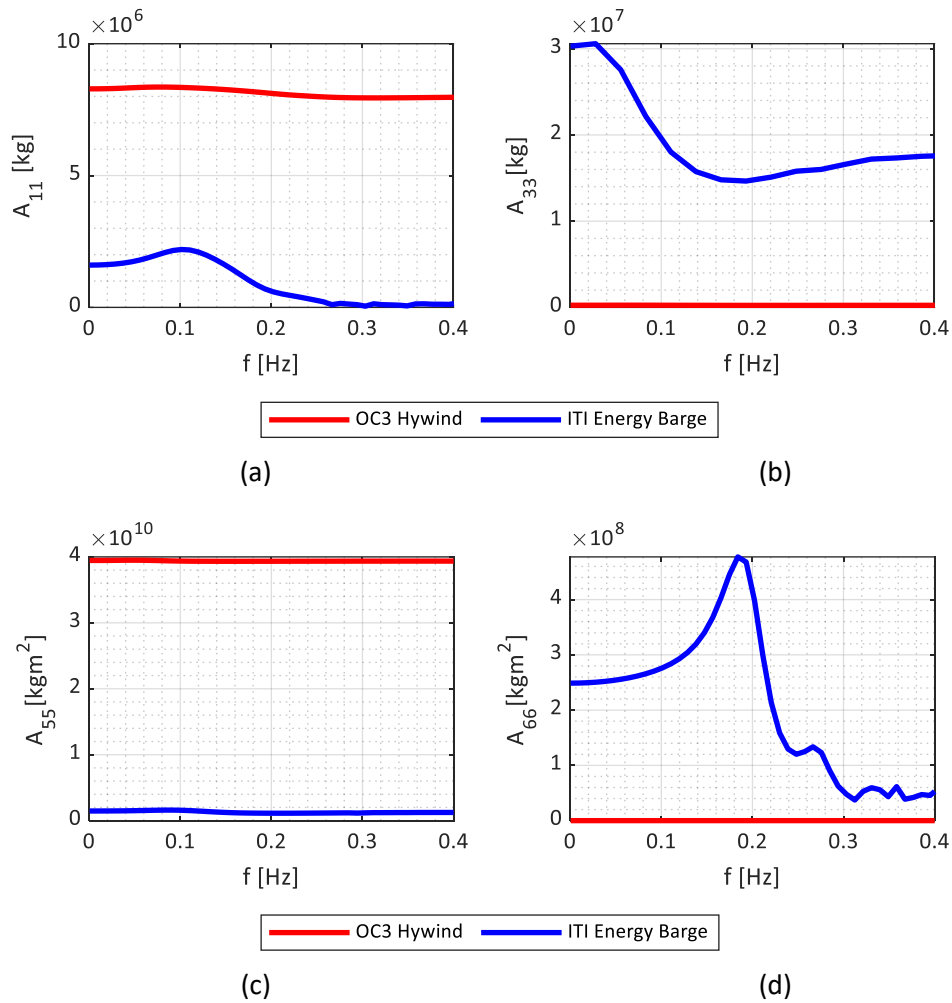
Figure 10: Comparison of OC3 Spar and ITI Energy Barge Added Mass coefficients from 0 Hz to 0.4 Hz: Surge-Surge (a), Heave-heave (b), Pitch-Pitch (c) and Yaw-Yaw (d).

As far as it regards Radiation Damping (Figure 11), ITI Energy Barge scores higher results with respect to the OC3 Hywind Spar. This is caused by the different orientations of the faces of the two hulls. The lateral surfaces of the barge platform lies completely in xz and yz planes, orthogonal to Surge and Sway directions. This leads to higher damping effects, caused by the fluid which surrounds the floater while moving, in all the DoFs, but in particular in Surge (Figure 11a) and Pitch (Figure 11c). As already explained for the coefficients A_{33} (Figure 10b) and A_{66} (Figure(10d), Heave-Heave (Figure 11b) and Yaw-Yaw (Figure 111d) Radiation damping coefficients of the spar platform are almost zero.
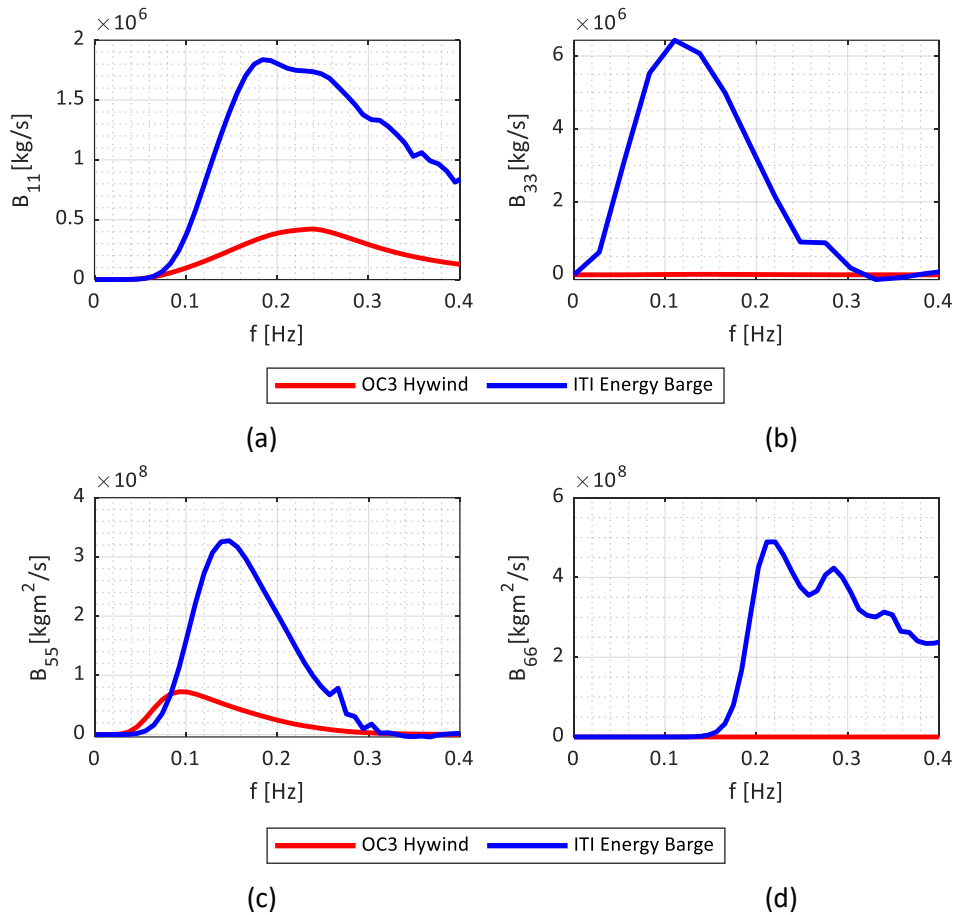
Figure 11: Comparison of OC3 Spar and ITI Energy Barge Added Mass coefficients from 0 Hz to 0.4 Hz: Surge-Surge (a), Heave-heave (b), Pitch-Pitch (c) and Yaw-Yaw (d).

The comparison of the Exciting Forces is presented in Figure 12. The magnitude of the hydrodynamic forcings is presented for Surge (Figure 12a), Heave (Figure 12b) and Pitch (Figure 12c). As it is possible to observe, the Barge platform presents larger loads per unit wave amplitude since it is a bluffer element compared to the Spar, therefore the pressures arising from incident and scattering waves are higher. For the same reason, the phase shift of such exciting forces is smoother for the Spar than the Barge, which presents an irregular trend, which starts from 0.1 Hz, for all the DoFs presented. As far as it regards Figures 12d and 12f, it is possible to observe that Surge and Pitch exciting forces are almost *in-phase* for the ITI Energy Barge, and almost in anti-phase (phase shift of about 180°) as far as it regards the OC3 Spar.
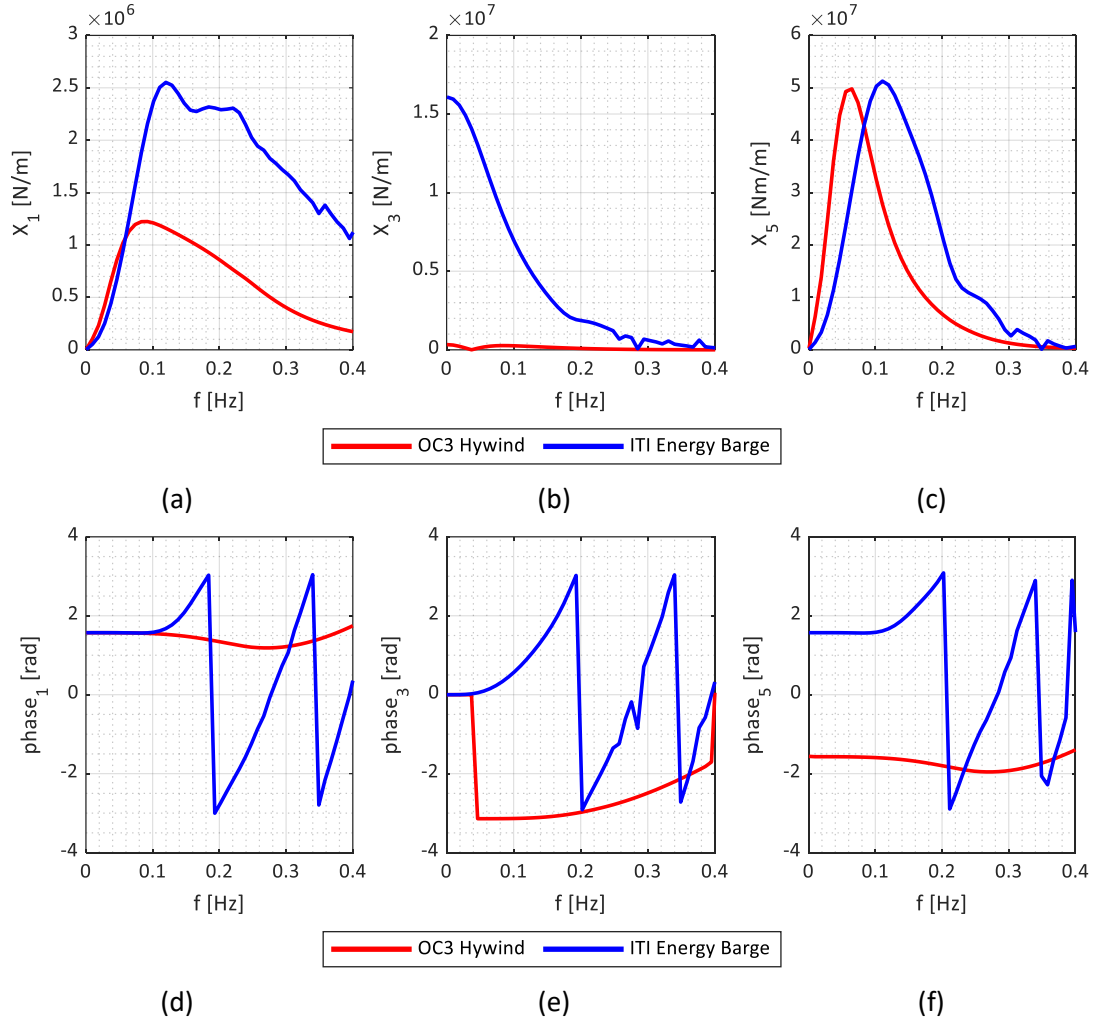
Figure 12: Comparison of OC3 Spar and ITI Energy Barge Exciting forces (per unit wave amplitude) from 0 Hz to 0.4 Hz: Surge (a), Heave (b) and Pitch (c) magnitude, Surge (d), Heave (e) and Pitch (f) phase shift.

2.2 Time domain representation

Adopting the widely adopted Cummins approach [54], the total external loads exerted on the floating platform, $F_i^{Platform}(t)$, subjected to an irregular sea state, can be written considering the contribution of hydrostatic, moorings and hydrodynamic [54]:

$$F_i^{Platform}(t) = -\mathrm{A}_{ij}\ddot{q}_j(t) + F_i^{Hydrodyn}(t) + F_i^{Lines}(t), \qquad (2.40)$$

where A_{ij} is the ij-th component of the impulsive hydrodynamic added mass matrix which derives from Eq. 2.39b [54]:

$$\mathrm{A}_{ij} = \lim_{\omega \to \infty} \mathrm{A}_{ij}(\omega), \qquad (2.41)$$

$F_i^{Hydrodyn}(t)$ and $F_i^{Lines}(t)$ are respectively the i-th components of the applied loads on the platform coming from the hydrodynamics and the mooring lines. $F_i^{Lines}(t)$ and mooring modelling will be discussed in Chapter 3. As already discussed, $F_i^{Hydrodyn}(t)$, results from the superimposition of the hydrostatic and hydrodynamic problems [54]:

$$F_i^{Hydrodyn}(t) = F_i^{Waves}(t) + \rho_{h2o}gV_0\delta_{i3} - C_{ij}^{Hydro}q_j(t) - \int_0^t K_{ij}(t-\tau)\dot{q}_j(t)d\tau, \qquad (2.42)$$

Where the terms $\rho_{h2o}gV_0\delta_{i3} - C_{ij}^{Hydro}q_j(t)$ refers to the hydrostatic contribution coming from the buoyancy forces (Eq. 2.1) and the restoring stiffness matrix (Eqs. 2.4-2.5). $F_i^{Waves}(t)$ is the represents the excitation load on the support platform from the incident waves. Considering first order wave theory, and modelling the irregular sea state (described by a certain wave spectrum, $S_{\eta\eta}(\omega)$) as a superimposition of infinite regular wave components, the wave elevation $\zeta(t)$ can be written as [54]:

$$\zeta(t) = \frac{1}{2\pi}\int_0^\infty W(\omega)\sqrt{2\pi S_{\eta\eta}(\omega)}e^{j\omega t}d\omega, \qquad (2.43)$$

where $W(\omega)$ represents the Fourier transform of a realization of a white noise process which follows a Standard Normal Gaussian distribution. $S_{\eta\eta}(\omega)$ is the one-sided wave spectrum. $F_i^{Waves}(t)$ follow directly form the definition of $\zeta(t)$ [54]:

$$F_i^{Waves}(t) = \frac{1}{2\pi}\int_0^\infty W(\omega)\sqrt{2\pi S_{\eta\eta}(\omega)}X_i(\omega)e^{j\omega t}d\omega, \qquad (2.44)$$

Where $X_i(\omega)$ is the i-th component of the first order wave exciting forces (Eq. 2.39a). as can be seen from Eqs. 2.42 and 2.43, each component of $\boldsymbol{X}(\omega)$ represents the transfer function from the wave elevation to the wave load in each DoF of the floating platform.

The term $-\int_0^t K_{ij}(t-\tau)\dot{q}_j(t)d\tau$ in Eq. 2.42 also derives from the radiation problem solution. It is a convolution integral which represent the contribution from wave-radiation damping, $\boldsymbol{B}(\omega)$ (Eq. 2.39c):

$$K_{ij}(t) = \frac{2}{\pi}\int_0^\infty B_{ij}(\omega)\cos(\omega t)\,d\omega, \qquad (2.45)$$

K_{ij} is the ij component of the wave-radiation-retardation kernel, i.e. the impulse response function of the radiation problem [54]. In the very particular case of regular waves and without considering the buoyancy force, Eq. 2.42 simplifies:

$$F_i^{Hydrodyn}(t) = -A_{ij}(\omega)\ddot{q}_j(t) + Re\{\zeta X_i(\omega)e^{j\omega t}\} - C_{ij}^{Hydro}q_j(t) - B_{ij}(\omega)\dot{q}_j(t), \qquad (2.46)$$

2.3　　　Frequency domain representation

Without considering wind turbine and mooring systems contribution, Eq. 2.46 represents the 6-DoF equation of motion of the floating platform for a given incident regular wave. Restraining the attention only to the steady state response of the system, $q(t)$ can be rewritten as [24]:

$$q(t) = \hat{q}(\omega)e^{j\omega t}, \tag{2.47}$$

where $\hat{q}(\omega)$ is the complex amplitude of the displacement vector of the platform. Thus, $\dot{q}(t)$ and $\ddot{q}(t)$ can be rewritten by using recursive derivatives. Focusing the attention on irregular sea state, neglecting any transient effect and invoking Eq. 2.7, the equation of motion can be rewritten as [24]:

$$-\omega^2(A(\omega) + M^{Float})\,\hat{q}(\omega)e^{j\omega t} + j\omega B_{rad}(\omega)\,\hat{q}(\omega)e^{j\omega t} + C^{hydro}(\omega)\,\hat{q}(\omega)e^{j\omega t} = X(\omega)\sqrt{2S_{\eta\eta}(\omega)\Delta\omega}e^{j\omega t}$$

$$\left[-\omega^2(A(\omega) + M^{Float}) + j\omega B_{rad}(\omega) + C^{hydro}(\omega)\right]\hat{q}(\omega) = X(\omega)\sqrt{2S_{\eta\eta}(\omega)\Delta\omega}, \tag{2.48}$$

where, M^{Float} is the mass matrix of the floating platform. Eq. 2.48 represents the Equation of motion of a floating platform in the FD. The solution to the frequency-domain problem is generally given in terms of a Response Amplitude Operator (RAO), which is the complex-valued amplitude of motion of a floating platform normalized per unit wave amplitude:

$$RAO(\omega) = \left[-\omega^2(A(\omega) + M^{Float}) + j\omega B_{rad}(\omega) + C^{hydro}(\omega)\right]^{-1} X(\omega), \tag{2.49}$$

2.4　　　Motions of slender elements

Potential flow theory (whether linear or nonlinear) allows to describe platform hydrodynamics under the hypothesis of non-viscous fluid. This valid if the body characteristic dimensions are comparable with respect to the wavelength. Introducing the slenderness as:

$$\alpha = \frac{\lambda}{D}, \tag{2.50}$$

where λ, is the wavelength and D is a characteristic length of the element subjected to the wave action. If $\alpha < 5$ the element can be considered *hydrodynamically bluff*, which means that the effects of viscosity, i.e., flow separation, can be neglected. Potential flow theory is enough to satisfactory describe body hydrodynamic. In the case of slender elements, $\alpha < 5$, viscous forces arising from the flow separation cannot be neglected. This can be the case of cross braces which connect semisubmersible platform

pontoons. Inertial and viscous drag forces per unit-length can be expressed by Morison equation [56] for moving cylinders as [47]

$$dF^{Morison}(t) = \frac{\pi}{4}\rho C_M D^2 \dot{u}(t) - \frac{\pi}{4}\rho C_A D^2 \ddot{q}(t) + \frac{1}{2}\rho C_D D\big(u(t) - \dot{q}(t)\big)|u(t) - \dot{q}(t)|, \qquad (2.51)$$

where $u(t)$ is the wave velocity component normal to the member axis, $\dot{q}(t)$, $\ddot{q}(t)$ are the cylinder velocity and acceleration, C_M is the inertial coefficient, C_A is the added-mass mass coefficient and C_D is the viscous drag coefficient. The dominance between inertial and drag forces depends both on wave and element features. As can be seen from Eq. 2.41, the viscous drag term is quadratic, which can be handled by most of the hydrodynamic time domain solvers. However, in the case of linear system (FD models) the term needs to be linearized. Borgman developed an iterative procedure [57] in which the nonlinear drag term is approximated with an equivalent linear term written as

$$dF_{Drag} = \frac{1}{2}\rho C_D D(u-\dot{q})|u-\dot{q}| \cong \frac{1}{2}\rho C_D D\sqrt{\frac{8}{\pi}}\sigma_{u-\dot{q}}(u-\dot{q}), \qquad (2.52)$$

where $\sigma_{u-\dot{q}}$ is the standard deviation of the relative velocity between waves and body motions.

2.4.1. Frequency domain representation of the viscous drag forces

As widely discussed in literature [37][26][27], the Morison's forces are represented in the FD neglecting the inertial and the forcing terms and linearizing the drag term according to Eq. 2.47. Furthermore, only the body motions are considered in the estimation of $\sigma_{\dot{q}}$:

$$dF_{Drag} \cong \frac{1}{2}\rho C_D D\sqrt{\frac{8}{\pi}}\sigma_{u-\dot{q}}(u-\dot{q}) \cong -\frac{1}{2}\rho C_D D\sqrt{\frac{8}{\pi}}\sigma_{\dot{q}}\dot{q}, \qquad (2.53)$$

Following the procedure similar to Pegalajar-Jurado et al [26], Eq. 2.49 is integrated over the submerged parts of the floating platform. A symmetric viscous drag term B_{visc} is derived considering different DoFs. Referring to surge motion, the integration gives the total viscous force in the x direction:

$$F_{Drag,1} = -\int_{drf}^{0} \frac{1}{2}\rho C_D D\sqrt{\frac{8}{\pi}}\sigma_{\dot{q}}\dot{q}_1\,dz, \qquad (2.54)$$

where drf refers to the deepest submerged part, i.e., the platform draft. The integral in Eq. 2.50 requires the estimation of drag coefficients and the computation of wave kinematics at several locations on the submerged structure, which can be involved for complex geometries. Therefore, representative, global values of σ_u and C_D are adopted. The total force become:

$$F_{Drag,1} = -\frac{1}{2}\rho C_D \dot{q}_1 \sqrt{\frac{8}{\pi}}\sigma_{\dot{\mathbf{q}}} \int_{drf}^{0} D \, dz = -\frac{1}{2}\rho C_D \dot{q}_1 \sqrt{\frac{8}{\pi}}\sigma_{\dot{\mathbf{q}}} A_x \equiv -b_{visc,11}\dot{q}_1, \tag{2.55}$$

where A_x is the floater's are projected on the yz plane. $b_{visc,11}$ is the surge-surge element of the viscous drag matrix. Similarly, other damping coefficients ca be derived. For example, by considering the pitch moment, $M_{\text{Drag},51}$, exerted by the drag forces in the surge direction around the reference frame origin (the point of floatation), $b_{visc,51}$ can be calculated:

$$M_{\text{Drag},51} = -\frac{1}{2}\rho C_D \dot{q}_1 \sqrt{\frac{8}{\pi}}\sigma_{\dot{\mathbf{q}}} \int_{drf}^{0} Dz \, dz = -\frac{1}{2}\rho C_D \dot{q}_1 \sqrt{\frac{8}{\pi}}\sigma_{\dot{\mathbf{q}}} S_{y,A_x} \equiv -b_{visc,51}\dot{q}_1, \tag{2.56}$$

Where S_{y,A_x} is the first moment of area A_x about the pitch axis y. Similarly, other viscous damping coefficients can be derived. The final viscous Damping matrix can be written as [26]

$$\mathbf{B}_{visc} = \frac{1}{2}\rho C_D \sqrt{\frac{8}{\pi}}\sigma_{\dot{\mathbf{q}}}\begin{bmatrix} A_x & 0 & 0 & S_{x,A_y} & S_{y,A_x} & 0 \\ 0 & A_y & 0 & 0 & 0 & 0 \\ 0 & 0 & A_z & 0 & 0 & 0 \\ S_{x,A_y} & 0 & 0 & I_{x,A_y}+I_{x,A_z} & 0 & 0 \\ S_{y,x} & 0 & 0 & 0 & I_{y,A_x}+I_{y,A_z} & 0 \\ 0 & 0 & 0 & 0 & 0 & 0 \end{bmatrix} \tag{2.57}$$

where, A_y, A_z are the floater are projected on the xz and xy planes, respectively. S_{x,A_y} and S_{y,A_x} are the first moment of area A_y, A_x about the roll, x, and pitch axis, y, respectively. I_{x,A_y}, I_{x,A_z} and I_{y,A_x}, I_{y,A_z}, are second moments of areas.

As can be seen from Eq. 2.57, the viscous damping matrix depends on the response of the system trough σ_u, which are not known *a priori*. Therefore, an iterative procedure must be established to properly estimate the linearized damping term $\mathbf{B}_{visc}$.

2.4.2. Transverse flow

Similarly to Eq. 2.49, the hydrodynamic loads on cylinders subjected to transverse flow can be described with a modified Morison equation [47]. This is the case of heave plates, a typical element composing semisubmersible platforms (Figure 13).
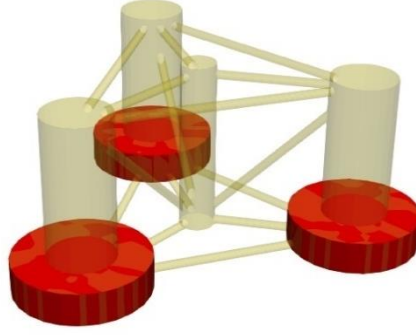
Figure 13: Heave plates.

For such elements, the hydrodynamic force can be written as [47]:

$$dF_z^{Morison} = \rho_{h2o} C_{Az} V_R D_h^2 (\dot{w} - \ddot{q}_3) + \frac{1}{2}\rho_{h2o} C_{Dz}\frac{\pi}{4}D_h^2(w - \dot{q}_3)|w - \dot{q}_3| + \frac{\pi}{4}D_h^2 p_b - \frac{\pi}{4}(D_h^2 - D_c^2)p_t, \quad (2.58)$$

where $C_{Az} = 1$ is the added mass coefficient in the Heave direction; C_{Dz} is the drag coefficient in the Heave direction; w is the vertical component of the wave particle velocity; $\dot{q}_3$ is the Heave velocity of the Heave plates; D_h is the diameter of the Heave plates; D_c is the diameter of the upper column; and p_b and p_t are respectively the dynamic pressures, projected in the direction of the normal vectors, at the bottom and at the top of the Heave plates. V_R is the reference volume, i.e., the volume of fluid that is displaced by the oscillations of the Heave plates, calculated as

$$V_R = \frac{A_{33}(0)}{3\rho_{h2o}}, \quad (2.59)$$

where $A_{33}(0)$ is the zero-frequency added mass coefficient in the Heave direction. The viscous drag term can be linearized according to [58] as follows:

$$dF_{Drag,z}^{Morioson} \cong \frac{1}{3}\rho_{h2o} C_{Dz} D_h^2 \omega a(w - \dot{q}_3), \quad (2.60)$$

where ω is the wave frequency and a is the average of all the Heave plates oscillations amplitude. This term is not known a priori like σ_u, therefore another iteration procedure must be established. In as similar way as for Eq. 2.50, the terms related to the wave velocity is neglected.

Chapter 3.
Mooring system modelling

The mooring system provides primarily the required stabilizing force in the surge direction. It consists in a set of cables which anchors the platform to the seabed. Depending on the effectiveness of the moorings contribution to the hydrostatic stability in roll/ pitch motions, two main concepts can be identified (Figure 14):

- Taut line moorings;
- Slack catenary moorings;

<div align="center">(a)   (b)</div>
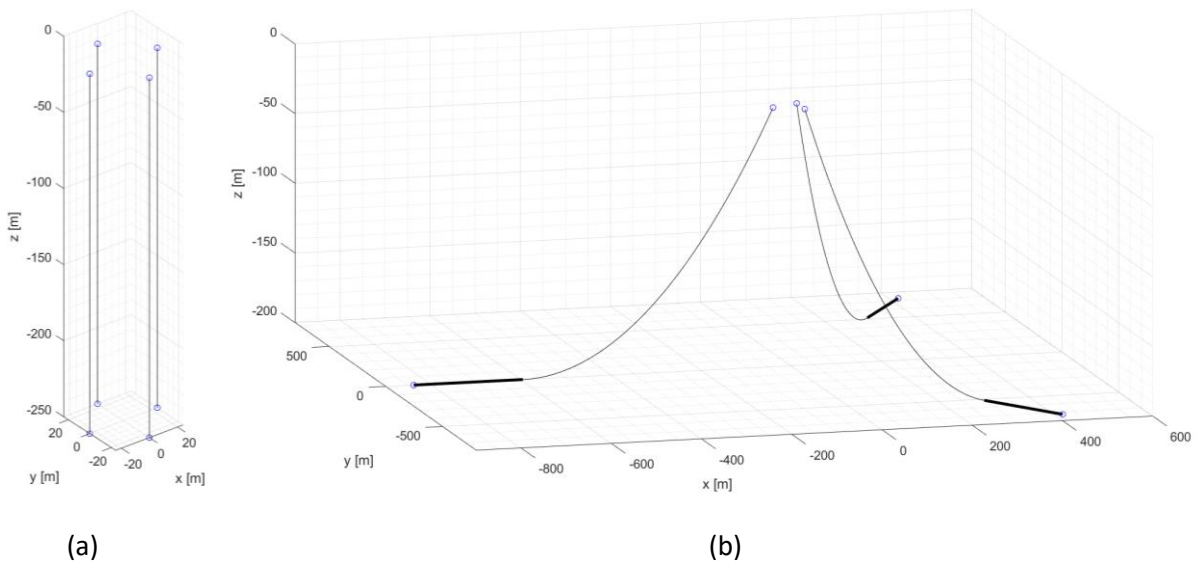
Figure 14: Mooring systems for FOWT: Tension leg (a), a taut system where tendons are vertical at rest, and slack catenary (b), which can have a portion of line resting on the seabed or not.

The first one provides roll/ pitch stability to the system thanks to their pre-tensioning, stressing the anchoring system with vertical and horizontal forces. The latter does not provide rotational stability but, thanks to the dead weight, the anchors can be stressed only by horizontal forces. Different representation can be adopted for the mooring lines. The simplest considers a quasi-static approach which, at each time step, iterates the catenary system of equation in order to change the stiffness of the mooring and the

forces exerted at the platform fairleads. More accurate tools discretize the cable with finite elements. Among these, lumped mass models are widely adopted. Each element is a rigid mass connected to each other by means of springs and dampers. The dynamic equilibrium is imposed for each segment. Moreover, applying Morison's equation, hydrodynamic loads due to sea waves and current can be distributed along the cables. Latest development allows also to consider localised rotational stiffness which arises when mooring chain rings rub together. When the analysis is performed in the FD, quasi-static models are widely adopted due to the reduced computational effort. In dynamic analyses, quasi-static formulations can be accurate enough if and only if the mass of the mooring lines is small with respect to the overall mass of the system, which means of the order of 8% [59]. In this chapter, the quasi-static formulation is described. Especially, the formulation of the stiffness matrix for both catenary and taut mooring lines is introduced. In conclusion, two simple cases are presented.

3.1 Quasi-static model

Quasi-static cable approach is totally based on static assumptions. Ignoring the cable dynamic, the nonlinear catenary system of equation is solved for a given position of the anchor and the fairlead. The unknown is the tension exerted by each cable at the fairlead, which is iteratively used to update the platform position. The following hypotheses are necessary:

- horizontal seabed;
- cable contained in a vertical plane, implying that the forces exerted by the moorings on the platform at the fairlead are contained in a vertical plane;
- negligible bending stiffness;
- absence of currents. The presence of current would imply the presence of distributed, dynamic forces along the cable which need to be described by means of Morison equation;
- inertia and damping of the mooring line negligible. It is a result of neglecting the dynamic of the cable;
- mooring line completely submerged in a homogeneous fluid;

Under these hypotheses, as shown in Figure 15, the cable is contained in the xz vertical plane. The nonlinear catenary system of equations is written in this 2D reference frame. The origin is placed at the anchor, z-axis is considered positive upwards. Given the cable end points position at a certain instant, the cable is subjected to the tension forces at the anchor and the fairlead, and to the distributed gravity and buoyancy loads, which are considered jointly. Namely, let μ_c be the mass of the line per unit length and D_{cable} the cable diameter, then, the apparent weight in fluid of the cable per unit length, w, can be written as:

$$w = \left(\mu_c - \rho_{h2o} \frac{\pi D_{cable}^2}{4} \right) g, \tag{3.1}$$

where ρ is the water density and g is the gravity acceleration.
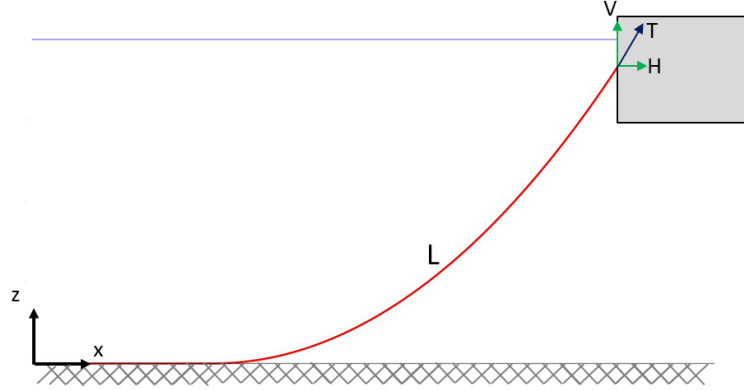
Figure 15: Mooring cable reference frame.

The quasi-static formulation presented by Jonkman is herein described only for a cable resting on the seabed. in this approach, the contact with the seabed is simply modelled by introducing friction forces, proportional to a friction coefficient C_B, which modify the distribution of the horizontal tension. Thus, the system of nonlinear equations which relates the fairlead position (x_F, z_F) to the components of the tension force at the fairlead (H, V) can be written as:

$$x_F(H,V) = L - \frac{V}{w} + \frac{H}{w} \ln\left[\frac{V}{H} + \sqrt{1 + \left(\frac{V}{H}\right)^2} \right] + \frac{HL}{EA} + \frac{C_B \omega}{2EA} \left[-\left(L - \frac{V}{w}\right)^2 + \left(L - \frac{V}{w} - \frac{H}{C_B w}\right) \max\left(L - \frac{V}{w} - \frac{H}{C_B w}, 0\right) \right],$$

$$z_F(H,V) = \frac{H}{w} \ln\left[\sqrt{1 + \left(\frac{V}{H}\right)^2} - \sqrt{1 + \left(\frac{V - wL}{H}\right)^2} \right] + \frac{1}{EA}\left[VL - \frac{wL^2}{2} \right], \tag{3.2}$$

where L is the unstretched length of the cable, w is the apparent weight in fluid, and EA is the axial stiffness. An iteration procedure is necessary to solve the nonlinear system. The system of equations embeds the elastic stretching of the mooring and the relaxation of the portion resting on the seabed due to the friction. This length, L_B, can be estimated once V is known as:

$$L_B = L - \frac{V}{w} \tag{3.3}$$

Normally, when dealing with slack catenary moorings a portion of the line is always required to rest on the seabed, to ensure that the anchor is not subjected to uplift forces. If the portion resting on the seabed is long enough to let the friction overcome H, the reaction force at the anchor vanishes. Once (H, V) are known, the position of each cable point can be found as follows:

$$
x(s) = \begin{cases}
s & 0 \le s \le L_B - \dfrac{H}{C_B w} \\[2em]
s + \dfrac{C_B w}{2EA}\left[\begin{array}{l} s^2 - 2\left(L_B - \dfrac{H}{C_B w}\right)s + \\ + \left(L_B - \dfrac{H}{C_B w}\right)max\left(L_B - \dfrac{H}{C_B w}, 0\right)\end{array}\right] & L_B - \dfrac{H}{C_B w} \le s \le L_B \\[2em]
L_B + \dfrac{H}{w}\ln\left[\dfrac{w(s-L_B)}{H} + \sqrt{1 + \left(\dfrac{w(s-L_B)}{H}\right)^2}\right] + \dfrac{Hs}{EA} + \\ \quad + \dfrac{C_B w}{2EA}\left[-L_B^2 + \left(L_B - \dfrac{H}{C_B w}\right)max\left(L_B - \dfrac{H}{C_B w}, 0\right)\right] & L_B \le s \le L
\end{cases}
\tag{3.4}
$$

$$
z(s) = \begin{cases}
0 & 0 \le s \le L_B \\[1.5em]
\dfrac{H}{w}\ln\left[\sqrt{1 + \left(\dfrac{w(s-L_B)}{H}\right)^2} - 1\right] + \dfrac{w(s-L_B)^{2'}}{2EA} & L_B \le s \le L
\end{cases}
\tag{3.5}
$$

here $x(s)$ is the x-coordinate of the cable point identified by the progressive, coordinate s, which is aligned with the cable (see Figure 15); similarly, $z(s)$ identifies the vertical coordinate. As can be seen, they are both piecewise functions. the three expressions of $x(s)$ refer to: 1) the part of the cable lying on the seabed which is not stretched since the friction forces are larger than the tension forces (if exists); 2) the part of the cable, which is still lying on the seabed, but it is stretched; 3) the part of the cable which is suspended between L_B and L. The two functions of $z(s)$ are defined in the same way. The tension forces $T(s)$, can be found by imposing the static equilibrium of a generic section of the cable:

$$
T(s) = \begin{cases}
max(H + C_B w(s - L_B), 0) & 0 \le s \le L_B \\[1.5em]
\sqrt{H^2 + \left(w(s - L_B)\right)^2} & L_B \le s \le L
\end{cases}
\tag{3.6}
$$

The reaction forces the anchor must withstand are found imposing $T(s = 0)$ in Eq. 3.6. Figure 16 shows one of the three catenary cables which moored the 5MW OC4 DeepCwind semisubmersible FOWT [47]. As can be noticed (Figure 16a), such system requires longer lines (in this case $L = 835m$) with respect to taut system, leading to an increasement of the overall footprint of the FOWT. The portion resting on the seabed is around 240m. Despite L_B is nearly the 30% of the total length, The overall friction force developed at the contact with the seabed are not sufficient to vanish the tension force at the anchor (see Fig. 16b).

(a)

(b)
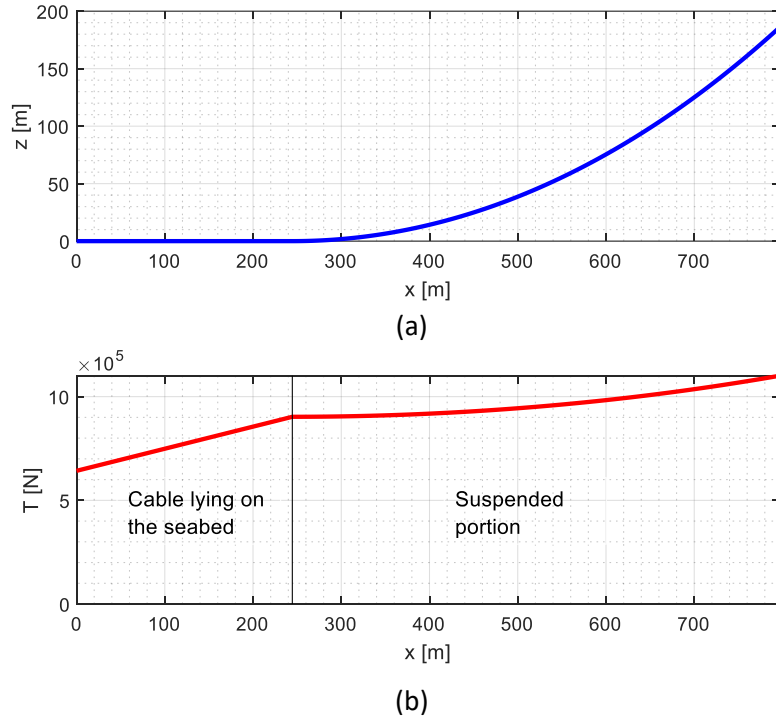
Figure 16: 5MW OC4 DeepCwind semisubmersible FOWT [47] catenary cable at rest: position (a) and tension forces (b).

3.2 Single cable stiffness matrix

Once the position of the mooring is known, it is possible to obtain the in-plane stiffness matrix of the cable. The calculation is different whether the cable is slack or taut.

3.2.1. Slack catenary cable stiffness matrix

Considering the horizontal and vertical components, of the fairlead tension and the projection of the catenary shape on x and z axes, l and h (Figure 17), the stiffness matrix of the cable, $\boldsymbol{K^P}$, is expressed as [60] [61]:

$$\boldsymbol{K^P} = \begin{bmatrix} K_{11}^P & K_{12}^P \\ K_{21}^P & K_{22}^P \end{bmatrix} = \begin{bmatrix} \dfrac{\partial H}{\partial l} & \dfrac{\partial H}{\partial h} \\ \dfrac{\partial V}{\partial l} & \dfrac{\partial V}{\partial h} \end{bmatrix}, \tag{3.7}$$
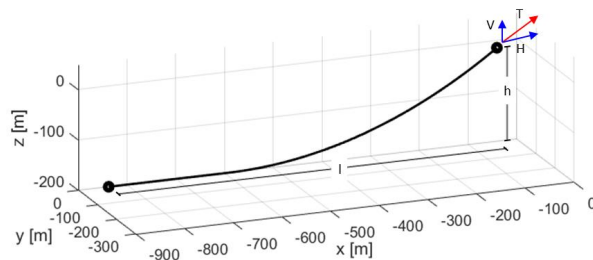
Figure 17: Slack catenary mooring line.

The procedure for calculating the partial derivatives of H and V with respect to l and h generally depends on the mooring system. In the case of catenary cables, whether resting on the seabed or not, introducing the flexibility matrix $\boldsymbol{F^P}$, s.t:

$$\begin{Bmatrix} dl \\ dh \end{Bmatrix} = \boldsymbol{F^P} \begin{Bmatrix} dH \\ dV \end{Bmatrix} = \begin{bmatrix} \frac{\partial l}{\partial H} & \frac{\partial h}{\partial H} \\ \frac{\partial l}{\partial V} & \frac{\partial h}{\partial V} \end{bmatrix} \begin{Bmatrix} dH \\ dV \end{Bmatrix}, \tag{3.8}$$

The stiffness matrix, $\boldsymbol{K^P}$, can be found as the inverse of $\boldsymbol{F^P}$. The element of the flexibility matrix can be determined differentiating the system of nonlinear equations at the fairlead Eq. 3.5 with respect to H and V.

3.2.2.   Taut cable stiffness matrix

Taut mooring systems are realized by loading the cables with design tension forces due to an excess of platform buoyancy. They are generally subjected to higher stresses with respect to catenaries therefore larger sections are adopted (diameter of the order of 15 cm). A taut system allows to design lighter platforms but requires attention to the dynamic design of the overall system, as well as the anchoring design. Geometrically, the line is taut, and it has no sag, i.e., $H/V \approx l/h$. in this case, it can be modelled accurately as a massless spring [60]. This assumption dramatically simplifies the analysis and obviates the need to use catenary equation, providing and accurate approximation also for TLPs, i.e., taut vertical moorings. introducing the cable stiffness K_I, as:

$$K_I = \frac{EA}{L} \tag{3.9}$$

where L is the unstretched length and EA is the axial stiffness. Thus, the tension force T given by an elongation of the cable equal to ΔL can be written according to the Hooke's law:

$$T = K_I(L' - L\ ) = K_I \Delta L, \tag{3.10}$$

The spring approximation allows to directly write the components of the stiffness matrix $\boldsymbol{K^P}$ for a taut line as:

$$\begin{aligned} \frac{\partial H}{\partial l} &= \frac{\partial(T\cos\alpha)}{\partial l} = \cos(\alpha)\frac{\partial T}{\partial L'}\frac{\partial L'}{\partial l} - T\sin(\alpha)\frac{\partial \alpha}{\partial l} \\ \frac{\partial H}{\partial h} &= \frac{\partial(T\cos\alpha)}{\partial h} = \cos(\alpha)\frac{\partial T}{\partial L'}\frac{\partial L'}{\partial h} - T\sin(\alpha)\frac{\partial \alpha}{\partial h} \\ \frac{\partial V}{\partial l} &= \frac{\partial(T\sin\alpha)}{\partial l} = \sin(\alpha)\frac{\partial T}{\partial L'}\frac{\partial L'}{\partial l} + T\cos(\alpha)\frac{\partial \alpha'}{\partial l} \\ \frac{\partial V}{\partial h} &= \frac{\partial(T\sin\alpha)}{\partial h} = \sin(\alpha)\frac{\partial T}{\partial L'}\frac{\partial L'}{\partial h} + T\cos(\alpha)\frac{\partial \alpha}{\partial h} \end{aligned} \tag{3.11}$$

where α is the inclination of the cable with respect to the horizontal direction (see Appendix A, Figure 132). Considering Eq. 3.10, the partial derivatives of T, α and L', can be written as:

$$\frac{\partial T}{\partial L'} = \frac{dT}{dL'} = K_I; \quad \frac{\partial L'}{\partial l} = \cos(\alpha); \quad \frac{\partial L'}{\partial h} = \sin(\alpha);$$
$$\frac{\partial \alpha}{\partial l} = -\frac{\sin(\alpha)}{L'}; \quad \frac{\partial \alpha}{\partial h} = \frac{\cos(\alpha)}{L'},$$

(3.12)

Thus, considering Eq. 3.7, the expression of $\boldsymbol{K^P}$ for a taut mooring, inclined of α, can written in the final form as

$$\boldsymbol{K^P} = \begin{bmatrix} K_{11}^P & K_{12}^P \\ K_{21}^P & K_{22}^P \end{bmatrix} = \begin{bmatrix} \cos^2(\alpha)\,K_I + \frac{T}{L'}\sin^2(\alpha) & \cos(\alpha)\sin(\alpha)\left(K_I - \frac{T}{L'}\right) \\ \cos(\alpha)\sin(\alpha)\left(K_I - \frac{T}{L'}\right) & sin^2(\alpha)\,K_I + \frac{T}{L'}\cos^2(\alpha) \end{bmatrix}$$

(3.13)

3.3   Mooring system stiffness matrix

The mooring stiffness matrix at equilibrium is required in the preliminary design and dynamic analyses of the floating structures. The previous considerations are valid only referring to the cable reference frame. When a mooring line is attached to a floating platform, the fairlead undergoes a general displacement, which depends on the six rigid-body DoFs. To represent properly the contribution to the platform kinematics, the mooring line 6 x 6 stiffness matrix must be derived. The completed description of this procedure can be found in APPENDIX A. When the platform is at rest, and the cables are identical and symmetrically distributed, the expression of the mooring system stiffness matrix simplifies.

3.3.1.   Slack catenary mooring system stiffness matrix

Referring to Figure 18, assuming that the mooring system is composed by n lines (n>=3) which have both anchors and fairlead uniformly distributed in two circles of radius R_c and R, respectively, the stiffness matrix of the individual cable can be found by substituting $\beta_i = \pi + 2\pi\,(i-1)/n$, for line $i = 1, \dots, n$ and imposing the equilibrium position.
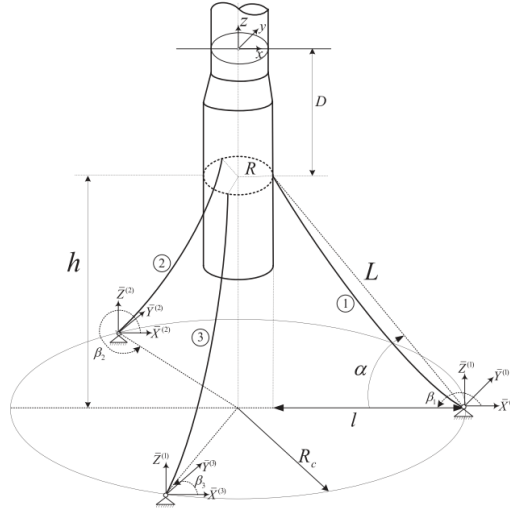
Figure 18: Symmetric 3-tethered slack catenary mooring system, courtesy of [60].

The mooring system stiffness matrix at equilibrium is symmetric, the only non-zero terms can be expressed as:

$$K_{11} = K_{22} = \frac{1}{2}n\left[K_{11}^p + \frac{H}{l}\right]$$

$$K_{34} = n[K_{22}^p]$$

$$K_{15} = K_{51} = -K_{24} = -K_{42} = -n\left[-\frac{R}{2}K_{12}^p + \frac{D_r}{2}K_{11}^p + \frac{DH}{l}\right] \quad ,$$

$$K_{55} = K_{44} = \left[-D_r R K_{12}^p + \frac{D^2}{2}K_{11}^p + \frac{R^2}{2}K_{22}^p + D_r V + \frac{HR}{2} + \frac{D_r^2 H}{2l}\right]$$

$$K_{66} = n\left[\frac{HR^2}{l} + HR\right]$$

(3.14)

Here D is the fairlead depth with respect to the platform reference frame. H and V can be found solving the catenary nonlinear equation. K^P is found according to Eq. 3.7

3.3.2. Taut mooring system stiffness matrix

The taut mooring system stiffness matrix can be derived similarly to the case of catenary mooring but following Eqs. 3.7 and 3.11. K^P is expressed recalling the spring approximation of the tethers presented in Eq. 3.10. Thus, the non-zero coefficients of the stiffness matrix Km of n taut cables inclined of alpha with respect to the horizontal direction can be expressed as:

$$K_{11} = K_{22} = \frac{1}{2}n\left[\frac{T}{L'}(1 + sin^2(\alpha)) + cos^2(\alpha)K_I\right]$$

$$K_{33} = n\left[sin^2(\alpha)K_I + \frac{T}{L'}cos^2(\alpha)\right]$$

$$K_{51} = -K_{24} = -K_{42}$$

$$K_{15} = -n\left[-\frac{T}{2L'}(D + D\,sin^2(\alpha) + R\,cos(\alpha)\,sin(\alpha)) + \frac{K_I}{2}(D_r\,cos^2(\alpha) - R\,cos(\alpha)\,sin(\alpha))\right]$$

(3.15)

$$K_{55} = n\left\{T\left(D_r\,sin(\alpha) + \frac{1}{2}R\,cos(\alpha)\right) + \frac{1}{2}\frac{T}{L'}[(R\,cos(\alpha) + D_r\,sin(\alpha))^2 + D^2] + \frac{K_I}{2}(D_r\,sin(\alpha) - R\,cos(\alpha))^2\right\}$$

$$K_{44} = K_{55}$$

$$K_{66} = n\frac{TR}{L}(R + L'\,cos(\alpha))$$

In the very particular case of TLP cables, Eq. 3.15 simplifies:

$$K_{11} = K_{22} = n\frac{T}{L'}$$

$$K_{33} = nK_I$$

$$K_{15} = K_{51} = -K_{24} = -K_{42} = -n\frac{TD_r}{L}$$

$$K_{55} = K_{44} = n\left[\frac{TD_r^2}{L'} + \frac{1}{2}K_I R^2 + TD_r\right]$$

$$K_{66} = n\frac{TR^2}{L'}$$

(3.16)

3.4   Average system response calculation

When the platform is moving under the action of wind and waves, the total forces exerted by the mooring system can be calculated as [54]:

$$\mathbf{F}^{Lines} = \mathbf{F}^{Lines,0} - \mathbf{C}^{Moor}\mathbf{q}$$

(3.17)

where, $\mathbf{F}^{Lines,0}$ is the static moorings force vector, $\mathbf{C}^{Moor}$ is the mooring system stiffness matrix and $\mathbf{q}$ is the platform displacement vector. As discussed in the previous sections, $\mathbf{C}^{Moor}$ depends on $\mathbf{q}$, therefore, an iteration procedure must be established to identify the displaced position of the system. If the attention is restrained only to the mean displacement of the system under wind-wave action, a static equilibrium equation can be established:

$$\left(\mathbf{C}^{hydro} + \mathbf{C}^{Moor}\right)\mathbf{q} = \mathbf{F}^{TOT} = \mathbf{F}^{Lines,0} + \mathbf{F}^{buoyancy} + \mathbf{F}^{Grav} + \mathbf{F}^{Aero}$$

(3.18)

where $\mathbf{C}^{hydro}$ is the hydrostatic stiffness matrix, $\mathbf{F}^{buoyancy}$ and $\mathbf{F}^{Grav}$ are the buoyancy and gravity load vectors, while $\mathbf{F}^{Aero}$ represent the mean aerodynamic forces exerted at the hub height, namely the thrust force and its moment. Assuming a uniform, monodirectional wind speed aligned with the surge direction, the total force vector can be calculated as:

$$\mathbf{F}^{TOT} = \begin{bmatrix} F_1^{Aero} \\ 0 \\ F_3^{Aero} + F_3^{Buoyancy} + F_3^{Grav} + F_3^{Lines,0} \\ 0 \\ F_1^{Aero}z_{hub} + F_3^{Grav}x_G - F_3^{Buoyancy}x_B \\ 0 \end{bmatrix}$$

(3.19)

where, z_{hub} is the hub height with respect to the SWL, x_G and x_B are the instantaneous positions of the centre of gravity and the centre of buoyancy, respectively. The wave loads can be neglected when calculating the average motions of the system [37]. The solution of Eq. 3.18 is fundamental for the floating foundation (platform + moorings) design since the maximum average motions of the system must be kept in the range of operativity of the wind turbine [37]. The procedure can be summarized as follows:

1. Calculation of C^{hydro} and $C^{Moor,0}$ at the equilibrium position;

2. Calculation of $q^0 = \left(C^{hydro} + C^{Moor,0} \right)^{-1} F^{TOT,0}$

3. Calculation of $C^{Moor,1}$ and $F^{TOT,1}$, considering the new position q^0

4. Calculation of $q^1 = \left(C^{hydro} + C^{Moor,1} \right)^{-1} F^{TOT,1}$

5. Repetition of point 3 and 4 until the convergence of the displacement.

Figure 19 and 20 shows the average motions of a 5MW FOWT at the rated wind speed (11.4 m/s) when two different floating systems are adopted. In Figure 19, results referring to the MIT NREL TLP FOWT are presented. Figure 19a and 19b presents the floater concept and the system displaced position, respectively. Average surge and pitch motions are shown in Figure 19c. Left y axis (blue) refers to surge motion, expressed in m, right y axis (red) refers to pitch motion, expressed in deg. Results are plotted at each iteration step, x axis. As can be seen, convergence is reached after 4 iterations.

(a)   (b)   (c)
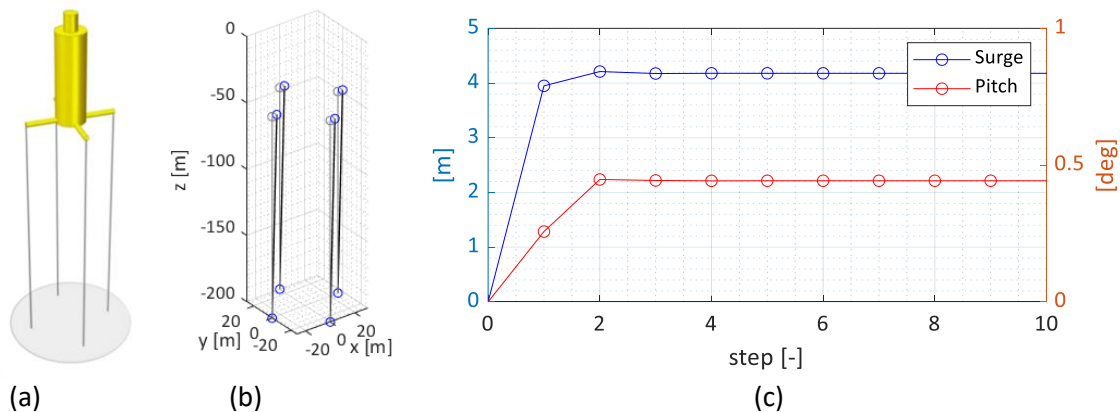
Figure 19: 5MW MIT-NREL TLP FOWT (a): mooring system (b) and iteration of the static equilibrium position in terms of Surge and Pitch (c).

Similarly, Figure 20 presents the maximum average motions of the OC4 DeepCwind semisubmersible FOWT. Figure 20a and 20b presents the floater concept and the system displaced position, respectively. Average surge and pitch motions are shown in Figure 20c. As can be seen comparing Figure 19c with 20c, a larger number of iterations are needed in this case for reaching the convergence of the displacements. Moreover, the equilibrium position at rated wind speed is achieved with higher surge and pitch with respect to the TLP system.

(a)

(b)

(c)
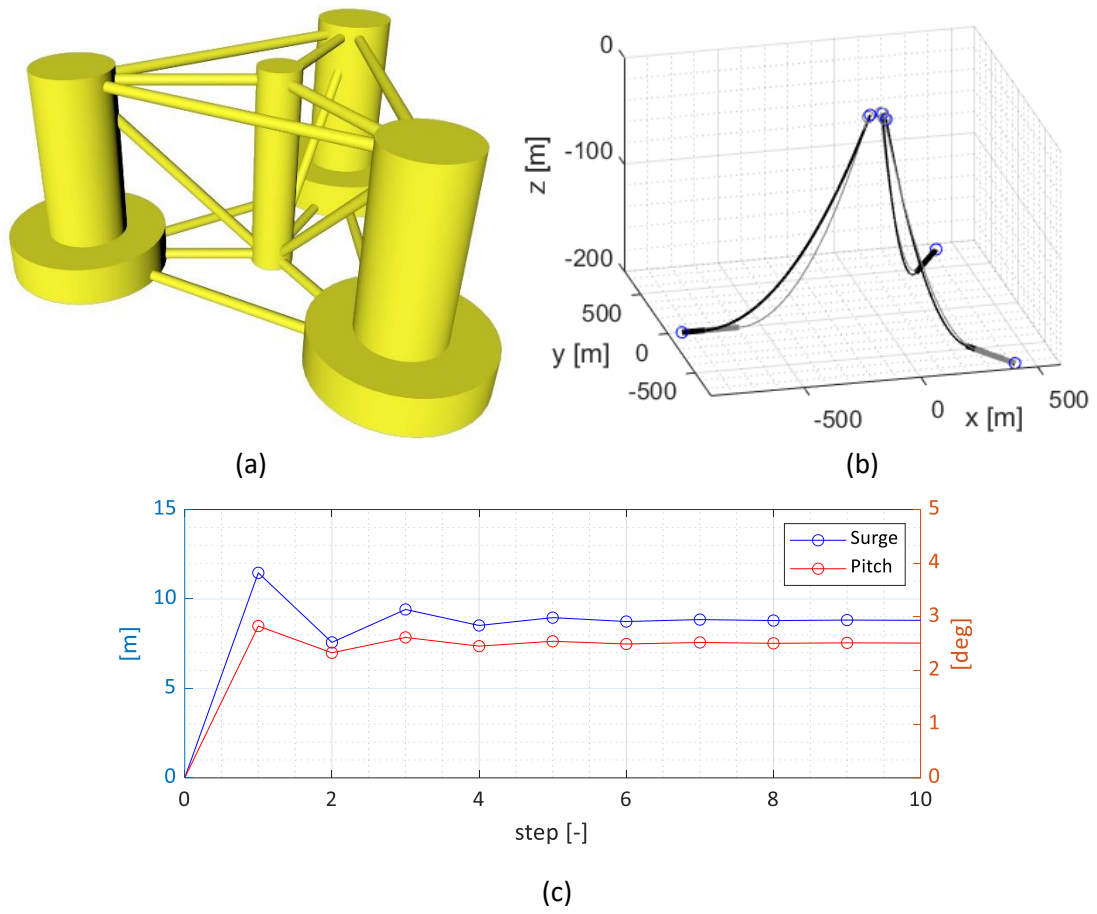
Figure 20: 5MW DeepCwind NREL FOWT (a): mooring system (b) and iteration of the static equilibrium position in terms of Surge and Pitch (c).

Chapter 4.
Wind turbine modelling

In this chapter the wind turbines modelling is presented. The attention is focused on two approaches which can be adopted for FD analysis. The first consists in a procedure which is implemented in the code FAST for the linearized simulations. The second is a simplified approach, which represents the wind turbine as a single DoF to be added to the 6 rigid body DoFs of the platform. In both cases, the coupling with the hydrodynamic and mooring system models is detailed described.

4. 1   Wind turbines aerodynamics

Winds are originated by movements of air masses relative to the planet's surface. Different wind scales can be identified such as local breezes and global winds. The firsts last for hours and occur at altitude lower than 100 m, where the orography of the soil and the effects of obstacles becomes not negligible. They are originated mainly by pressure gradients caused by difference of air temperatures (Figure 21). Global and Geostrophic winds are instead generated whether by global difference of heating between poles and equator or by the rotation of the planet (Coriolis effect). They are not influenced by the soil orography (surface roughness).
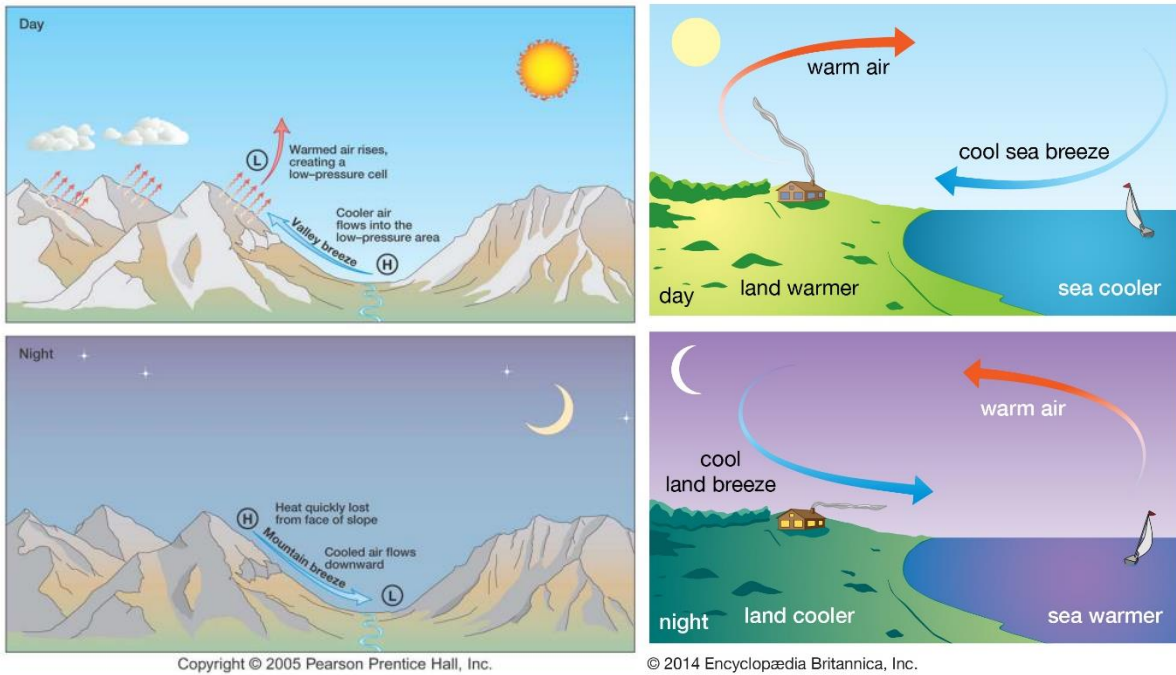
<div align="center">(a)   (b)</div>

Figure 21: Local wind: Air circulation generated by temperature gradients due to valley effect (a) and sea effect (b).

Land based WTs always operate in the local wind scale. Recent developments in the FOWT field, bring to 10 MW and 15 MW machines. Due to the bigger dimension and to the reduced surface roughness of open sea sites, they may operate out of the boundary layer.

A Wind turbine is a device which converts the kinetic energy of the wind flow into mechanical energy applied to the rotor blades, and then into electric energy. The amount of energy a turbine can extract from the wind depends on wind speed, flow density and rotor area swept. The exchanging energy process can be described as follow: As the wind flow approaches the rotor, it increases its pressure (the rotor is seen as an obstacle) and reduces its speed, consequentially its volume increases. Subsequently, the energy exchange between the flow and the rotor takes place. The pressure drops down instantaneously and then progressively returns to the undisturbed value far from the rotor (Figure 22).
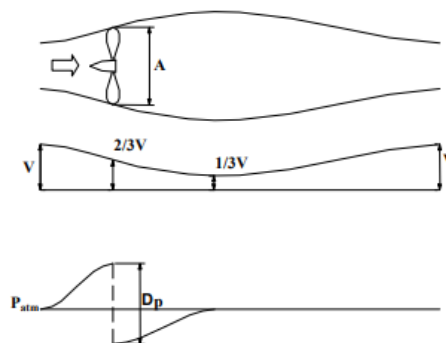
Figure 22: Example of power take-off caused by a wind turbine.

The maximum energy that, theoretically, can be extracted from a wind flow is defined by the Betz's law. the maximum power coefficient Cp is found by imposing the continuity equation to the stream tube presented in Figure 22 and writing the expression of power. Normalizing the power with respect to the undisturbed power of the flow, the expression of the power coefficient is found. Differentiating it, the maximum theoretical power coefficient can be found. The approach described above is also known as Blade Element Momentum theory, it allows to estimate the extracted power but also the forces acting on the blades and therefore their dynamic behaviour.

For a structural point of view, aero-hydro-servo-elastic codes represent the WT with a combined modal- and multibody-dynamics formulation. Slender elements such as blades and tower, which can undergo in large deformations, are modelled as flexible elements, adopting a linear modal formulation. Blades and tower representation involves a restrained number of DoFs, which depends on the simulated phenomenon. Their flexibility is characterized by distributed stiffness and mass properties along the span of the member. As far as it regards the blades, two flapwise and one edgewise bending-mode DOFs are considered. For the tower, two fore-aft and two side-to-side bending-mode DOFs are used. Heavy, bluff components such as rotor hub and nacelle, are represented as rigid bodies, characterized by lumped mass and inertia, interacting with the flexible elements, i.e., multi-body formulation. In the following, the turbine modelling approach is presented. It is done by performing a linearized simulation in FAST and then transforming the results in the non-rotating frame by means of the Multi-Blade Coordinate (MBC) transformation utility [62]. This allows to estimate the not only the cross-coupling effects between the WT tower and the floating platform, but also to estimates aerodynamic and gyroscopic damping coming from the rotating rotor.

4. 2   FAST linearization adopting MBC

The dynamics of wind turbine rotor blades are generally expressed in rotating frames attached to the individual blades. The tower-nacelle subsystem sees the combined effect of all rotor blades, not the individual blades. This is because the rotor responds as a whole to excitations which occur in a nonrotating frame. Multi-blade coordinate transformation (MBC) helps integrate the dynamics of individual blades and express it in a fixed (nonrotating) frame [62].

Considering a rotor with three blades that are equally spaced around the rotor azimuth. The azimuth location, ψ_b, of the bth blade is given by [62]

$$\psi_b = \psi + \frac{2\pi}{3}(b - 1) \qquad (4.1)$$

where ψ is the azimuth of the first blade, assumed to be equal to 0. Introducing a particular rotating DoF, q_b, MBC relates q_b to new non-rotating DoFs, which are the projections of q_b onto the non-rotating (fixed) frame, by means of a linear transformation [62]

$$q_0 = \frac{1}{3}\sum_{b=1}^{3} q_b \,; \quad q_c = \frac{2}{3}\sum_{b=1}^{3} q_b \cos(3\psi_b)\,; \quad q_s = \frac{2}{3}\sum_{b=1}^{3} q_b \sin(3\psi_b)\,; \tag{4.2}$$

here q_0, q_c, q_s are called non-rotating DoFs, which are called coning mode, cosine cyclic mode and sine cyclic mode, respectively. They express the cumulative behaviour of all the rotor blades in the fixed frame. The physical interpretation of each rotor coordinate depends on the degree of freedom it refers to, example can be found in [62]. Inverting the transformations in Eq. 4.2, the bth blade DoF can be written as

$$q_b = q_0 + q_c \cos(\psi_b) + q_s \sin(\psi_b)\,; \qquad b = 1,2,3 \tag{4.3}$$

4.2.1. Second-Order System Matrices transformation

Second-order system equation may be written as [62]

$$M\ddot{X} + B\dot{X} + CX = Fu + F_d w_d, \tag{4.4}$$

where M, B, C, F, and F_d, are respectively the mass, damping, stiffness, control, and disturbance matrix. u and w_d are the control and disturbance vectors, respectively. F is associated with the control system, which keeps the rotor to a prescribed rotational speed by changing the blades pitch, while F_d is associated with disturbances related to the input, i.e., the wind turbulence, such as variations in the horizontal wind speed at hub height. F_d can be seen as a transfer function between the incoming turbulent wind and the aerodynamic loads acting at rotor hub.

M, B, and C matrices contain direct and cross-coupling terms between the tower and the rotating blades. Moreover, the damping matrix contains the gyroscopic effects on the chosen fixed frame DoFs in addition to the structural damping. Similarly, the stiffness matrix contains centrifugal and aerodynamic stiffness effects. X is called physical vector in literature, it contains the nF non-rotating frame DoFs, X_F, and m rotating DoFs for each blade [62]

$$X = \begin{bmatrix} X_F \\ q_1^1 \\ q_2^1 \\ q_3^1 \\ \vdots \\ q_1^j \\ q_2^j \\ q_3^j \\ \vdots \\ q_1^m \\ q_2^m \\ q_3^m \end{bmatrix}, \tag{4.5}$$

Eq. 4.4 needs to be transformed to the non-rotating frame. To do so, two methods can be adopted: the operational method and the substitution method. FAST MBC utility adopts the substitution method.

4.2.1.1. Substitution method

Using Eq. 4.3, the rotational DoFs are substituted with rotor coordinates, transferring the jth DoF for each of the three blades (q_1^j, q_2^j, q_3^j) to the non-rotating coordinates (q_0^j, q_c^j, q_s^j) adopting [62]

$$
\begin{Bmatrix} q_1^j \\ q_2^j \\ q_3^j \end{Bmatrix} = \tilde{t} \begin{Bmatrix} q_0^j \\ q_c^j \\ q_s^j \end{Bmatrix} = \begin{bmatrix} 1 & cos(\psi_1) & sin(\psi_1) \\ 1 & cos(\psi_2) & sin(\psi_2) \\ 1 & cos(\psi_3) & sin(\psi_3) \end{bmatrix} \begin{Bmatrix} q_0^j \\ q_c^j \\ q_s^j \end{Bmatrix},
\tag{4.6}
$$

where $\tilde{t}$ is a rotation matrix. Adopting Eq. 4.6, the full-system rotating frame DoFs vector X, is then expressed in the non-rotating frame as follows [62]:

$$
X = T_1 X_{NR} = \begin{bmatrix} I_{nF \times nF} & & & & \\ & \tilde{t} & & & \\ & & \ddots & & \\ & & & \tilde{t} & \\ & & & & \tilde{t} \end{bmatrix}_{(nF+m) \times (nF+m)} \cdot X_{NR},
\tag{4.7}
$$

differentiating Eq. 4.7 leads to [62]

$$
\dot{X} = T_1 \dot{X}_{NR} + \Omega T_2 \dot{X}_{NR} = \begin{bmatrix} I_{nF \times nF} & & & & \\ & \tilde{t} & & & \\ & & \ddots & & \\ & & & \tilde{t} & \\ & & & & \tilde{t} \end{bmatrix} \dot{X}_{NR} + \Omega \begin{bmatrix} 0_{nF \times nF} & & & & \\ & \tilde{t}_2 & & & \\ & & \ddots & & \\ & & & \tilde{t}_2 & \\ & & & & \tilde{t}_2 \end{bmatrix} X_{NR},
\tag{4.8}
$$

$$
\ddot{X} = T_1 \ddot{X}_{NR} + 2\Omega T_2 \dot{X}_{NR} + (\Omega^2 T_3 + \dot{\Omega} T_2) X_{NR}
\tag{4.9}
$$

where Ω is the rotor angular velocity and $\dot{\Omega}$ is the rotor angular acceleration. T_3 is defined as [62]:

$$
T_3 = \begin{bmatrix} 0_{nF \times nF} & & & & \\ & \tilde{t}_3 & & & \\ & & \ddots & & \\ & & & \tilde{t}_3 & \\ & & & & \tilde{t}_3 \end{bmatrix}_{(nF+m) \times (nF+m)},
\tag{4.10}
$$

Here $\tilde{t}_2$ and $\tilde{t}_3$ are defined as [62]:

$$
\tilde{t}_2 = \begin{bmatrix} 0 & -sin(\psi_1) & cos(\psi_1) \\ 0 & -sin(\psi_2) & cos(\psi_2) \\ 0 & -sin(\psi_3) & cos(\psi_3) \end{bmatrix}; \quad \tilde{t}_3 = \begin{bmatrix} 0 & -cos(\psi_1) & -sin(\psi_1) \\ 0 & -cos(\psi_2) & -sin(\psi_2) \\ 0 & -cos(\psi_3) & -sin(\psi_3) \end{bmatrix},
\tag{4.11}
$$

Substituting Eqs. 4.7-4.9 into Eq. 4.4, the dynamic system of equations of motion in the non-rotating frame is obtained [62]:

$$M_{NR}\ddot{X}_{NR} + B_{NR}\dot{X}_{NR} + C_{NR}X_{NR} = F_{NR}u_{NR} + F_d w_d, \tag{4.12}$$

the expression of the non-rotating matrices in Eq. 4.12 are reported in Appendix B. Note that the disturbance vectors, F_d, w_d, are already expressed in the non-rotating frame, therefore they are not affected by the transformation.

4.2.2.   Wind turbine contribution to the equation of motion in the frequency domain

To proper represent the wind turbine and aerodynamic contribution to the platform equation of motion presented in Eq. 2.48, FAST and MBC are adopted. Firstly, the so-called steady state operating point, q_{op} (i.e., the average motions of the system), needs to be calculated. Given a steady wind input, and all the structural characteristics of the FOWT, q_{op} can be found following the procedure discussed in section 3.4 Alternatively, a simplified time domain simulation in still water can be carried on in FAST. Secondly, a linearized simulation adopting FASTv7 code is performed without considering hydrodynamic effects. Finally, the linearized simulation outputs are transformed in the non-rotating by means of MBC utility and added to the equation of motion 2.48:

$$\left[-\omega^2[A(\omega) + M_{NR}] + i\omega[B_{rad}(\omega) + B_{NR}] + \left[C^{hydro}(\omega) + C_{NR} \right] \right] \hat{q}(\omega) =$$
$$= F_d\sqrt{2S_{wind}(\omega)\Delta\omega} + X(\omega)\sqrt{2S_{\eta\eta}(\omega)\Delta\omega}, \tag{4.13}$$

where, M_{NR}, B_{NR}, C_{NR} and F_d includes all the structural contributions of turbine, platform, and mooring in the non-rotating frame 6 DoFs of the platform. $S_{wind}(\omega)$ is the wind spectrum, which can be estimated according to IEC regulation. This approach has been successfully adopted in [63] to perform coupled steady-state analysis in the FD of FOWTs.

4. 3   Identification of the tower natural frequencies

In order to perform such kind of linearized simulations and then performing MBC [62], it is firstly necessary to evaluate the eigenfrequencies and modeshapes of the WT tower. This modal analysis can be restricted to the identification of the first four modes (first and second Fore-Aft (FA) and Side-to-Side (SS) modes), and is a pre-process necessary for any simulation preformed FAST [1]. Even tow the isolated tower can be studied as a simple vertical cantilever (see Figure 23) [64], complexities arise from the non-uniform cross-

section and the lumped mass and inertia of the Rotor Nacelle Assembly (RNA) connected rigidly with the tower-top.

(a)   (b)
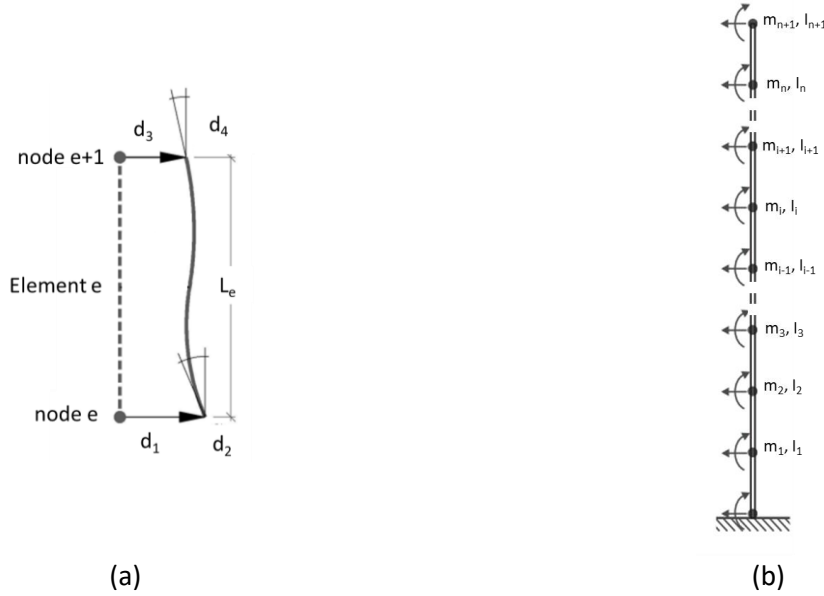
Figure 23: FE discretization of a WT tower [64]: (a) local element DoFs notation and tower model (b).

This makes necessary the use of Finite Element modal analysis. The tower is discretized in n elements. Each of them has a 4 DoFs (axial displacements and torsion are not considered). Thus, the undamped free-vibration equation of motion of the WT tower can be written as [64]:

$$M_{TW}\ddot{d} + C_{TW}d = 0,$$

(4.15)

where M_{TW} is the turbine tower mass matrix, which contains both mass and inertia terms related to each DoFs. C_{TW} is the WT tower stiffness matrix, resulting of the local element stiffness matrices assembling. For the derivation of the element stiffness matrices reference [64] is made. $\ddot{d}$ and d are the acceleration and the displacement vector of each DoF. Assuming harmonic oscillations, Eq. 4.15 transforms into

$$(-\omega^2 M_{TW} + C_{TW})d = 0,$$

(4.16)

The solution of the eigenvalue problem in Eq. 4.16nprovides the natural frequencies of the structural system, $\omega_i, i = 1, 2, \ldots, n_{DoFs}$, and the eigenvector associated with ω_i, $\phi_i(z)$. A numerical example is presented in Figure 24. The FE modal analysis is performed on the 10 MW NAUTILUS DTU FOWT [44], whose tower has been adopted for the optimization procedures carried out in Chapter 6 and Chapter 8. Attention is focused only on the first two modes. Figure 24a represents the FOWT concept, while Figure 24b shows the first two mode shape functions, normalized with respect to the maximum displacement, and their first and second derivatives.
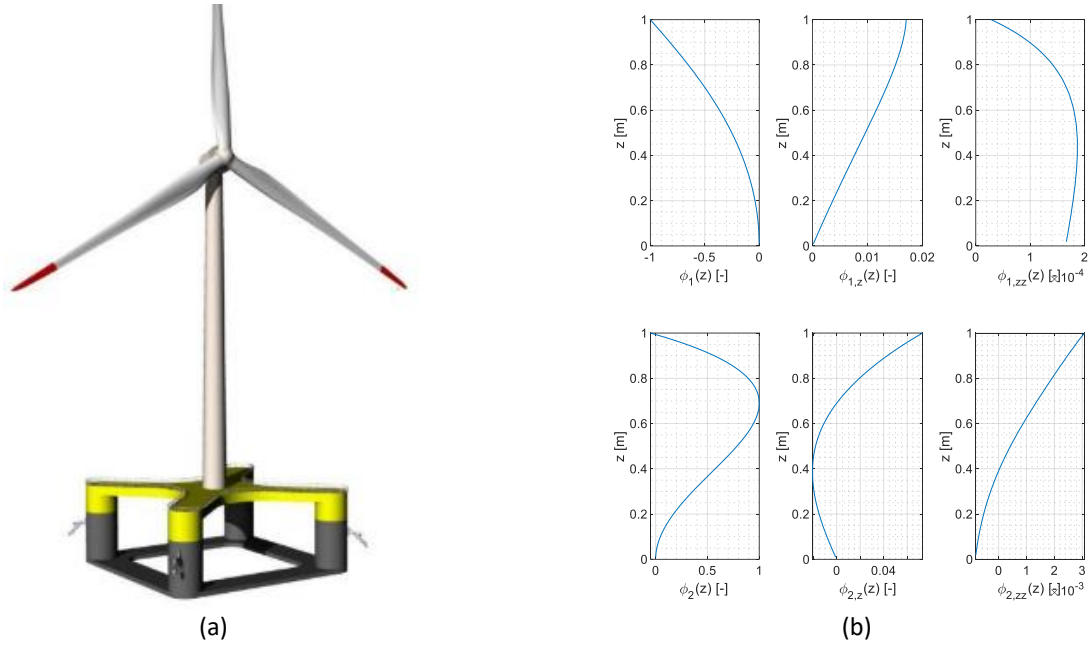
Figure 24: 10 MW NAUTILUS DTU FOWT [45]: (a) FOWT concept and modal analysis results (b).

The obtained natural periods of the first two modes are compared against the ones presented in [45]. Table 3 summarized such results.

Table 3: ITI Energy 10 MW NAUTILUS DTU FOWT modal analysis of the tower: comparison of the first two natural frequencies in the Fore-Aft direction.

	1st mode	2nd mode
FAST [Hz]	0.411	2.254
FE model [Hz]	0.397	2.237
Error [%]	3.53	0.76

As can be seen, even with a simplified FE analysis, a very good agreement on mode shapes is achieved.

4.3.1. Structural stiffness and mass matrices

Once the mode shapes, $\phi_i(z)$, normalized with respect to the maximum displacement, are known, they are adopted as input in FAST [1], which internally evaluates the modal mass, $M_{77,FA}$, and stiffness, $C_{77,FA}$. Considering the first modeshape in the Fore-Aft direction of the tower, $\boldsymbol{\phi_1}$, as seventh DoF, they can be evaluated as follows:

$$M_{77,FA} = \boldsymbol{\phi_1^t} \boldsymbol{M_{TW}} \boldsymbol{\phi_1}; \quad C_{77,FA} = \boldsymbol{\phi_1^t} \boldsymbol{C_{TW}} \boldsymbol{\phi_1},$$

(4.17)

Cross-coupling terms in Surge and Pitch DoFs can be evaluated similarly, considering the contribution of the Rotor-Nacelle tower-top mass and inertia:

$$M_{17,FA} = M_{71,FA} = m_{RN}\phi_1(h_{hub}) + \sum \tilde{\rho}_i h_i \phi_1(z_i);$$

$$M_{75,FA} = M_{57,FA} = m_{RN}\phi_1(h_{hub})h_{hub} + I_{RN}\phi_{1,z}(h_{hub}) + \sum \tilde{\rho}_i h_i \phi_1(z_i)z_i, \qquad (4.18)$$

$$C_{57,FA} = C_{75,FA} = -m_{RN}\phi_1(h_{hub}) - \sum \tilde{\rho}_i g \phi_1(z_i)h_i$$

where m_{RN} and I_{RN} are the Rotor-Nacelle mass and inertia respectively; $\tilde{\rho}_i h_i$ is the i-th tower element mass; $\phi_1(z_i)$ and $\phi_{1,z}(z_i)$ are the mode mode shape and its slope evaluated at i-th tower element height.

4. 4   On alternative estimations of the Aerodynamic contributions

Alternatively to the procedure herein adopted, in which the contributions related to aerodynamic and gyroscopic effects are estimated directly from the linearized simulations performed in FAST [1] and MBC [62], different procedures have been proposed in literature. Jurado et al [26] adopted numerical simulation reproducing free decay tests to estimate aerodynamic damping for a 10 MW FOWT. Van der Tempel [65] describes different approaches, such as the Garrad method and the numerical linearization. Bachynski [66] adopted a procedure based on the estimation of changes in the thrust force due a change in wind speed, without considering the effect of control system, to estimates the aerodynamic damping for a TLP FOWT. For this purpose, FAST simulations on the isolated rotor, subjected to a range of constant wind speeds where performed. Additional simulations are carried on increasing and decreasing the wind speed of 0.25 m/s. The ratio between the difference in the thrust forces, dF_T, caused by the difference in the incoming wind speed, dU, dF_T/dU, is adopted to estimate the aerodynamic damping. Figure 25 shows the aerodynamic damping evaluation for the 10 MW DTU FOWT presented above. Aerodynamic damping is normalized by the critical damping of the first tower fore aft mode.
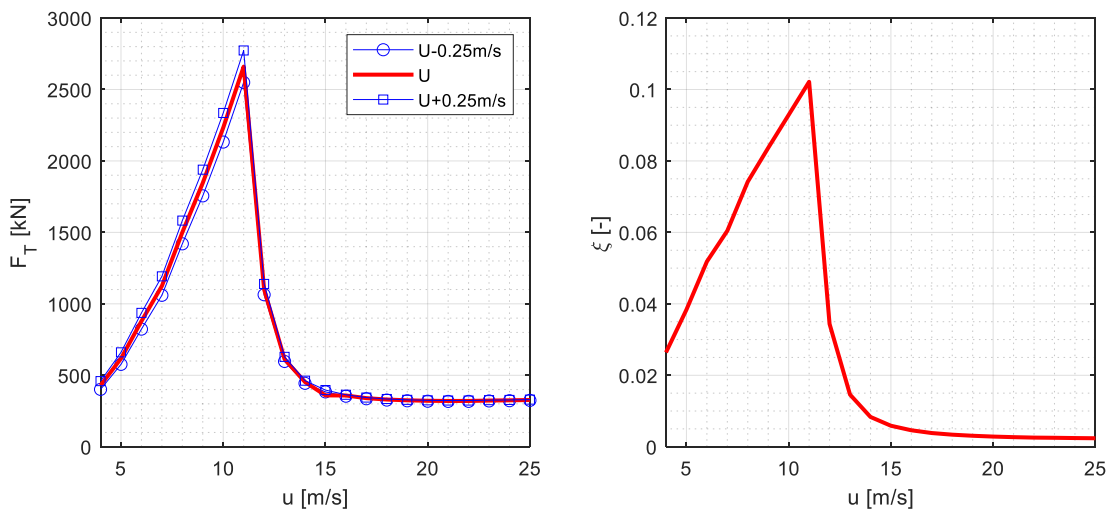
Figure 25: Aerodynamic damping calculation: Thrust forces (a) and damping coefficient, normalized with respect to the first fore-aft mode critical damping (b).

Similar to the Aerodynamic damping, the representations in the FD of the aerodynamic loads presents critical aspects, since they depend on the square of the relative wind speed seen by the blades. To properly estimate the relative velocity, several contributions need to be defined at each time step, such as blade structural velocity. This cannot be done in the FD. A possible alternative proposed in [26] is to extract aerodynamic from time domain simulations, considering a fixed hub with rigid blades subjected to a turbulent wind. Although such methods are independent on linearized simulations, they still requires analyses performed in the time-domain, whether numerical free-decay tests and/or analyses on the isolated rotor under constant wind speed. Moreover, these methods are based on a number of assumptions which may introduce errors in the simulations. For this reason, in the present work the aerodynamic and gyroscopic effects, are evaluated directly adopting linear analysis in FAST [1] and performing MBC [62]. As far as it regards the damping contributions, they are included in the $\boldsymbol{B}$ matrix presented in Eq. 4.4 ($\boldsymbol{B_{NR}}$ when the contribution from the rotating blades are transported in the non-rotating reference frame), while the aerodynamic loads, $\boldsymbol{F_d}\sqrt{2S_{wind}(\omega)\Delta\omega}$, are estimated according to Eq. 4.13 by means of the disturbance vector, $\boldsymbol{F_d}$, once the turbulence spectrum, $S_{wind}(\omega)$ is chosen.

4. 5   Aerodynamic loads

As discussed for the wave load in Section 2.1.5, the wind load is a stochastic process, which needs to be represented statistically. IEC 61400-1 regulation [67] defines the wind condition according to reference wind speed (averaged over 10 min), V_{ref}, turbulence intensity, I_{ref}, and turbine class. These parameters depend on the site. They are reported in Table 4.

Table 4: IEC 61400-1 [67] basic parameters for wind turbine classes.

WT class		I	II	III	S
V_{ref} [m/s]		50	42.5	37.5	
	A		0.16		Value specified by the designer
I_{ref} [-]	B		0.14		
	C		0.12		

The reference wind speed, Vref, represent the maximum wind speed at hub height that a WT is designed to withstand. For the sake of simplicity, IEC61400-1 groups external condition in the so-called Design Load Cases (DLCs) which are defined by combining [67]:

• Normal design situations and appropriate normal or extreme external conditions;

• Fault design situations and appropriate external conditions;

• Transportation, installation and maintenance design situations and appropriate external conditions.

The randomness of the wind is taken into account by using appropriate turbulence models. Kaimal model is one of the most adopted in the research field [24]. The turbulence spectrum is defined as [67]

$$S_K(f) = \frac{4\sigma_K^2 \frac{L_K}{\overline{u_{hub}}}}{\left(1 + 6f \frac{L_K}{\overline{u_{hub}}}\right)^{\frac{5}{3}}},$$ (4.21)

where the k subscript refers to the three component of the wind velocity, k= u, v, w; L_K is the turbulence length scale and σ_K is the standard deviation. They are defined according to the chosen turbulence model. If the IEC 61400-1 Normal Turbulence Model (NTM) is chosen, then [67]

$$\sigma_1 = I_{ref}(0.75\overline{u_{hub}} + 5.6) \qquad \Lambda_1 = \begin{cases} 0.7z & z \le 60m \\ 42m & z \le 60m \end{cases},$$ (4.22)

where Λ_1 is the turbulence scale parameter at hub height, and I_{ref} is the turbulence intensity. $\overline{u_{hub}}$, is the 10 min average wind speed at hub height, considering a power law wind profile [67]. According to the NTM, σ_1 and I_{ref} can be found graphically from Figure 26a as function of WT class and $\overline{u_{hub}}$.

(a)   (b)
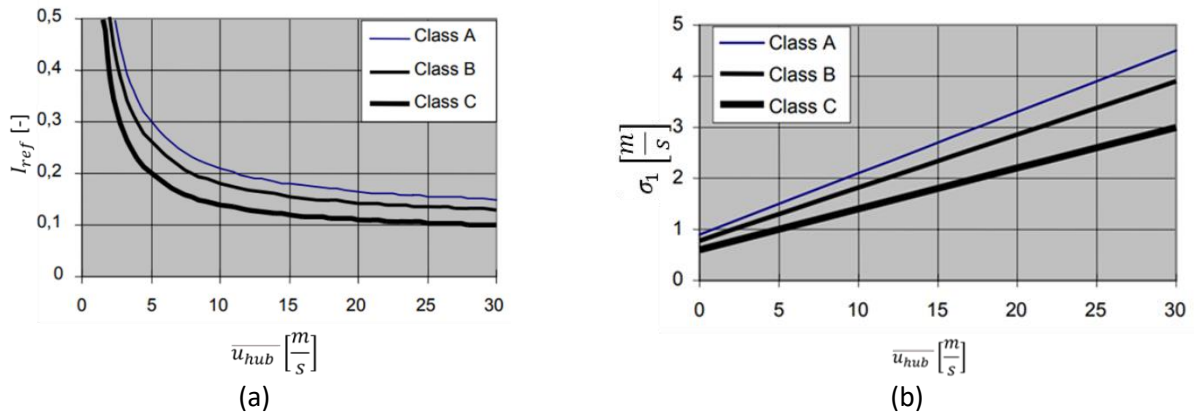
Figure 26: IEC 61400 NTM [67]: Turbulence intensity (a) and representative value of the turbulence standard deviation (b) as function of the mean wind speed at hub height.

Then, the parameter σ_K and L_K, necessary for the definition of the Kaimal Spectrum in Eq. 4.21, can be evaluated according to Table 5.

Table 5: IEC 61400-1 [67] basic parameters for NTM

	u	v	w
σ_k	σ_1	$0.8\sigma_1$	$0.5\sigma_1$
L_k	$8.1\Lambda_1$	$2.7\Lambda_1$	$0.66\Lambda_1$

In the present work, wind turbulence is modelled by means of the Kaimal Spectrum, considering a NTM. The code TurbSim can be adopted to generate the wind input [68]. It is an opensource code which sis generally adopted as pre-processor of FAST when it is necessary to simulate stochastic wind loads. For the optimizations presented, Eq. 4.21 by IEC 61400 [67] has been adopted to calculate the wind turbulence spectrum, $S_{wind}(\omega)$ (Eq. 4.13), Aerodynamic loads are then estimated in the FD by multiplying the turbulent wind amplitude $\sqrt{2S_{wind}(\omega)\Delta\omega}$ by the disturbance force vector, $\boldsymbol{F_d}$.

Chapter 5.
Development and verification of the FD coupled FOWT model

In this section, the development and validation of the FD, coupled, FOWT model is presented. The coupled response of a FOWT can be studied directly in the FD assuming steady state conditions and harmonic motions. This allows to estimate the response of the system in terms of amplitudes.

5.1   FD coupled FOWT system response

The response in the FD of a FOWT results from the contribution of the WT, the floating platform, and the mooring lines. As presented in section 4.2., an efficient technique to estimate the structural contribution of WT, platform and mooring lines consists in performing a FAST linearized simulation around a steady state operating point. As far as it concerns the platform hydrodynamic contribution, as described in section 2.3 and 2.4, motions on bluff and slender elements must be considered. For the first ones, the contribution to the equation of motion is completely determined by solving the velocity potential problems of Radiation and Diffraction. This is done adopting the software ANSYS AQWA [48]. While for the second ones, a linearization of the Morison equation is needed. Moreover, following the procedure described in section 2.4.1 and 2.4.2, the viscous drag Damping matrix can be evaluated. Such a contribution depends both on the excitation frequency and the systems motions, therefore an iteration procedure is required. Hydrostatic stiffness, C^{Hydro}, and platform mass, M^{Float}, matrices are calculated according to [52] and used as input to FAST. The mooring lines are modelled adopting the quasi-static formulation presented in Chapter 3, developed by Jonkman [54]. The overall 7 DoFs equation of motion of the FOWT, under the joint action of wind and wave loadings, can be written as

$$
\begin{aligned}
\Big[-\omega^2\big(A(\omega) + M^{Float} + M^{Turb}\big) + j\omega\Big(B_{rad}(\omega) + B^{Turb} + B^{Mor}(\omega, \sigma, a)\Big) + \big(C^{hydro} + C^{Moor} + \\
C^{Turb}\big)\Big]\, \breve{q}(\omega) = \Big(X(\omega)\sqrt{2S_{\eta\eta}(\omega)\Delta\omega} + F_d\sqrt{2S_{wind}(\omega)\Delta\omega}\Big),
\end{aligned}
\tag{5.1}
$$

where ω is the circular frequency; $\breve{q}(\omega)$ is the amplitude of the dynamic response of the system with seven DoFs; $A(\omega)$ is the added mass matrix; $B_{rad}(\omega)$ is the radiation damping matrix; C^{hydro} is the hydrostatic stiffness matrix, while C^{Moor} is the mooring lines stiffness matrix; $B^{Mor}(\omega, \sigma, a)$ is the viscous drag damping matrix [63]; $X(\omega)$ is the hydrodynamic force vector while F_d is the disturbance force vector which allows to account for the

effect of aerodynamic loads in the 7-DoF system; $S_\eta(\omega)$ represents the irregular wave spectrum, whereas $S_{wind}(\omega)$ the turbulent wind spectrum. In the present, work only horizontal turbulence effects are considered. The IEC 61400 Normal Turbulence Model (NTM) Kaimal model [67] is adopted for the wind and the JONSWAP spectrum is used for the waves. The full linear system is developed and solved in MATLAB Figure 27 shows the workflow of the developed FD model for the calculation of the RAOs for a selected input wave direction.
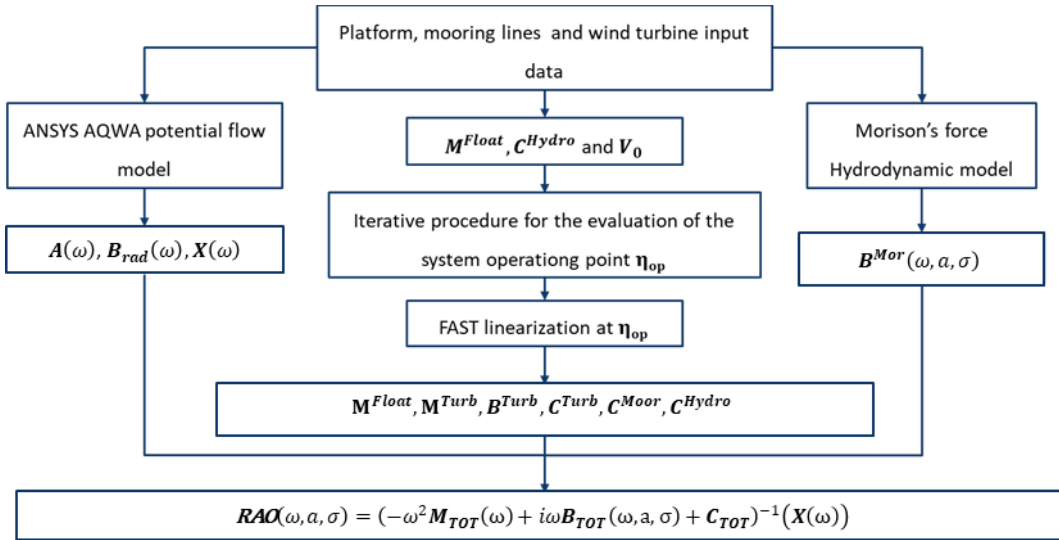
Figure 27: RAO of the FOWT calculation is the FD: workflow of the algorithm.

5.2   Code verification

To verify the developed FD model, the 5MW OC4 DeepCwind semisubmersible FOWT [47] has been analysed. The platform is presented in Figure 28. It consists of a main column, attached to the tower, and three offset columns which start above the SWL and continue beneath the water until a depth of 14 m. From 14 m to the total draft of 20 m, the diameter of the columns doubles. Such wider base column are called heave plates. They help to suppress motion particularly in the heave direction, but also in surge, sway, roll, and pitch. for such elements, hydrodynamic can be modelled adopting the modified Morison equation for transverse flow (Eq. 2.54).

(a)   (b)
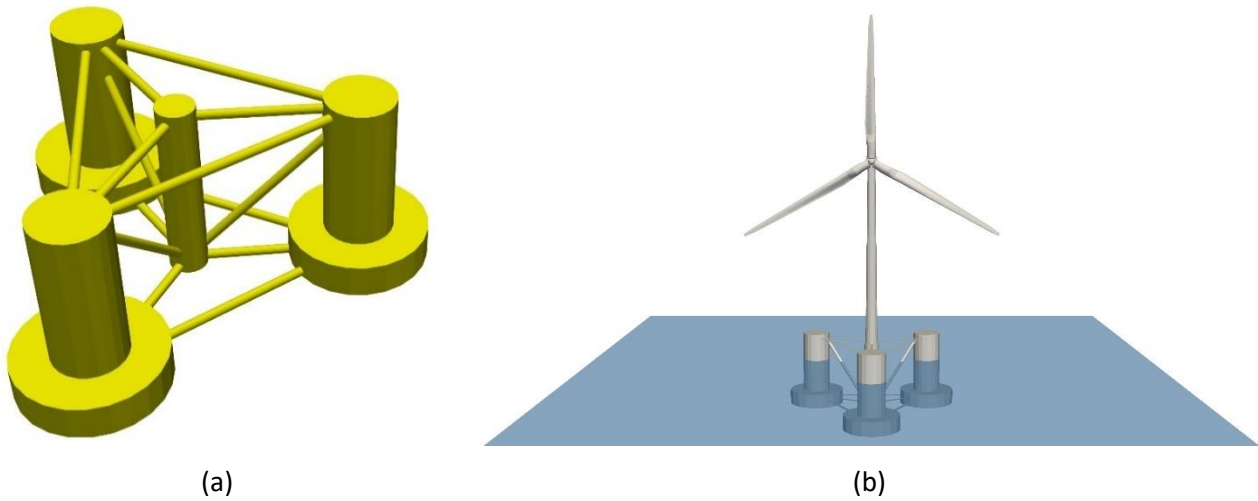
Figure 28: 5MW OC4 DeepCwind semisubmersible FOWT [36]: platform concept (a) and FOWT (b).

2 cross braces structures connect the main column and the offset columns one to each other. A set of two horizontal braces connects the offset columns one to each other. Two horizontal and one diagonal brace connect each offset column with the central, main column. These sets result in a sort of lattice, spatial structure, which grants rigidity to the whole platform. The main platform specifications are reported in Table 6.

Table 6: 5 MW NREL DeepCwind semisubmersible platform specifications [47].

5MW NREL DeepCwind Platform	
Depth of platform base below SWL	20 m
Elevation of main column above SWL	10 m
Elevation of offset columns above SWL	12 m
Length of upper columns	26 m
Length of Heave plates	6 m
Depth to top base columns below SWL	14 m
Diameter of main columns	6.5 m
Diameter of offset columns	12 m
Diameter of Heave plates	24 m
Diameter of pontoon and cross-braces	1.6 m
Platform CM location below SWL	13.46 m
Water depth	200 m

5.2.1   Potential flow hydrodynamic platform verification

To estimate the linear hydrodynamic coefficients of added mass, radiation damping and DFK forces, a Hydrodynamic Diffraction analysis has been performed by means of the ANSYS AQWA. The code solves the Radiation-Diffraction problem by discretizing the wetted surface of the platform by means of quadrilateral panel. Only bluff elements are modelled. The mesh size is chosen accordingly to the highest wave frequency adopted. Figure 29 shows the modelled surface mesh.
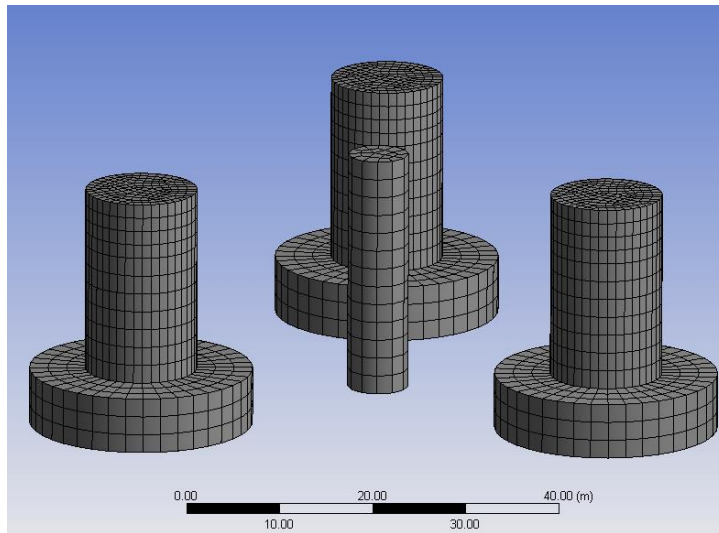
Figure 29: 5MW OC4 DeepCwind semisubmersible FOWT [36]: hull modeling in ANSYS AQWA.

The results of the hydrodynamic model are verified with those calculated by NREL in [47] adopting WAMIT (Figure 30). ANSYS AQWA results are plotted with solid lines, while the WAMIT ones provided in [47] are represented with circle markers In Figure 30a and 30b, the comparison between the added mass coefficients is presented. Radiation damping coefficients are shown in Figures 30c and 30d, while hydrodynamic forces are illustrated in Figure 30e and 30f. As can be seen in the figures, a very good agreement is achieved.

(a) (b)
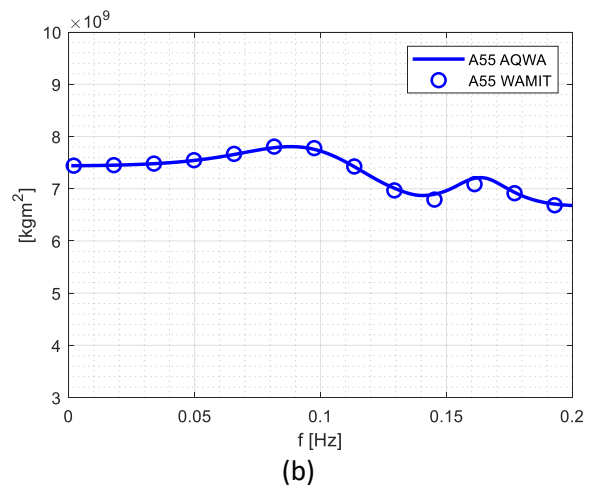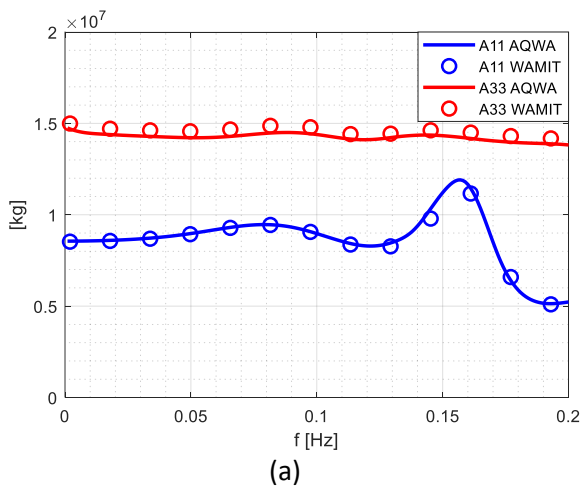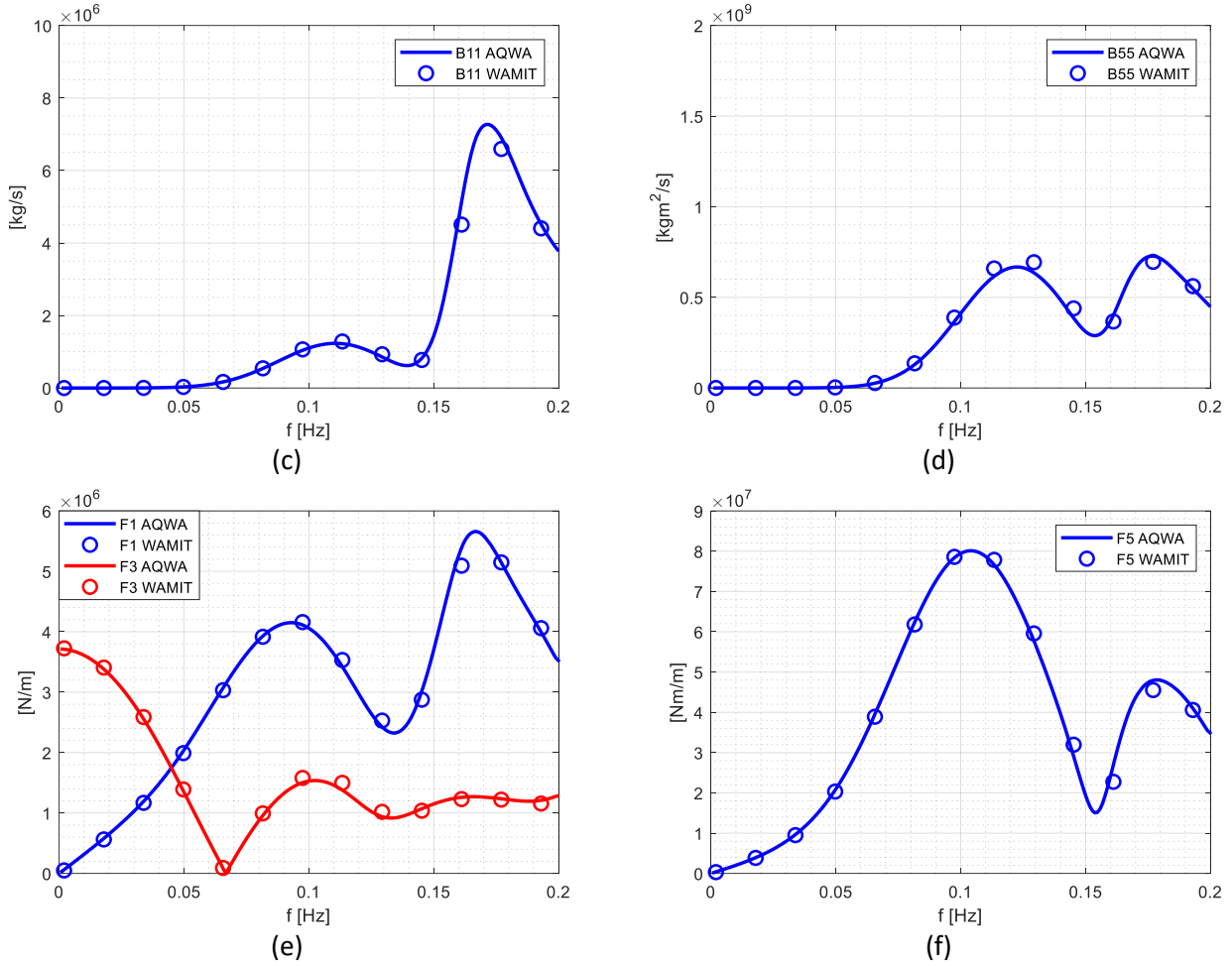
Figure 30. Verification of the ANSYS AQWA model of the 5MW NREL semisubmersible platform: (a) Surge-Surge (blue) and Heave-Heave (red) added mass; (b) Pitch-Pitch added mass; (c) Surge-Surge radiation damping; (d) Pitch-Pitch radiation damping; (e) Surge (blue) and Heave (red) Diffraction + Froude-Krilov forces; (f) Pitch Diffraction + Froude-Krilov force.

5.2.2 Model verification- RAOs

The FD model verification has been performed in two phases. Firstly, a comparison between RAOs obtained in the FD and by time domain simulation has been carried out. Secondly, the system response under turbulent wind and irregular waves has been compared.

As described in Section 2.3, the system response in the FD can be represented in terms of RAOs Being RAOs the linearized transfer functions of the dynamic system, their magnitude can be calculated from time domain results following this relation:

$$S_\eta(\omega) = S_{wave}(\omega)\|RAO(\omega)\|^2, \tag{5.2}$$

where $S_{\eta\eta}(\omega)$ is the input wave spectrum and $S_R(\omega)$ is the response spectrum in one of the six DoFs of the system. In the FD, RAOs of the platform DoFs are the results of the linear system of equation presented in Figure 27. From the RAOs of the system motions in Surge, Heave and Pitch, the Fairlead tension RAO of the

cable aligned with the 0° wave heading direction is calculated. Since the platform is a rigid body and the hypothesis of small rotations holds, the displacements of the cable Fairlead is obtained as superimposition of a pure translation (Surge-Heave) and a pure rotation (Pitch). Therefore, the corresponding RAO can be evaluated as

$$\mathbf{RAO_{FairDisp}}(\omega) = \begin{bmatrix} RAO_1(\omega) \\ RAO_3(\omega) \end{bmatrix} + \begin{bmatrix} RAO_5(\omega)z_F \\ RAO_5(\omega)x_F \end{bmatrix}, \tag{5.3}$$

where $RAO_1(\omega)$, $RAO_3(\omega)$ and $RAO_5(\omega)$ are respectively platform Surge, Heave, and Pitch RAOs. (x_F, z_F) are the Fairlead coordinates with respect to the platform reference frame (see Figure 4). Since in the quasi-static approach the cable dynamics is neglected, the horizontal and vertical components of Fairlead tension are found by multiplying the Fairlead displacement by the stiffness matrix of the single cable (evaluated at the steady state equilibrium point of the system)

$$\mathbf{RAO_{FairF}}(\omega) = \begin{bmatrix} RAO_{FairH}(\omega) \\ RAO_{FairV}(\omega) \end{bmatrix} = \mathbf{K^P RAO_{FairDisp}}(\omega), \tag{5.4}$$

where $RAO_{FairH}(\omega)$ and $RAO_{FairV}(\omega)$ are Horizontal and Vertical Fairlead tension RAOs. $\mathbf{K^P}$ the 2x2 stiffness matrix of the selected cable of the mooring systems. In the case of slack catenary mooring lines, it can be calculated as [60]

$$\mathbf{K^P} = \begin{bmatrix} K_{11}^P & K_{12}^P \\ K_{21}^P & K_{22}^P \end{bmatrix} = \begin{bmatrix} \frac{\partial l}{\partial H} & \frac{\partial l}{\partial V} \\ \frac{\partial h}{\partial H} & \frac{\partial h}{\partial V} \end{bmatrix}^{-1} = \left(\mathbf{F^P} \right)^{-1}, \tag{5.5}$$

where $\mathbf{F^P}$ is the flexibility matrix which is made of the partial derivatives of the cable profile l and h (see Figure 31), with respect to horizontal and vertical tensions [60]

$$\frac{\partial l}{\partial H} = \frac{L}{EA} + \frac{1}{\omega} \left[\frac{-V}{\sqrt{H^2+V^2}} + sinh^{-1}\left(\frac{V}{H} \right) \right],$$

$$\frac{\partial l}{\partial V} = \frac{\partial h}{\partial H} = \frac{1}{\omega} \left[\frac{H}{\sqrt{H^2+V^2}} - 1 \right], \tag{5.6}$$

$$\frac{\partial h}{\partial V} = \frac{V}{\omega} \left[\frac{1}{\sqrt{H^2+V^2}} + \frac{1}{EA} \right],$$
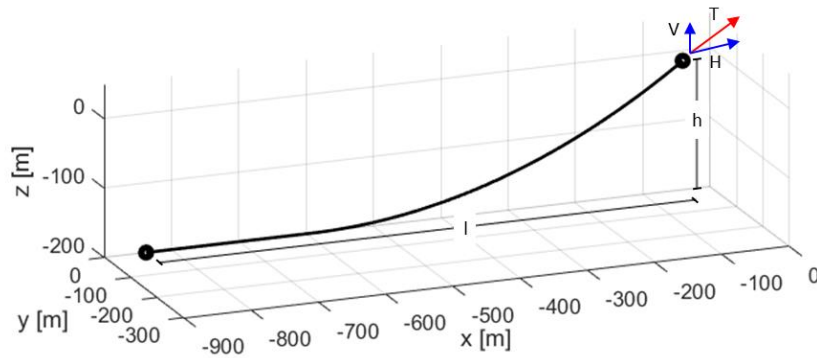
Figure 31. Catenary mooring system loads at the fairlead.

Here L is the unstretched length of the cable, ω is the cable mass in water per unit length, EA is the axial stiffness of the cable V and H are the horizontal and vertical tensions at the fairlead. H and V are calculated by means of quasi-static cable model [69], which solves the catenary nonlinear system of equations with Newton–Raphson iterative procedure.

Ramachandran et al. presented a procedure to directly evaluate RAOs for a FOWT in FAST [70]. Herein the same simulation set up is adopted. Six computations of 8000s length are performed discarding the first 2000s. A white noise sea spectrum in the frequency band between 0.005 Hz to 0.2 Hz of 1m/Hz2 is applied, changing the wave seeds. PSDs of significant quantities, such as platform displacements and cable tension, are evaluated for each of the six simulation and averaged out. In order to reproduce FASTv7 mooring lines model, the module MAP++ of FASTv8 is adopted to simulate cable dynamics. Out of diagonal terms of the viscous damping matrix, $B_{\text{Morison } i,j}$, are neglected according to [47].

A first FD analysis considering only the 6 DoFs related to the platform, i.e., assuming a rigid tower, is performed. Results are presented from Figure 32 to Figure 35. As can be seen, a very good agreement is achieved for the Surge, Heave and Pitch DoFs, but also for the Fairlead Tension RAO of the upwind cable (evaluated according to Eqs. 5.2-5.4). The surge RAO presented in Figure 32 shows a good agreement with the results obtained from TD simulation in FAST. The eigenfrequency peak is clearly visible at 0.0085 Hz (around 117 s). Moreover, due to the cross coupling between Surge and Pitch motions, a second, smaller, peak is noticeable around 0.040 Hz (around 25 s), which is the Pitch eigenfrequency.
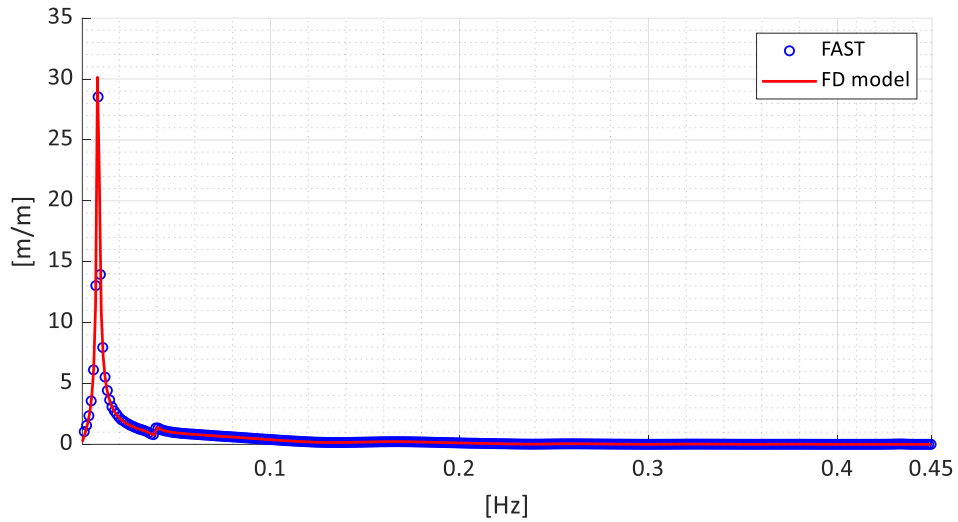
Figure 32. 5 MW NREL DeepCwind FOWT 6-DOF model: Surge RAO.

Heave RAO verification is presented in Figure 33, again a good agreement is achieved. The eigenfrequency is around 0.058 Hz (17 s).
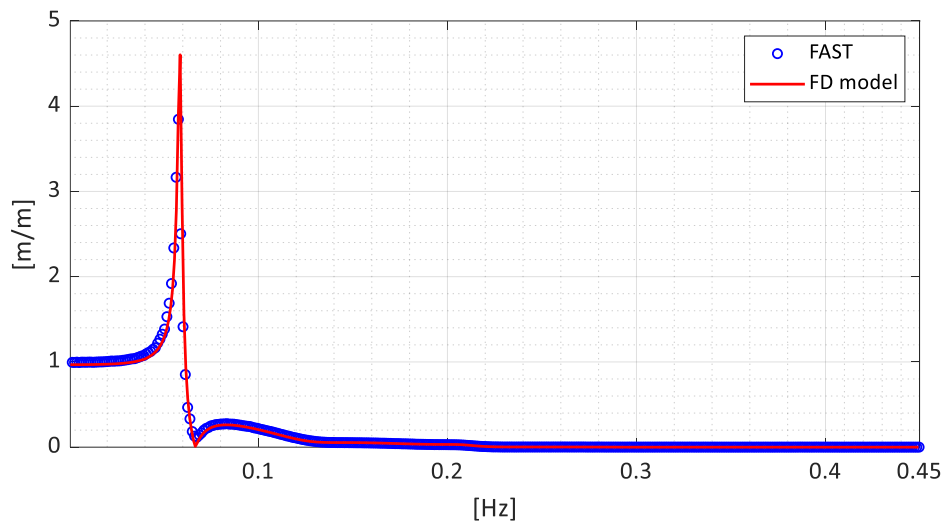
Figure 33. 5 MW NREL DeepCwind FOWT 6-DoF model: Heave RAO.

Figure 34 shows the Pitch RAO verification. Overall, a very good agreement is achieved. The Surge-Pitch coupling is clearly noticeable at low frequencies. Focusing the attention from 0.4 Hz to 0.45 Hz, it is possible to observe that the 6 DoFs FD model is not capable to catch the First Fore-Aft tower mode shape, around 0.44Hz (2.27 s).
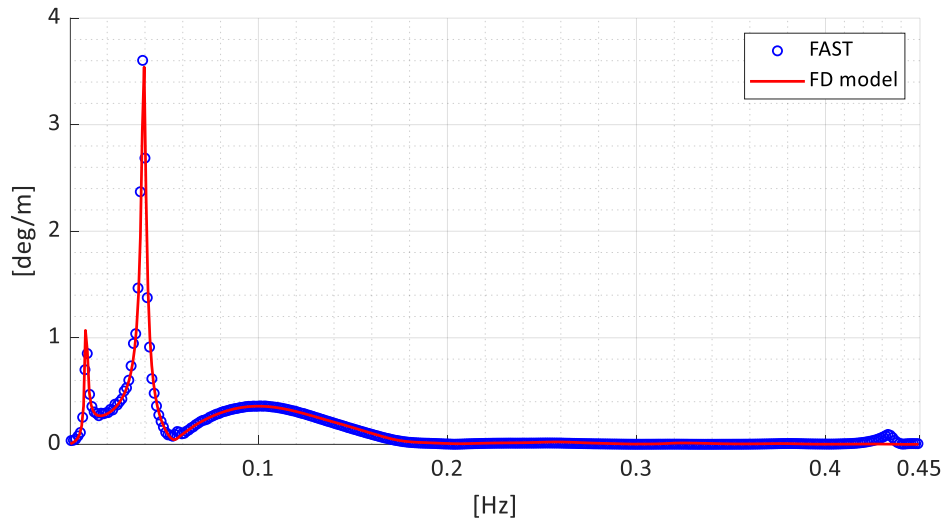
Figure 34. 5 MW NREL DeepCwind FOWT 6-DoF model: Pitch RAO.

In conclusion, Fairlead tension RAO is presented in Figure 36. Three peaks are noticeable at the Surge, Pitch and Heave eigenfrequencies since the Fairlead displacement results from the combination of these three platform motions (see Eq. 5.2). A very good agreement is again reached.
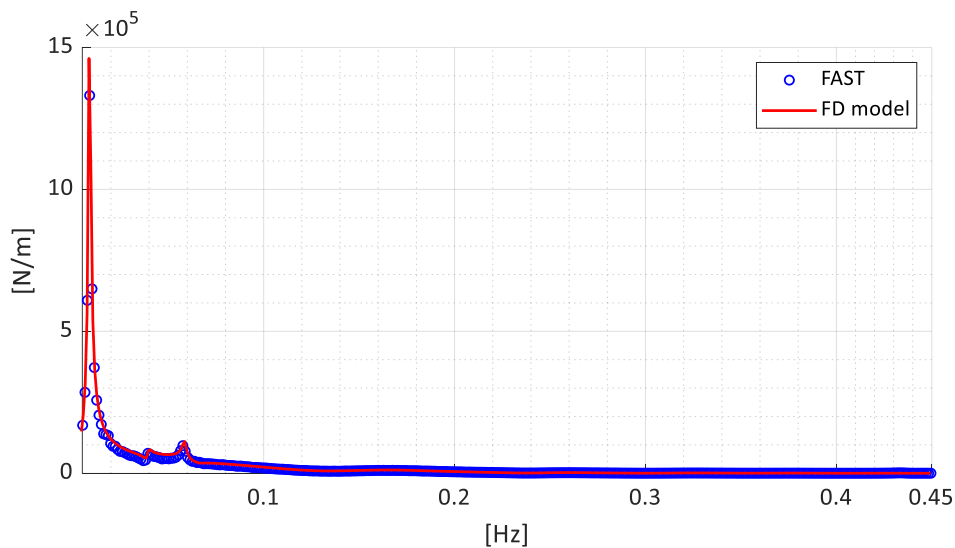
Figure 35. 5 MW NREL DeepCwind FOWT 6-DoF model: Fairlead tension RAO.

In order to characterize the dynamic behavior of the turbine directly in the FD model, the Fore-Aft deflection of the tower top has been added as 7th DoF to the system. This is done by adopting the procedure discussed in section 4.2, performing a linearized analysis in FAST with 7 DoFs enabled. This allows to estimate the tower deflection RAO, but also to evaluate the RAO of stresses like shear and bending moment ones. To do so, A similar procedure to the Fairlead tension calculation has been adopted. The tower is assumed to behave like a vertical cantilever, subjected to an imposed displacement to its free

end. Being $\mathbf{C_{TOT}}(7,7)$ the modal stiffness associated with the 7th DoF, adopting equilibrium assumptions, the shear force RAO at the tower base, $\mathrm{RAO}_{V\_base}(\omega)$, is evaluated as follows:

$$\mathrm{RAO}_{V\_base}(\omega) = \mathbf{C_{TOT}}(7,7)\mathrm{RAO}_7(\omega), \tag{5.7}$$

Where $\mathrm{RAO}_7(\omega)$, is the tower top deflection RAO, which is calculated solving the FD system of equations of motion. Similarly, the tower base bending moment RAO, $\mathrm{RAO}_{M\_base}(\omega)$, is evaluated as:

$$\mathrm{RAO}_{M\_base}(\omega) = \mathrm{RAO}_{V\_base}(\omega)h_{TT}, \tag{5.8}$$

Where h_{TT} is the height of the tower top, with respect to the to the tower based. In the Figures below, the RAOs obtained from the 7-DoF FD model are compared against FAST results. Figures 36 to 39 show the Surge, Heave, Pitch and Fairlead tension RAOs, which again present a good agreement with respect to FAST results. Moreover, since the model is now capable to predict the tower-platform coupling, the First Fore-Aft tower mode shape eigenfrequency peak is clearly visible in the Pitch RAO (Figure 38).
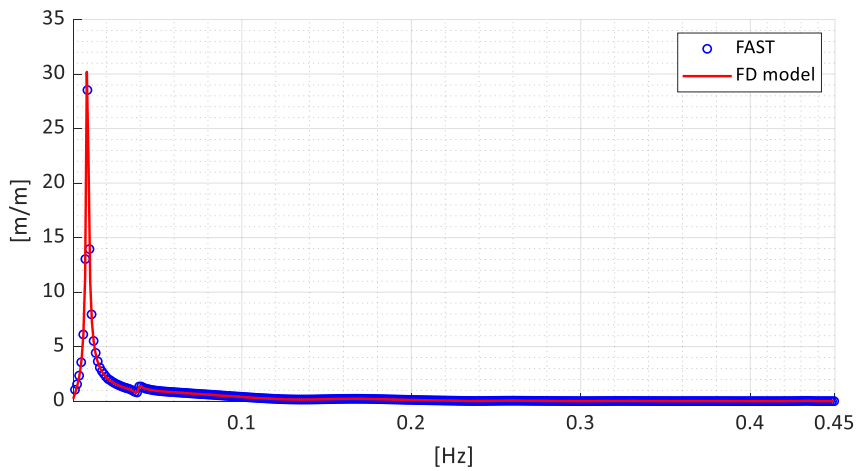
Figure 36. 5 MW NREL DeepCwind FOWT 7-DoF model: Surge RAO.
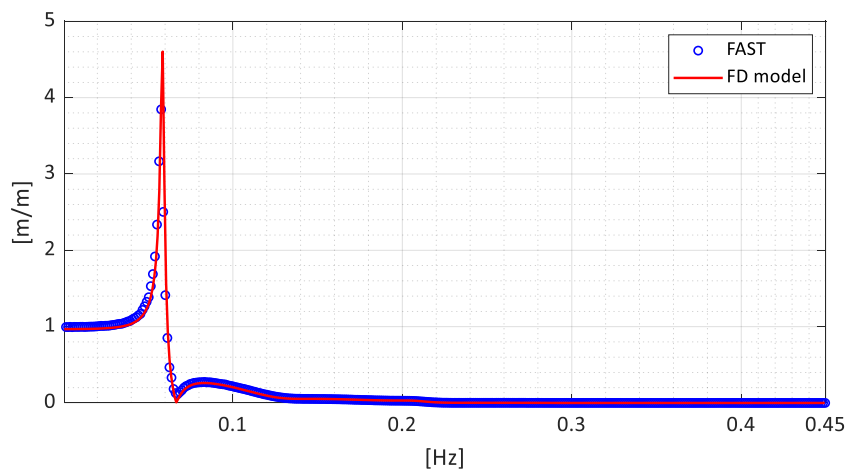
Figure 37. 5 MW NREL DeepCwind FOWT 7-DoF model: Heave RAO.
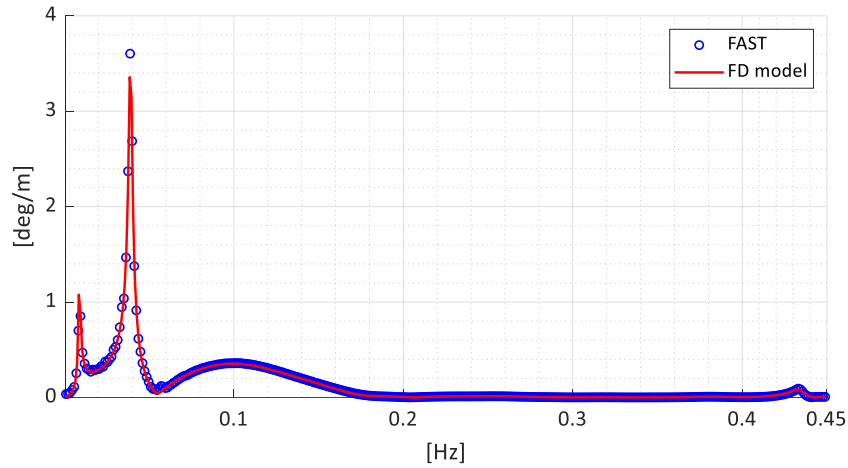
Figure 38. 5 MW NREL DeepCwind FOWT 7-DoF model: Pitch RAO.
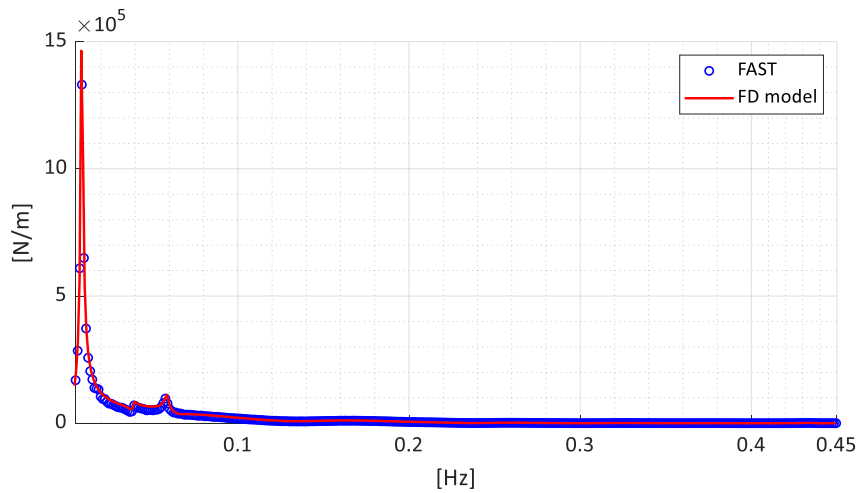
Figure 39. 5 MW NREL DeepCwind FOWT 7-DoF model: Fairlead tension RAO.

Figures 40 to 42 show the verification of the WT tower results obtained from the FD model. Overall, a good agreement is achieved both for displacement and stresses. The tower top displacement RAO is presented in Figure 40. Surge and Pitch eigenfrequencies are noticeable at low frequency, denoting the coupling between tower and platform motions. The FA eigenfrequency (0.44 Hz) peak amplitude is well predicted.
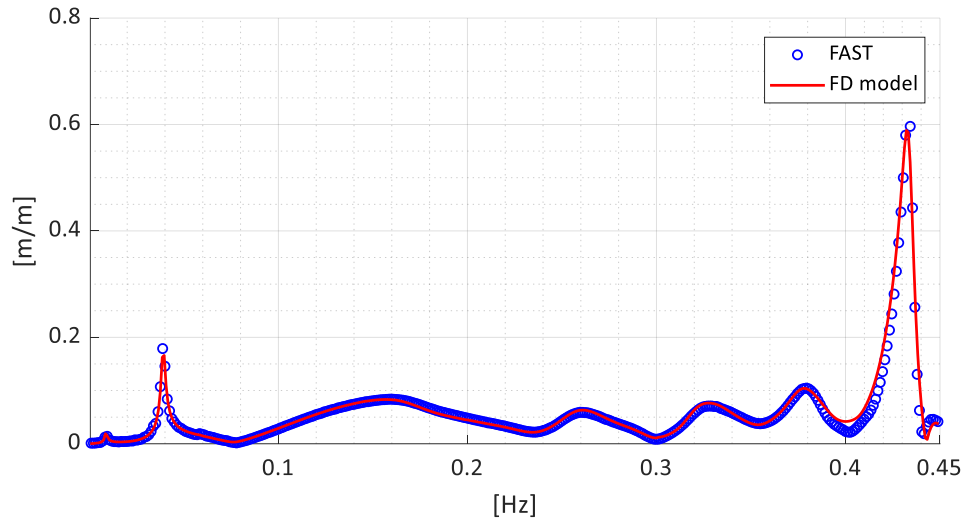
Figure 40. 5 MW NREL DeepCwind FOWT 7-DoF model: Tower top FA deflection RAO.

Tower base shear, $RAO_{V\_base}(\omega)$, and bending moment, $RAO_{M\_base}(\omega)$, RAOs are presented in Figure 41 and 42. A fairly good agreement is reached for both of these results, despite a slight underprediction of Surge and Pitch peaks for what regards $RAO_{V\_base}(\omega)$ (Figure 41).
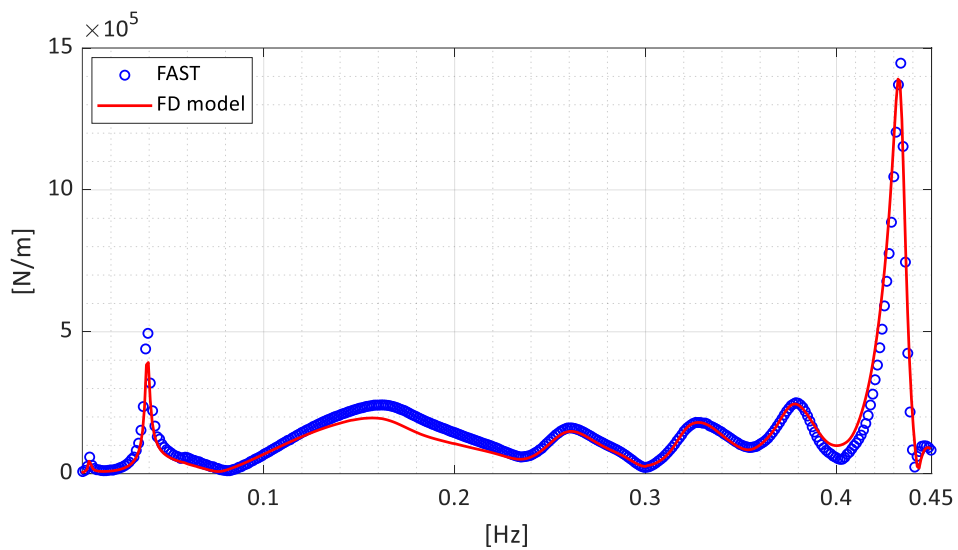
Figure 41. 5 MW NREL DeepCwind FOWT 7-DoF model: Tower base shear force RAO, evaluated according to Eq. 5.6.
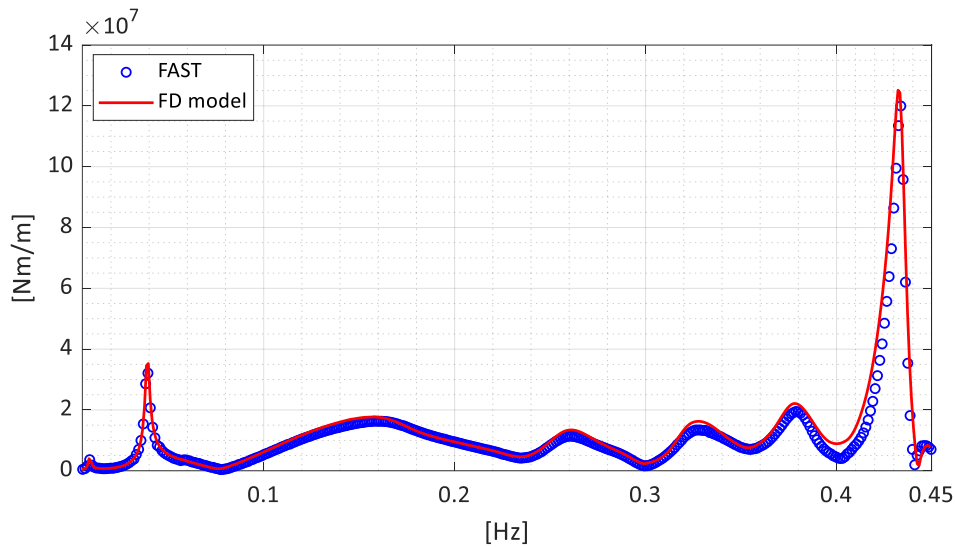
Figure 42. 5 MW NREL DeepCwind FOWT 7-DoF model: Tower base shear force RAO, evaluated according to Eq. 5.7.

Overall, the FD model results present good agreement in terms of RAO with respect to FAST TD simulation results.

5.2.3   Model verification – Response in turbulent wind and Irregular waves

The FD model capabilities has been verified also considering the combined action of a turbulent wind and an irregular wave. As show in Figure 27, to properly estimate the turbine and moorings contributions, the system linearization in FAST has to be done around an equilibrium point. As already discussed, in linear wave theory, the mean displacements of a FOWT can be accurately found considering only the wind action. Firstly, a simulation in FAST has been performed to identify the equilibrium position of the system. Then, the linearization is performed in this *displaced* configuration. For this test, rotor speed and blade pitch has been set properly to simulate the power production load condition. IEC 61400 [67] Kaimal NTM model for turbulent wind has been adopted, with mean wind speed at hub height equal to 11 m/s, i.e. the rated wind speed (Figure 43). An irregular wave, represented by a JONSWAP spectrum, with 2 m significant wave height and 10 s peak spectral period has been adopted (Figure 44).
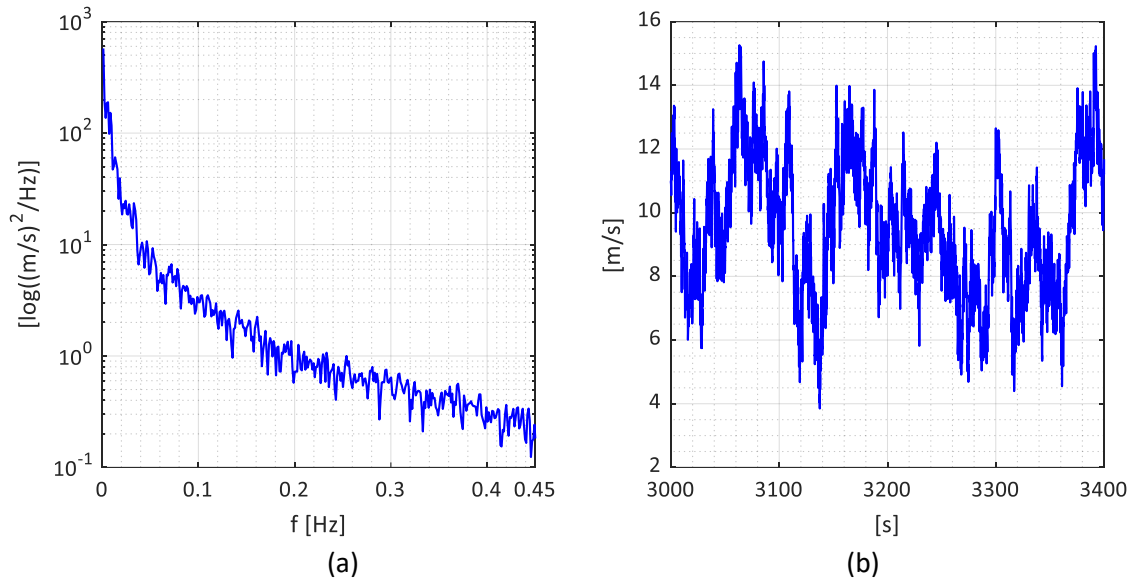
Figure 43. Turbulent wind generated according to IEC Kaimal NTM (σ_1) with $\overline{u_{hub}} = 11 \, m/s$: wind speed PSD (a) and generated time series (b).
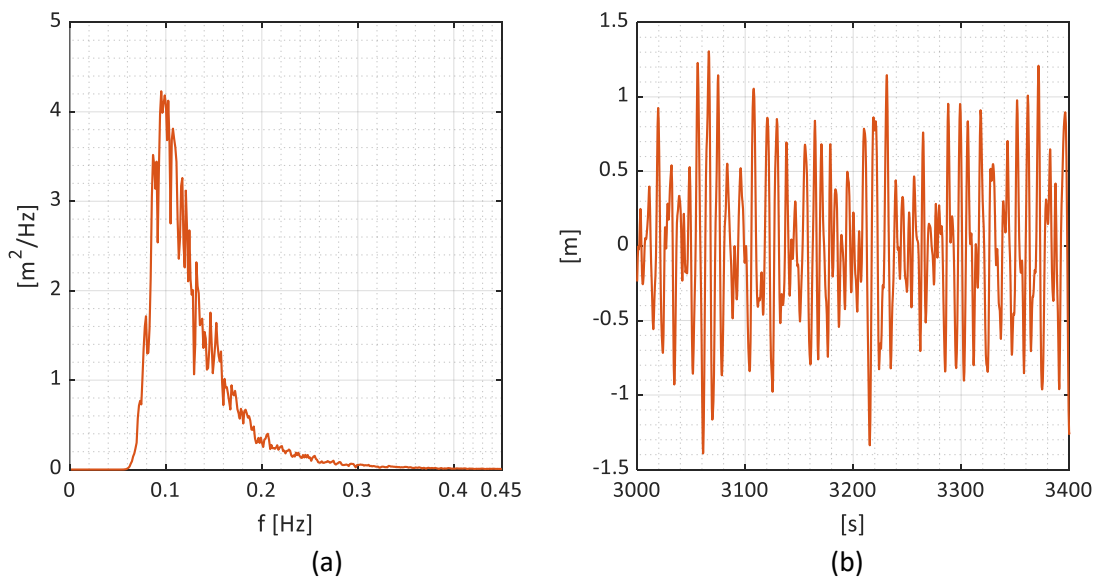
Figure 44. Irregular wave generated according to a JONSWAP spectrum with significant wave height equal to 2 m and peak spectral period equal to 10 s: wave height PSD (a) and generated time series (b).

The time domain simulation has been performed in FASTv8 with the same settings presented in the previous section. Wind process has been generated adopting TurbSim [68], while the wave process directly in HydroDyn [71]. The same spectra and mean platform displacements have been applied as input to the FD model.

Figure 45 shows the comparison in the Surge DoF. Amplitude of motions are presented in Figure 45a, red curve refers to the FD model while blue dots present the time-domain simulation results. As it is possible to observe, results are in very good agreement. As expected, the excitation of the Surge eigenfrequency is caused by the turbulent wind, while the wave loadings tend to influence the frequency bands around 0.1

Hz. From the amplitude of motions, the time history (Figure 45b) of the Surge motion can be reconstructed and compared with FAST results. For this comparison, amplitudes from 0 to 0.45 Hz have been considered. The same phase angles, uniformly distributed between 0 and 2π, are applied to the harmonics presented in Figure 45a. Overall, results of the FD model present a good agreement also in terms of time-history.

(a)

(b)
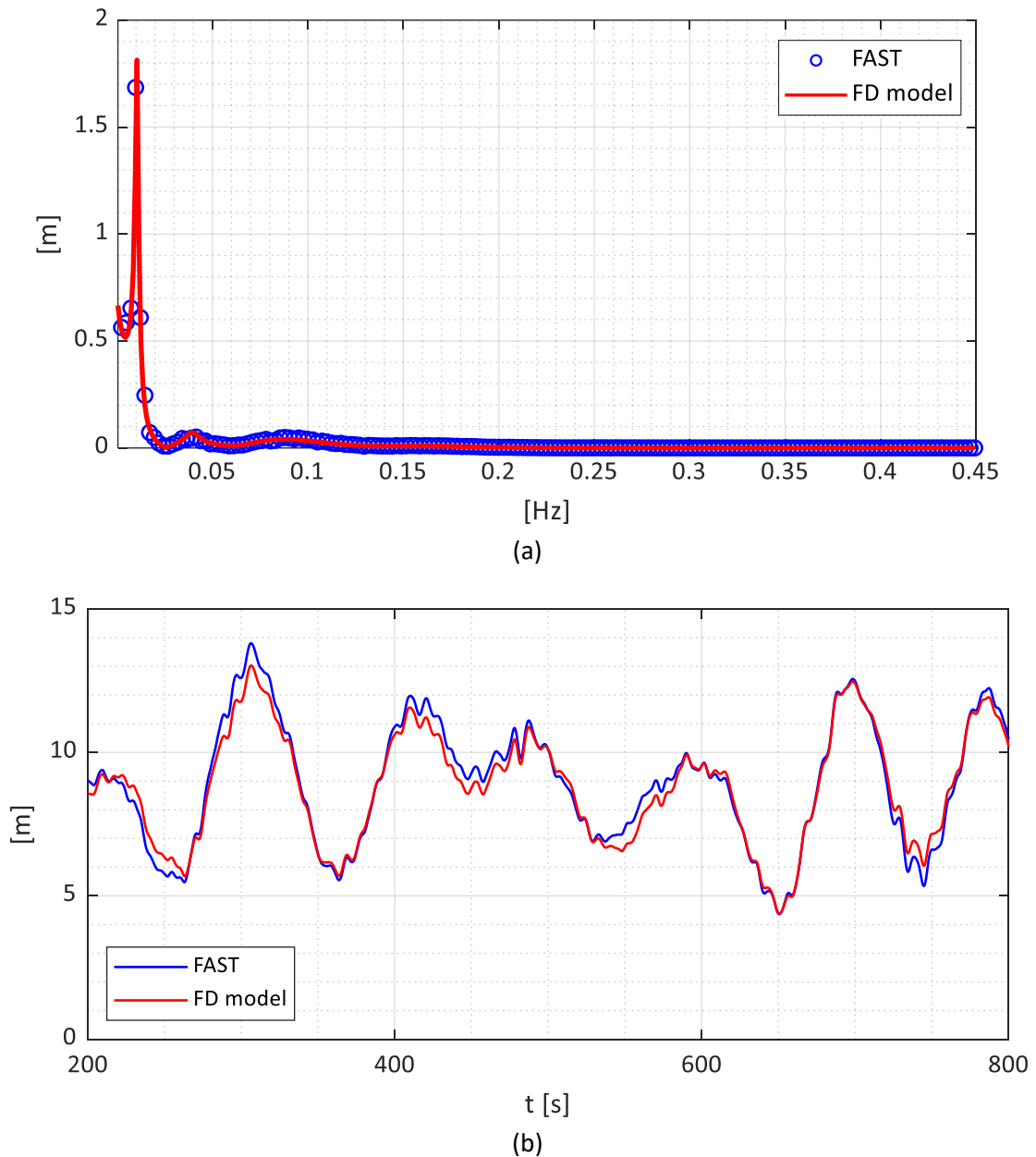
Figure 45. Response in turbulent wind and irregular waves: comparison of the amplitude of motions in Surge (a) and time histories (b), reconstructed assuming the same phase angles for both the processes presented.

Figure 46 shows the comparison in the Heave DoF. Amplitude of motions are presented in Figure 46a, red curve refers to the FD model while blue dots present the time-domain simulation results. As it is possible to observe, results are in relatively good agreement. The FD model presents larger excitations at the pitch

eigenfrequency with respect to the time-domain simulations and smaller around the heave eigenfrequency and in the band excited by the sea spectrum. Results are compared also in terms of time history (Figure 46b). For this comparison, amplitudes from 0 to 0.45 Hz have been considered. The same phase angles, uniformly distributed between 0 and 2π, are applied to the harmonics presented in Figure 46a. Overall, results of the FD model present a good agreement in terms of time-history.

(a)

(b)
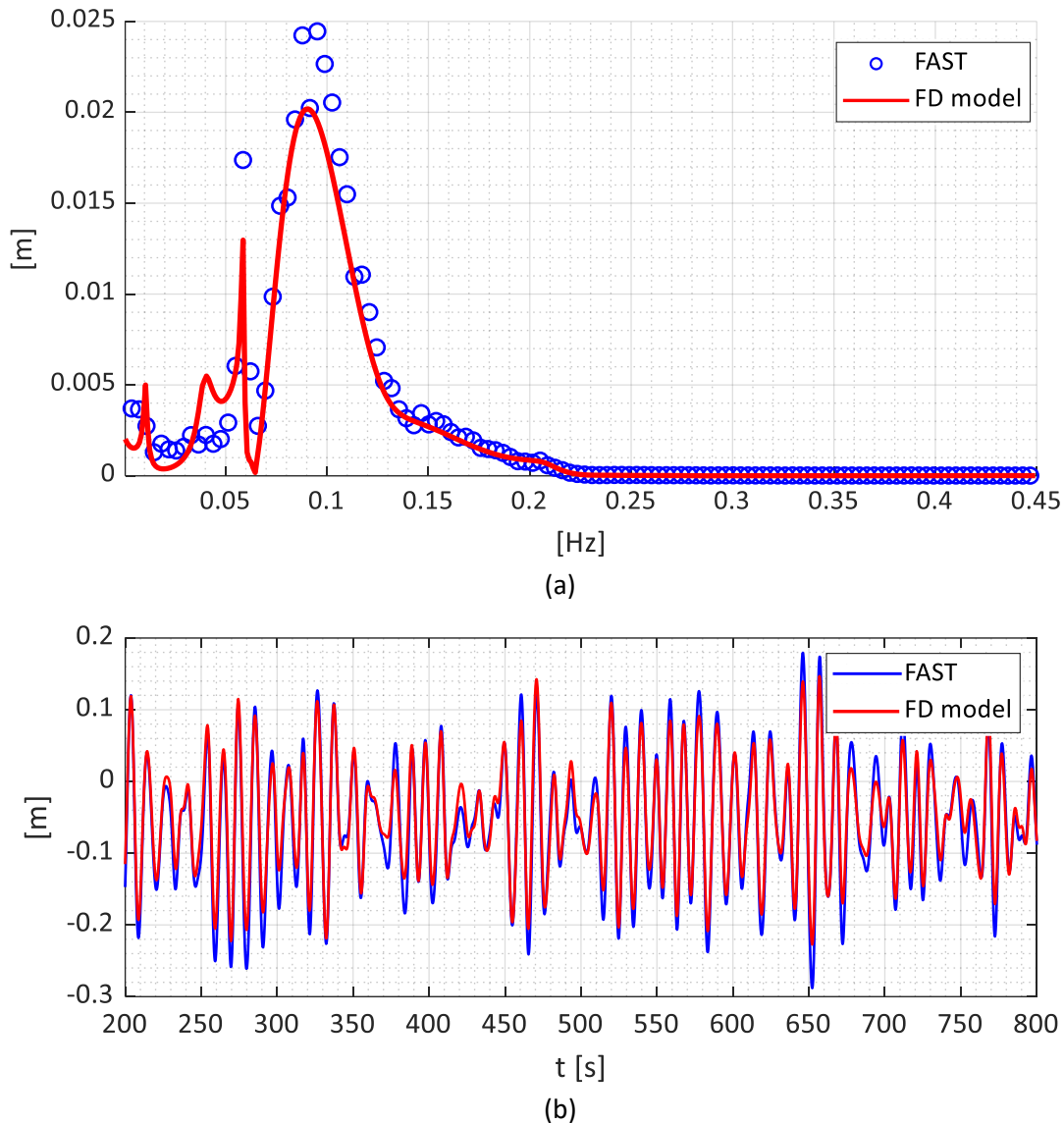
Figure 46. Response in turbulent wind and irregular waves: comparison of the amplitude of motions in Heave (a) and time histories (b), reconstructed assuming the same phase angles for both the processes presented.

The comparison in the Pitch DoF is presented in Figure 47. Amplitude of motions are presented in Figure 47a, red curve refers to the FD model while blue dots present the time-domain simulation results. As it is possible to observe, results are in relatively good agreement. The FD model presents larger excitations at the pitch eigenfrequency with respect to the time-domain simulations. Results are compared also in terms of time history (Figure 47b). For this comparison, amplitudes from 0 to 0.45 Hz have been considered. The

same phase angles, uniformly distributed between 0 and 2π, are applied to the harmonics presented in Figure 47a. Overall, results of the FD model present a good agreement in terms of time-history.

(a)

(b)
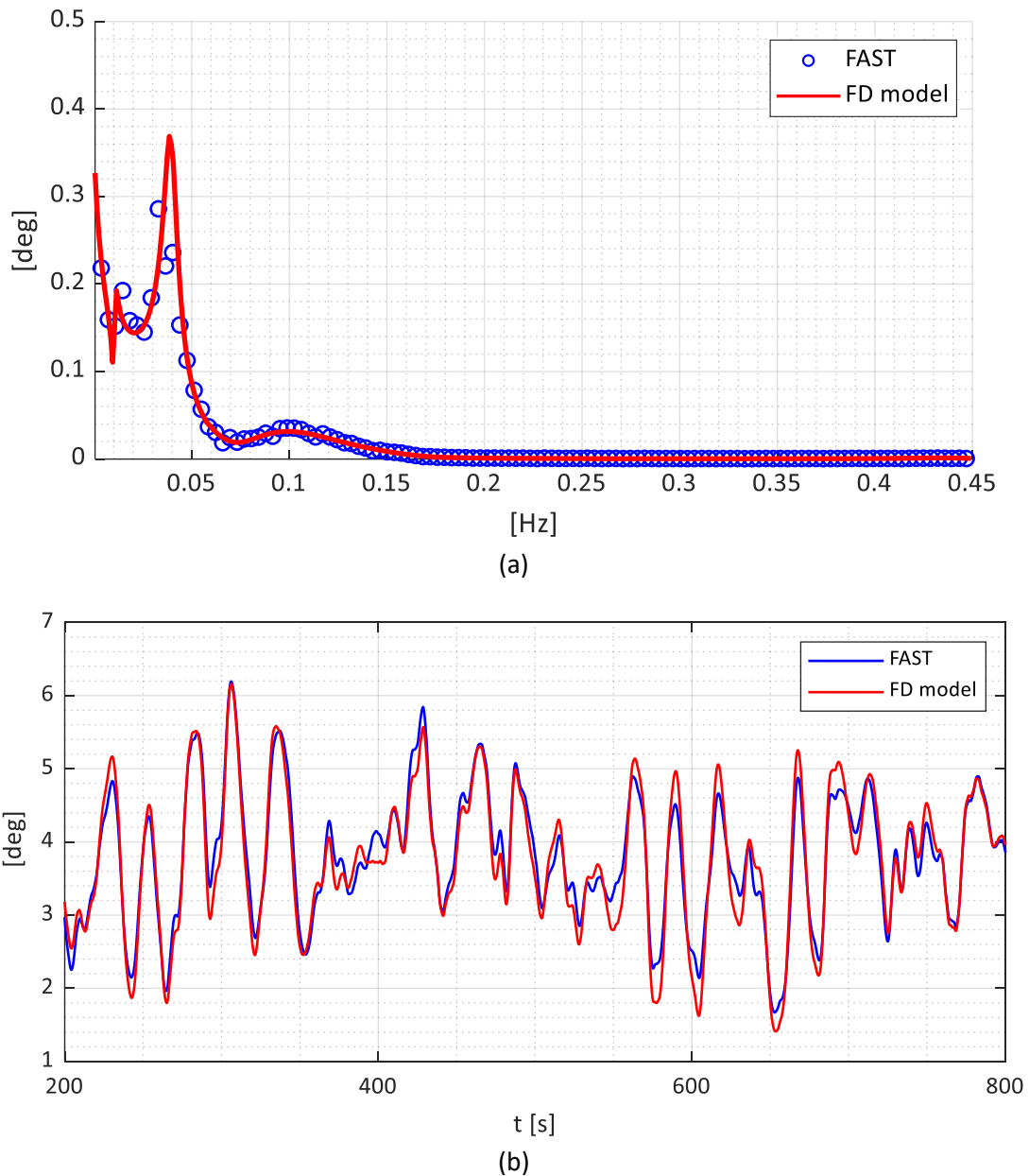
Figure 47. Response in turbulent wind and irregular waves: comparison of the amplitude of motions in Pitch (a) and time histories (b), reconstructed assuming the same phase angles for both the processes presented.

Tower top deflection results are presented in Figure 48. Amplitude of motions are presented in Figure 48a, red curve refers to the FD model while blue dots present the time-domain simulation results. As it is possible to observe, results are in relatively good agreement. The FD model slightly underpredicts the response from 0.1 Hz to 0.2 Hz. The excitation at the tower Fore-Aft eigenfrequency is clearly noticeable around 0.44 Hz. Results are compared also in terms of time history (Figure 48b). For this comparison, amplitudes from 0 to 0.45 Hz have been considered. The same phase angles, uniformly distributed between

0 and 2π, are applied to the harmonics presented in Figure 48a. A mean deflection of the tower of 0.44 m is noticeable. Moreover, it is noticeable how the tower is more affected by higher frequency excitations with respect to the platform. Overall, results of the FD model present a good agreement in terms of time-history.

(a)

(b)
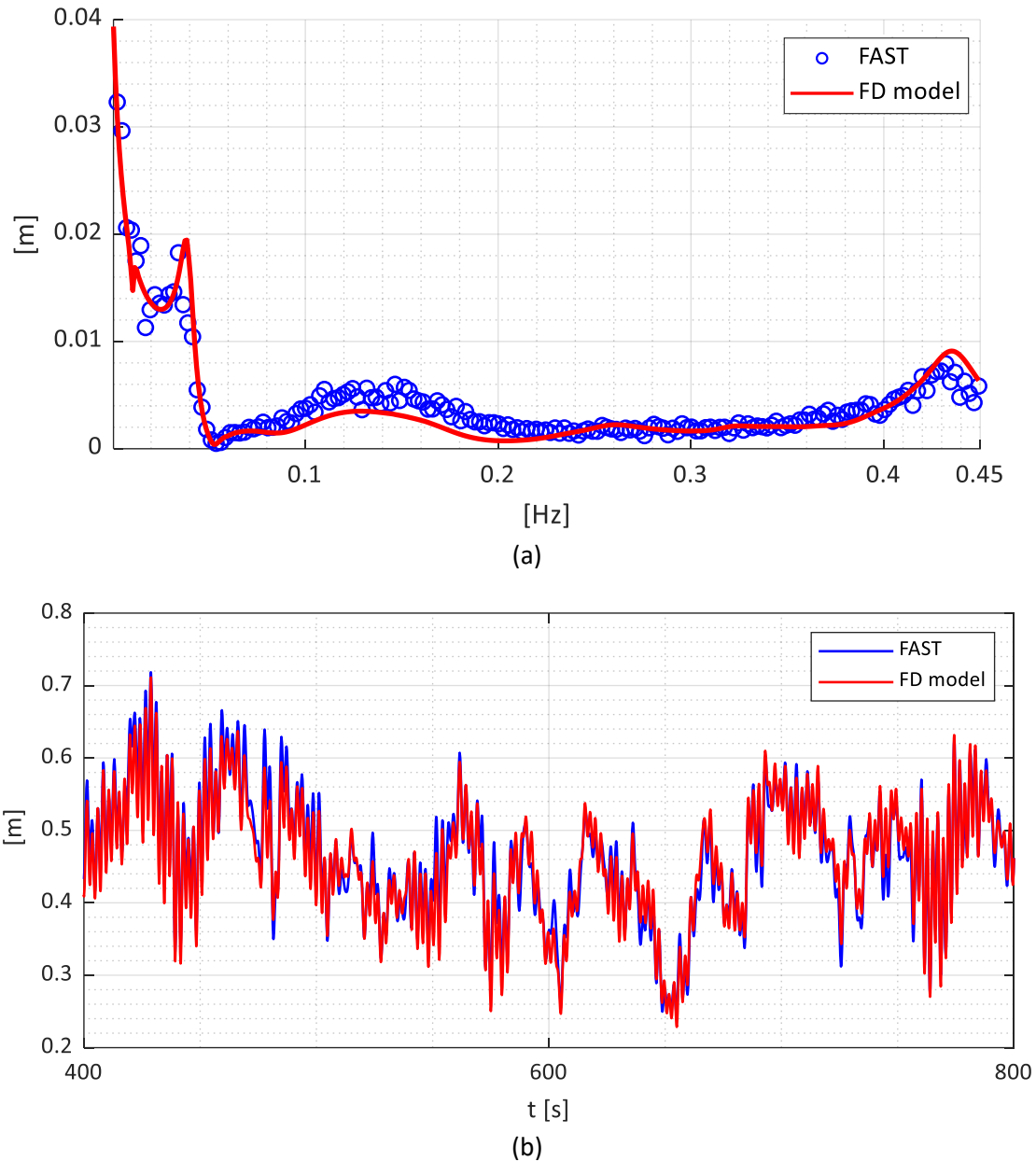
Figure 48. Response in turbulent wind and irregular waves: comparison of the amplitude of the tower top deflection (a) and time histories (b), reconstructed assuming the same phase angles for both the processes presented.

Tower base shear force are obtained from the tower top deflection. Results are presented in Figure 49. Shear force amplitude are presented in Figure 49a, red curve refers to the FD model while blue dots present the time-domain simulation results. As shown in Figure 49a, the FD model slightly underpredicts the response from 0.1 Hz to 0.2 Hz. The excitation at the tower Fore-Aft eigenfrequency is clearly

noticeable around 0.44 Hz. Results are compared also in terms of time history (Figure 49b). For this comparison, amplitudes from 0 to 0.45 Hz have been considered. The same phase angles, uniformly distributed between 0 and 2π, are applied to the harmonics presented in Figure 49b. Overall, results of the FD model present a good agreement in terms of time-history.
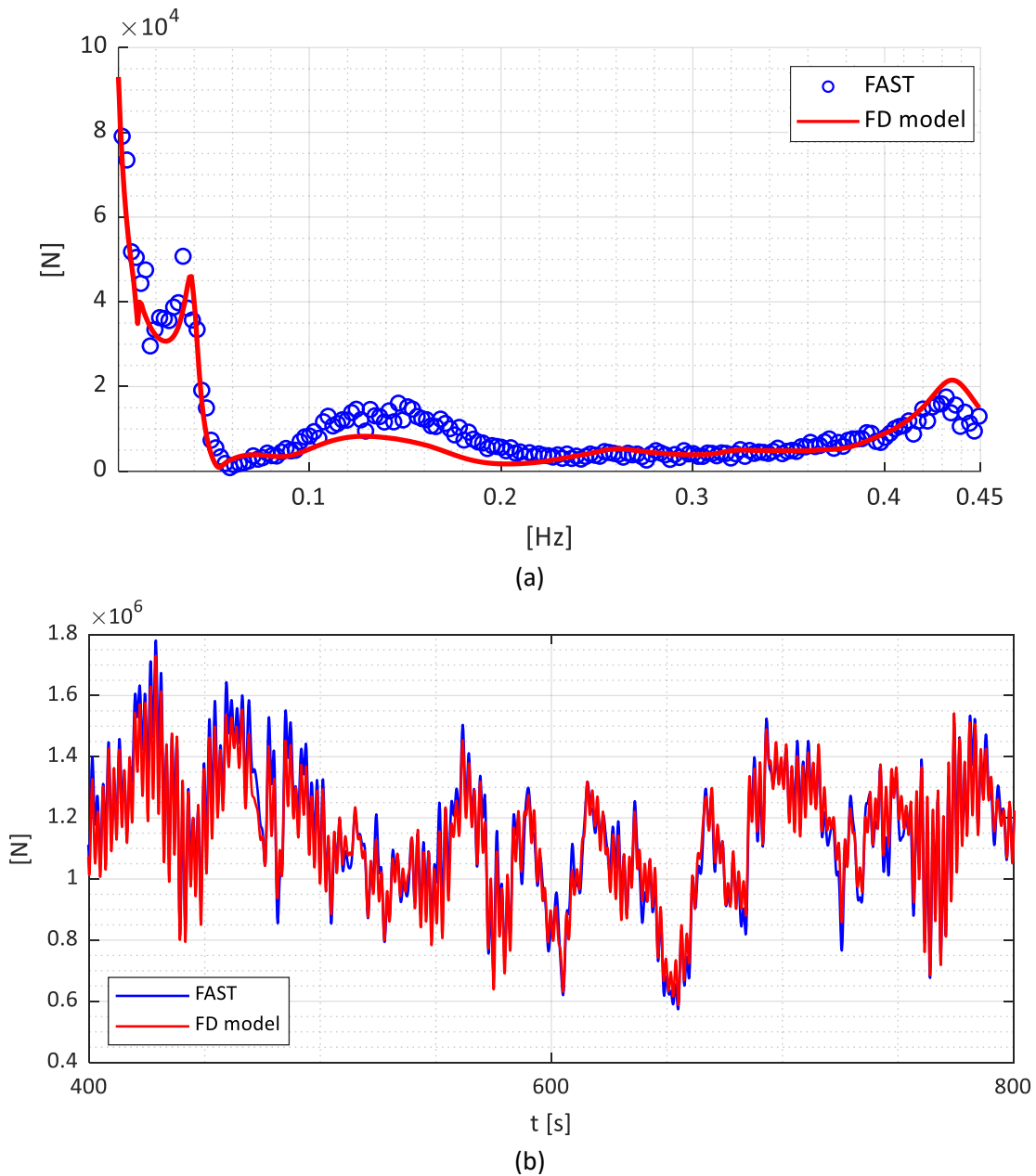
Figure 49. Response in turbulent wind and irregular waves: comparison of the amplitude of the tower base shear force (a) and time histories (b), reconstructed assuming the same phase angles for both the processes presented.

Results related to the Tower base bending moment comparisons are presented in Figure 50. Bending moment amplitude are shown in Figure 50a while the load process comparisons are shown in Figure 50b. As shown in Figure 50a, the FD model slightly underpredicts the response from 0.1 Hz to 0.2 Hz. The excitation at the tower FA eigenfrequency is clearly noticeable around 0.44 Hz. Results are compared also

in terms of time history (Figure 50b). For this comparison, amplitudes from 0 to 0.45 Hz have been considered. The same phase angles, uniformly distributed between 0 and 2π, are applied to the harmonics presented in Figure 50b. Overall, results of the FD model present a good agreement in terms of time-history.
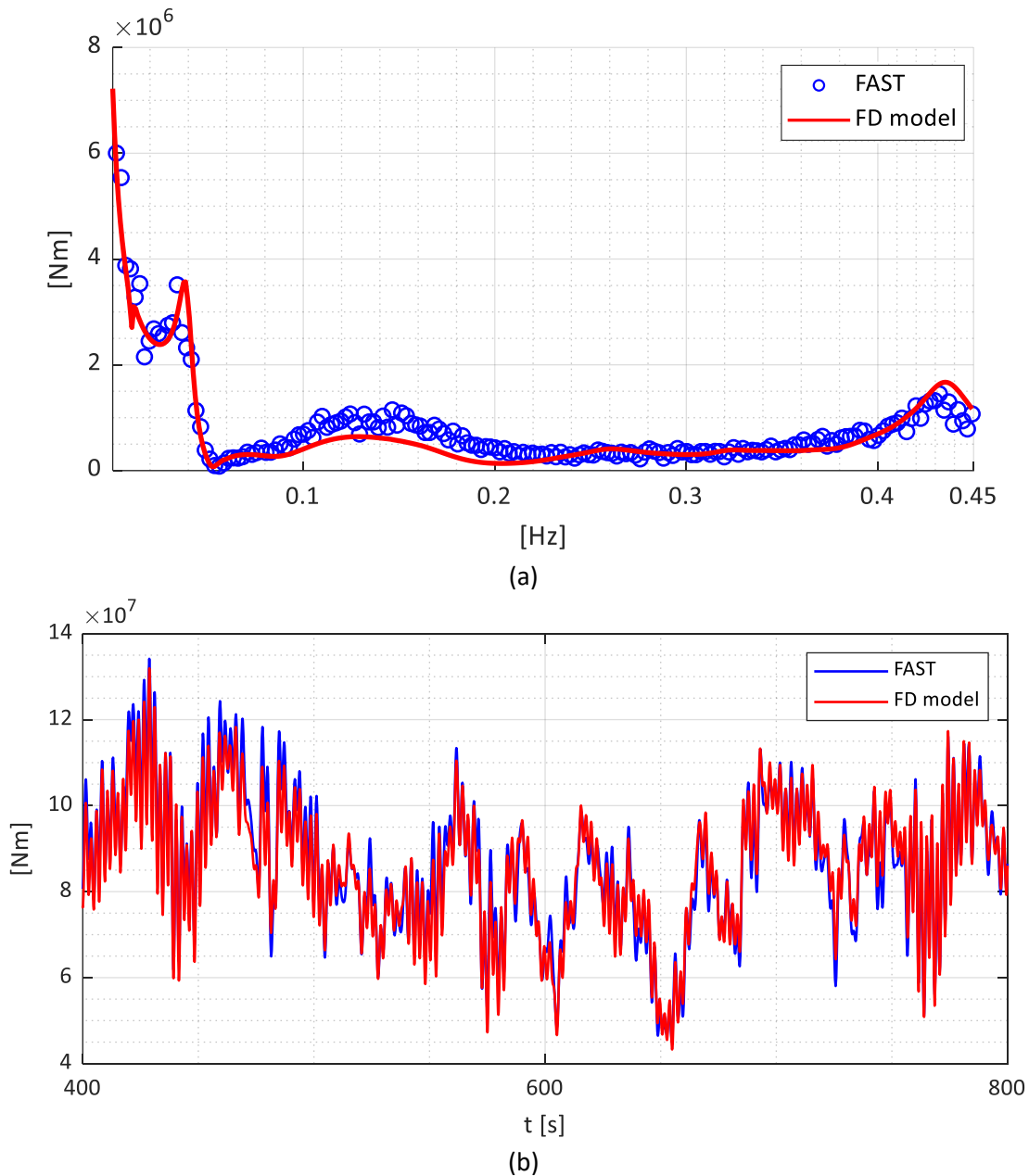
Figure 50. Response in turbulent wind and irregular waves: comparison of the amplitude of the tower base bending moment (a) and time histories (b), reconstructed assuming the same phase angles for both the processes presented.

In conclusion, mooring loads results are also compared. Fairlead tension is calculated following the procedure presented in section 5.2.2. The 2x2 stiffness matrix $\boldsymbol{K^P}$ of a catenary cable is calculated at the mean displace position of the system. Results are presented in Figure 51. Amplitudes of tension obtained in the FD are presented in Figure 51a, red curve refers to the FD model while blue dots present the time-

domain simulation results. appears to be in very good agreement with time-domain simulations (Figure 51a). As it is possible to observe from Figure 51b, the load process is characterized by lower frequency components such as Surge, Heave and Pitch motions. Overall, the results obtained show that, the procedure for the extrapolation of the mooring loads from FD results, presented in section 5.2.2, is applicable in any condition.

(a)

(b)
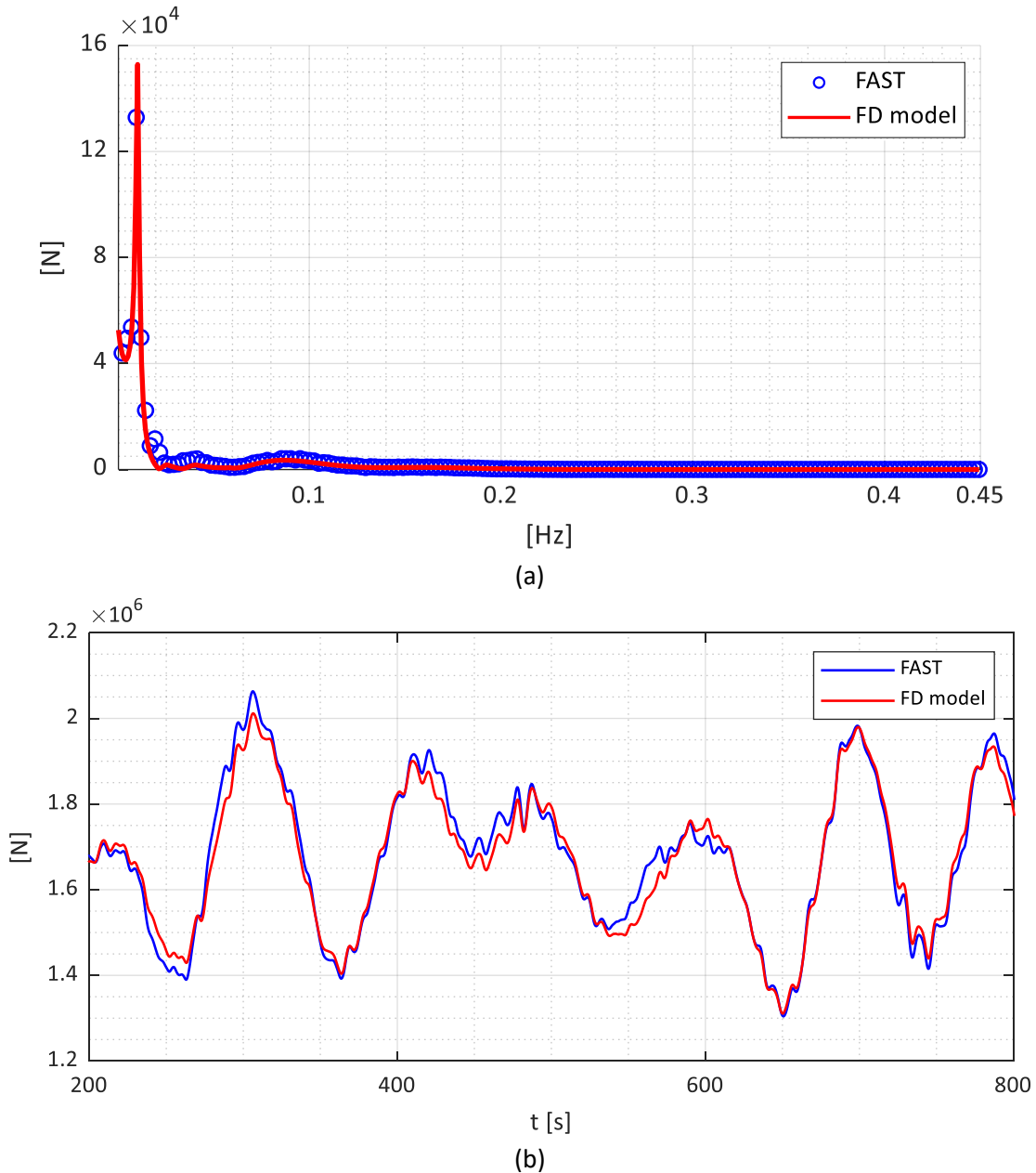
Figure 51. Response in turbulent wind and irregular waves: comparison of the amplitude of the tower base bending moment (a) and time histories (b), reconstructed assuming the same phase angles for both the processes presented.

Overall, the linear FD model is capable to effectively reproduce results obtained from a nonlinear time-domain model even considering the joint action of turbulent wind and irregular waves. Moreover, significant quantities for tower and mooring design can be obtained from the 7 DoFs response of the

system following the procedures presented in section 5.2.2. Especially regarding the mooring lines tension, this is an innovative aspect of the developed FD model, which may allow to perform pre-design optimization even on the cables.

In the following chapter, the implementation in an GA based optimization procedure is presented. The attention is focused on the identification of significant constraints which can lead the procedure towards an optimal substructure in terms of construction costs and system performances.

Chapter 6.
Optimization of 10MW semisubmersible FOWTs

In this chapter, the FD model developed is adopted to perform the optimization of a semisubmersible platform suitable for the installation of a 10MW WT. The 10MW DTU reference WT (Table 7) is implemented in FAST v7 for this purpose [72].

Table 7: DTU 10 MW WT characteristics [73].

10MW DTU wind turbine for floating application	
Wind regime	IEC Class 1A
Cut-in wind speed	4 m/s
Cut-out wind speed	25 m/s
Rated wind speed	11.4 m/s
Rated power	10MW
Tower height above SWL	114.67 m
Tower base above SWL	7.66 m
Rotor diameter	178.3 m
Hub mass	1.05e5 kg
Nacelle mass	4.46e6 kg

Firstly, only platform-related geometrical variables are considered, then, mooring system related variables are added, leading to a complete optimization of the floating foundation. Both parked and power production states are investigated. Feasibility constraints related to mean displacements and mooring layout are considered, ensuring not only the correct behaviour of the WT in power production, but also the safety of dynamic electric cables and anchors [74]. The objective function is the value of the Response Amplitude Operator (RAO) at the eigenfrequency of the selected degree of freedom (DoF) of the system. The performances of the optimal systems are compared with the ones of a platform obtained by upscaling.

6.1   Upscaled semisubmersible platform

Upscaling is a design approach ([36], [34], [44]) which allows to obtain a platform suitable for a particular turbine by scaling a platform designed for a different turbine. This is carried on by scaling all the geometry by the square root of the ratio between the powers of the two turbines. Although it is a very fast and simple procedure, it may lead to overdesigned systems made of unnecessary material, resulting in an uneconomic design. In the present study, the optimized systems are compared with an upscaled one, obtained adopting the 5MW NREL OC4 DeepCwind semisubmersible platform as starting geometry. Thus, the scaling factor adopted is

$$S_f = \sqrt{\frac{10MW}{5MW}} = \sqrt{2},$$
(6.1)

The main geometry dimension of the new platform obtained by upscaling each length by S_f are reported in Table 8. The diameter of the central column was scaled with a different scaling factor to match the turbine tower base diameter.

Table 8: 10 MW upscaled semisubmersible platform.

10MW upscaled platform	
Depth of platform base below SWL (draft)	28.30 m
Elevation of main column above SWL	14.14 m
Elevation of offset columns above SWL	16.97 m
Length of upper columns	36.77 m
Length of Heave plates	8.48 m
Depth to top base columns below SWL	19.80 m
Diameter of main columns	8.30 m
Diameter of offset columns	16.97 m
Diameter of Heave plates	33.94 m
Diameter of pontoon and cross-braces	1.6 m
Platform CM location below SWL	21.27 m
Water depth	200 m
Total mass	3.846e+7 kg

The ballast is recalculated in order to maintain the upscaled draft of 28.30 m. Moreover, due to the higher loads, it is supposed to be made of concrete to increase the draft of the platform centre of mass (COM). Figure 52 shows the 5MW and the upscaled 10MW platform.

(a)   (b)
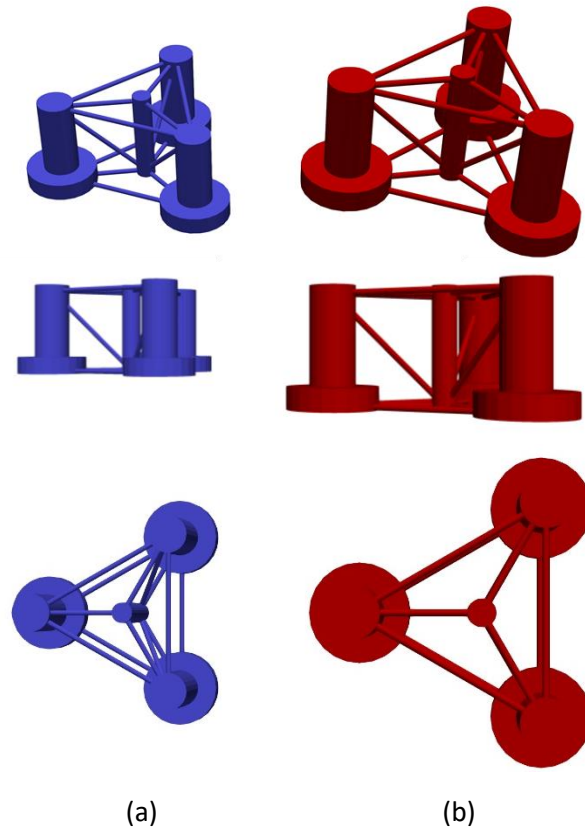
Figure 52. Platform Upscaling: 5MW NREL DeepCwind semisubmersible platform (a); 10 MW upscaled platform (b).

As far as it regards the mooring system characteristics, the fairlead is kept in the same position, namely on top of the heave plates. The cable diameter is equal to the one of the DTU platform presented in [44], specifically chosen to restrain a semisubmersible platform for a 10MW turbine. Considering the change of the fairleads position, the unstretched cable length is modified to avoid a reduction of the mooring system stiffness in the surge direction. The mooring lines linearized stiffness is highly dependent on the catenary shape of the cables. A small modification in the hanging points would lead to high variation of the overall mooring lines stiffness. Therefore, to maintain almost constant their stiffness contribution, the unstretched length of each cable is reduced in order to let the 10MW cable catenary shape at the equilibrium point match the 5MW one. This is done by controlling the Surge stiffness of the mooring system at rest, calculated according to Eq. 3.14 [69].

6.2 Platform optimization

The investigated platform is shown in Figure 53. Such concept achieves stability by waterplane area and centre of gravity draft; therefore, it is widely investigated in literature for large WTs [21],[42],[43]. Three platform-related geometrical variables are identified to most effectively modify the dynamic characteristics of the platform:

- The side-column diameter, d: being lateral column bluff elements, they are mainly subjected to hydrodynamic contributions coming from the integration of the velocity potential on the wetted surface of the platform. A larger d will result in a bigger column subjected to large wave-induced forces. On the contrary, when the diameter increases, waterplane area and the associated inertia moment with respect to the SWL raise (see Section 2.1.2), enhancing the rotation stability of the whole structure. Thus, the choice of such geometrical variable is nontrivial, since on one hand by increasing the column diameter affects positively the system stability, on the other hand raw cost of the floater will increase, together with the total hydrodynamic forces on each column.

- The platform radius, r: this variable tends to influence mostly the rotational response of the system, since a wider platform will present larger moment of inertia of the waterplane and therefore a larger hydrostatic stiffness in pitch and roll. This positive contribution sums up with the one achieved with larger d, but with reduced increase of the hydrodynamic forces. If the columns are connected by light, slender cross-braces, this variable will marginally influence the manufacturing cost of the floater.

- The platform draft, drf: as discussed in section 2.1.2, the rotational stability of a floating body can be enhanced by increasing the depth of the CoM. This can be done by increasing the draught of the platform, allowing to deep-down the ballast. Moreover, this may allow to achieve stable platforms with smaller columns, resulting in reduced wave-induced loads, since the wave velocity profile is exponential, with its maximum at the sea surface and rapidly decreasing towards the seabed.

The combination of these three platform-related geometrical variables clearly affects many aspects of the whole system, such as stability, amplification of the dynamic response and nevertheless manufacturing costs. Moreover, as already introduced in section 1.2, considering the features of these design variables, they influence the WT performances, and therefore the energy production. As far as it regards, cross braces (i.e., the members connecting the side columns), they are not considered in the current optimization since they are very slender and "transparent" to the wave loads if compared to bluff elements such as the side columns. Their length is updated according to platform radius and columns diameter, in order to maintain their layout fixed. Also, the number of columns are kept unchanged with respect to the OC4 DeepCwind 5 MW NREL platform [30]. Due to their complex behaviour and the uncertainties in the definition of the drag

coefficients which, as reported in [44], usually requires experimental tests and CFD calculations, Heave plates characteristics are not considered as design variables. Heave plates diameter and thickness are set, according to the OC4 DeepCwind 5 MW NREL platform, to two times the side column diameter and to 6 m, respectively. A symmetric 3-catenary-line mooring system is adopted to anchor the system. The nominal diameter and the mechanical properties of the cables are chosen accordingly to the ones of the upscaled system. In this 3-variable optimization, mooring lines length is updated according to the platform dimensions maintaining the system stiffness in the surge direction as constant as possible. This means that the catenary shape of the mooring at rest remains almost unaltered when d, r, and drf vary.
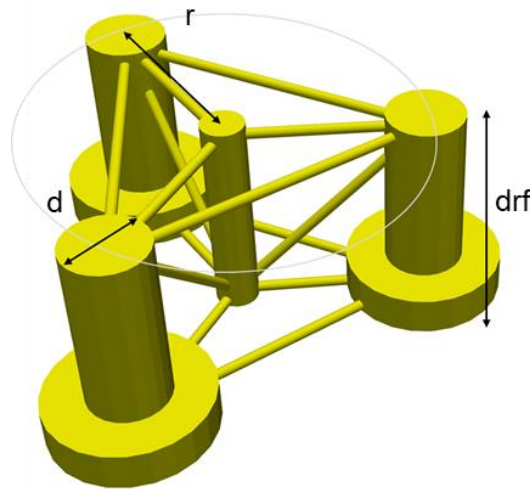
Figure 53. Platform optimization: geometrical variables.

6.2.1　　　First-order hydrodynamic coefficient for the optimization analysis

Even though FD model increases the efficiency of the optimization procedure, the calculation of the hydrodynamic coefficients by solving the potential flow problem still requires a high computational cost, which is proportional to the highest frequency at which the Radiation-Diffraction problems need to be solved. Therefore, running this calculation inside the optimization loop slows down the process. To overcome this issue, the sensitivity of Added mass, Radiation damping and Hydrodynamic forces to variations of the platform geometry is investigated (see Figure 54). Figure 54a upper plot presents Surge-Surge Added mass coefficient (A_{11}) surfaces at a constant side columns diameter equal to 14m, but different platform radius and draft. x and y axes are labelled with the frequency and the platform radius, respectively. The value of A_{11} is shown on the vertical axis. Different surfaces refer to different drafts, spanning from 20m (blue surface) to 32m (green surface). Similarly, the bottom of Figure 54a illustrates the Pitch-Pitch Added mass coefficient (A_{55}) surfaces. These two plots reveal that when the shape of the platform is fixed and only few geometrical quantities vary (such as d, r and drf), Added Mass, Radiation Damping, Diffraction and Froude Krilov forces are relative smooth functions of such platform dimensions.

Therefore, they can be evaluated off-line over a grid of values and then be interpolated on-line. This procedure is adopted herein and multidimensional fitted functions for the hydrodynamic parameters are evaluated over a grid of values of the design space variables, see Figure 54b. This procedure allows not to call the potential flow solver (ANSYS AQWA) at every run in the optimization algorithm, leading to a drastic reduction of the computational time.

(a)   (b)
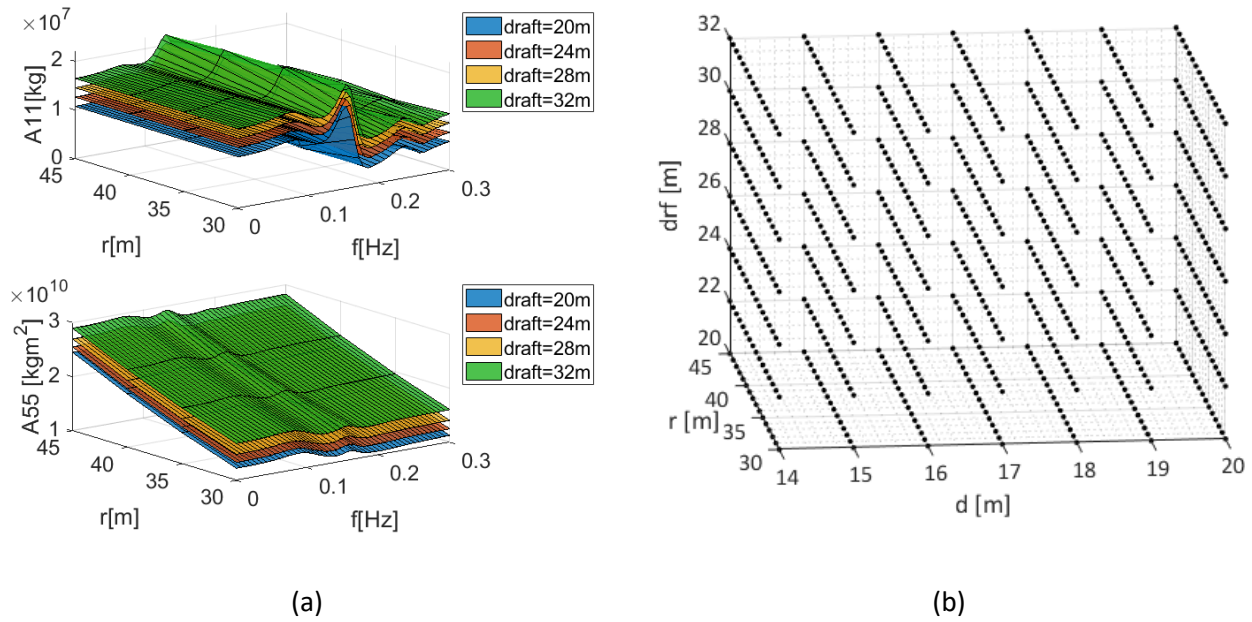
Figure 54: Added mass coefficients for a semisubmersible-like platform of 14 m side column diameter, varying platform radius (y axis), frequency (x axis) and platform draft from 20 m to 32 m (a); grid of platforms adopted for the fitting of the hydrodynamic coefficients (b).

6.2.2   Optimization procedure

The optimization procedures are performed adopting a Genetic Algorithm (GA) [75], which is widely adopted for the solution of highly nonlinear optimizations problems. The method generates at each time step a population of individuals. Following the process of natural selection [75], GA repeatedly modifies the generated population until it evolves towards an optimal solution.

6.2.2.1   Objective functions

The Surge, Heave and Pitch RAO amplitudes at the respective eigenfrequencies are chosen as objective functions to be minimized. The three RAOs considered are not only indicators of the platform dynamic response, but also of the turbine (and mooring system, as discussed later in Section 5.2) performances. Indeed, by combining Surge and Pitch RAOs, assuming a rigid displacement, the RAO of the nacelle acceleration can be estimated as

$$\text{RAO}_{\delta \ddot{n}ac}(\omega) = -\omega^2(\text{RAO}_1(\omega) + \text{RAO}_5(\omega)h_{nac}), \tag{6.2}$$

where $\text{RAO}_1(\omega), \text{RAO}_5(\omega)$ are respectively Surge and Pitch RAOs and h_{nac} is the height of the nacelle above SWL. This quantity has been widely adopted in literature (e.g., [19] and [24]) to assess the WT performances in the FD. Considering Eqs 5.3 and 6.2, it is possible to state that optimizing for Surge, Heave and Pitch means to indirectly optimize the turbine performances.

For each platform generated by GA, the RAOs are calculated by means of the FD model. Following the load case adopted for the validation, a white noise sea spectrum in the frequency band between 0.005 Hz to 0.2 Hz of 2m/Hz^2 is applied. Wind speed is set to zero and the turbine is placed in parked condition.

6.2.2.2   Constraints

A first optimization constraint regards the static displacements of the system under the maximum turbine thrust configuration. Such condition is expected when a wind speed of about 11.4 m/s is acting at hub height. Since the static displacements of a FOWT are mostly affected by aerodynamic loads, in this case the wave load is neglected. Constraints are enforced both on Pitch and Surge DOFs. A maximum allowable mean Pitch angle of 5° is adopted in order to avoid any effect on the turbine functioning even at the rated wind speed. Namely, the Pitch constraint reads as

$$q_{5,mean} \leq 5° \text{ with } V_{hub} = 11.4 \text{ m/s,} \tag{6.3}$$

It is noted that the mean Pitch value is mainly affected by the hydrostatic stiffness of the platform $C_{\text{Hydrostatic}}(5,5)$. On the contrary, Surge static displacement of the system is completely determined by mooring lines stiffness since the hydrostatic platform stiffness in Surge is zero. An uncontrolled translational displacement of the system may lead to the failure of the dynamic electric cables connecting the wind farm to land. For this reason, according to [74], a platform admissible offset (Δx_{offset}) to water depth ratio of 0.15 is employed as a constraint

$$\frac{\Delta x_{offset}}{z_{depth}} \leq 0.15. \tag{6.4}$$

Finally, also one mass constraint has been considered. It is requested that the total mass of the substructure (platform +mooring system), M_{tot}, should not be higher than the mass of an upscaled semisubmersible platform, $M_{upscaled}$):

$$M_{tot} \leq M_{upscaled} \tag{6.5}$$

6.2.2.3 Design variables space

In the first set of optimizations a total of 3 design variables is considered (Figure), namely side column diameter, d, platform radius, r, and draft, drf. For each variable, lower and upper bounds, and the considered spacing are listed in Table 9.

Table 9: Design variables space of the Platform Optimization.

Design variable [-]	Lower bound [m]	Upper bound [m]	Spacing [m]
d	14	20	0.5
r	30	45	0.5
drf	20	32	0.5

6.2.2.4 Optimization settings

The platform optimization procedure aims to find the floating system which minimizes the response in a single degree of freedom at a time, namely Surge, Heave and Pitch. A maximum number of 5 generations, each of them composed by 200 individuals, are considered. After the first generation, the next populations are chosen accordingly to the fraction of crossover children, set to be the 80%, and the number of elite children, 2. Table 10 summarizes the optimization set up.

Table 10: Platform optimization procedures set up.

	Surge optimization	Heave optimization	Pitch optimization
Population [-]	200	200	200
N° of generations [-]	5	5	5
Cross-over fraction [%]	80	80	80
Elite children [-]	2	2	2

6.2.3 Platform Optimization results

In this section, the results of the optimizations with 3 design variables are presented. Results of the 5-variable optimizations are discussed in the following section. For both cases, platforms corresponding to minimum Surge, Heave and Pitch RAOs are compared with the upscaled platform.

6.2.3.1   Surge RAO Optimization

Figure 55 presents the result of the Surge RAO optimization. Figure 55a shows the objective function, i.e., the Surge RAO peak, at each generation compared with corresponding value associated with the upscaled platform (solid black line). Figures 55b-55c illustrate the values of the Heave (55b) and Pitch RAO peaks (55c) for the optimal platform, again compared with the upscaled one. It is observed that the minimum Surge peak (Fig 55a) remains almost constant and significantly below the upscaled peak value for all the generations. A different trend can be seen for the Heave peak (Fig 55b), which after 1st generation drops down below the upscaled result, scoring its minimum equal to 2.48 m/m (Gens 2 and 3). From Gen 4, an increase can be noticed, leading to a final value of 2.76 m/m. The Pitch peak shows a similar trend to the Heave one. Figure 55d shows the evolution of the geometry, in terms of the design variables d, r, and drf. The Heave peak trend shown in Fig 55b appears to follow the draft pattern (magenta line Figure 55d) from generation 1 to 5. When the draft reduces from 30 m to 21 m, the Heave peak drops dramatically. As far as it regards Pitch peak, its variation appears to be related to platform draft and radius (red line Fig. 55d). The minimum Surge peak is achieved with a relatively slender platform with 14m column diameter, 39m platform radius and 22.5m draft. In conclusion, compared with the upscaled platform, the Surge optimized one presents a noticeable reduction of Surge, Heave, and Pitch RAO peaks.

(a)   (b)   (c)
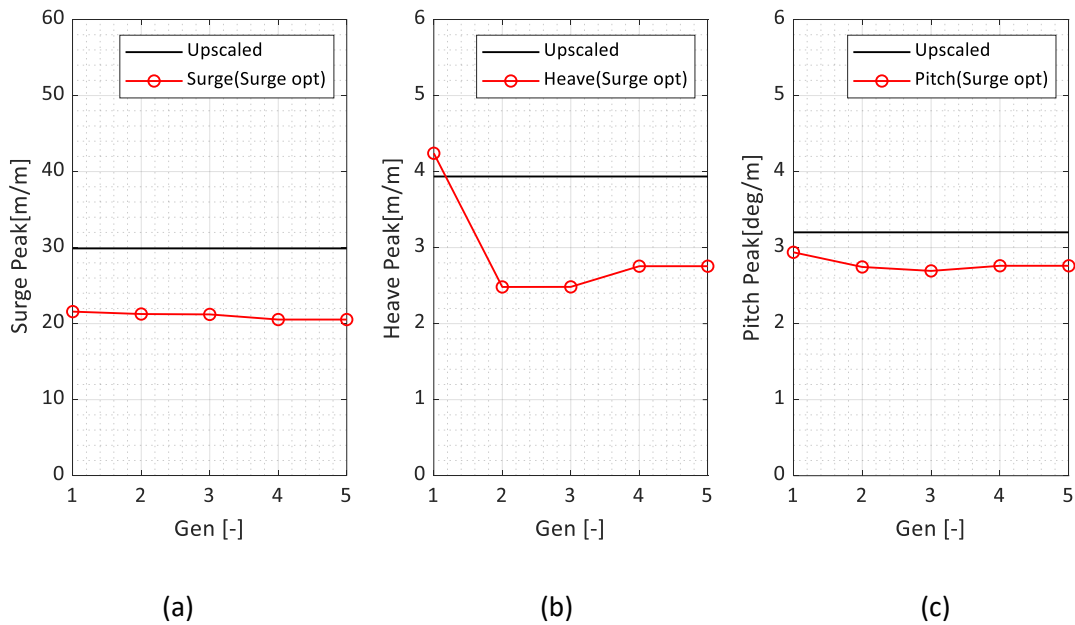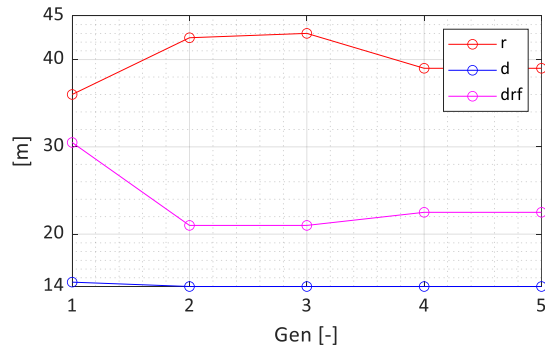
(d)

Figure 55: 3-variable Surge optimization results; evolution of the Surge (a), Heave (b), Pitch (c) peaks during the Surge peak optimization; platform geometry evolution (d).

6.2.2.5   Heave RAO Optimization

Figure 56 shows results of the Heave RAO peak optimization. It is possible to observe from Figure 56a that the optimized platform presents a smaller decrease of the Surge peaks if compared with Figure 55a. Both Heave (Fig. 56b) and Pitch (Fig. 56c) peaks are noticeably below the upscaled values and do not exhibit significant variations, attaining a minimum value of 2.30 m/m and 2.64 m/m, respectively. As can be seen in Figure 56d, the combination of a larger platform radius and side column diameter (blue line Fig. 56d), leads to the increase of the Surge peak in 1st and 2nd generations with respect to the upscaled result. On the contrary, such dimensions affect positively the Pitch peak, which reaches its minimum where the Surge is maximum. Overall, the Heave optimized solution is achieved with side column diameter of 17m, platform radius of 33m and draft equal to 20m. Heave optimization leads to smaller platform radius, minimum draft, and larger columns with respect to Surge optimization.
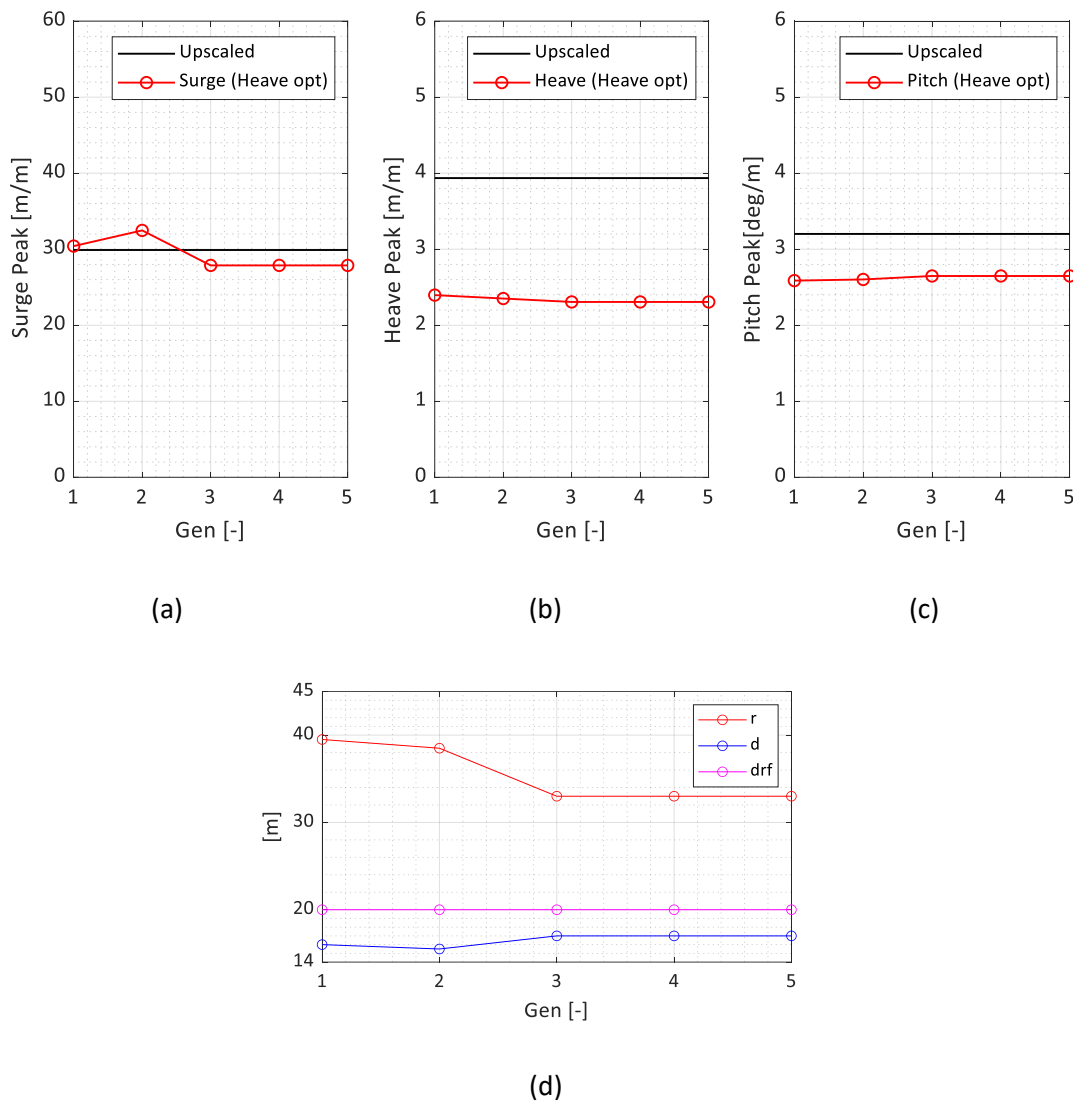
Figure 56: 3-variable Heave optimization results; evolution of the Surge (a), Heave (b), Pitch (c) peaks during the Heave peak optimization; platform geometry evolution (d).

6.2.3.2   Pitch RAO Optimization

Pitch optimization results are presented in Figure 11. Surge peak (Fig. 57a) presents a significant increase, reaching a final value of 40 m/m which is 30% larger than the upscaled result. Heave peak (Fig. 57b) shows a reduction to 2.90 m/m. As regards the Pitch peak (Fig 57c), a more regular trend can be seen. Moreover, the final value of 2.15 deg/m reduces the upscale result of 1 deg/m. This is achieved by maximizing both side column diameter (20m) and platform radius (45m) (Fig 57d). Such a heavy platform assures the best performance in Pitch, but the worst in Surge among the optimized ones. This is a clear effect of the coupling between these two DoFs. Comparing the side column diameter pattern (blue line Fig. 57d) with Surge peak one (Fig. 57a), an inverse relationship between these two quantities can be noticed. As for the

previous results, the draft remains equal to 20 m. Overall, the Pitch optimized platform shows a reduction of Pitch and Heave peaks respect to the upscaled one, but a dramatic increase of the Surge RAO peak.

(a)   (b)   (c)

(d)

Figure 57: 3-variable Pitch optimization results; evolution of the Surge (a), Heave (b), Pitch (c) peaks during the Pitch peak optimization; platform geometry evolution (d).

6.2.3.3   Comparison of the results

Results of the first set 3 optimizations are summarized in Table 11. As it is possible to observe, a reduced draft has a positive effect in all the investigated DoFs. Surge and Pitch optimal platforms show opposite value of column diameter, which can be explained by the coupled behaviour between these two DoFs. Moreover, the minimization of the Pitch motion leads to a significant increase of the Surge response (Figure 57a). The three optimized platforms are presented in Figure 58.
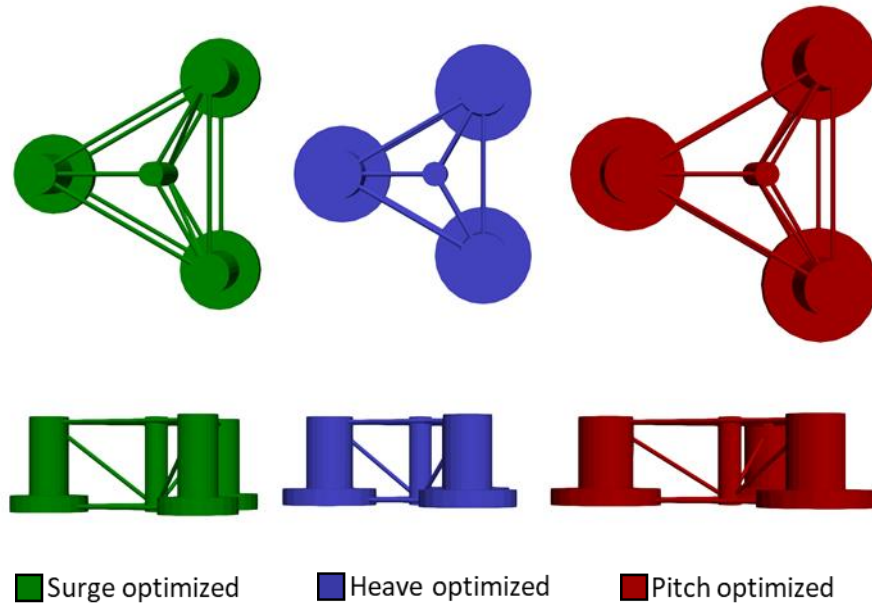
Figure 58: 3-variable optimized platforms plane view and lateral view.

Following the consideration of section 3.2.1, the mitigation of the Pitch motions is considered of primary importance however, the Surge optimized solution shows a better behaviour than the upscaled one in all the 3 investigate DoFs. This case is deemed to be the best geometrical arrangement when 3 design variables are considered.

Table 11: 3 variables Optimization results.

	Surge optimization	Heave optimization	Pitch optimization	Upscaled platform
d [m] (14 − 20)	14	16.5	20	17
r [m] (30 − 45)	39	33	45	40
drf [m] (20 − 32)	22.5	20	20	28
Surge peak [m/m]	20.53	27.87	40.71	29.90
Heave peak [m/m]	2.76	2.30	2.90	3.94
Pitch peak [deg/m]	2.76	2.64	2.15	3.20

6.3   Platform and moorings optimization

After the platform optimization, 2 geometrical variables related to the mooring lines are added, with the intent of improving the results obtained by the first set. In particular, the anchor distance from platform centreline, x_{anch}, and the unstretched mooring line length, L are added to the set of variables (See Figure

59 and Table 12). These two variables have been recently adopted by Zhou et al. in the framework of a global sensitivity study on FOWT [37]. From a structural point of view, x_{anch} and L jointly influence the stiffness of the mooring system, and consequently determine the mean displacement of platform. Moreover, being the Surge stiffness completely provided by the moorings, cables contributes also to the Surge dynamic response and, by cross-coupling effects, to the dynamic Pitch and FA deflection at low frequencies. As discussed in section 1.2, these aspects play a primary role also on the WT performances in power production and therefore in the energy output.

Table 12: Design variables space.

Design variable [-]	Lower bound [m]	Upper bound [m]	Spacing [m]
d	14	20	0.5
r	30	45	0.5
drf	20	32	0.5
x_{anch}	570	950	10
L	x_{anch} -20	x_{anch} +20	10
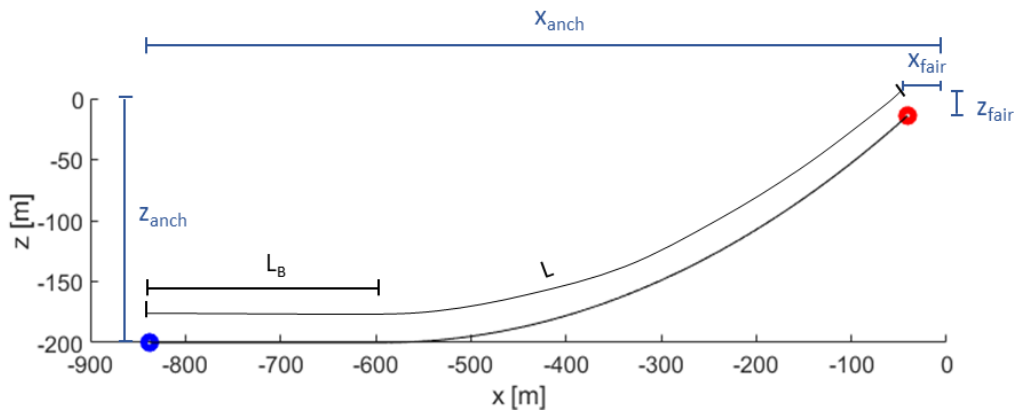
Figure 59: Catenary cable quantities related to mooring system constraints.

The introduction of these new design variables requires the introduction of two constraints related to the mooring system.). The first one, ensure that the triangle side length criterion is satisfied:

$$L > \sqrt{(x_{anch} - x_F)^2 + (z_{depth} - z_F)^2}, \tag{6.6}$$

Where L is the cable unstretched length, x_{anch}, x_{fair} are respectively the horizontal distances from platform centreline to the anchor point to the seabed and to the fairlead; $z_{depth} - z_{Fair}$ is the vertical distance between the fairlead and the seabed (see Figure 8). A constraint on a minimum portion of the cable resting on the seabed, L_B, prevent the anchor to be largely stressed by uplift forces that can provoke

failures. As suggested by Zhou et al. [37], at least one tenth of the mooring line is required to rest on the seabed. Assuming a quasi-static cable model [76], L_B can be evaluated as:

$$L_B = L - \frac{|V_{Fair}|}{W} \geq \frac{L}{10},$$

(6.7)

where V_{Fair} is the vertical tension at the fairlead.

Due to the increasing of the design space, the GA settings are changed with respect to the platform optimization. The population size is raised to 500 individuals in order to deal with the enrichment of the design space, while the number of generations is reduced to 4. Crossover fraction is set to 50% and elite children count to 1. Table 13 summarizes the optimization set up.

Table 13: Optimization procedures set up.

	Surge optimization	Heave optimization	Pitch optimization
Population [-]	500	500	500
N° of generations [-]	4	4	4
Cross-over fraction [%]	50	50	50
Elite children [-]	1	1	1

6.3.1   Platform and mooring optimization results

The 5-variables optimizations (platform and mooring) are performed adopting the settings presented in Table 13. A larger number of individuals per generation is adopted. Also, in order to increase the flexibility of the analysis, the number of elite children and the crossover fraction have been reduced, allowing the algorithm to span the design space with less restriction than in the previous optimizations. In the following, the results are discussed and compared with the ones obtained with three design variables and the upscaled platform.

6.3.1.1   Surge RAO Optimization

Figure 60 shows the 5-variable Surge optimization. To facilitate a direct comparison, the optimal value (at the 5th generation) obtained with the 3-variable optimizations is also reported in the figures (solid blue line). A reduction of the Surge and Heave peaks (Figure 60a-60b) can be seen with respect to the 3-variable case (compare with Figure 55a and 55b). Also, the Pitch peak (Figure 60c) decreases with respect to Figure 55c. As it is possible to observe from Figure 60d, these results are achieved with a smaller radius, 35 m, and

draft, 20.5 m. Such platform is very similar to the Heave optimized one, however, thanks to the optimized mooring system, Surge peaks remain low if compared to Figure 55b. Figure 60e presents the evolution of the cable design variables. The distance between the anchor and the fairlead (L_{hyp}) (the square root term in Eq. 6.6) is plotted instead of x_{anch}, this allows to qualitatively estimates how slack/taut are the cables. As can be seen, the reduction of the Pitch peak results in an expensive cable, which lies in the upper bound of the domain (x_{anch}=970m and L=950m). This solution might be unfeasible due to the high costs; however, it is important to highlight that a possible trade-off between moorings length and system behaviour is achieved also in generations 1 and 2, with a very reduced cable system (x_{anch}=730m, L=710m).
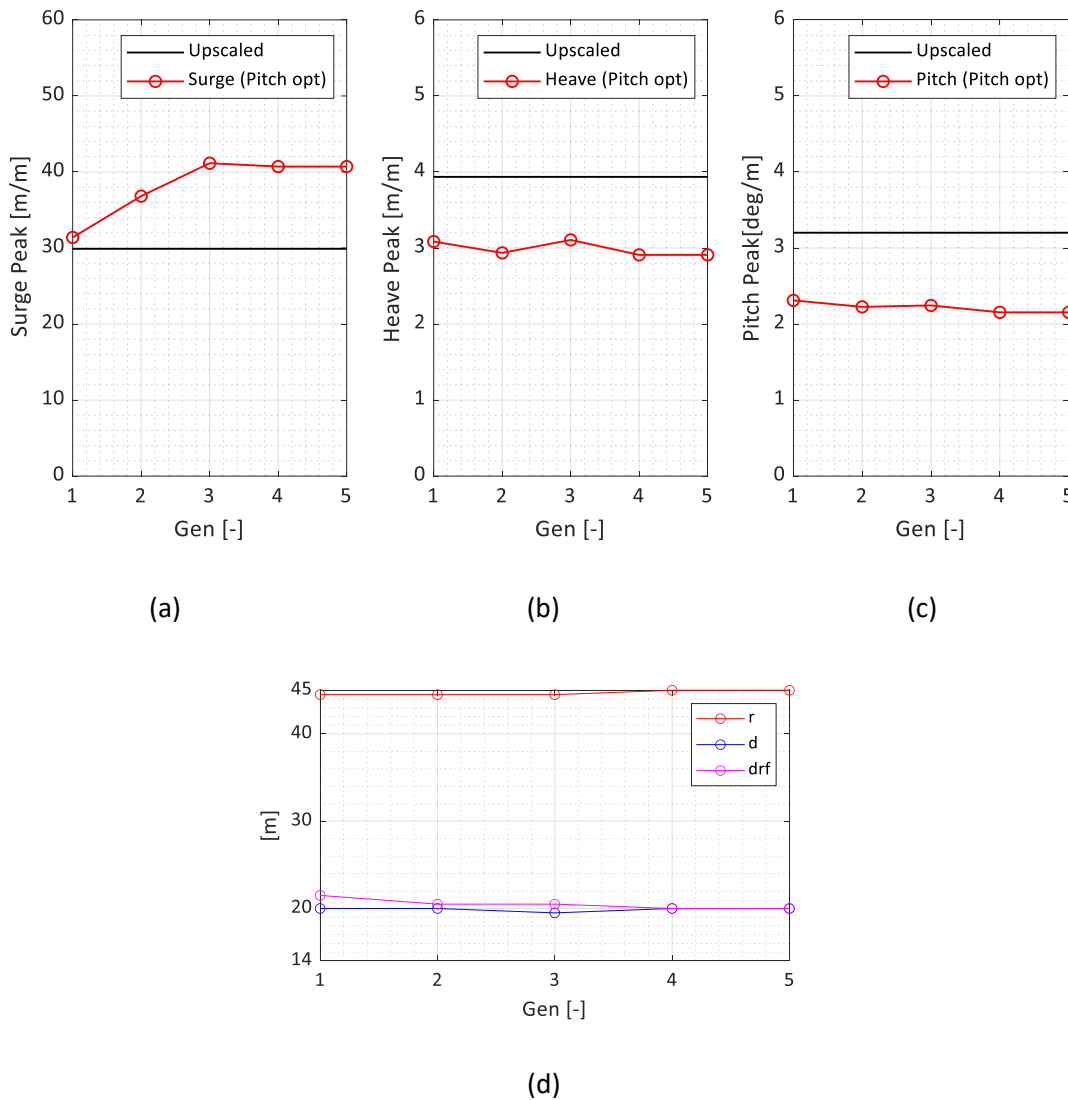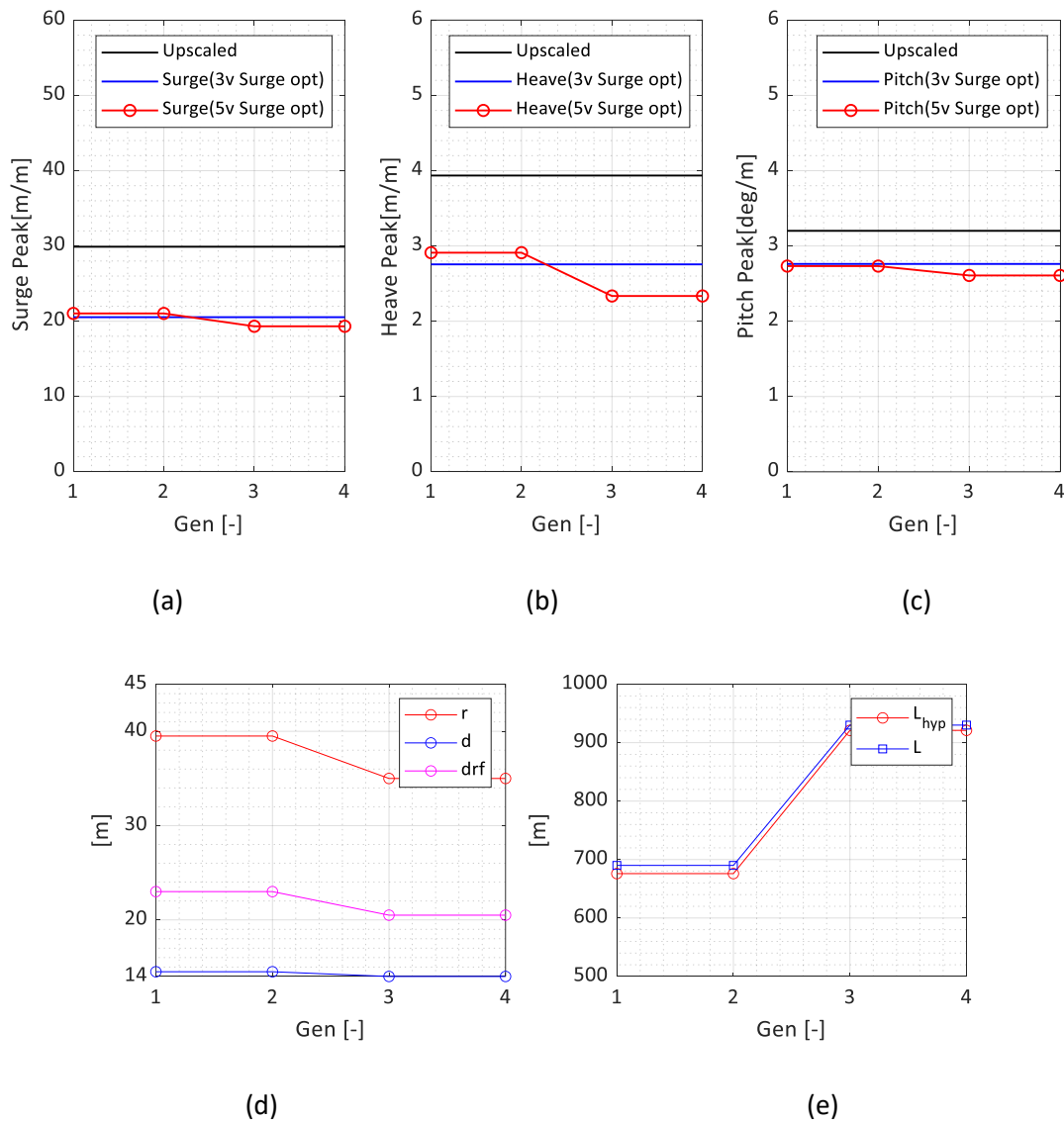

Figure 60: 5-variable Surge optimization results; evolution of the Surge (a), Heave (b), Pitch (c) peaks during the Surge peak optimization; platform (d) and mooring system (e) geometry evolution.

6.3.1.2　　Heave RAO Optimization

Also for the 5-variable Heave optimization (Figure 61), a significant gain is obtained with respect to the 3-variables case (Figure 56) is achieved in the Surge peak (Figure 61a), which drops to 20 m/m. Heave (Figure 61b) and Pitch (Figure 61c) peaks shows a slight reduction. As it is possible to observe from Figure 61d, such results are obtained with a slender platform compared to the Heave optimized in Figure 59 and Table 11. Side column diameter decreases from 17 m to 14.5 m, and platform radius from 33 m to 31 m. As it is possible to observe in Figure 61e, a larger distance between L and L_{hyp} curves can be noticed compared to Figure 60e for 1st to 3rd generation. Qualitatively, it means that this mooring arrangement is slacker and tends to increase its vertical stiffness with respect to the horizontal ones. This leads to larger Surge oscillations and to smaller Heave and Pitch oscillations. In generation 4, a tauter and stiffer mooring system is achieved, leading to the reduction of the Surge peak value.

(a)　　　　　　　　　　　　　(b)　　　　　　　　　　　　　(c)
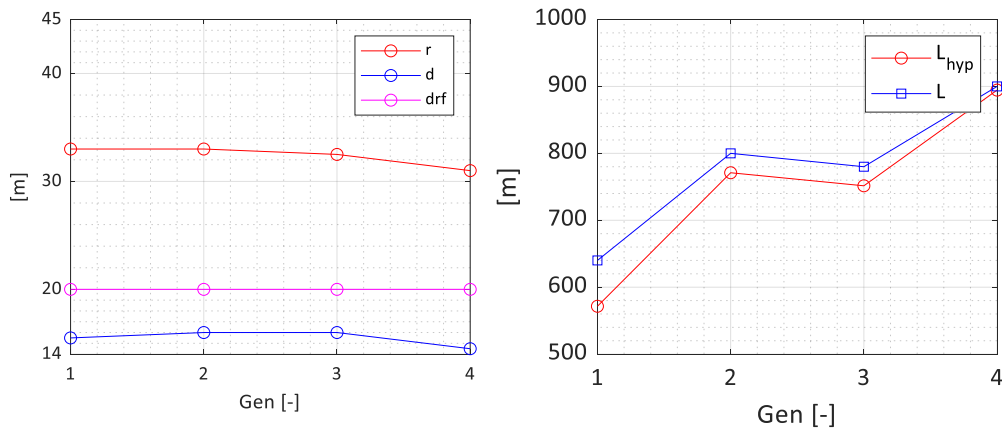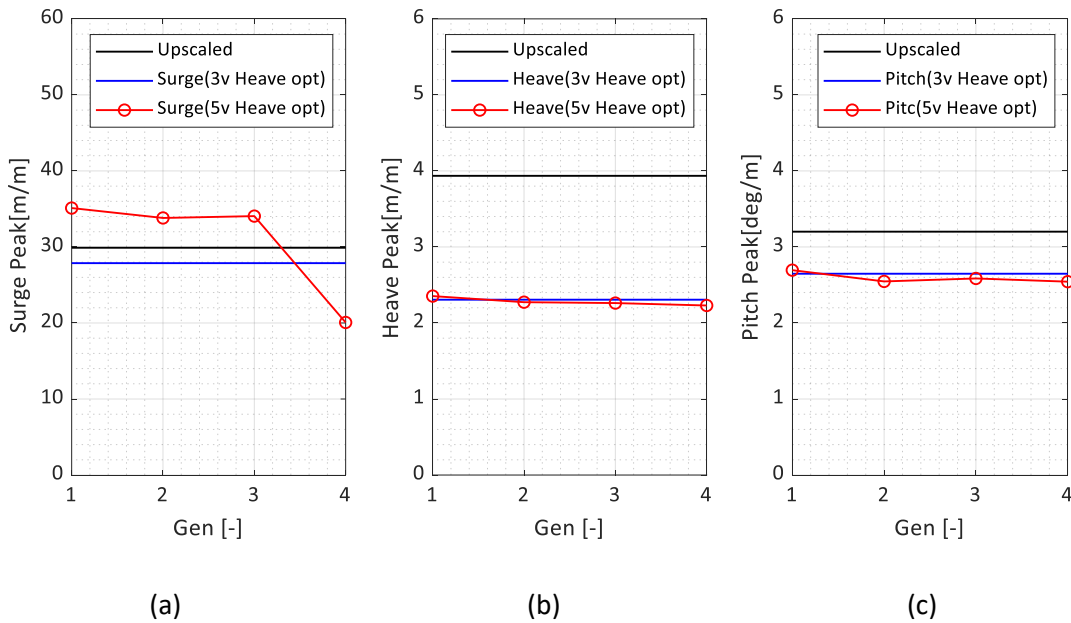
(d)   (e)

Figure 61: 5-variable Heave optimization results; evolution of the Surge (a), Heave (b), Pitch (c) peaks during the Heave peak optimization; platform (d) and mooring system (e) geometry evolution.

6.3.1.3   Pitch RAO Optimization

Results of Pitch optimization are reported in Figure 62 where, an increase of the Surge and Heave peak can be noticed (Figures 62a and 62b) and basically no reduction in Pitch (Figures 62c). Again, the platform remains almost unchanged (d=19.5m r=45m drf=20m). Such a large and heavy structure reduces any effects of mooring lines in these two degrees of freedom. As can be seen from Figure 62e, the optimized cable arrangement lies in the lower bound of the design variable domain. As expected, this leads to an increase of the Surge peak in Figure 62a for generation 4 with respect to the 3-variable Pitch optimized.
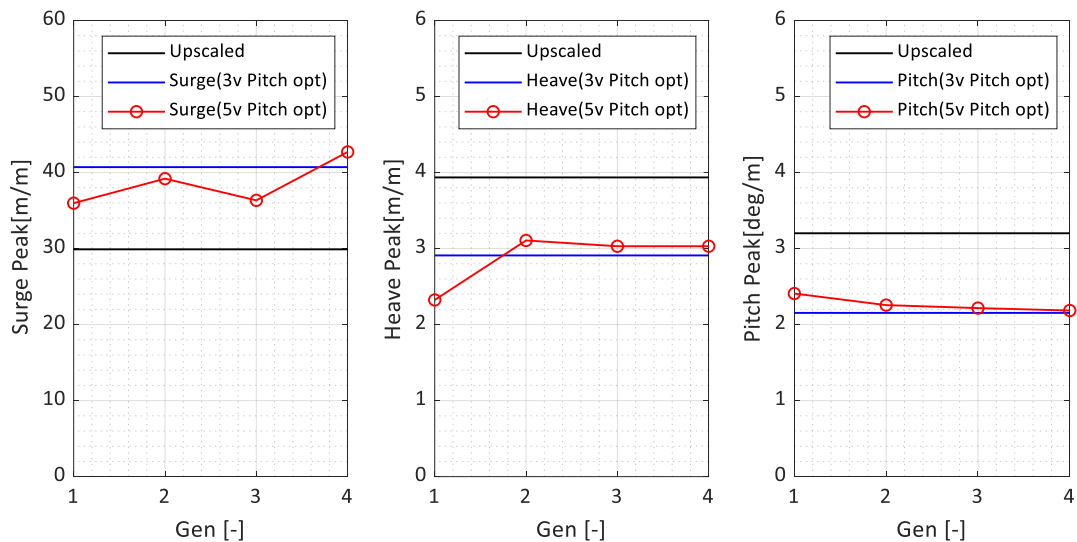
(a)   (b)   (c)
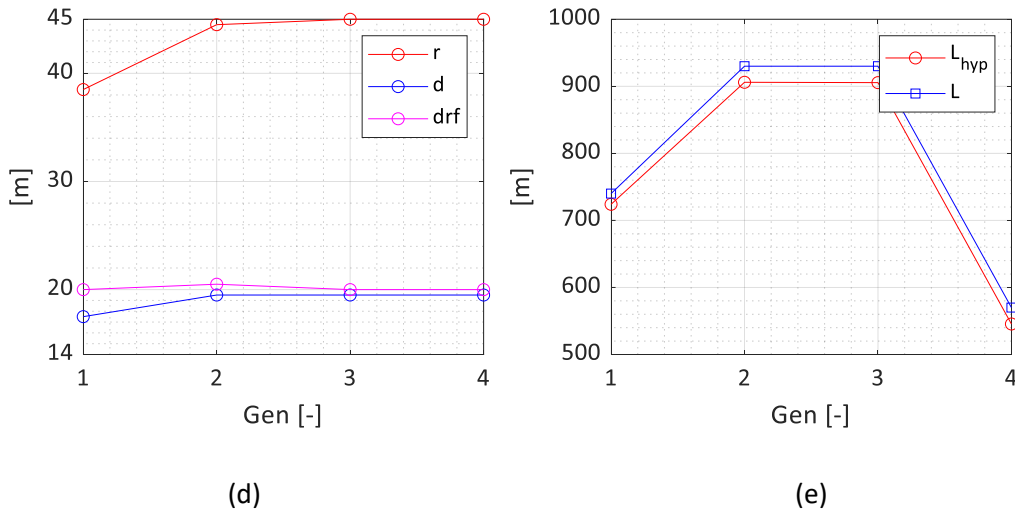
Figure 62: 5-variable Pitch optimization results; evolution of the Surge (a), Heave (b), Pitch (c) peaks during the Pitch peak optimization; platform (d) and mooring system (e) geometry evolution.

The 5-variable optimized platforms are plotted in Figure 63.
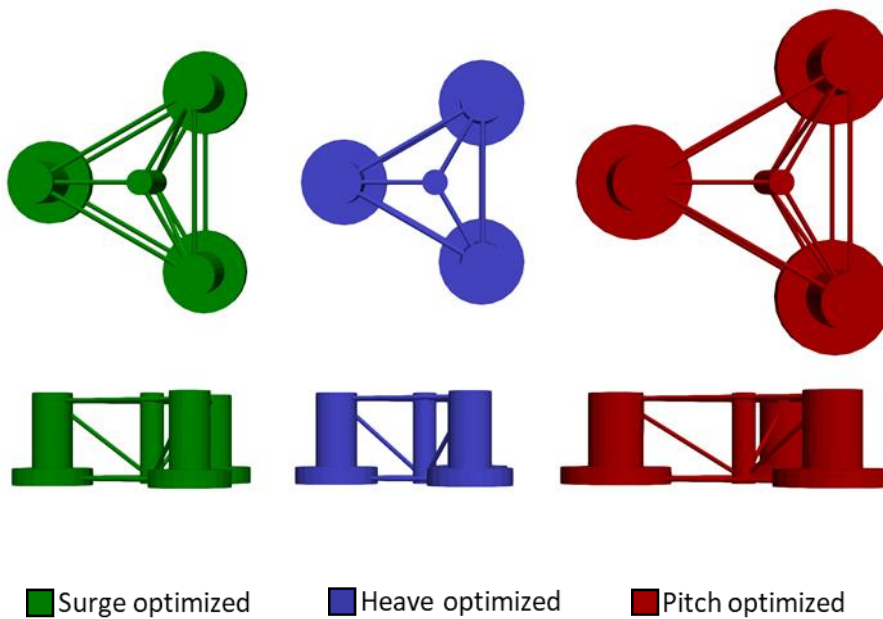
Figure 63: 5-variable Pitch optimization results; evolution of the Surge (a), Heave (b), Pitch (c) peaks during the Pitch peak optimization; platform (d) and mooring system (e) geometry evolution.

6.4 Comparison of the results

All the optimizations performed are focused on the mitigation of the system response at the floating platform eigenfrequencies, by optimizing the substructure geometry when the turbine is in a parked state. Figure 64 summarizes the results obtained for Surge, Heave, and Pitch DoFs. Blue gradient bars refer to 3-

variable optimizations, while red gradient ones to 5-variables optimizations. In Figures 64a-64c, vivid colours (blue and red) refer to the optimized DoF, whereas lighter colours indicate what happens in the considered DoF when RAO of other DoFs are being minimized. For example, in Figure 64a Surge 3v and Surge 5v indicate that the Surge RAO peak is minimized with 3 and 5 variables, respectively. Heave 3v and Heave 5v indicate what happens to the Surge RAO peak when Heave RAO peak is minimized under 3 and 5 variables, respectively. No significant improvement of the results can be noticed moving from 3 to 5 variables in the corresponding DoF of the optimization (vivid blue and red bars in Figure 64a-64c are basically equal). Focusing the attention on the Surge peak (Figure 64a), Pitch optimized platforms are found to behave worse than the upscaled platform (taller column bars). Such an increase may lead to fatigue problems in mooring lines in harsh sea states. On the contrary, both in Heave (Figure 64b) and Pitch (Figure 64c) peaks, all the 6 optimized platforms behave significantly better than the upscaled one. Due to the beneficial effect of a tauter and wider mooring system (Fig. 60e, 61e), Surge 5v and Heave 5v optimized platforms perform better that the corresponding 3-variable ones in all the three DoFs. On the contrary, the 5-variable Pitch optimized, due to a slacker mooring system (Fig. 62e), exhibits an increase in Surge and Heave peaks.

(a) (b) (c)
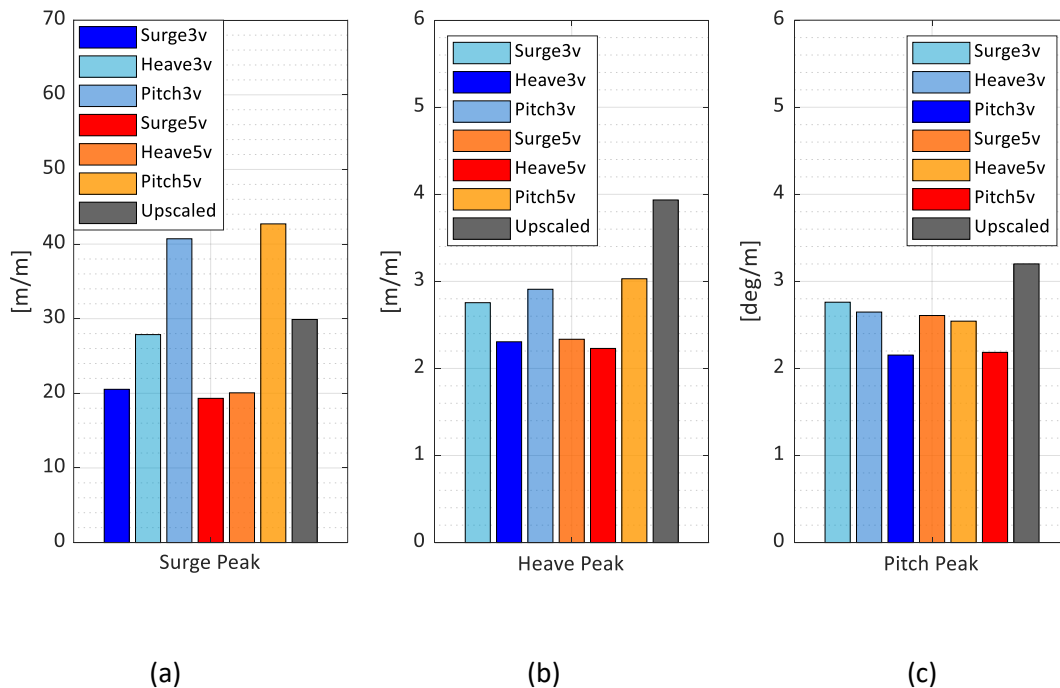
Figure 64: Optimization procedures comparison: Surge (a), Heave (b) and Pitch (c) peaks values among 3-variables (blue gradient colours), 5-variables (red gradient colours) optimizations and upscaled (grey) values.

6.4.1 Effects of the turbine in power production

As already mentioned, the results presented so far are all referred to the case with the turbine in a parked state. The dynamic response of coupled system with the turbine in power production must also be accounted. To this end, a third set of 5-variable optimizations is performed aiming at minimizing RAO peaks in power production condition. A constant wind speed of 11.4 m/s is applied at the hub height. As explained in section 3.2.2, this is the most critical condition for static displacement of the system and therefore for tower and cables stresses. In the present FD model, aerodynamic and rotating rotor effects result in an added damping, which is expected to reduce mostly the Pitch DoF RAO peak with respect to the parked condition. Values obtained from this third set are compared with those corresponding to the power production case with an upscaled system, and to the 3 and 5-variable cases (optimized in parked condition), see Figure 59 and Figure 63. Results are shown in Figure 65 where green gradients bars refer to the 5-variable power production optimization, whereas blue and red gradient bars refer to the 3 and 5-variabe optimized for the parked state but set here in power production for the sake of comparison. The added damping leads to a significant reduction of the peaks in the Surge (Fig. 65a) and Pitch (Fig.65c) DoFs among all the optimized systems. On the contrary, due to the large damping caused by the Heave plates, Heave DoF peaks (Fig. 65b) remain almost constant with respect to Fig. 64b. As it is possible to observe in Figure 18a, Surge power production optimized system (vivid green bar) achieves a better behaviour with respect to the parked optimized ones (vivid blue and red bars), the peak is reduced from 18.4 m/m to 16.2 m/m. as far as it regards Figure 65c, an interesting trend is noticeable. The Pitch optimized in parked condition appears to behave worse than all the other optimized systems. This is probably caused by the difference in platform sizes. As can be seen in Figures 59 and 63, parked Pitch optimized platforms are characterized by the largest column diameters and radii, which result in the highest stiffnesses in rotational DoFs and in the lowest mean rotations. On the opposite, their dynamic behaviour in power production worsens. Indeed, power production Pitch optimized systems (vivid green bar) presents a slender platform.
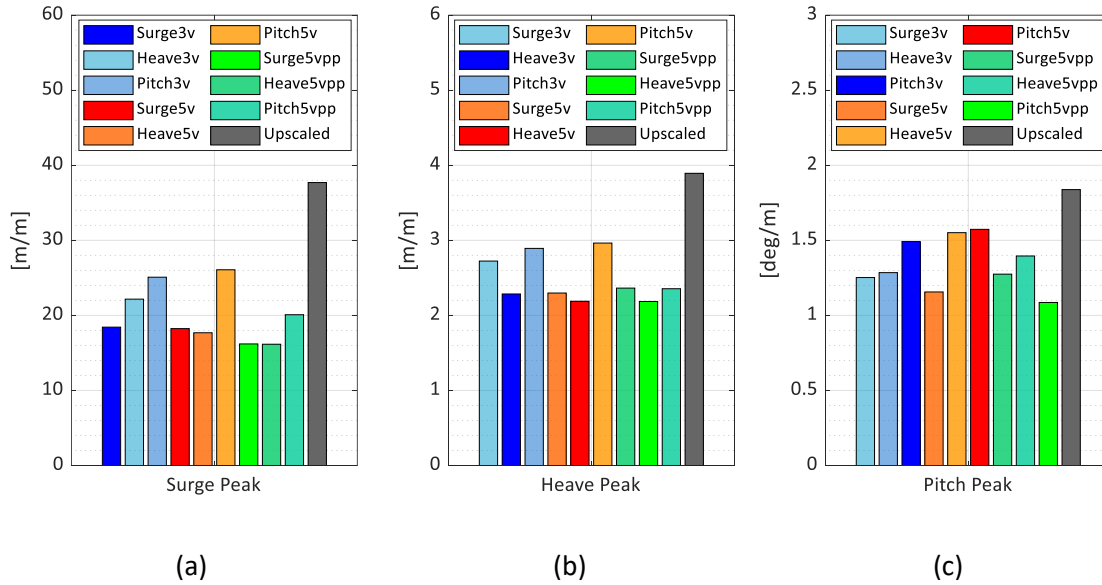
Figure 65: Power production RAO peaks comparisons: Surge (a), Heave (b) and Pitch (c) peaks values among 3-variables parked (blue gradient colours), 5-variables parked (red gradient colours) optimizations, 5-variable power production optimizations (green gradient colours) and upscaled (grey) values.

6.4.2 Mean value of the systems responses in power production

Mean values of displacements and stresses have not been considered as objective functions therefore some of the optimized configurations could be unfeasible due to excessively high steady responses. These quantities are mainly affected by mean aerodynamic loads and they are maximum at the WT rated wind speed [37]. For this reason, steady Surge, fairlead tension, Pitch, and tower base bending moment, are calculated by means of a time domain simulation in FAST with no incoming wave and steady rated wind speed (11.4 m/s) at hub height. Results are presented in Figures 66-68. 3-variable optimizations show a similar mean Surge displacement since the cable properties are updated according to the platform geometry to keep the mooring stiffness almost constant (Figure 66a). A significant decrease of the Surge drift can be seen for the 5-variable Surge and Heave optimized due to the tauter mooring system. The maximum Surge displacement is reached by the power production Pitch optimized. Overall, the minimum Surge displacement is achieved for the 5-variables Heave optimized, which is 2.4 times lower that the upscaled one. Despite its taut cables, 5-variable Pitch optimized steady Surge increases with respect to the other 5-variables optimized platform. This is caused by the smaller footprint of the mooring system (x_{anch}=610m, see Fig. 62e), which leads to a reduced stiffness in Surge DoF. As can be seen from Figure 66b, despite the smaller footprint of the mooring system, the cable fairlead tension of the 5-variable Pitch optimized remains almost constant with respect to the 3-variable optimizations, leading to a huge reduction of the dimension of the whole system (platform + moorings). Moreover, by comparing Figures 62a and 62b, it results that steady Surge and steady fairlead tension are inversely related.

(a)   (b)
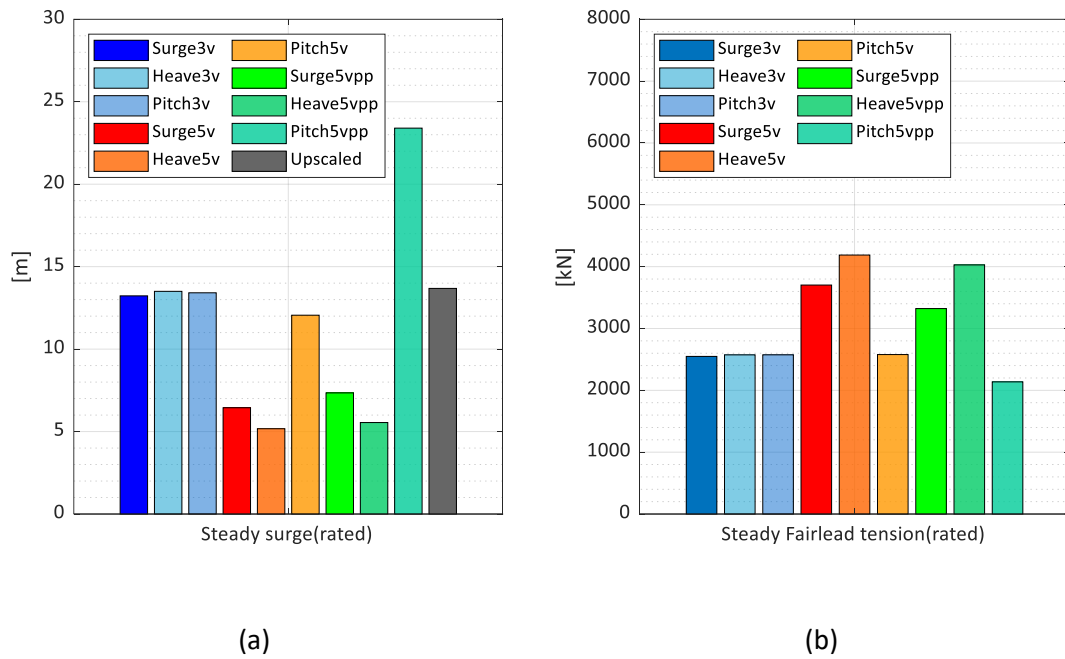
Figure 66: Steady response comparison: Surge (a) and Fairlead tension (b) under rated aerodynamic loads (11.4 m/s at hub height), 3-variables (blue gradient colours), 5-variables (red gradient colours) optimizations and upscaled (grey) values.

Figure 67 presents the steady (mean) Pitch angle and the mean tower base bending moment values at rated wind speed. In contrast with Figure 66, steady Pitch (Figure 67a) and tower base bending moment (Figure 67b) are in direct proportion. Larger Pitch angles lead to the increase of the eccentricity of the Rotor-Nacelle (RN) mass with respect to the reference frame, which results in a larger mean tower base bending moment with respect to the upscaled geometry (see Figure 67b). As expected, this is not the case when Pitch is minimized in parked condition (see bright blue and red bars in Figure 67a and 67b). Especially in Figure 67a, it is possible to observe that small and light platforms, such as Surge (d=14m, r=35m, drf=20.5m) and Heave (d=14.5m, r=31m, drf=20.5m) 5-variables parked optimized, Heave and Pitch power production optimized (d=14m, r=33.5m, drf=20.5m), exhibit larger pitch rotations.

(a)   (b)
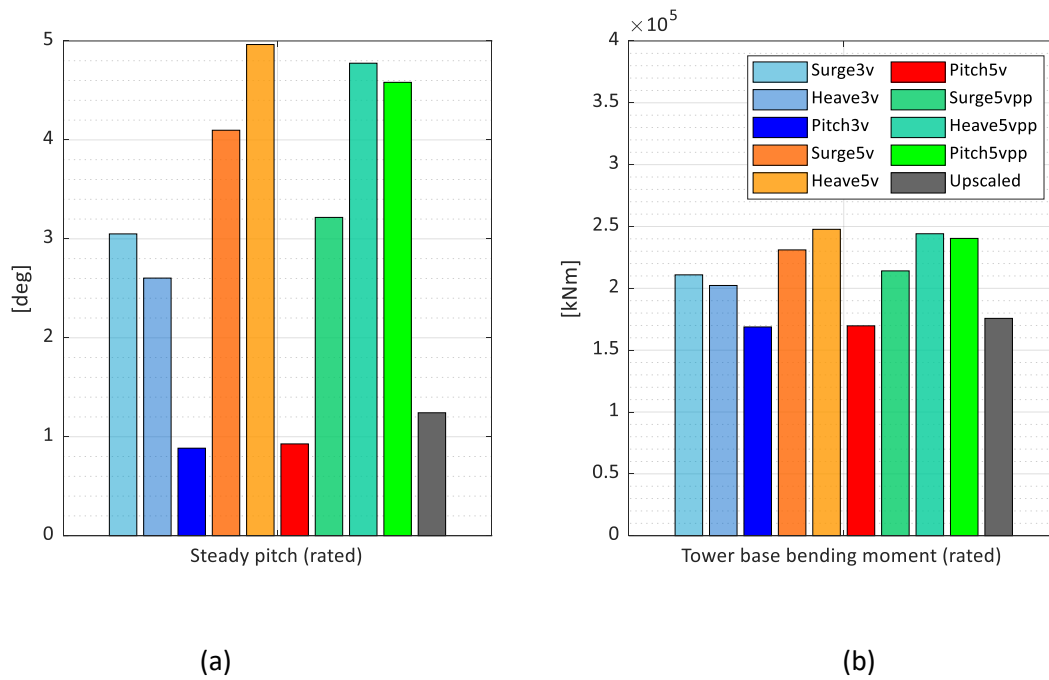
Figure 67: Steady response comparison: Pitch (a) and Tower base bending moment (b) under rated aerodynamic loads (11.4 m/s at hub height), 3-variables (blue gradient colours), 5-variables (red gradient colours) optimizations and upscaled (grey) values.

Finally, in Figure 68, a comparison in terms of platform mass is shown. Even if in the parked Pitch optimized case the columns diameter and radius are larger than the upscaled platform, the reduced draft always ensures an overall mass smaller than the upscaled case.
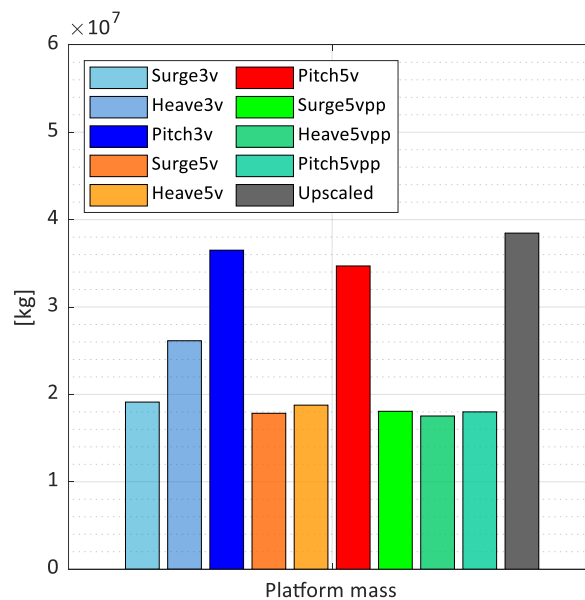
Figure 68: Platform mass comparison: 3-variables (blue gradient colours), 5-variables (red gradient colours) optimizations and upscaled (grey) values.

Considering Figures 66-67, the reduction attained by the power production Pitch optimized system (see vivid green bar in Figure 18c), which is about 0.5 deg/m with respect to the corresponding parked optimized, cannot justify the high Surge (Fig. 66a), Pitch (Fig. 67a) displacements and tower stresses (Fig. 67b). Therefore, this platform is considered unfeasible.

6.4.3   Conclusions

Chapter 6 presents the results of an optimization procedure which aims at finding the best substructure (platform + moorings) for a semisubmersible 10 MW FOWT in terms of reduction of the excitation at platform eigenfrequencies.

A first set of optimizations with 3 design variables related to platform geometry, reveal that lightness and reduced platform footprint can limit Surge and Heave amplifications at the eigenfrequencies. On the contrary, Pitch oscillations minimization requires the maximization of platform column diameter and waterplane area. A minimum draft seems to be ideal for the peaks mitigation of all the DoFs. A second set of optimizations is performed adding two design variables related to mooring lines. Results show that the improvement in the optimization of the specific DoF is negligible. However, benefits can be achieved on the other DoFs. Indeed, the optimization of the cable geometry for the minimization of the Surge peak, leads to the reduction also of the Pitch dynamic response. The study is completed with a third set of optimizations in power production condition and with the comparison of the mean values of some significant quantities, such as Pitch and tower base bending moment. Among these sets, three optimized system are identified. The Surge optimized platforms (3-variable parked, 5-variable parked and 5-variable power production) seem to be the best solution for the reduction of the 3 DoFs dynamic amplification at the natural frequencies, controlling the steady displacements and stresses on tower and cables. This is achieved with very similar platform dimensions: minimized columns diameter (14 m), draft (20.5m to 22.5m) and radii from 39.5m (3v parked and 5v power production) to 35m (5v parked). Considering the mooring lines, the minimum cable length is achieved by the Surge power production optimized (770m), while the parked ones reach a length of 828.4m for the 3-variable, and 950 m for the 5-variable. Despite the very high Surge peak, also the Pitch optimized in 5-variable seems to be a competitive solution for the steady response, gaining low Surge, Pitch displacement and tower stresses. This is achieved with a wide platform (d=20m, r=45m, drf=20m) and a reduced mooring system (L=590m, x_{anch}=610m) which may compensate the higher costs of the floater. Overall, for each optimizations set, an optimal solution can be identified, that is the Surge 3-variable parked and 5-variable power production system, and the Pitch 5-variable parked system.

However, the response under turbulent wind and irregular wave has not been considered. Also, the cost of the structure, including the manufacturing cost) has been neglected. In the following chapters, the development of efficient reliability-based procedure will be studied in order to identify floating

configurations optimized for a chosen site. To do so, Chapter 7 presents the procedure adopted for the identification of the environmental conditions at 3 different sites: one in the North Sea and two in the Mediterranean Sea. Chapter 8 illustrates the proposed optimization procedures. Objective functions related to the response of the system both under extreme and serviceability load cases will be considered. Also the full cost of the substructure will be considered (anchors, moorings, and floater).

Chapter 7.
Design load environment identification for long-term Site-specific optimizations

In this chapter, the estimation of design loads from a database of environmental conditions is detailed described. This involves the extrapolation of marginal and conditioned distributions of wind and wave characteristics of the selected site. Three databases have been chosen, one in the North Sea and two in the Mediterranean Sea. First-Order-Reliability-Method (FORM) is herein adopted for constructing a surface of extreme events which is called Environmental Contour Surface (ECS).

7.1 Determination of site-specific design conditions

The site-specific design conditions shall denote all external influences that act on the FOWT from outside. These are influences resulting from sources. Focusing the attention on Floating Offshore installation, the relevant data for loads and site conditions are meteorological data, oceanographic data, bathymetry, seabed and scouring data.

To completely represent the site condition for a FOWT, wind and wave need to be statistically described relying on long-term Metocean data. To do so, neglecting wind-wave misalignment, generally three variables are sufficient: 10 min averaged wind speed, U, significant wave height, Hs, and peak spectral period, T_p. In this work, three Metocean databases have been adopted for the identification of three possible design environments for the design of a FOWT. The first one is a North Sea database, while the other two are in the Mediterranean Sea. FINO platforms (https://www.fino-offshore.de/en) are 3 well known measuring stations in the North Sea, which have been adopted worldwide for research purposes. FINO 1 database is herein adopted due to the larger number of measurements. On one hand this allows for accurate statistical characterization of wind and wave, but on the other hand, the very shallow-water of the site, might not be realistic for the identification of the environmental conditions which a FOWT must withstand (shallow-water and breaking waves).

For this reason, two deep-water sites in the Mediterranean Sea have been added. For both of them , wind records have been obtained from the DHI Metocean Data Portal (https://www.dhigroup.com/data-portals/metocean-data-portal), while the wave records have been taken from the Copernicus Portal

(https://resources.marine.copernicus.eu/products). These two databases cover a window of around 27 years, spanning from 01/01/1993 to 31/12/2019 with hourly records. Since the measurements were not collected at the same position, wave data have been taken from 4 stations, placed at the corner of the closest square centered above the wind station, and averaged out. The first Mediterranean database is located 30 km far from the Tuscany coastline and presents 200m water depth. It has been chosen due to the identical bathymetric level with respect to the 5MW OC4 DeepCwind FOWT, without considering the wind characteristics. The second one is 35 km far from the south-west coast of Sardinia, 370 m of water depth. the main aspects which drive this choice are again the bathymetry (which is going to be challenging for the future design of any FOWT in the Mediterranean Sea), but also the proximity to the site where it is planned the installation of a 504 MW wind farm (42x12MW FOWT) [77].

Significant characteristics such as 50-year average wind speed, 50-year significant wave height and the mean value of the peak spectral period, are reported from Table 14 to 16. As it is possible to observe, FINO 1 site presents significantly higher 50-year average wind speed with respect to the Mediterranean ones since the measurements were recorded 34 m above the SWL instead of 10 m. Moreover, being a shallow-water site, FINO 1 presents also the maximum mean value of the peak spectral period. The Tuscany site scores the lowest 50-year average wind speed. The Sardinia site presents probably the highest wind speed

Figure 69: FINO 1 site location (https://www.google.it/intl/it/earth).

Table 14: FINO 1 Platform significant characteristics.

FINO 1 Platform- North Sea		
Water depth	[m]	30
Distance to shore	[km]	45
50-year mean wind speed (34 m)	[m/s]	30.6
50-year significant wave height	[m]	8.63
Mean value of peak spectral period	[s]	6.99

Figure 70: Tuscany site location (https://www.google.it/intl/it/earth).

Table 15: Tuscany site significant characteristics.

Tuscany- Mediterranean Sea		
Water depth	[m]	200
Distance to shore	[km]	30
50-year mean wind speed (10 m)	[m/s]	19.12
50-year significant wave height	[m]	9.61
Mean value of peak spectral period	[s]	4.85.

Table 16: Sardinia site significant characteristics.

Sardinia- Mediterranean Sea		
Water depth	[m]	370
Distance to shore	[km]	35
50-year mean wind speed (10 m)	[m/s]	27.20
50-year significant wave height	[m]	10.02
Mean value of peak spectral period	[s]	5.62
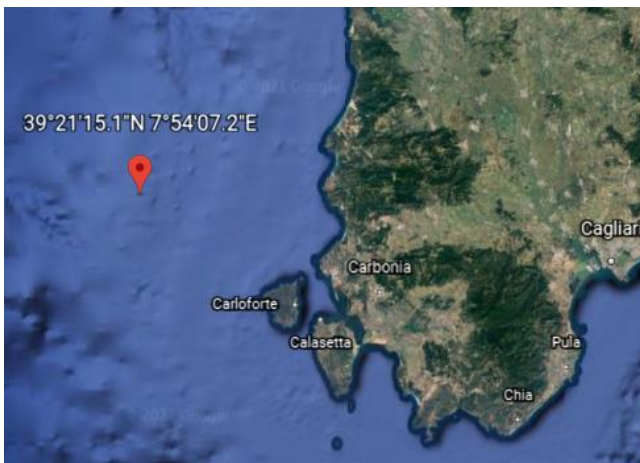
Figure 71: Sardinia site location (https://www.google.it/intl/it/earth).

7.2 Prediction of long-term Environmental Conditions

The procedure for the extrapolation of long-term environmental conditions requires the definition of the marginal and conditional distributions of mean wind speed at 10 m height, U_w, Significant wave height, Hs, and peak spectral period, T_P. For a given return period, T$_R$, an Inverse First Order Reliability Methods (IFORM) can be adopted to obtain the so-called Environmental Contour Surface (ECS), i.e., an ensemble of events (U_w, H_s, T_p) which have a return period equal to T$_R$. IFORMs have been widely adopted in literature for the extrapolation of environmental loads on Offshore structures due to their efficiency with respect to

direct methods ([78], [79], [34]). The reliability problem is inversely solved. Adopting the Rosenblatt transformation [80], the design, physical, space, $\mathbf{X}_{env} = [u_w, h_s, t_p]$, is converted into a non-physical space, $\mathbf{U} = [u_1, u_2, u_3]$, of independent standard Gaussian (zero mean and unit variance Gaussian distributed) variables, so that

$$\|\mathbf{U}\|^2 = u_1^2 + u_2^2 + u_3^2 = \beta_{REL}{}^2, \tag{7.1}$$

where β_{REL}, is a target reliability index, related to the target return period and to the duration of each sea state event. Eq. 7.1 represents a sphere in the U-space of radius β_{REL}. In the case of $T_R = 50$ years and 1-hour event

$$\beta_{REL} = \Phi^{-1}\left(1 - \frac{1}{T_R}\right) = \Phi^{-1}\left(1 - \frac{1}{50 \cdot 365.25 \cdot 24}\right) = 4.58, \tag{7.2}$$

where $\Phi(\cdot)$ is the Cumulative Density Function (CDF) of the standard Gaussian distribution. Finally, the T_R-year ECS can be obtained by mapping the 3-D sphere back to the physical random variables space $\left(U_w, H_s, T_p\right)$ invoking the following transformation:

$$\Phi(u_1) = F_{U_w}(u_w), \tag{7.3a}$$

$$\Phi(u_2) = F_{H_s|U_w}(h_s|u_w), \tag{7.3b}$$

$$\Phi(u_3) = F_{T_P|H_s,U_w}(t_p|h_s, u_w), \tag{7.3c}$$

where $F_{U_w}(u_w)$, is the CDF of the wind speed marginal distribution; $F_{H_s|U_w}(h_s|u_w)$, is the CDF of the conditional distribution of H_s for given U_w; $F_{T_P|H_s,U_w}(t_p|h_s, u_w)$, is the conditional distribution of T_P for given H_s and U_w. As it is possible to observe from Eqs. 7.3, the sea state $\left(H_s, T_p\right)$ is dependent from the wind speed, being the sea waves of interest wind induced. The joint probability distribution of $\left(U_w, H_s, T_p\right)$ can be estimated based on the three distributions presented in Eqs. 7.3 as:

$$f_{U_w,H_s,T_p}(u_w, h_s, t_p) = f_{U_w}(u_w) \cdot f_{H_s|U_w}(h_s|u_w) \cdot f_{T_P|H_s,U_w}(t_p|h_s, u_w) \tag{7.4}$$

where $f_X(x)$ denotes the probabiliy density function of the variable x.

As discussed by Li et Al. in [81], the process for the evaluation of $f_{T_P|H_s,U_w}(t_p|h_s, u_w)$, is very complicated and it may not lead to establish reasonable relationship between the distributions parameters and U_w. Therefore, they proposed the following simplification of the joint PDF

$$f_{U_w,H_s,T_p}(u_w, h_s, t_p) \approx f_{U_w}(u_w) \cdot f_{H_s|U_w}(h_s|u_w) \cdot f_{T_P|H_s}(t_p|h_s) \tag{7.5}$$

where $f_{T_P|H_s}(t_p|h_s)$ is the conditional PDF of T_P for given H_s. The same approximation is proposed for Eq. 7.3c.

7.3 Marginal and conditional distribution estimation at the three sites

In this section, the process of extrapolation of marginal and conditional distributions of U_w, H_s and T_p by fitting the real data is presented for all the three sites. Consequently, the obtained ECSs are provided.

7.3.1 Marginal distribution of the mean wind speed

Raw data at the three selected sites show that the mean wind speed follows a Weibull distribution. Two alternative distributions are proposed: a 2-parameter Weibull (black solid line), whose significant properties are reported in Eqs. 7.6, and an exponentiated Weibull (red solid line).

$$f_{U_w}(u_w) = \frac{\alpha_U}{\beta_U}\left(\frac{u_w}{\beta_U}\right)^{\alpha_U-1}\exp\left[-\left(\frac{u_w}{\beta_U}\right)^{\alpha_U}\right] \tag{7.6a}$$

$$F_{U_w}(u_w) = 1 - \exp\left[-\left(\frac{u_w}{\beta_U}\right)^{\alpha_U}\right] \tag{7.6b}$$

$$\mu_{U_w} = \beta_U\Gamma\left(1+\frac{1}{\alpha_U}\right); \quad \sigma^2_{U_w} = \beta_U{}^2\left[\Gamma\left(1+\frac{2}{\alpha_U}\right)-\Gamma^2\left(1+\frac{1}{\alpha_U}\right)\right] \tag{7.6c}$$

here Eq. 7.6a and 7.6b, express the 2-parameter Weibull PDF and CDF, respectively, while mean value and variance are presented in Eq. 7.6c; α_U and β_U are the shape and scale parameters, while $\Gamma(\cdot)$ is the gamma function. PDF and CDF of the Exponentiated Weibull distribution are presented in Eq. 7.7a and Eq. 7.7b, respectively

$$f_{U_w}(u_w) = \gamma_U\frac{\alpha_U}{\beta_U}\left(\frac{u_w}{\beta_U}\right)^{\alpha_U-1}\left\{1-exp\left[-\left(\frac{u_w}{\beta_U}\right)^{\alpha_U}\right]\right\}^{\gamma_U-1}exp\left[-\left(\frac{u_w}{\beta_U}\right)^{\alpha_U}\right] \tag{7.7a}$$

$$F_{U_w}(u_w) = \left\{1-\exp\left[-\left(\frac{u_w}{\beta_U}\right)^{\alpha_U}\right]\right\}^{\gamma_U} \tag{7.7b}$$

where α_U and β_U are the shape and scale parameters, while γ_U is the second shape parameter (for the 2 parameter Weibull $\gamma_U = 1$). Mean values and variance can be found in [82].

In the following, Figure 72 presents the marginal distribution fittings. Figure 72a and 72b presents the fitting of the 34m-height wind speed marginal distributions to the raw data of FINO 1 platform. Both CDF (Figure 72a) and PDF (Figure 72b) are shown, comparing the two proposed distributions. As it is possible to observe from the PDF fitting, the Exponentiated Weibull distribution seems to better represent the mean

value of the raw data distribution, equal to 8.36 m/s. Both lower and upper tails are accurately fitted by the two distributions.

Figure 72c and 72d shows the fitting to the Tuscany site in the Mediterranean Sea. Again, the Exponentiated Weibull distribution better represents the mean value PDF of the raw data with respect to the two-parameter one. Moreover, as it is possible to observe comparing Figure 72d and Figure 72b, wind raw data of Tuscany site appear to be narrowed around the mean value (around 4.2 m/s), while FINO1 ones are spread on a wider range of wind speed. Finally, Sardinia wind speed CDF and PDF fittings are presented in Figure 72e and 72f, respectively. By comparing Figures 72d and 72f, it is possible to observe that the wind speed distribution at the Sardinia site is shifted towards higher values and spread on a broader band of wind speed with respect to the Tuscany site.

(a)

(b)

(c)

(d)

(e)   (f)
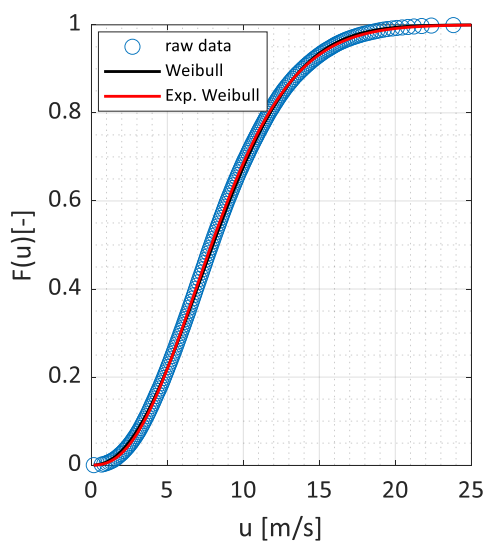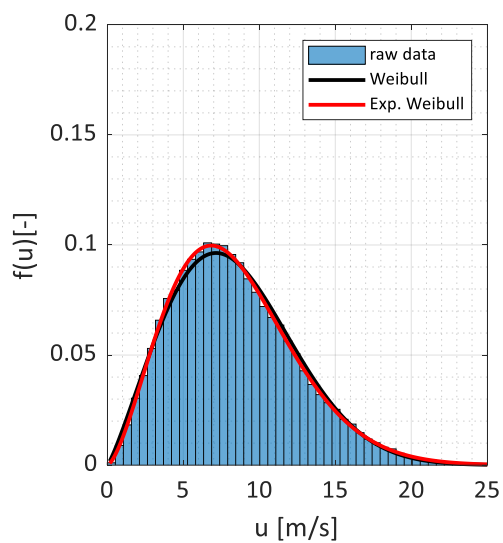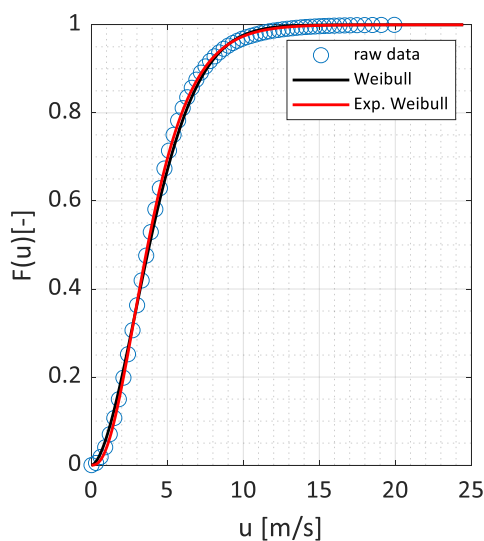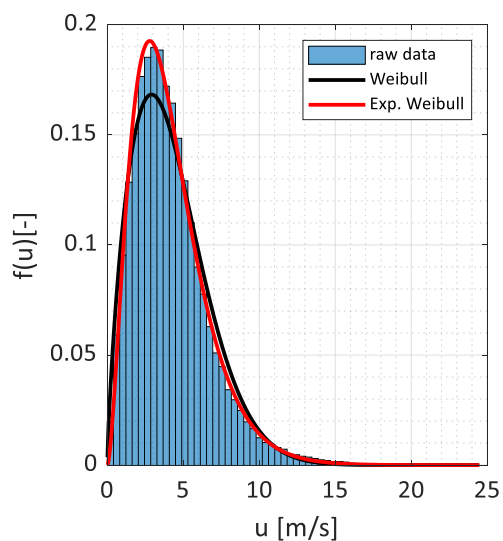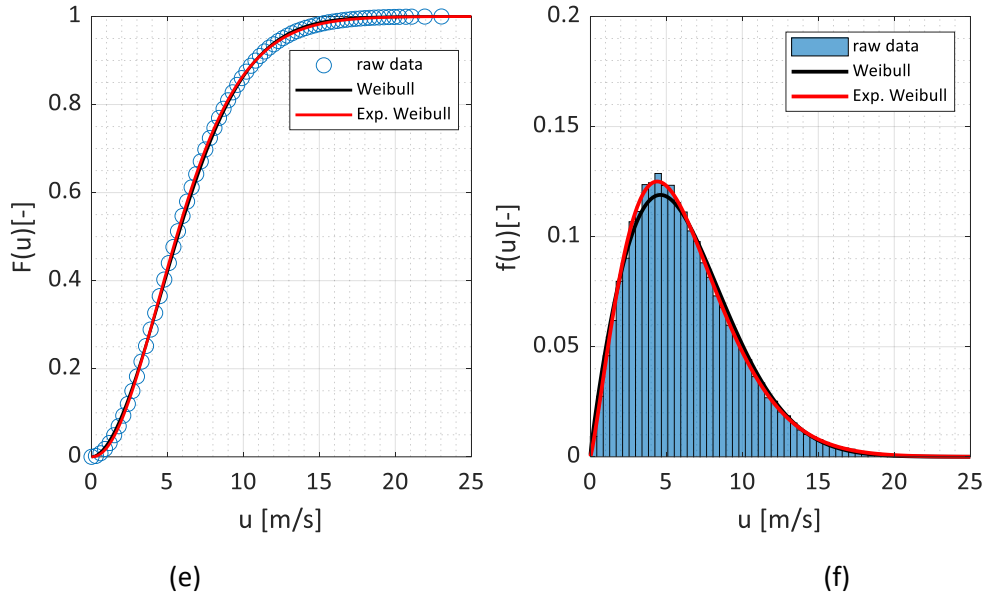
Figure 72: Wind speed marginal distribution to raw data: FINO 1 wind speed fitting, CDF (a) and PDF (b); Tuscany wind speed fitting, CDF (c) and PDF (d); Sardinia site, CDF (e) and PDF (f).

Parameters of the Weibull distributions at the three sites are reported in Table 17.

Table 17: Wind speed marginal distribution fitting.

	FINO 1		Tuscany		Sardinia	
	2-p Weibull	**Exp. Weibull**	**2-p Weibull**	**Exp. Weibull**	**2-p Weibull**	**Exp. Weibull**
α_U [-]	9.4599	8.2673	4.7154	3.0253	6.9253	5.8091
β_U [-]	2.1849	1.8393	1.7535	1.2404	1.8745	1.5587
γ_U [-]	-	1.3611	-	2.1546	-	1.4093

As already discussed, although the misaligned action of wind and waves could cause severe effects on FOWTs. International regulations identify particular Design Load Cases (DLCs) to be simulated in order to assure the required performances of the system [83]. In this work, wind and waves are assumed codirectional since wind-induced waves are considered. Future works will be dedicated to considering such particular load condition, constructing multi-dimensional ECSs which include both wind and waves directions.

7.3.2   Marginal distribution of the significant wave height, H_S

In order to estimate also a 2-dimensional ECS $\left(H_s, T_p \right)$, the marginal distribution of H_s is required. Data were fitted following the same procedure adopted for the wind speed (see Figure 73). As proposed by DNVGL standards [83] a three-parameter Weibull distribution is also adopted, whose CDF can be evaluated introducing a shifting parameter to the two-parameter one:

$$F_{H_S}(h) = 1 - \exp\left[-\left(\frac{h - \delta_H}{\beta_H}\right)^{\alpha_H}\right] \tag{7.8}$$

It was found that, for the FINO site (Figure 73a and 73b), the three-parameter Weibull represents better the wave height data with respect to a two-parameter one. Concerning the two Mediterranean environments (Figure 73c – 73f), an exponentiated Weibull provides better results with respect to the 3-parameter one.

(a)

(b)

(c)

(d)

(e)   (f)
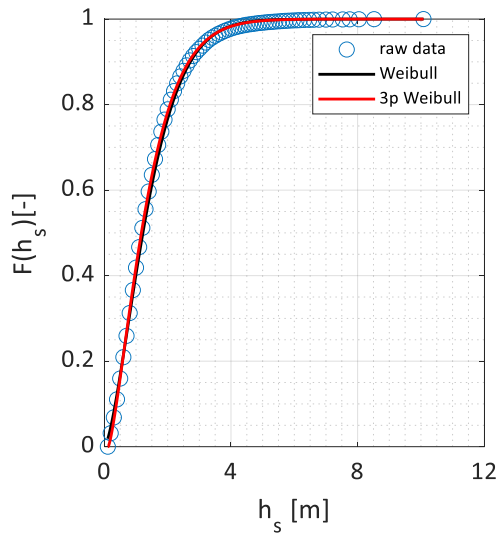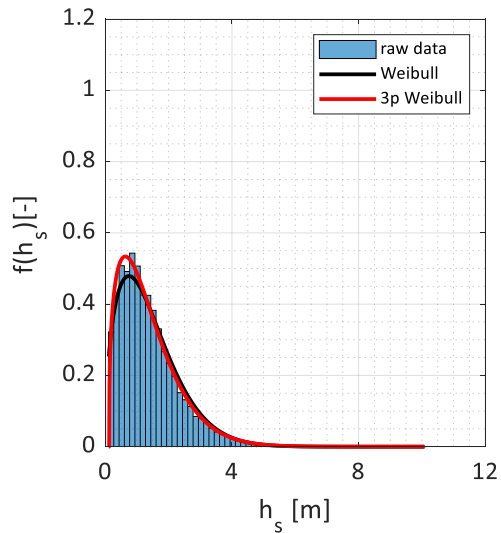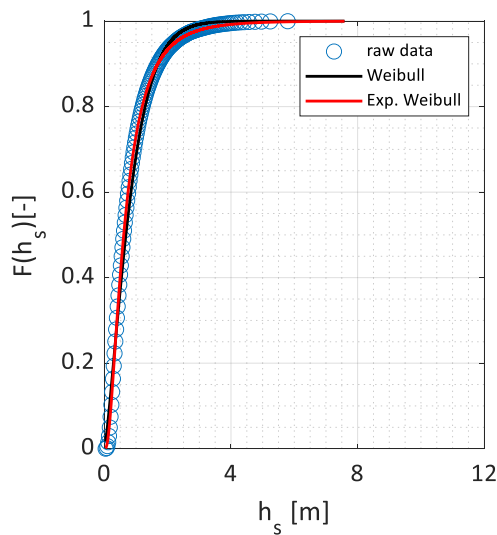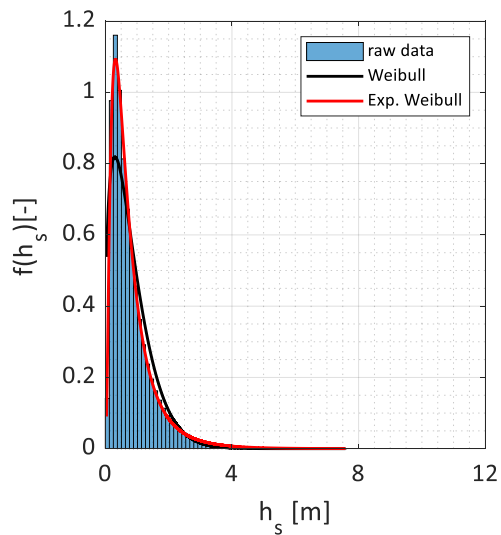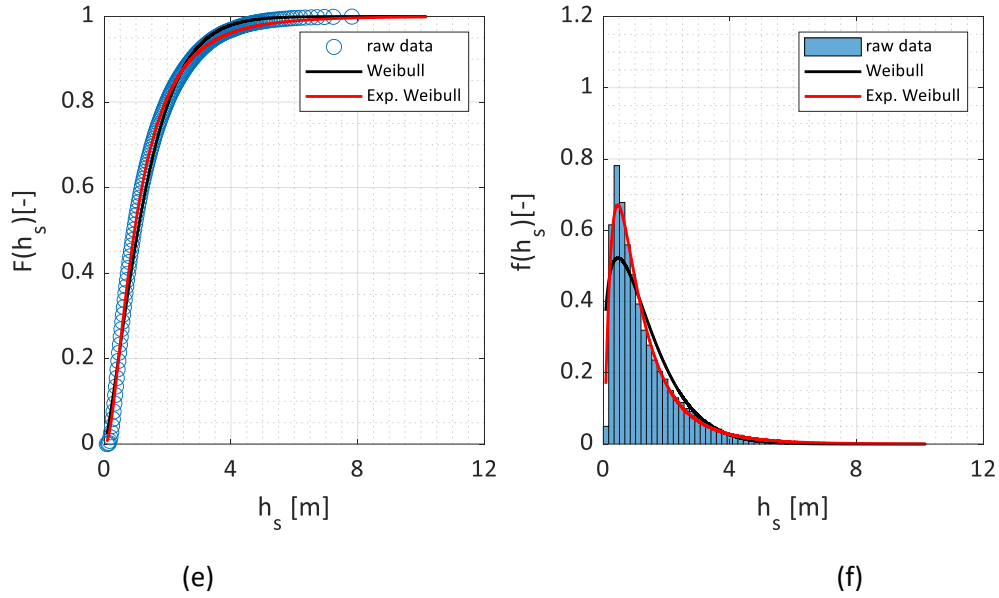
Figure 73: Significant wave height marginal distribution to raw data: FINO 1 wind speed fitting, CDF (a) and PDF (b); Tuscany wind speed fitting, CDF (c) and PDF (d); Sardinia site, CDF (e) and PDF (f).

Parameters of the marginal distribution of the significant wave height at the three sites are reported in Table 18.

Table 18: Wave height marginal distribution fitting

	FINO 1		Tuscany		Sardinia	
	2-p Weibull	**3-p Weibull**	**2-p Weibull**	**Exp. Weibull**	**2-p Weibull**	**Exp. Weibull**
α_H [-]	1.5556	1..3754	0.8977	0.1104	1.4074	0.2550
β_H [-]	1.4968	1.3538	1.3170	0.5407	1.3063	0.5828
δ_H [-]	-	0.1201	-	8.2773	-	5.6520

7.3.3   Conditional distribution of the significant wave height, H_S, for given wind speed, U_w

The conditional distribution of H_S is estimated for different classes of wind speed with a bin size of 1 m/s, spanning from 0.5 m/s to 25.5 m/s. Firstly, all the measurements denoted by a wind speed which fall in each of these classes are identified. A two-parameter Weibull fitting is then performed on the H_S values of these measurements. In this way for each interval, a different distribution is obtained as follows:

$$f_{H_S|U_w}(h|u) = \frac{\alpha_H(u)}{\beta_H(u)} \left(\frac{u_w}{\beta_H(u)}\right)^{\alpha_H(u)-1} \exp\left[-\left(\frac{u_w}{\beta_H(u)}\right)^{\alpha_H(u)}\right] \qquad (7.9)$$

In which $\alpha_H(u)$ and $\beta_H(u)$ are function of the wind speed, u. In order to express the conditionality of H_S on U_w, the shape and scale parameters are formed by smooth functions of U_w. This is done by performing a nonlinear fitting of $\alpha_H(u)$ and $\beta_H(u)$ adopting the following power functions

$$\alpha_H(u) = a_1 + a_2 u^{a_3}$$

$$\beta_H(u) = b_1 + b_2 u^{b_3} \qquad\qquad (7.10)$$

where $a_i, b_i, i = 1,2,3$, are the coefficients of the power functions, obtained adopting MATLAB nonlinear regression fitting model [84]. Results for the Mediterranean sites are presented in Figure 73. Overall, the fitted power functions represent well the trends of both shape and scale parameters.
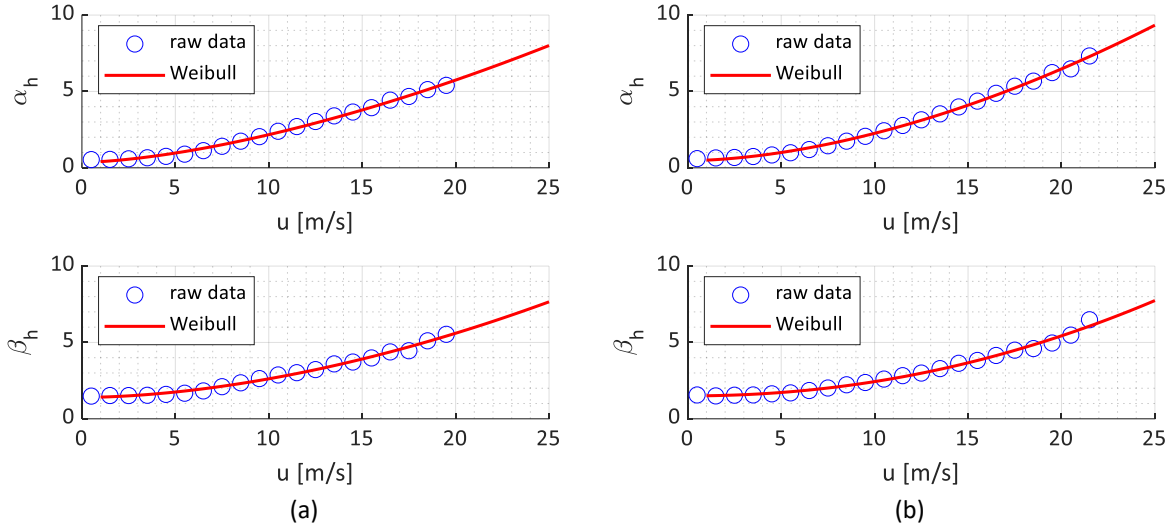
Figure 74: Conditional distribution of the significant wave height to a given wind speed: Tuscany site fitting (a), Sardinia site fitting (b).

For the three sites, the values of the power function coefficients $a_i, b_i, i = 1,2,3$, are reported in Table 19.

Table 19: Conditional distribution of the significant wave height to a given wind speed: coefficients for the fitting of the shape and scale parameters of the Weibull distributions.

	FINO	Tuscany	Sardinia
a_1 [-]	1.4923	0.0487	0.0319
a_2 [-]	0.0011	1.5708	1.7488
a_3 [-]	2.6106	0.3559	0.4702
b_1 [-]	2.9254	0.0199	0.0079
b_2 [-]	6.4192e-7	1.7865	2.0727
b_3 [-]	4.7185	1.4002	1.5012

7.3.4 Conditional distribution of the Spectral period for given Significant wave height

Similarly to the procedure presented in the previous section, the conditional distribution of the peak spectral period, T_P, is evaluated. As discussed in section 7.2, T_P is assumed independent by the wind speed, U_w, and conditioned only to H_S. A Lognormal model is chosen to fit the raw data of T_P for the different H_S classes:

$$f_{T_P|H_S}(t|h) = \frac{1}{\sqrt{2\pi}\sigma_{ln(T_P)}(h)} exp\left[-\frac{1}{2}\left(\frac{ln(t) - \mu_{ln(T_P)}(h)}{\sigma_{ln(T_P)}(h)}\right)^2\right] \qquad (7.11)$$

Mean value, $\mu_{ln(T_P)}(h)$, and variance, $\sigma^2{}_{ln(T_P)}(h)$, of the distributions are formed by the following power and exponential functions:

$$\mu_{ln(T_P)}(h) = c_1 + c_2 h^{c_3}$$

$$\sigma^2{}_{ln(T_P)}(h) = d_1 e^{(d_2 h)} \qquad (7.12)$$

where c_i, $i = 1,2,3$, and d_j, $j = 1,2$, are the coefficients of the power and the exponentiated functions adopted for the fitting of the conditional distribution. Results for the Mediterranean sites are presented in Figure 75.
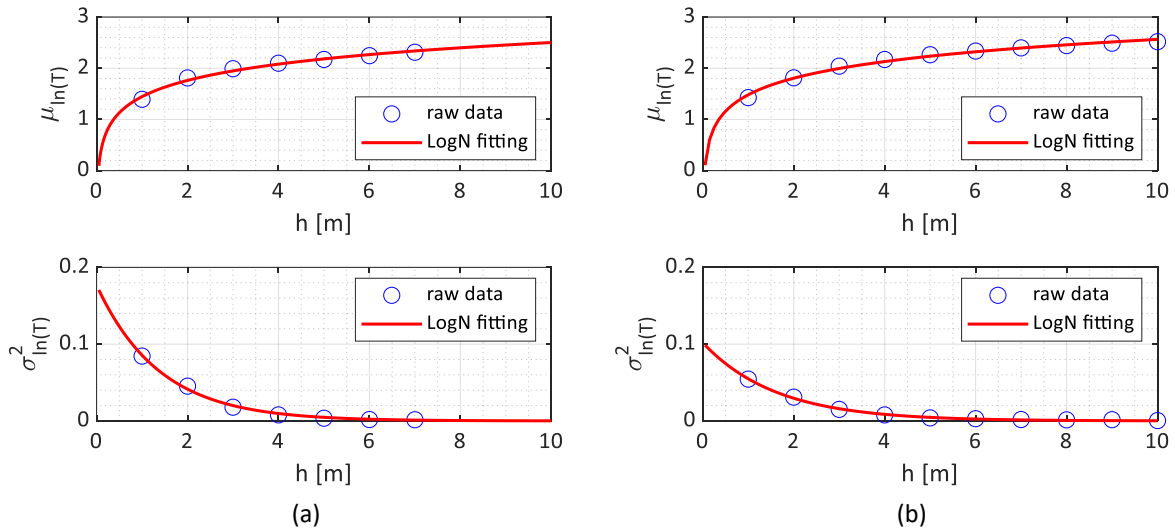
Figure 75: Conditional distribution of the peak spectral period to a given significant wave height: Tuscany site fitting (a), Sardinia site fitting (b).

The values of the coefficients c_i, d_i, are reported in Table 20. For The FINO site, the variance of the distribution has been approximated adopting a two-parameter exponential function.

Table 20: Conditional distribution of the peak spectral period to a given significant wave height: coefficients for the fitting of the shape and scale parameters of the LogNormal distributions.

	FINO	Tuscany	Sardinia
c_1 [-]	1.1884	71.0447	56.1314
c_2 [-]	0.5240	0.0064	0.0083
c_3 [-]	0.4328	-69.5990	-54.6469
d_1 [-]	0.0146	0.1768	0.1018
d_2 [-]	0.2076	-0.7260	-0.6182
d_3 [-]	-1.2701	-	-

7.4   50-year return period ECS

Following the procedure presented in section 7.2, the 50-year return period ECS can be obtained for the three sites. Events lasting 1 hour are herein considered, leading to the following ECSs (Figures 76-78) Figure 76 shows the FINO site ECS. The 3D EC is presented in Figure 76a, where the vertical axis refers to the 50-year wind speed at 10m above the SWL. In order to better represent the environmental conditions, Figure 76b shows a contour plot, where the x-axis and y-axis refer to the 50-year Peak spectral period and to the Significant wave height, respectively. Level curves shows the Sea state pairs (H_s, T_p) which occurs at the same wind speed, evaluated at Hub height (119 m) assuming a power law profile. Dashed black lines refer to the 4 m/s and the 25 m/s level curves, i.e., the cut in and cut out level curves for the reference 10MW WT. Solid red lines identifies the Sea State which occurs at a wind speed of 11.4 m/s, which the rated level curve.

(a)   (b)
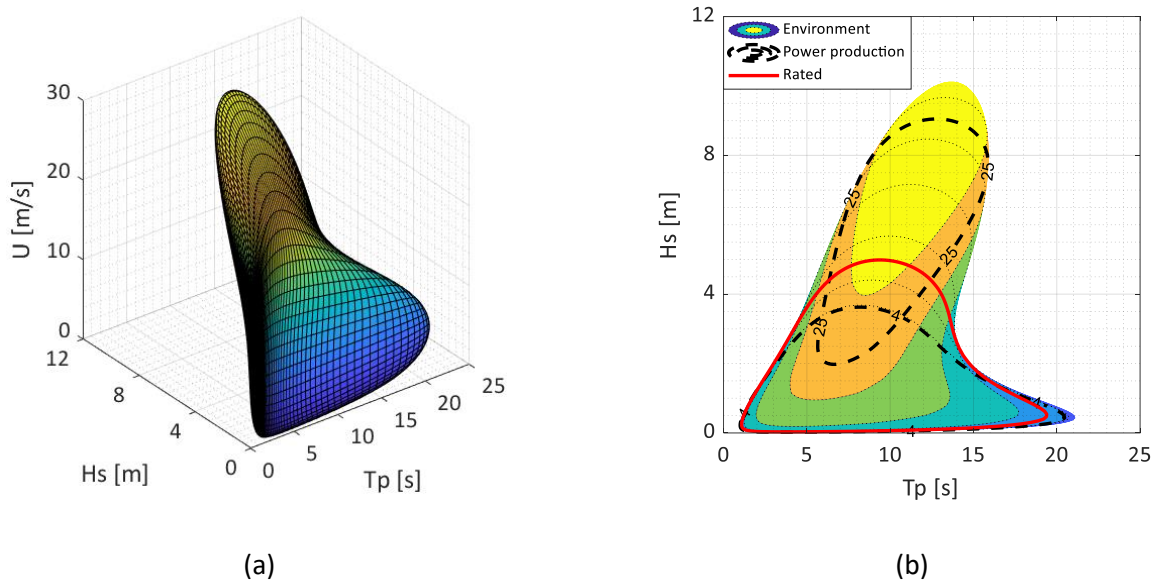
Figure 76: FINO1 Platform ECSs: 3D plot, z-axis refers to the wind speed at 10 m above the SWL (a); Contour plot of the ECs with wind speed at hub height (b).

Figure 77 shows the ECS of the Tuscany site. As it is possible to observe for Fig. 77a, this site I characterized by a sharper tip at high wind speeds with respect to Fig. 77a. In addition, Comparing Figure 77b with Figure 77b, The Tuscany EC presents lower Peak spectral period and wave height with. Such significant differences are probably related to the bathymetric and wave characteristics, being FINO a shallow-water and Tuscany a deep-water site. Moreover, Mediterranean Sea is generally milder than North Sea. The low wind speeds scored by the Tuscany sites makes it not very promising for the installation of a wind farm. On the contrary

the Sardinia site (Figure 78) is characterized by higher wind and wave height. This is probably caused by the marco-circulation of air over the Mediterranean basin.

(a)   (b)
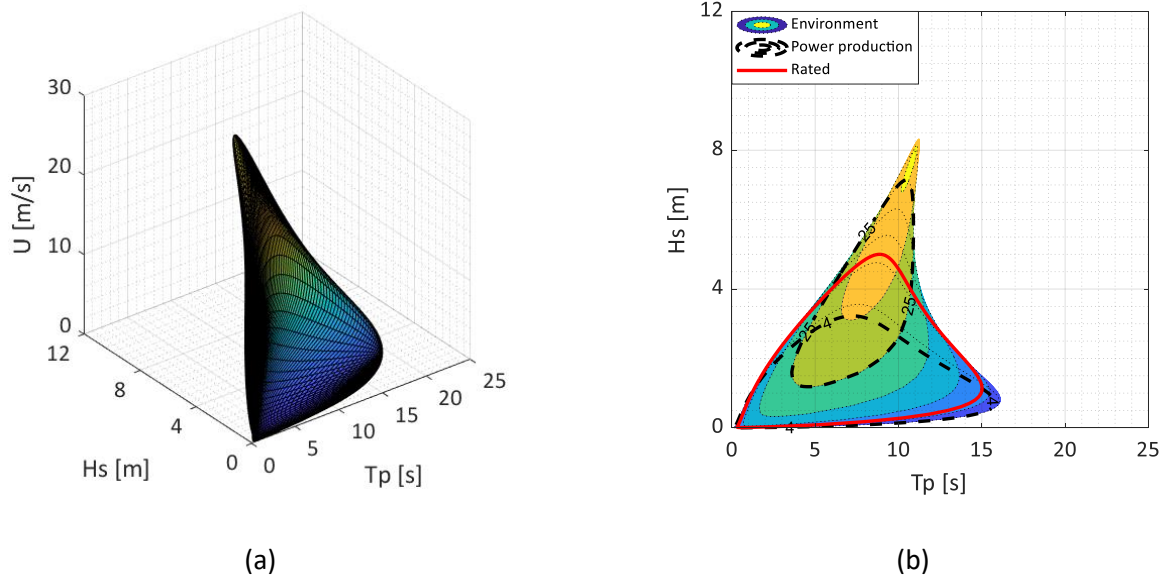
Figure 77: Tuscany site ECSs: 3D plot, z-axis refers to the wind speed at 10 m above the SWL (a); Contour plot of the ECs with wind speed at hub height (b).

(a)   (b)
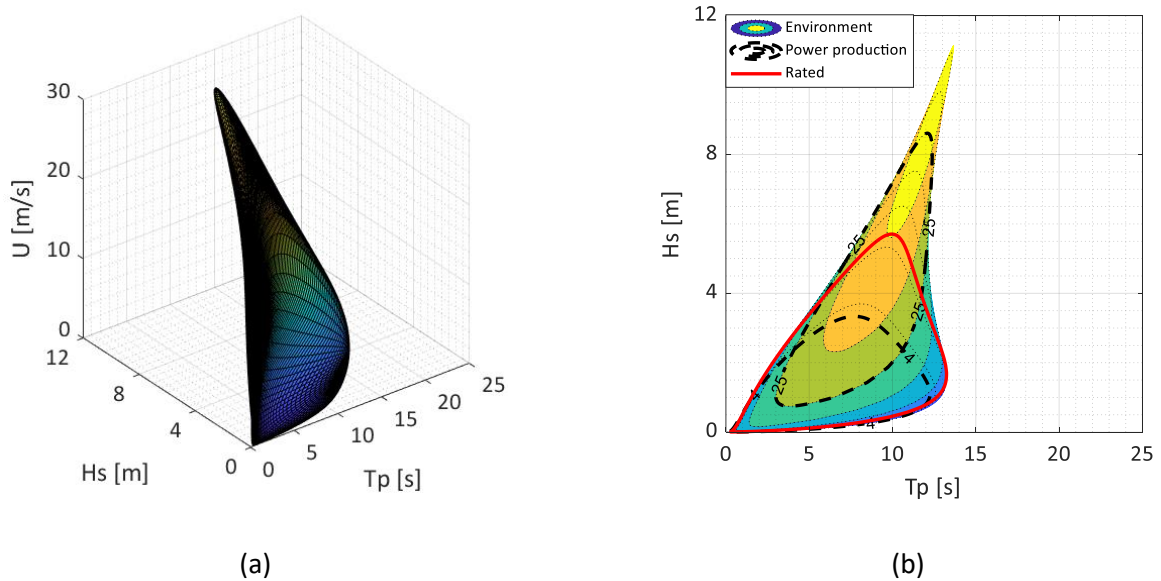
Figure 78: Tuscany site ECSs: 3D plot, z-axis refers to the wind speed at 10 m above the SWL (a); Contour plot of the ECs with wind speed at hub height (b).

By looking at Figure 79, where the yearly average wind speed at 100m above the SWL is presented, it is possible to observe that the strong wind field, channeled by the Pyrenean and the Alps mountains in the

gulf of Marseille, propagates towards the southwester coast of Sardinia leading to such a significant differences with respect to the Tuscany site, which seems to suffer the shade effect of Corsica island.
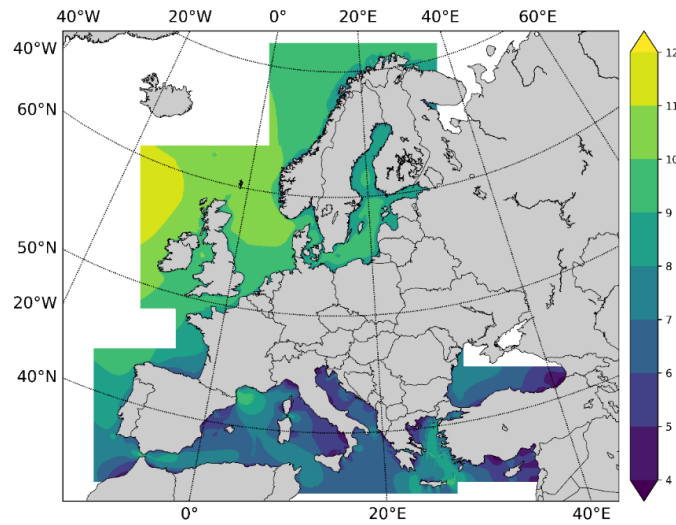
Figure 79: Yearly average wind speed at 100 m above the SWL in the European seas, courtesy of [85].

Among the environmental triplets (U_{HUB}, H_s, T_p), the ones considered most critical for the FOWT are identified, spanning from the cut-in to the cut-out wind speed. They are then adopted for the calculation of the wind-wave loading to be simulated for the Ultimate Strength (US) and Fatigue analysis in the site-specific reliability-based optimization

Table 21: Critical environmental states for 50 year-return period US analysis.

	FINO		Tuscany		Sardinia	
U_{HUB} [m/s]	T_P [s]	H_S [m]	T_P [s]	H_S [m]	T_P [s]	H_S [m]
11.00	6.03	4.05	6.01	3.99	6.02	3.95
11.00	10.79	4.47	8.68	4.93	9.15	5.47
11.00	13.78	2.73	10.34	4.23	10.81	5.12
25.00	9.76	8.08	9.72	6.84	11.64	8.44
25.00	12.43	8.47	10.47	7.14	12.11	8.61
25.00	14.69	8.08	10.80	6.84	12.33	8.44

Appendix C shows the Sea states associated with each mean wind speed are shown.

Chapter 8.
Site-specific Reliability Optimization

Reliability-based optimization allows to optimize a structural system over his service life, leading to cost-effective and efficient solutions. This can be done by minimizing the total cost, the long-term exceedance probability of a certain stress or the fatigue damage on sensitive elements of the system. The latter objective functions have a large computational cost, since a considerable number of design load cases needs to be simulated. For this reason, the developed FD model is adopted. This chapter describes the Site-specific Reliability Optimization procedure proposed. It involves the calculation of the joint-probability distribution of the environmental variables as presented in Chapter 7. The requirements of the international regulation are adopted for the calculation of the stresses on the WT tower. Also the construction costs of the floater and the mooring lines is chosen as objective function. This is a key quantity for the reduction of the cost of electricity produced which can lead to a larger and faster transition from fossils to green energy.

Figure 80: Cost of a FOWT(https://www.naweawindtech2021.org/).
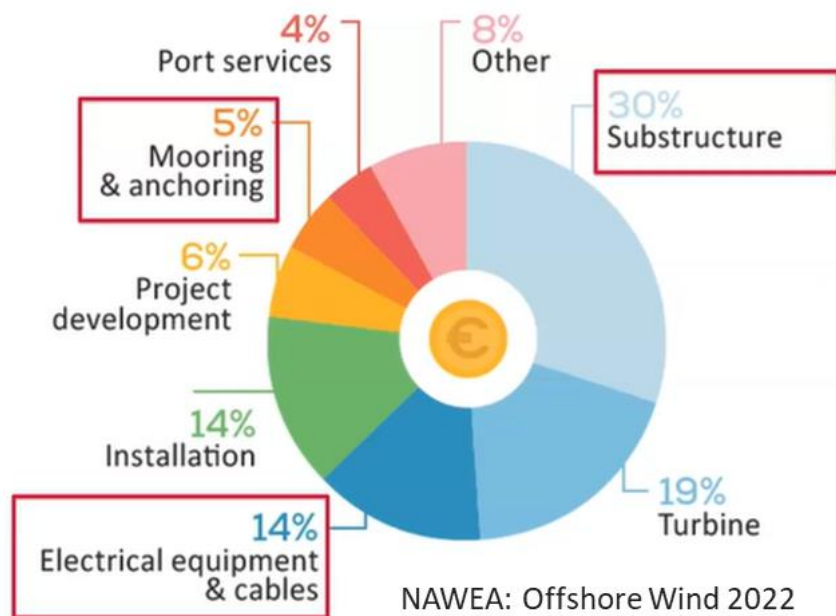
The same design variables presented in Chapter 6 are herein adopted for the site-specific optimization of the Tuscany site and the Sardinia site, presented in Chapter 7. Due to the shallower water, FINO1 site has not been adopted in the following. Due to the bathymetry differences between Tuscany and Sardinia, two different mooring and anchoring systems are designed.

8.1   Optimization procedure

The water depth of the Tuscany site allows to use simple steel chain catenary moorings, connected to the seabed by means of drag embedded anchors. The main strength of such technology is the simplicity in the design, but also in the installation [86]. On the other hand, since the anchors can hold only horizontal loads, a portion of the cable must always lie on the seabed, leading to longer moorings with may be unaffordable for very deep water (> 200m). The design space presented in Section 6.3 is slightly changed, reducing the spacing of the cable length variable to 5m.

Concerning the Sardinia site, the larger water depth (370 m) may not be compatible with slack catenary moorings and drag embedded anchors from an economical point of view. Therefore, suspended lines, made of spiral strand steel wire ropes with a nominal diameter of 0.121 m, have been adopted. This requires anchors capable to hold also vertical loads, such as suction pile and Vertical Loaded Anchor (VLA). The first one is applicable at any water depth; the only constraint is the soil type. It allows to obtain larger holding capacity with respect to the second, but the drawback is the anchor cost and the complex installation. VLAs are simpler and cheaper but they present a limited Ultimate Holding Capacity (UHC). For this reason, suction piles have been chosen for the Sardinia site. The mechanical properties of the mooring lines are taken from the Vryhof manual [51].

Table 22: Steel wire moorings properties [51].

Nominal diameter D_{nom} [m]	Nominal mass m [kg/m]	Axial Stiffness EA [MN]
0.1215	76.5	1353

8.1.1   Anchor dimensioning

Vryhof Stevpris Mk5 drag embedded anchors are adopted for the Tuscany site. The mass of the anchors is evaluated following the design equation for Vryhof Drag Anchors [50]:

$$UHC[kN] = a(W[ton])^b \tag{8.1}$$

here UHC and W are the Ultimate Holding Capacity and the mass of the single anchor, expressed in kN and ton, respectively. The coefficients a and b are parameters which depend on the soil characteristics and on the type of the anchors.
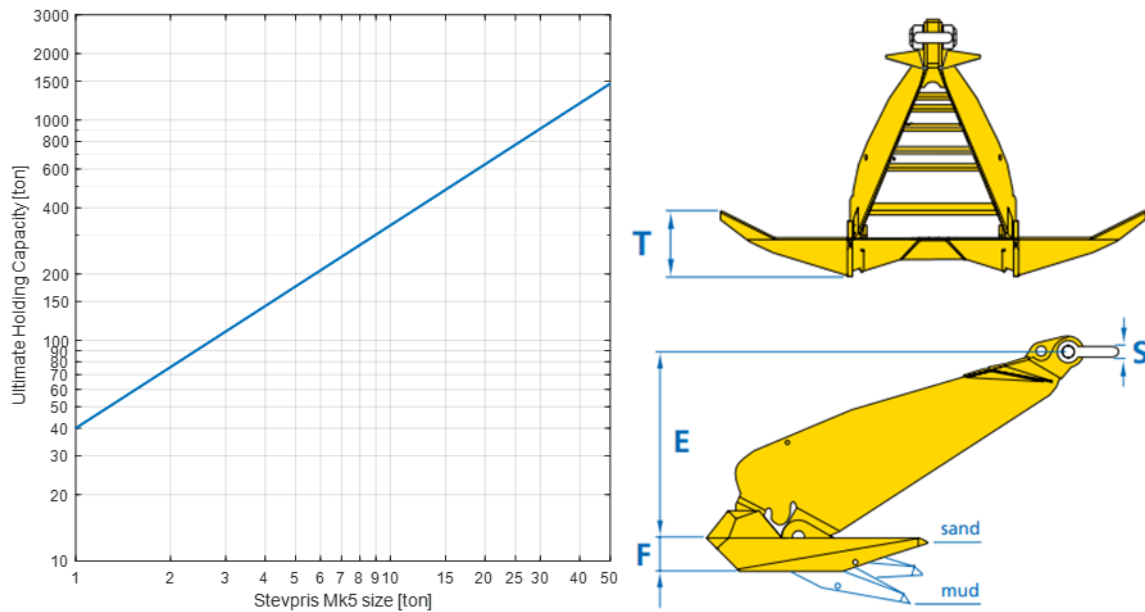
Figure 81: UHC preliminary design curve in very soft clay for Vryhof Stevpris Mk5 drag embedded anchors [51].

Assuming the case scenario of seabed characterized by very soft clay, such parameters are set to 392.28 and 0.92, respectively. In the present work, the mass of the drag anchors is calculated inverting Eq. 8.4 and considering as UHC 1.5 times the maximum tension in the cable at the anchor point under rated wind speed (11 m/s) and extreme wave loading.

As far as it regards the Sardinia site, suction piles are dimensioned according to the ABS technical report [50], which provides the design equations for the calculation of the pile length, diameter and thickness, as a function of the UHC:

$$L_{pile}[m], D_{pile}[m], t_{pile}[mm] = c(UHC[kN])^d \tag{8.2}$$

where $L_{pile}[m], D_{pile}[m], t_{pile}[mm]$ are the pile length, diameter, and thickness, respectively. c and d are parameters depending on the soil properties. Considering a seabed characterized by medium clay (k_{clay} equal to 2.67 kPa/m), c and d values are presented in Table 23.

Table 23: Parameters for the predesign of a suction pile anchor [50].

	L [m]	D [m]	t [mm]
c	0.5166	0.1260	0.8398
d	0.3995	0.3561	0.3561

The mass of the anchors is estimated from the volume of the piles calculated according to Eq. 8.2 and considering as UHC 1.5 times the maximum tension in the cable at the anchor point under rated wind speed (11 m/s) and extreme wave loading.
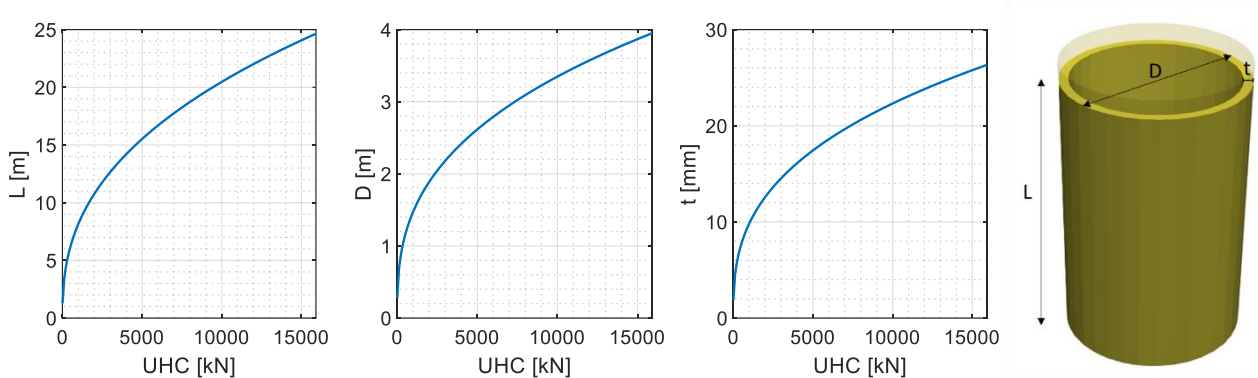
Figure 82: Suction pile design curve from ABS technical report [50].

8.2   Wind-wave design loads

The optimization is performed in a range of wind speeds which span from the cut-in to the cut-out, namely from 4 m/s to 25 m/s. A power law wind profile is herein adopted, with an exponent equal to 0.2, as suggested by IEC 61400-1 [67]. The wind turbulence at hub height is modelled with a Kaimal spectrum, following the IEC Normal Turbulence Model (NTM) (see Section 4.3.5). As fa as it regards the design wave environment, a fully developed sea is considered. A modified JONSWAP spectrum with a peak enhancement factor of 2.2. is adopted in order to effectively represent the Mediterranean waves. These two dynamic loads tend to excite different bands of frequencies. These may lead to the amplification of both platform and turbine response. Therefore, the joint action of wind and waves must be considered in the design phases. Figure 83 shows the PSDs of a 11 m/s wind (Kaimal NTM model) and a corresponding Sea state (JONSWAP) with 5.47 m wave height and 9.15 peak spectral period.
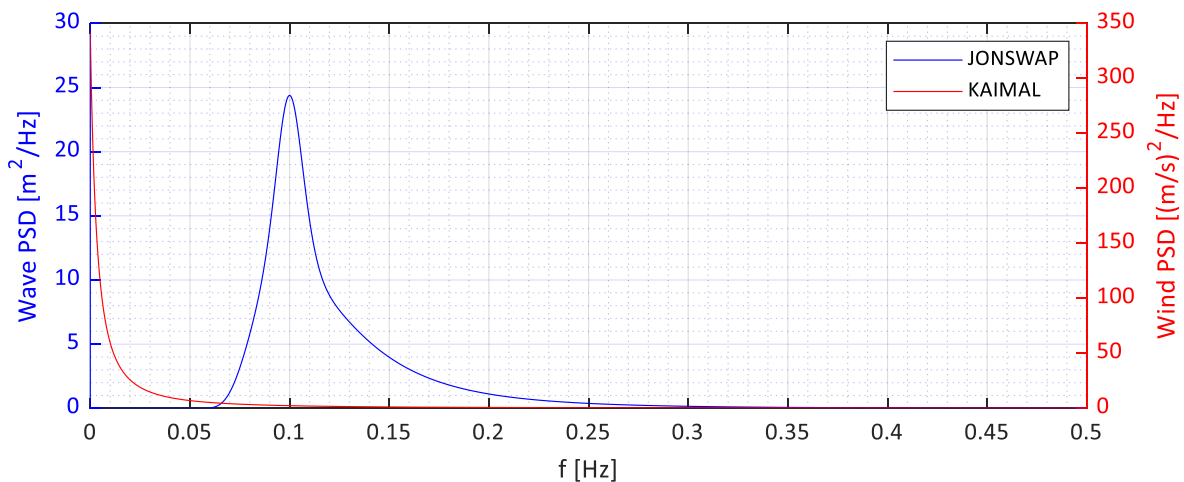
Figure 83: Wind-wave spectra.

Wind loading tends to excite the band of low frequency which contains the platform eigenfrequency of Surge, Heave and Pitch. On the contrary, wave processes are characterized by higher frequencies which may excite the first tower modeshape.

8.3   Objective function

Three significant quantities have been chosen as objective functions, namely the fatigue damage over the service life of the system, the maximum stresses under a 50-year return period Ultimate Load Condition system and the overall cost of the floating foundation (floater+ mooring).

Being FOWTs mainly subjected by dynamic loads, they are particularly prone to fatigue problems. The sea environment is extremely aggressive and local damages may evolve in the failure of components even in short time [87]. In this framework the optimization of the FOWT system with respect to fatigue damage is clearly an important aspect which must be taken into account from early-stage design phases. Besides the implication regarding the long-term reliability of the structure, this objective function influences also the LCOE. Namely, if the FOWT will suffer less damages it will likely to produce more energy over its service life since shut downs related to maintenance activities will be decreased ([28], [40]). Focusing the attention on the pitch rotation, it has been shown in the literature review ([41], [38], [5], [42], [43]) and in Chapter 6 that this DoF is directly related to the WT tower-base bending moment and therefore, considering Eq. 5.7, to the tower top deflection. Therefore, a minimization of the accumulated fatigue damage at the tower-base, will result from a reduction of the pitch oscillation amplitudes, which, as a consequence, brings to reduced motions of the rotors. If the blades oscillations due to platform dynamic motions are lowered, energy production will also benefit. Although such gains are difficult to be quantified from an economic point of view, fatigue damage minimization clearly affects positively the cost-reduction of the system and the power output.

Concerning the optimization under load condition with return period 50 years, severe sea states waves are characterized by longer periods and tend to excite lower frequencies. Considering Figure 83, it is clear how such rare events (which due to the climate change are going to occur more frequently) can lead to the excitation of platform natural frequencies by both wind and waves, leading to extreme aero-hydrodynamic loads. In this regard, solutions optimized for this very particular environmental scenario may be overdesigned but can be useful starts for the further design phases, focused on pursuing different targets without exceeding uncontrollably the maximum loads under such severe conditions.

As far as it regards the overall cost of the substructure of the single FOWT, it has been considered by many authors whether by objective function [24], or by constraint [28]. Zhou et al. [37] performed a global sensitivity analysis also on the manufacturing costs, in order to identify which variables of the substructure affect most such quantity. However, these works referred to design loads typical of northern Europe sites, very severe if compared to the environmental condition of the southern Europe ones. Researches

concerning possible installation sites in the Italian waters from an economic point of view have been carried in [49] and [39]. As highlighted in section 7.1, if on one hand sites like the Mediterranean are characterized by a lower wind resource, on the other hand the milder wave environment allows for lighter and slender floater, if the design is driven towards cost-effective solutions. This may open new possibility for the exploitation of deep-sea areas with limited wind power and the further reduction of the LCOE.

In conclusion the three objective functions identified cover various aspects of the design approach on new generation large FOWTs: maximization of the reliability and efficiency (also in terms of power output) of the structure, reduction of the maintenance operations, enhancement of structural performances for extreme load cases, minimization of the substructure cost in order to decrease the LCOE and therefore to cut the cost of electricity. In the following sections, the three objective functions adopted in the Site-specific optimizations for two installations in the Mediterranean sea are detailed described.

8.3.1 Cost function

The total construction cost of a floating substructure is composed of several aspects which are greatly influenced by the specific condition of the site, such as the bathymetry and the geotechnical properties of the seabed, and by the installation and transportation procedures. Nevertheless, when very deep water are considered (above 400m), the mooring and anchors design becomes very challenging since on one hand, shorter and taut lines may optimize the material cost, while on the other hand, a tensioned mooring system requires anchors capable to withstand uplift forces (proportional to the WT size) which are very expensive both in construction and installation phases. Especially when 10MW+ FOWTs are considered, dead weight anchors may become unaffordable and more sophisticated systems must be adopted, such as suction piles.

Therefore, as previously done by Zhou et al. [37], only manufacturing costs which are closely related to structural dimensions are herein considered. The cost of the raw materials consists in platform, mooring and ballast masses, multiplied by the price of steel and concrete, respectively. As far as it regards the manufacturing cost, welding and painting are the two processes considered. The first one depends largely on the dimensions of the raw steel plates which needs to be jointed, which must meet industry standards and limitations related to transportation and adopted machinery [37]. The welding process of the platform consists in a first phase of preparation, in which the raw plates are assembled and tacked. then they are welded together. Assuming raw plates 10m long and 4m wide, the time (expressed in minutes) related to the first process, T_1, can be estimated as follows [37]:

$$T_1 = C_1 \Theta_{dw} \sqrt{k \rho_{steel} V_s} \qquad (8.4)$$

where C_1 depends on the welding technology (equal to 1); Θ_{dw} is the difficulty factor, assumed to be 1; k is the number of the raw steel plates assembled; ρ_{steel} and V_s are the steel density and the volume of the steel structure, respectively.

The welding process time is strongly dependent by the technology employed. It can be estimated considering the actual welding time (expressed in minutes) and the time related to additional fabrications actions [37]:

$$T_2 = \sum_{i=1}^{N_w} C_{2i} \alpha_{wi}{}^{m_w} L_{wi} \quad T_3 = 0.3 T_2 \tag{8.5}$$

here N_w is the total number of welds; C_{2i} and m_w are parameters related to the welding technology, assumed equal to 0.1053 and 1.94 (Submerged Arc Welding approach with double K butt welds); α_{wi} and L_{wi} are respectively the welding width and length of the i-th element. Multiplying the total fabrication time by the labour price, the manufacturing cost of the floater is obtained. Paint cost is calculated by multiplying the paint price, taken as 12.5 €/m² [37], by the total surface of the floater. As far as it regards the anchoring system of the Tuscany site, according to Myhr et al. [86], chain and anchor costs are set to 2 €/kg and 6706 €/ton. While for the Sardina one, steel wire cables cost is set to 1.60 €/kg and pile cost to 10250 €/ton.

In conclusion, the total manufacturing cost of the floating foundation, MC, can be estimate as

$$MC = M_{Platform} P_{steel} + M_{Ballast} P_{concrete} + (T_1 + 1.3 T_2) P_{labor} + M_{Mooring} P_{moor} + M_{Anchor} P_{Anchor} + A P_{Paint} \tag{8.6}$$

here $M_{Platform}$, $M_{Ballast}$, $M_{Mooring}$ and M_{Anchor} are platform, ballast, mooring lines and anchors mass expressed in kg; A is the total floater surface; P_{steel}, $P_{concrete}$, P_{labor}, P_{moor}, P_{Anchor} and P_{Paint} are the prices of steel, concrete, labor, steel chain anchors and anti-corrosive paint (see Table 24 [37], [86]).

Table 24: Price adopted for the manufacturing cost estimation.

Price		Unit	Value
Steel		€/kg	0.5
Concrete		€/kg	0.1
Labour		€/h	17.05
Mooring	Chain	€/kg	2
	Wire	€/kg	1.60
Anchor	Mk5	€/ton	6706
	Pile	€/ton	10250
Paint		€/m²	12.5

MC is chosen as target to be minimized in the optimization procedure.

8.3.2 Fatigue Damage over the service life of the system

Especially for Offshore structure, which are mostly subjected to dynamic loadings, the design is typically driven by fatigue, where a large number of environmental conditions should be considered in order to evaluate the lifetime loads. The actual effect of wind and wave over the fatigue damage for a FOWT depends on several aspects, such as the site characteristics, the FOWT concept, and the presence of hotspot in the system. Moreover, as discussed in section 8.1, the large variability of a FOWT eigenfrequency may alter significantly the sensitivity of the system to wind and waves. In the present optimization procedure, the fatigue damage is directly evaluated in the FD adopting the Dirlik Method [88],[89].

8.3.2.1 Wind-wave Fatigue Damage

For a given wind-wave condition, the damage in T seconds for process with mean cyclic rate υ, D_{Fat}, is the expressed as [28]

$$D_{Fat} = \frac{\upsilon T}{K} (SCF \cdot \overline{S})^m \left(\frac{t_w}{t_{ref}} \right)^{mk} \tag{8.7}$$

where K is the intercept of the SN curve with the logN axis, while m is the slope of the SN curve and k is the thickness exponent, while SCF is the Stress Concentration Factor (SCF), which allows to account for misalignment between segments of the structure in the estimation of the nominal stresses; $\overline{S}$ is the equivalent nominal stress range; t_w and t_{ref} are the wall thickness and the reference thickness, equal to 25 mm for welded connections according to DNV-RP-C203 [87]; υ is the mean cyclic rate, which can be evaluated from the stress PSD. The SCF adopted is calculated as [28]

$$SCF = 1 + 3 \frac{\delta}{t_w} \exp \left[-\frac{0.91 L_w}{\sqrt{(D_w - t_w) t_w}} \right] \tag{8.8}$$

where δ is the misalignment, D_w is the outer diameter and L_w is the welded length. The misalignment between welded element always present due to fabrication tolerances, it can be take equal to $0.15 t_w$ [87]. The equivalent nominal stress range, $\overline{S}$, can be derived from the expected value of the stress range to power m:

$$\overline{S} = (E[S^m])^{\frac{1}{m}} \tag{8.9}$$

$E[S^m]$ is estimated using the Drilik method.

8.3.2.2   Dirlik method

Dirlik method [88] is a spectral method for fatigue load estimation which can be performed directly in the FD. It allows to avoid obtaining time series on loads from extensive simulation or field measurements that is typically followed by application of the Rainflow cycle-Counting Algorithm (RCA), and instead be able to obtain equivalent information to cycle counts, such as a stress-range probability density function, directly from a power spectrum. It is intended to be applied to wide- and narrow-band processes. The formula for the stress range PDF, $p(s)$, is a weighted combination of and exponential and two Rayleigh distributions:

$$p(s) = \frac{\frac{D_1}{Q}e^{-\frac{Z}{Q}} + \frac{D_2 Z}{R^2}e^{-\frac{Z^2}{2R^2}} + D_2 Z e^{-\frac{Z^2}{2}}}{2\sqrt{m_0}} \tag{8.10}$$

where Z is the normalized stress range:

$$Z = \frac{s}{2\sqrt{m_0}} \tag{8.11}$$

and m_n is the n-th spectral moment:

$$m_n = \int_0^\infty f^n P_S(f) df \tag{8.12}$$

here $P_S(f)$ is the stress range PSD. D_1, D_2, D_3, Q and R are empirical weight factors defined as follows:

$$D_1 = \frac{2(x_m - \gamma^2)}{1 + \gamma^2}, \quad D_2 = \frac{1 - \gamma - D_1 + D_1^2}{1 - R}, \quad D_3 = 1 - D_1 - D_2,$$

$$Q = \frac{1.25(\gamma - D_3 - D_2 R)}{D_1}, \quad R_D = \frac{\gamma - x_m - D_1^2}{1 - \gamma - D_1 + D_1^2}; \tag{8.13}$$

where x_m and γ are the mean frequency and the regularity factor, representing the expected ratio of zero-crossing to peak:

$$x_m = \frac{m_1}{m_0}\sqrt{\frac{m_2}{m_4}}, \quad \gamma = \frac{m_2}{\sqrt{m_0 m_4}}; \tag{8.14}$$

Moreover, the cyclic rate v, previously introduced in Eq. 8.4, can now be calculated as:

$$v = \sqrt{\frac{m_4}{m_2}} \tag{8.15}$$

Once the PDF in Eq. 8.7 is evaluated, the expected value of the stress range to power m can be calculated as:

$$E[S^m] = \int_0^\infty S^m p(S) dS \tag{8.16}$$

An important aspect to be considered in the solution of the indefinite integral in Eq. 8.13, is the estimation of the upper bound of the stress range. This can be evaluated as [90]

$$S^{UP} = \bar{Z} \sigma_S \tag{8.17}$$

where $\bar{Z}$ is the upper bound factor, depending on the slope of the SN curve, m, and on the expected life of the structural component; σ_S is the standard deviation of the stress process, directly evaluated from the 0th spectral moment m_0. Values of $\bar{Z}$ can be found tabulated in [90], where the procedure which leads to Eq. 8.17 is detailed described.

To compare Dirlik method [88] with respect to RCA, it is useful to frame the concept of fatigue damage in terms of an *equivalent fatigue load* (EFL), which is the constant-amplitude stress range that would, over the same number of cycles, cause an equivalent amount of damage as the original variable-amplitude stress time series:

$$EFL = \left(\sum_{i=1}^N \frac{S_i^m}{N} \right)^{\frac{1}{m}} \tag{8.18}$$

where N is the number of stress cycles that have been rainflow-counted. Thus, the damage fraction D_F, can be rewritten as

$$D_F = \frac{\sum_{i=1}^N S_i^m}{K} = \frac{N \cdot EFL_{RCA}{}^m}{K} \tag{8.19}$$

From the spectral method, the EFL can be directly evaluated from Eq. 8.9. The expected damage fraction, $E[D_F]$, can be estimated according to Eq. 8.20:

$$E[D_F] = \frac{T}{K} \upsilon E[S^m] = \frac{T}{K} \upsilon \cdot EFL^m = \frac{E[N] \cdot EFL_{DK}{}^m}{K} \tag{8.20}$$

where T is the duration of the stress process in seconds, while $[N] = T\upsilon$, is the expected number for cycles in T seconds.

To properly compare the EFLs obtained from (Eq. 8.20) and (Eq. 8.18):

- Results of the Dirlik method needs to be normalized according to the number of cycles calculated from the RCA:

$$E[D_F] = \frac{E[N] \cdot EFL_{DK}{}^m}{K} = \frac{N \cdot EFL_{RCA}{}^m}{K} = D_F$$

$$EFL_{RCA}{}^m = \frac{E[N] \cdot EFL_{DK}{}^m}{N}$$

(8.21)

- The upper bounds of the integral in Eq. 8.16 needs to be set equal to the maximum stress range S_i, calculated from the RCA.

The two methods has been applied to the Fore-Aft tower base bending moment process of a 5MW wind turbine subjected to a stochastic wind of average speed of 11.4 m/s (Figure 84).
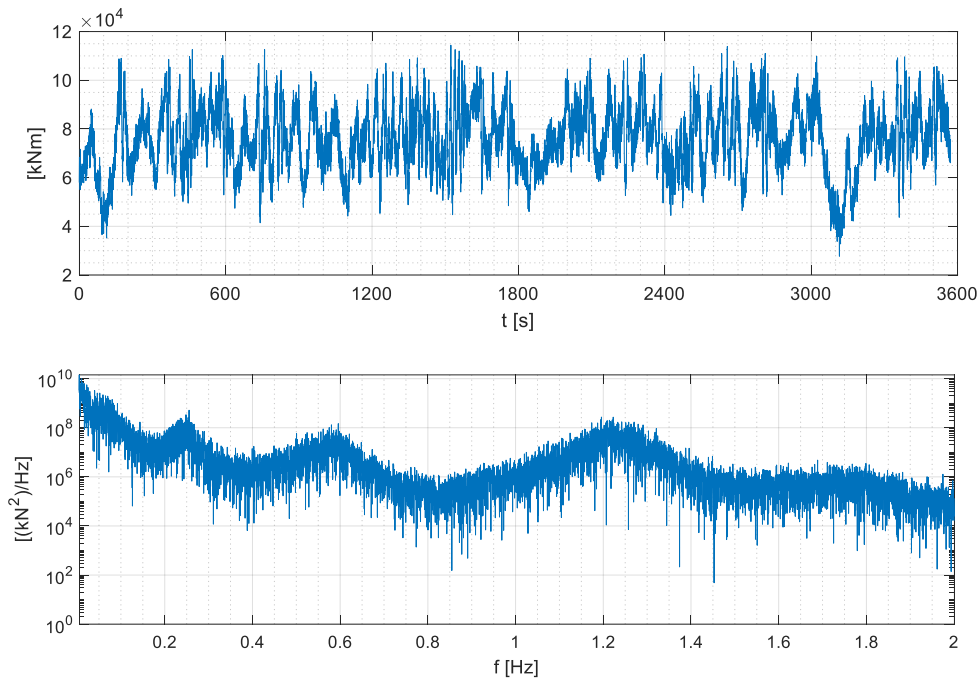
Figure 84: 5MW WT Tower-base bending moment: time history (a) and PSD (d) adopted for the fatigue damage estimation.

As it is possible to observe from the results presented in Table 25, an acceptable error (which is similar to the one obtained in [90] for an exponent m equal to 5) of 14.47% is obtained.

Table 25: Comparison of the fatigue damage estimation performed with Dirlik methods and RCA.

E[N] [-]	6.39E+04
N [-]	3.36E+04
T [s]	3570
$\overline{S}$ [kNm]	1.61E+04
EFL$_{DK}$	1.83E+04
EFL$_{RCA}$	1.60E+04
Error [%]	14.74

8.3.2.3   Total Fatigue damage of the FOWT

The total fatigue damage is chosen as objective function. It can be estimated as

$$D_{TOT} = \sum_{i=1}^{N_{EC}} D_{fat,i}$$

(8.18)

where $D_{fat,i}$ is the fatigue damage (evaluated from Eq. 8.4) associated with the environmental condition $\left(U_{HUB,i}, H_{s,i}, T_{p,i}\right)$. Significant environmental states have been chosen for the simulation, spanning from 9 m/s to the cut-out wind speed. Table 26 presents the selected states for the Tuscany and the Sardinia sites.

Table 26: Design Load Cases for the calculation of the total fatigue damage (Eq. 8.18).

	Tuscany site			Sardinia site	
Tp [s]	Hs [m]	U [m/s]	Tp [s]	Hs [m]	U [m/s]
7.83	3.77	9.00	8.62	4.17	9.00
8.15	4.11	11.00	9.12	4.69	11.00
8.41	4.41	13.00	9.53	5.16	13.00
8.65	4.69	15.00	9.89	5.59	15.00
8.87	4.95	17.00	10.22	6.00	17.00
9.07	5.21	19.00	10.53	6.39	19.00
9.25	5.44	21.00	10.83	6.78	21.00
9.40	5.64	23.00	11.11	7.17	23.00
9.47	5.72	25.00	11.38	7.55	25.00

For each of the presented above, the rotor configuration, namely blade pitch and rotor speed, is updated in order to follow the steady-state operational curves of the 10 MW DTU WT (see Figure 84 and Table 27), which are obtained from time domain simulation performed in FAST at steady wind speed.

(a)   (b)
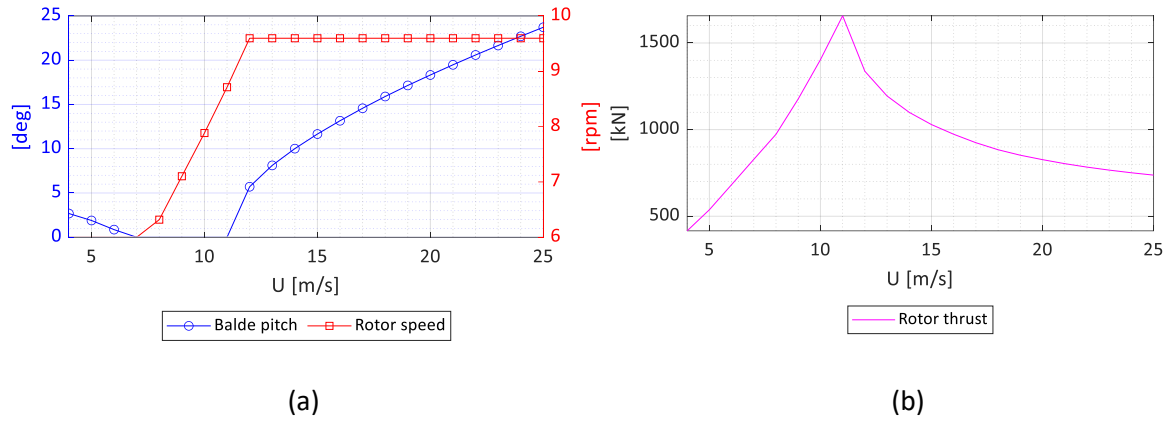
Figure 85: 10 MW WT steady-state configuration: Blade pitch and Rotor speed curves (a), Rotor thrust curve (b) from cut-in to cut out wind speed.

Table 27: 10 MW WT steady-state configuration: Blade pitch, Rotor speed and Rotor thrust, from cut-in to cut out wind speed.

U [m/s]	Blade pitch [deg]	Rotor speed [rpm]	Rotor thrust [kN]
4	2.68	6.000	415.66
5	1.90	6.000	537.38
6	0.86	6.000	682.31
7	0.00	6.000	828.28
8	0.00	6.318	973.06
9	0.00	7.103	1177.00
10	0.00	7.884	1403.47
11	0.00	8.712	1656.90
12	5.71	9.597	1336.81
13	8.12	9.597	1194.00
14	10.01	9.597	1099.41
15	11.66	9.597	1029.00
16	13.16	9.597	973.14
17	14.57	9.597	924.33
18	15.90	9.597	883.72
19	17.15	9.597	852.17
20	18.33	9.597	826.53
21	19.48	9.597	803.44
22	20.59	9.597	783.56
23	21.66	9.597	766.23
24	22.70	9.597	750.90
25	23.72	9.597	737.32

8.3.3 Ultimate Load Condition

Failure of a structure may occur when the stress at a critical location exceeds the resistant capacity of the material. Under the assumption that the local stress increases with the increased loading, the strength of a

structural component can be defined in terms of the ultimate load that causes failure. As reported in IEC 61400-3 the extreme response of a FOWT can be found as the 50-year return period response [67]. In the present procedure, an objective function related to the extreme response of the system, y^{max}, is adopted, considering both the mean value, μ, and the standard deviation of the response, σ:

$$y^{max} = \mu + \sigma \tag{8.21}$$

The mean value of the response of a FOWT is mostly produced by the mean wind loads, while the dynamic part of the response is produced by both wind turbulence and wave loadings. The first one is estimated during the FASTv7 time domain simulations in which the steady state operating point are evaluated. The latter is estimated directly in the FD. Fore-Aft Tower base bending moment is chosen as target to be minimized. As noticed in [63], the flexural response of the tower of a FOWT is primarily influenced by the wind loading, but the steady pitch of the platform tends to increase the bending moment at the tower base. This is found to be caused by the effect of the eccentricity of the Rotor-Nacelle-Assembly (RNA) dead weight on top of the tower, which increases the bending moment in proportion with the rotation of the system.

The extreme conditions can be extrapolated by means of an IFORM as discussed in Chapter 7. To evaluate the ULS objective function, two 50-year designs event have been considered: one at rated and the other at cut-out wind speeds, both characterized by the maximum wave height. Table 28, Figure 86 and 87 shows the extreme event. As already discussed in Chapter 7, the Sardinia site present larger wave height values with respect to the Tuscany site.
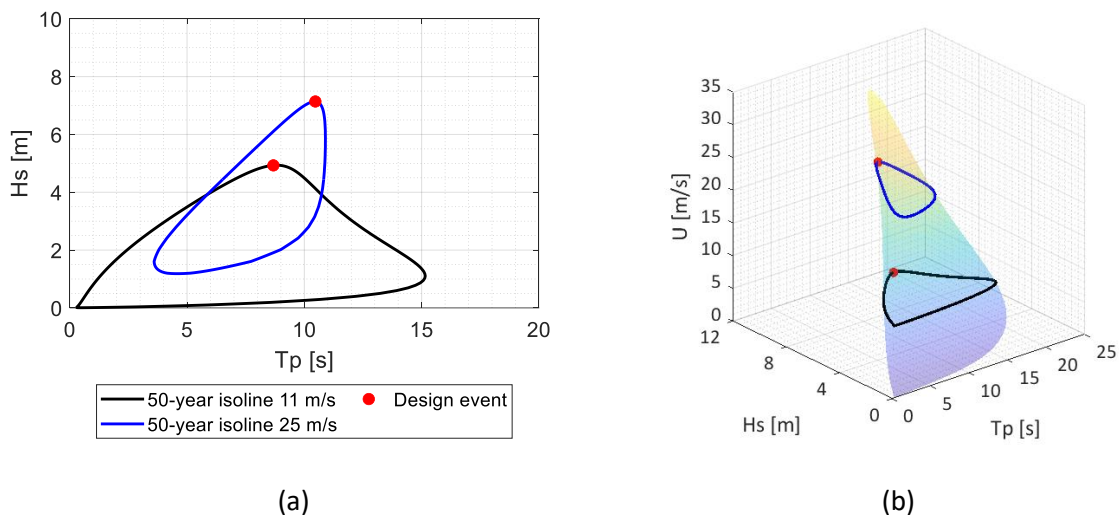

(a)   (b)

Figure 86: Tuscany site isolines at 11 m/s and 25 m/s wind speed (hub height) and design events: plain view in the Hs, Tp space (a), contextualization in the ECS (b).

(a)   (b)
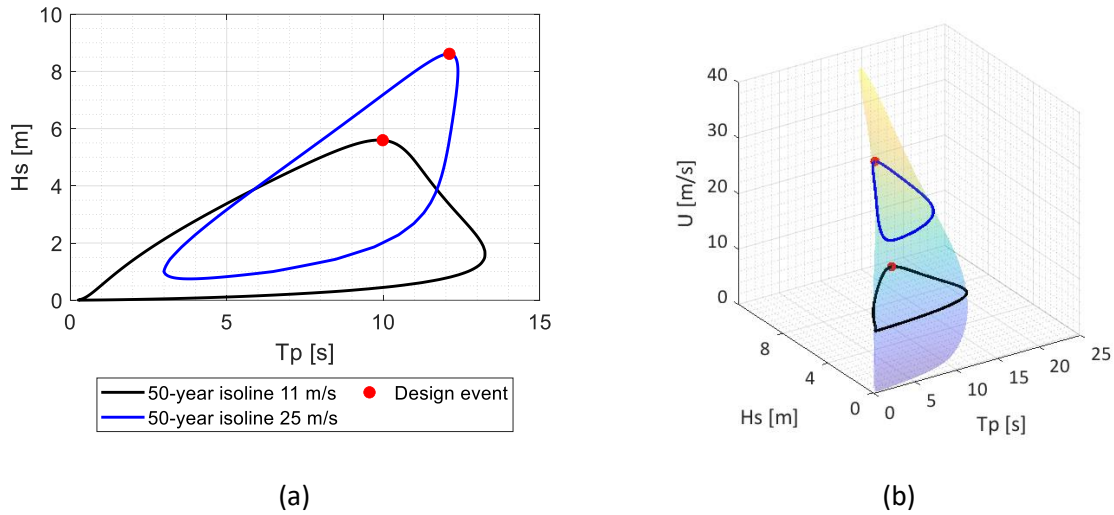
Figure 87: Sardinia site isolines at 11 m/s and 25 m/s wind speed (hub height) and design events: plain view in the Hs, Tp space (a), contextualization in the ECS (b).

Table 28: DLC for ULS analysis.

	Tuscany site			Sardinia site	
Tp [s]	**Hs [m]**	**U [m/s]**	**Tp [s]**	**Hs [m]**	**U [m/s]**
8.68	4.93	11.00	9.98	5.60	11.00
10.47	7.14	25.00	12.11	8.62	25.00

Rotor configuration is updated according to Figure 85 and Table 27.

8.4   Optimization set up

The site-specific optimizations are performed considering the same design variables adopted in Chapter 6 (see Table 29). The larger water depth of the Sardinia site requires a modification of the range of mooring lines length, L, that GA can generate, which varies from + 25m to +60m the anchor radius, x_{anch}.

Table 29: Design variable space for the Tuscany and the Sardinia sites.

	Tuscany site			Sardinia site		
	Lower bound [m]	Upper bound [m]	Spacing [m]	Lower bound [m]	Upper bound [m]	Spacing [m]
d	14	20	0.5	14	20	0.5
r	30	45	0.5	30	45	0.5
drf	20	32	0.5	20	32	0.5
x_{anch}	570	950	10	700	1000	10
L	x_{anch} -20	x_{anch} +20	5	x_{anch} +25	x_{anch} +60	5

The Site-specific optimization procedures are intended to find the platform and mooring arrangement which most effectively reduce both Ultimate Limit State (ULS) and Serviceability (fatigue) Limit State (SLS),

controlling costs. Therefore, in contrast with the previous procedures, the present optimizations are structured on various levels, considering information obtained from the previous step in the next one. Firstly, a ULS single-objective optimization is performed, aiming at minimizing the maximum fore-aft tower base bending moment under the wind-wave 50-year extreme event evaluated in section 8.3.3. Then, a multi-objective optimization is performed under the same load conditions. Both fore-aft tower base bending moment and substructure cost are considered as objective function. They are normalized with respect to the values scored by the optimal system obtained from the previous optimization. This allows to identify the most promising system which reduces platform, moorings, and anchors costs, with a controlled increase of the stresses on the turbine tower. Finally, another single-objective optimization is performed on a reduced design space around the multi-objective optimal solution. The fatigue damage is chosen as target to be minimized. Constraints related to the maximum tower base bending moment and the platform cost are adopted to prevent contradictory results with respect to the ULS optimization. In the following sections, the results of the two optimizations are presented.

8.5   Tuscany site optimization

In this section, the results of the 3-stage optimization for the site in Tuscany are presented.

8.5.1   First-stage single-objective optimization

The first stage considers ULS conditions presented in Table 28 (see section 8.3.3). Being the rotor thrust significantly higer when the wind speed at hub height is 11 m/s (see Figure 85b), the first condition presented in Table 28 is definetly the most critical for the stresses at the tower base.Therefore, a single-objective optimization is performed, considering the event $U_{hub} = 11 \, m/s$, $H_s = 4.93m$ and $T_p = 8.68m$. The maximum tower-base bending moment, calculated following Eq.8.21, is set as target to be minimized. The same constraints described in section 6.2 and 6.3. 4 generations composed by 200 individuals are simulated with GA algorithm. Crossover fraction is set to 80% and 1 Elite children is considered (see Table 30).

Table 30: Optimization procedures set up.

	ULS single-objective optimization
Population [-]	200
N° of generations [-]	4
Cross-over fraction [%]	80
Elite children [-]	1

GA optimization results are presented form Figure 88 to Figure 91. Figure 88 shows the mean value (blue line) and the maximum value (red line) of the tower base bending moment scored by the optimum system at each generation, while the black solid line refers to the maximum value calculated performing the analysis of the upscaled platform. As can be seen, the objective function tends to diminish progressively during the optimization, but results are always lower than the upscaled solution.

From the second generation, the distance between the two curves (red and blue lines), i.e., the standard deviation, does not change, which means that the optimal solutions have a very similar dynamic behaviour.
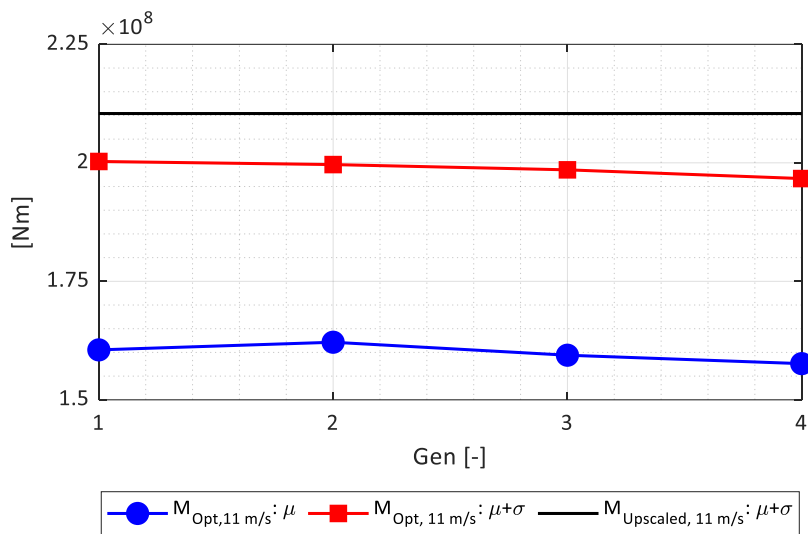

Figure 88: Tuscany site single-objective ULS optimization results: evolution of tower base bending moment during the optimization.

Mean values of the displacements of the optimal systems are presented in Figure 89. Blue line shows the Surge DoF, while red line refers to the Pitch DoF. As already discussed in section 6.3, A direct proportion can be noticed between the mean system rotations and the mean tower-base bending moment (blue line Figure 88). This relationship does not hold if the steady Pitch is compared to the maximum values of the loads at the tower base (red line Figure 88), where the trend does not present any increase at the second generation. The optimized concepts present small rotations, below 1°, under rated wind speed. Moreover, the slight increase for the Second generation, where the steady Pitch reaches 1.10°, is linked to the decrease of the Surge offset, which drops down to 12.40 m. This can be due to significant variation in the platform dimensions and of the mooring lines. In conclusion, the optimal system which minimizes the loads at the tower-base of the turbine, is characterized by small rotation and large horizontal displacement.
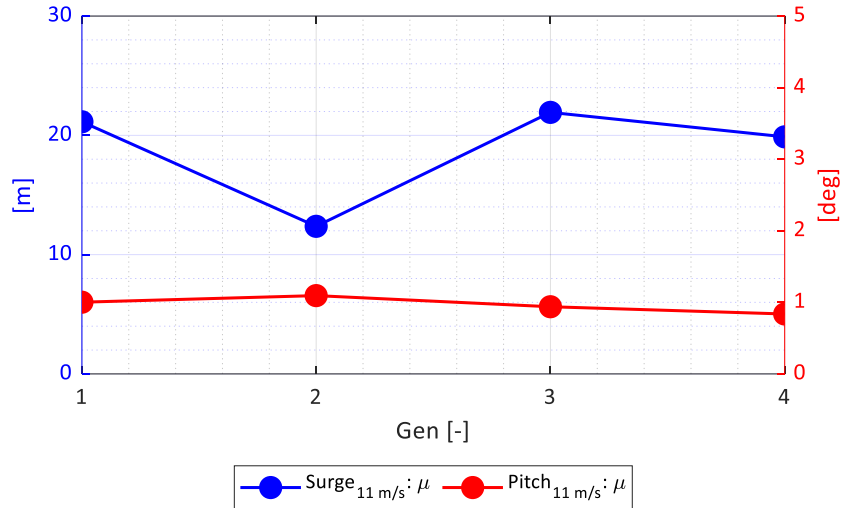
Figure 89: Tuscany site single-objective ULS optimization results: evolution of the mean displacements during the optimization.

To investigate the features which leads to the minimization of the tower-base bending moment, the evolution of the platform and mooring geometry is presented in Figure 90. The three design variables related to the floater dimensions are shown from Figure 90a to Figure 90c, while the ones referred to the moorings layout in Figure 90d. Moreover, the distance between the anchor and the fairlead (L_{hyp}) (the square root term in Eq. 6.6) is plotted instead of x_{anch}, this allows to qualitatively estimates how slack/taut are the cables. Concerning the side column diameter (Figure 90a), d, the optimal solutions show large values, between 19 m and 20 m. A similar behaviour is noticeable for the platform radius (Figure 90b), r. These two results agree with the one obtained in Chapter 6 for the RAO minimization, where the system for the minimization of the Pitch peaks was found to be to one which maximizes both d and r. Also the trend for the draft (Figure 90c), drf, shows that a large value, between 30m and 31.5m, is beneficial for the minimization of the loads on the turbine tower.

This result is in contrast with the ones of the RAO optimization, where a smaller draft was found to be effective for the reduction of the excitation at the platform eigenfrequencies.

This is probably due to the fact that in the present optimization:

- the target to be minimized involves all the DoFs, being the Tower motion also related to the 6 DoFs of the platform;
- the calculation of the standard deviation of the bending moment in the FD requires the integration of the load PSD over all the excited frequencies, while in Chapter 6, the minimization of the RAOs considers a single frequency, the eigenfrequency.

Comparing Figures 90a-90c with Figure 88, it is possible to highlight that, as far as it regards the mean values of the turbine loads (blue line in Figure 88), a direct proportion with the platform radius is noticed,

which is found to be the variable which mist effectively reduces the pitch rotation. Furthermore, the different trend of the maximum turbine loads (red line Figure 88), which does not present an increase of the value at the 2nd generation, is probably linked to the increase of the column diameter and the draft (Figures 90a and 90b. These results enforced the fact that a large draft provides a beneficial effect for the reduction of the dynamic loads at the tower-base. Overall, the best configuration is achieved with d=20m, r=45m and drf= 31.5m.

As far as it regards the mooring-related variables (Figure 90d), the trend of the cable length varies from 880m to a final value of 825m. Moreover, the distance between L and L_{HYP} (red and blue line in Figure 90d, respectively) denotes that 2nd generation in characterized by tauter and stiffer chains, which are responsible for the reduction of the Surge displacement in Figure 88. In the end the optimal layout after the fourth generation presents anchor distance, x_{anch}, equal 840m and a cable length of 825m.
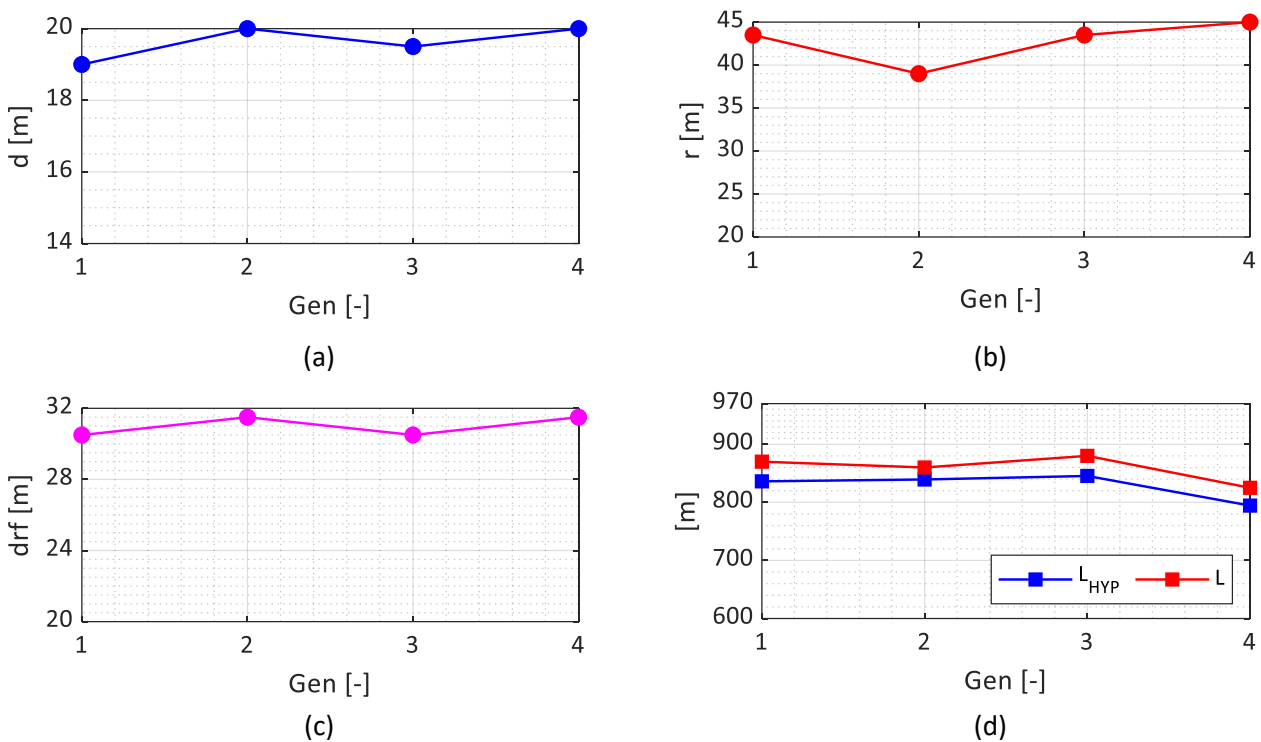

Figure 90: Tuscany site single-objective ULS optimization results: evolution of side column diameter (a), platform radius (b), draft (c) and mooring system layout (d) during the optimization.

Figure 91 presents the cost, evaluated according to Eq. 8.6, of the optimal substructures (red line) compared with the cost of the upscaled system (black line), which was set as constraint. The cost of the scored at the 2nd generation is the largest among the optimized solutions. This is caused by the increase of the column diameter (Figure 90a) and the draft (Figure 90b), but primarily by the tauter mooring system, which calls for bigger and expensive anchors to holds the higher tensions. Furthermore, the cost of the substructure is more sensitive to variations of the column diameter and draft than to variation of the platform radius (see 3rd generation results in Figures 90a-90c and Figure 91).

In conclusion, the optimal solution is achieved with a cost equal to 8.421+06 €, which is 98% the upscaled value, denoting that for the minimization of the tower stresses, the maximization of the platform dimension, i.e., the costs, is necessary.
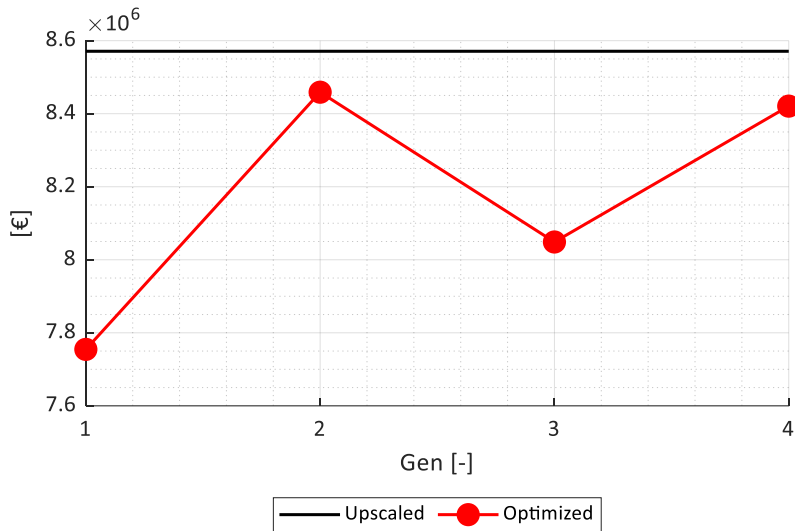

Figure 91: Tuscany site single-objective ULS optimization results: evolution of the substructure during the optimization.

Table 31 summarizes the results of the first stage optimization. In Figure 92, a comparison between the optimal system (green) and the upscaled one (red) is presented. Top view and lateral views of the two platform concepts are shown in Figure 92a and Figure 92b. As can be seen, the optimized system is wider and has larger column diameter and draft. However, the upscaled one scores a higher cost since it presents a larger freeboard: 16m against 12m, and thicker heave plates: 8.41m against 6m. Figures 92c and 92d show the layout of the most stressed mooring, with respect to the cable reference frame (the origin is at the anchor point, z-axis positive upwards and x-axis pointing in the direction of the platform), of the optimal and the upscaled solutions, respectively. Dashed lines refer to the position at rest of the catenaries, while solid lines to the shifted position, obtained imposing the mean values of the maximum displacements. In both cases, the portion of the lines resting on the seabed is shown in black, while the suspended portion are plotted accordingly to the colours of Figures 92a and 92b.

By comparing the two catenaries at rest, it is noticeable that the optimized solution presents *slacker* cables, therefore a more flexible mooring system. This results in larger Surge motions, which are noticeable comparing the solid lines in Figure 92c and 92d.

Table 31: ULS single objective optimization results.

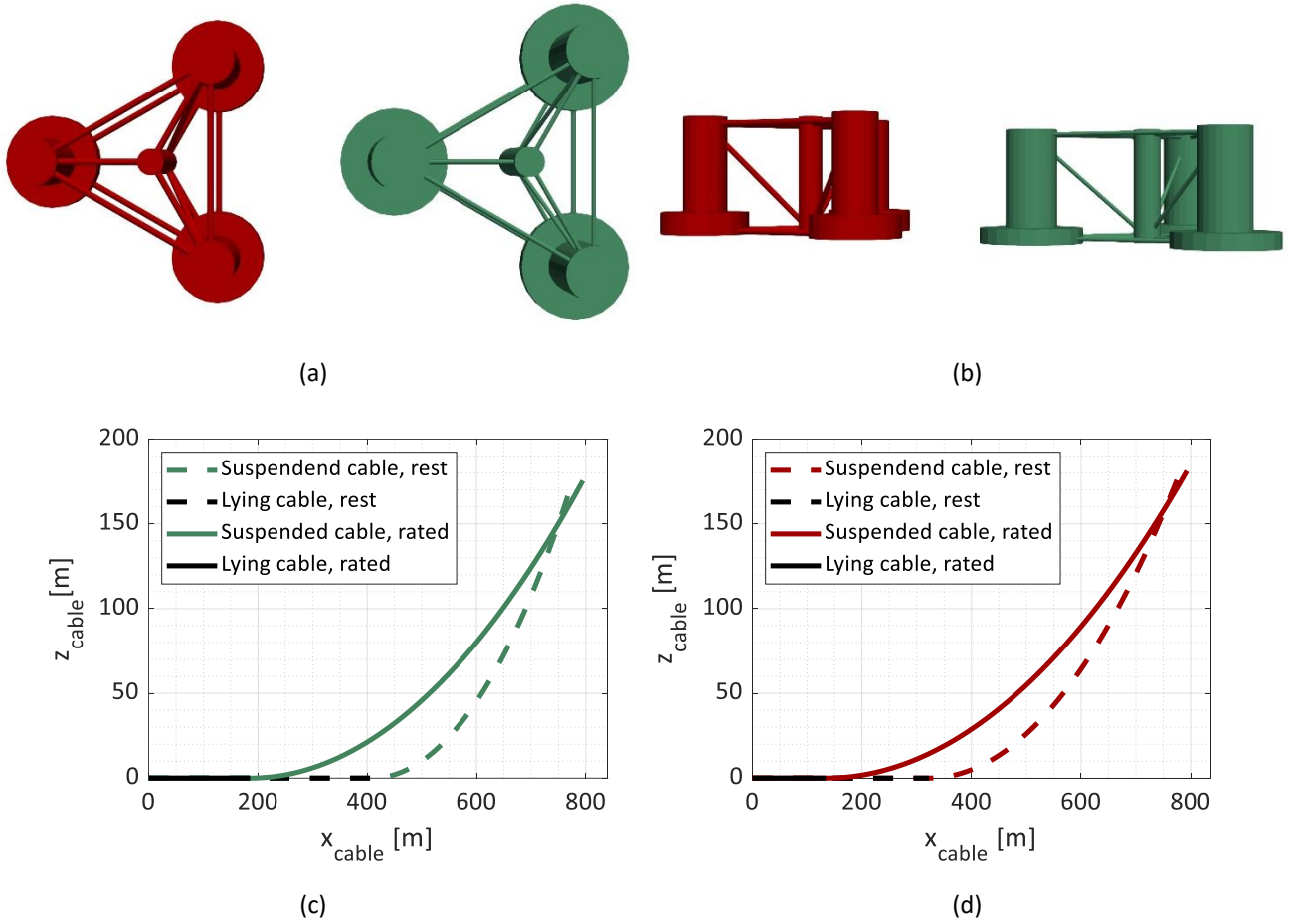| d	r	drf	x_{anch}	L	M11m/s: µ+σ	Surge	Pitch	Cost
[m]	[m]	[m]	[m]	[m]	[Nm]	[m]	[m]	[€]
20	45	31.50	840	825	1.9668e+08	19.870	0.837	8.42e+06

(a)

(b)

(c)

(d)

Figure 92: Tuscany site single-objective ULS optimization results: evolution of the substructure during the optimization.

8.5.2   Second-stage multi-objective optimization

With the intention of reducing the cost of the substructure, the second stage optimization is performed considering a multi-objective procedure. The two objective functions chosen allow to both consider the tower-base bending moment and the substructure costs as target to be *jointly* minimized. They are normalized by the results of the previous optimization as presented in Eq. 8.22:

$$\min_x \boldsymbol{f}_{obj}(\boldsymbol{x}) \rightarrow \boldsymbol{f}_{obj}(\boldsymbol{x}) = \left[\frac{M_{max}(\boldsymbol{x})}{M^I_{max}} \quad \frac{Cost(\boldsymbol{x})}{Cost^I}\right] = \left[\frac{M_{max}(\boldsymbol{x})}{1.9668e08\text{Nm}} \quad \frac{Cost(\boldsymbol{x})}{8.42e06\text{€}}\right],$$ (8.22)

where M^I_{max}, $Cost^I$ are the maximum bending moment and substructure cost obtained from the previous optimization and presented in the table above. Being the first objective function normalized by a quantity which have been minimized in the previous optimization, it is expected to be always above 1. This second stage is intended to find a floating configuration which significantly reduces the cost, without increasing excessively the loads on the turbine tower.

The optimization is performed with MATLAB GA algorithm. 3 generations of 200 individuals are considered. Cross over fraction is set to 80%. 30 optimal candidates have been identified. Figure 93 presents the Pareto

front, i.e., the results of the multi-objective optimization in the objective function space $\left(f_{obj,1}(x), f_{obj,2}(x)\right)$. X-axis refers to the normalized bending moment, while y-axis refers to the normalized cost of the substructure. As expected, the pareto front shows that the two targets have an inverse relationship. Nevertheless, a large cost reduction of more than the 40% can be achieved with a small increase of the stresses at the tower base, between 10%-15% with respect to the result scored in the previous optimization.
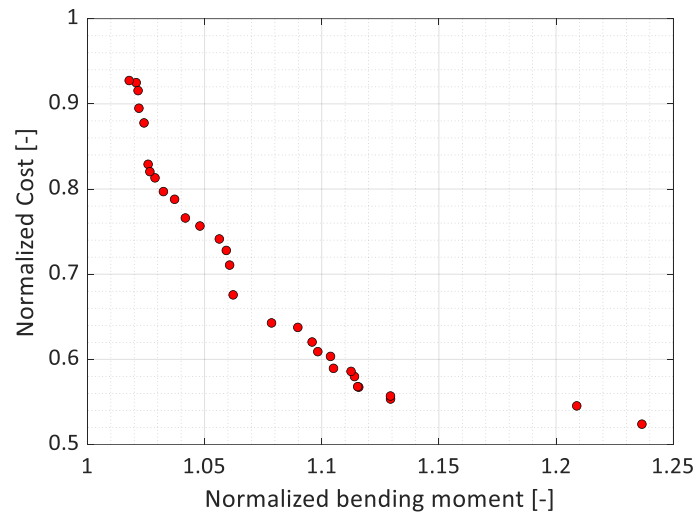

Figure 93: Second stage multi-objective optimization results: Pareto front.

To better understand the features of the 30 optimal systems, Figure 94 shows the results progressively from 1 to 30. Seven optimal concepts are found to effectively reduce the substructure costs (Figure94a) with a reduced increase of the tower loads (Figure94b). These are highlighted in the following Figures with black lines and circles. Among these, the one which minimizes the costs, and, consequently, maximises the bending moment is the 4° configuration. For this reason this optimal solution is discarded.
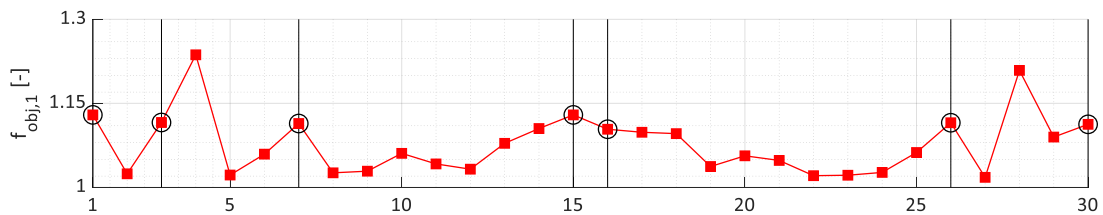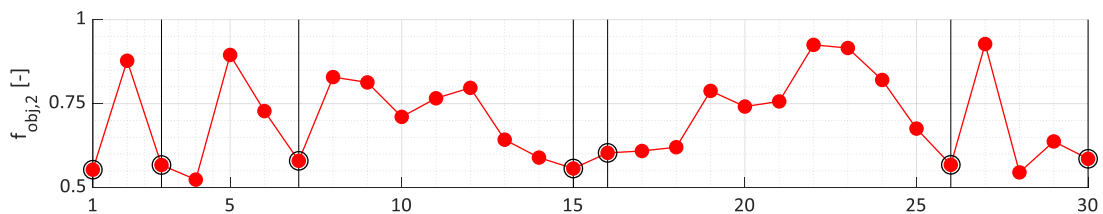
(a)

(b)

Figure 95 presents the platform dimensions of the 30 optimal systems. A large variation in the side column diameter (blue line), d, is noticeable in Figure 95a. However, the six candidates higlighted in Figure94 score the lower values, spanning from 14m to 15m (column diameter of the 3rd and 26th configurations).

On the contrary, large platform radius (red line in Figure 95b), r, can be seen for all the platforms. Among these, the ones which maximizes r belongs to the group of the six optimal systems. The lowest radius scored by configuration 4th may probably explain the correspoing increase of bending moment (Figure94a) and also the minimization of the substructure cost (Figure94b). Optimal platforms present also a variable draft (magenta line in Figure 94c) and, similarly to Figure 94a, the best configurations score relatively small drafts, from 20.5m to 25m.

(a)

(b)

(c)
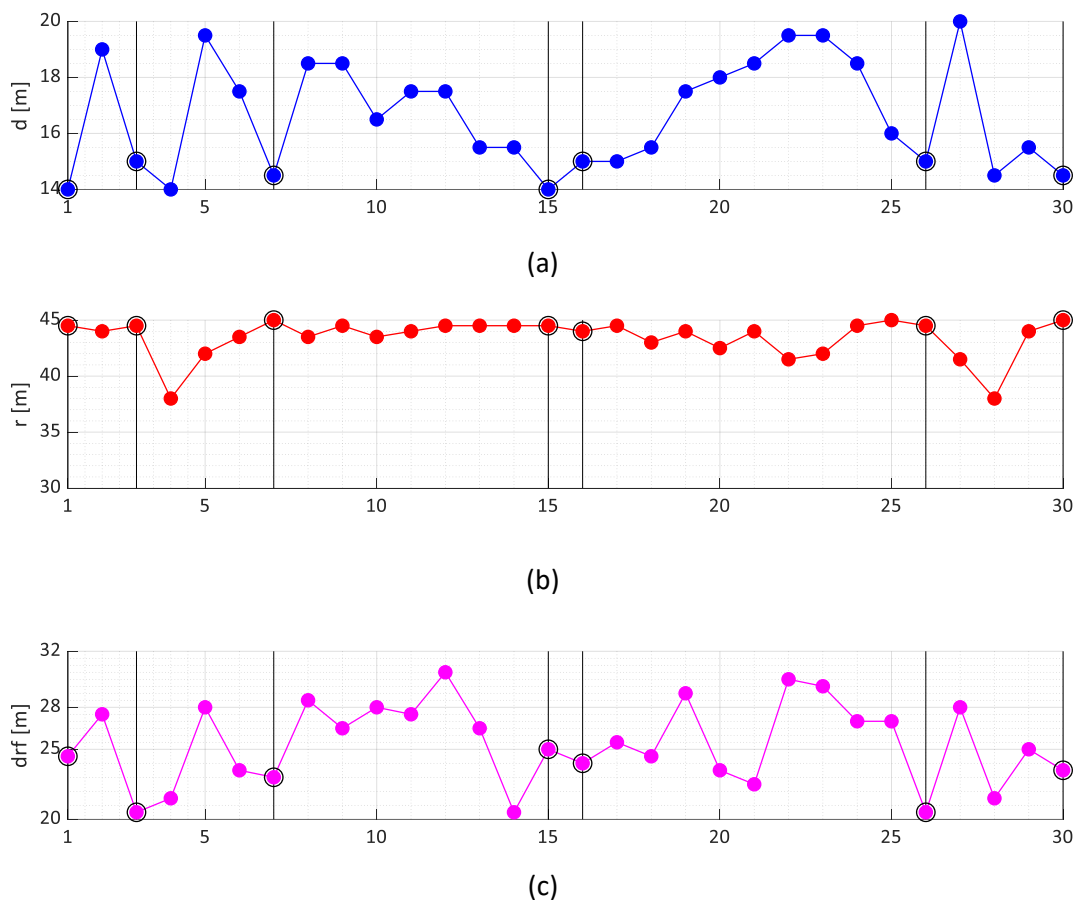
Figure 95: Second stage multi-objective optimization results: optimal side column diameters (a), platform radii (b) and drafts (c).

Mooring lines characteristics of the optimal concepts are presented in Figure 96. L_{HYP} (blue line) is plotted in Figure 96a, while the unstretched cable length (red line) , L, is shown in Figure 96b. Overall, these two curves have similar trends, as expected by catenary moorings, L_{HYP} is always smaller than L. To have a better understanding on the mooring system mechanical properties, the difference between the cable unstretched length (Figure 96b), L, and L_{HYP} are shown in Figure 96c. This quantity is proportional to the catenary sag and allows to immediately identify how *slack* a cable is. As can be seen, the six optimal

configurations score values which spans from 29m to 38.5m. This leads to different surge behaviour of the systems due to the different flexibility of the moorings.

(a)

(b)

(c)
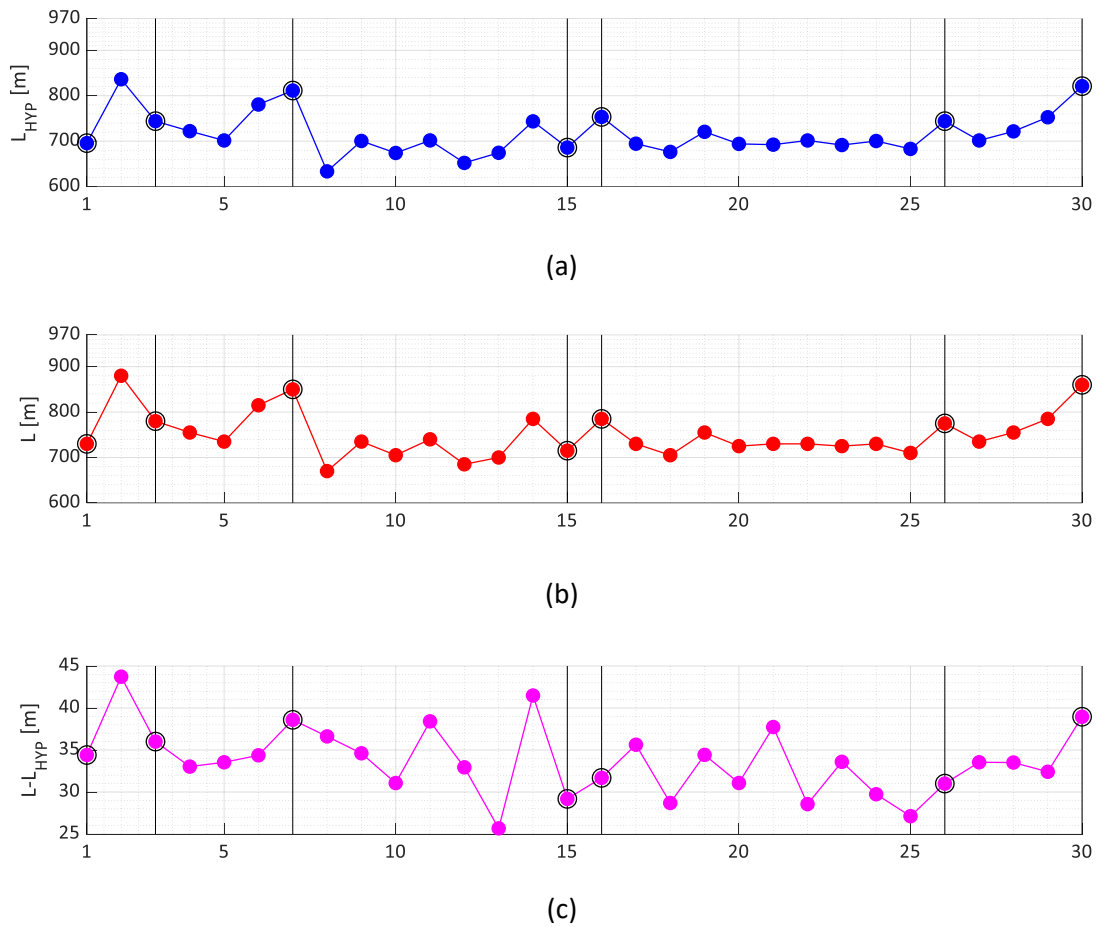
Figure 96: Second stage multi-objective optimization results: L_{HYP} (a), cable unstretched length, L, (b) and difference between L and L_{HYP} (c).

Mean displacement of the optimal systems in Surge and Pitch are presented in Figure 97. Surge DoF results are plotted in Figure 97a. All the configurations presents large horizontal displacements under rated wind speed, which confirms the results obtained in the first-stage optimization (Figure 89). Also, It presents a very similar trend to L-L_{HYP} curve (Figure 96c) as expected. Similarly, Figure 97b shows the inverse relationship between the Pitch rotation and the platform radius (Figure 95b). Configuration 7 scores the maximum pitch angle due to the reduction in the platform radius (Figure 95b).

(a)
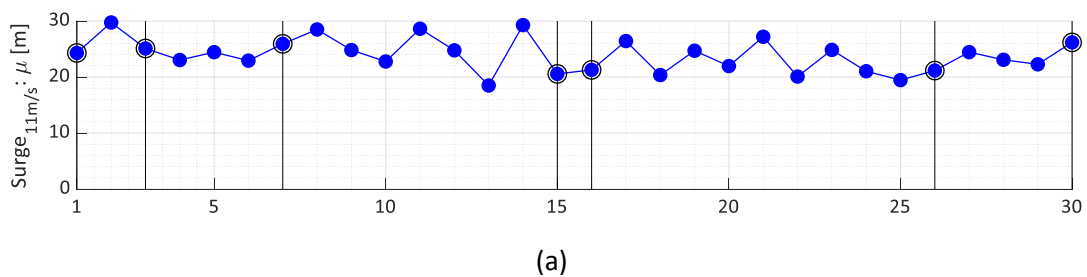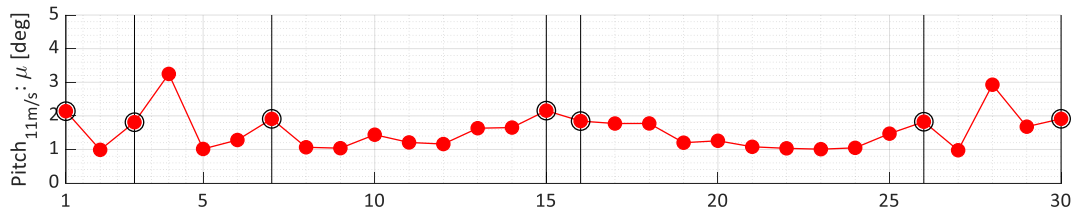
(b)

Figure 97: Second stage multi-objective optimization results: Surge (a) and Pitch (b) mean displacements.

In the end, the cost of the optimal systems are compared in Figure 98 with the costs of the upscaled and the bending moment optimized (section 8.5.1) solutions. As it is possible to observe, the reduction of the substructure cost can be quantified in about 3.5 million of euro.

Figure 98: Second stage multi-objective optimization results: Substructure cost
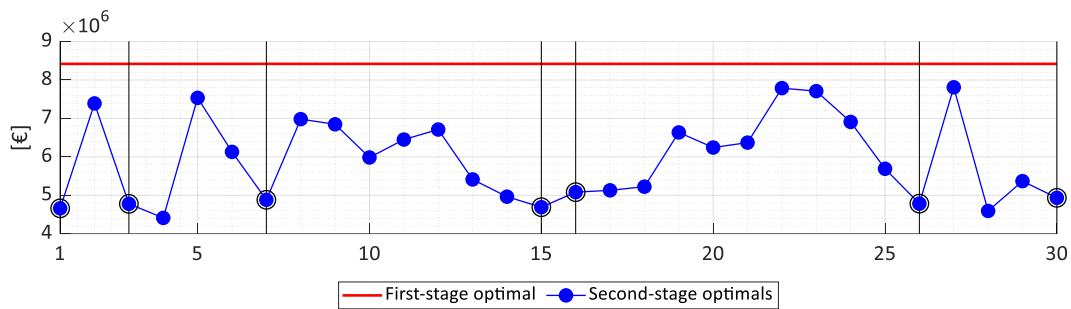
The results related to the seven configurations identified in the Second-stage multi-objective optimizations are summarized in Table 32. Figure 99 compares the geometries of the most significant 2nd stage optimized platforms (blue) with the upscaled (red) and 1st stage optimized (green) ones. These floaters presents a wide radius, very small side column diameter and smaller drafts.

Table 32: Second-stage multi- objective optimization results.

| ID	d	r	drf	x_{anch}	L	$f_{obj,1}$	$f_{obj,2}$	Surge	Pitch	Cost
[-]	[m]	[m]	[m]	[m]	[m]	[-]	[-]	[m]	[m]	[€]
1	14	44.5	24.5	730	730	1.129	0.553	24.30	2.14	4.660E+06
3	15	44.5	20.5	780	780	1.116	0.567	25.10	1.81	4.778E+06
7	14.5	45	23	850	850	1.114	0.580	25.93	1.91	4.882E+06
15	14	44.5	25	720	715	1.129	0.557	20.56	2.16	4.690E+06
16	15	44	24	790	785	1.104	0.603	21.28	1.84	5.082E+06
26	15	44.5	20.5	780	775	1.115	0.568	21.16	1.83	4.783E+06
30	14.5	45	23.5	860	860	1.113	0.586	26.18	1.91	4.934E+06
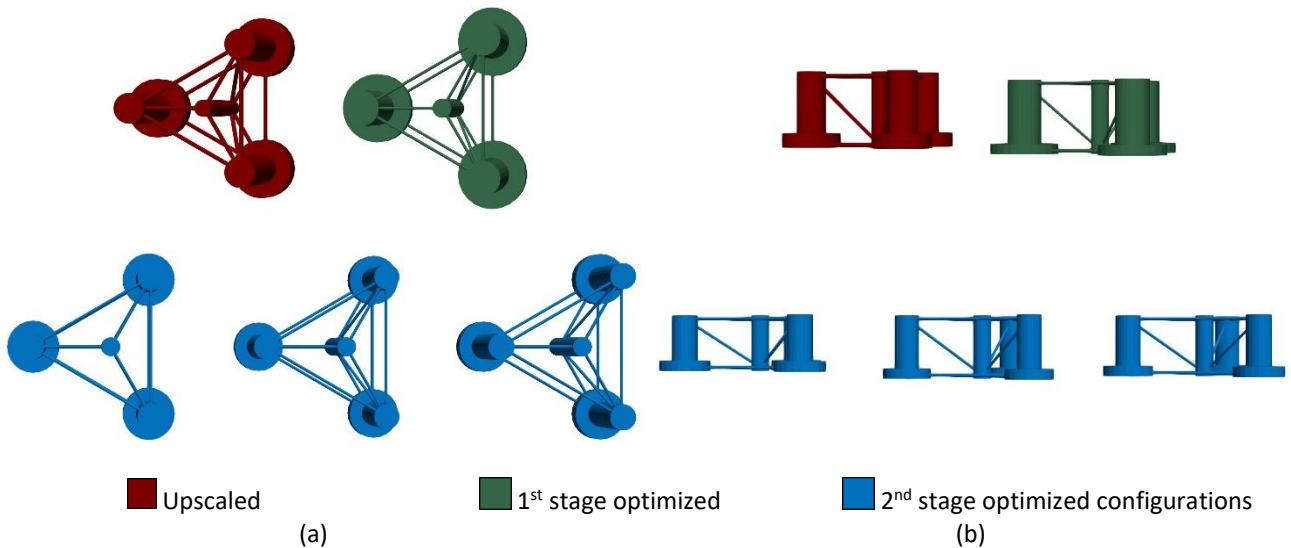
Figure 99: Comparison of the most significant optimal configurations after 2nd stage optimization; configuration IDs presented from left to right: n° 3, n° 15 and n° 30.

The mooring lines of the most significant 2nd stage optimized systems are presented in Figure 100.
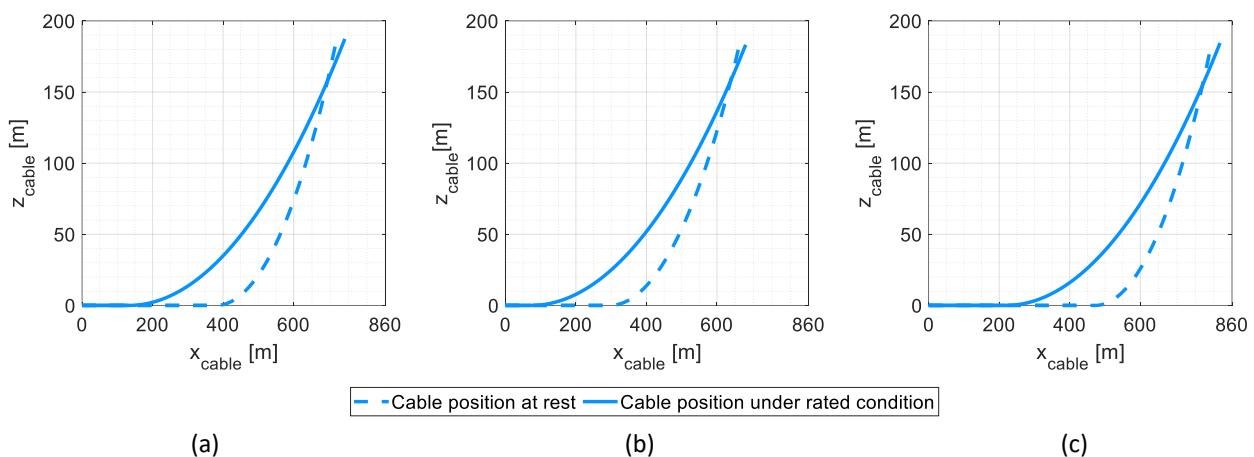
Figure 100: Comparison of the most significant mooring systems after 2nd stage optimization; configuration IDs presented from left to right: n° 3 (a), n° 15 (b) and n° 30 (c).

8.5.3   Third stage SLS optimization

The results of the second-stage optimization shows that the configurations which most effectively reduce the substructure costs without significant increase of the turbine stresses lie in a restricted region of the design space. Figure 101 compares the results obtained from the two optimizations. The optimal configuration obtained from the 1st stage optimization is plotted with a red dot, while all the 28 individuals found from the 2nd stage are represented with blue dots. The seven optimal configurations identified in Table 32, are shown with green dots. Platform geometries are presented in Figure 101a. As it is possible to observe, the seven optimal configurations (green dots) present very similar platform geometries. Side

column diameters span from 14 m to 15 m, while radii are located in a range even more restricted, from 44.5 m to 45 m. Drafts variability varies from 20 m to 25 m.

Mooring-related design variables, x_{anch} and L, are presented in Figure 101b. Due to the slack catenary constraints, the optimal systems identified during all the optimizations lie in a diagonal band of the domain of interest, which spans from 700 m to 880 m.

In conclusion, 2nd stage optimization results allow to significantly reduce the design space. 3rd stage SLS optimization is then performed in a restrain domain of variables which is presented by a shaded green region both in Figure 101a and 101b.

(a)   (b)

● 1st stage optimal ● 2nd stage optimals ● 2nd stage optimal configurations ▢ 3rd stage design space
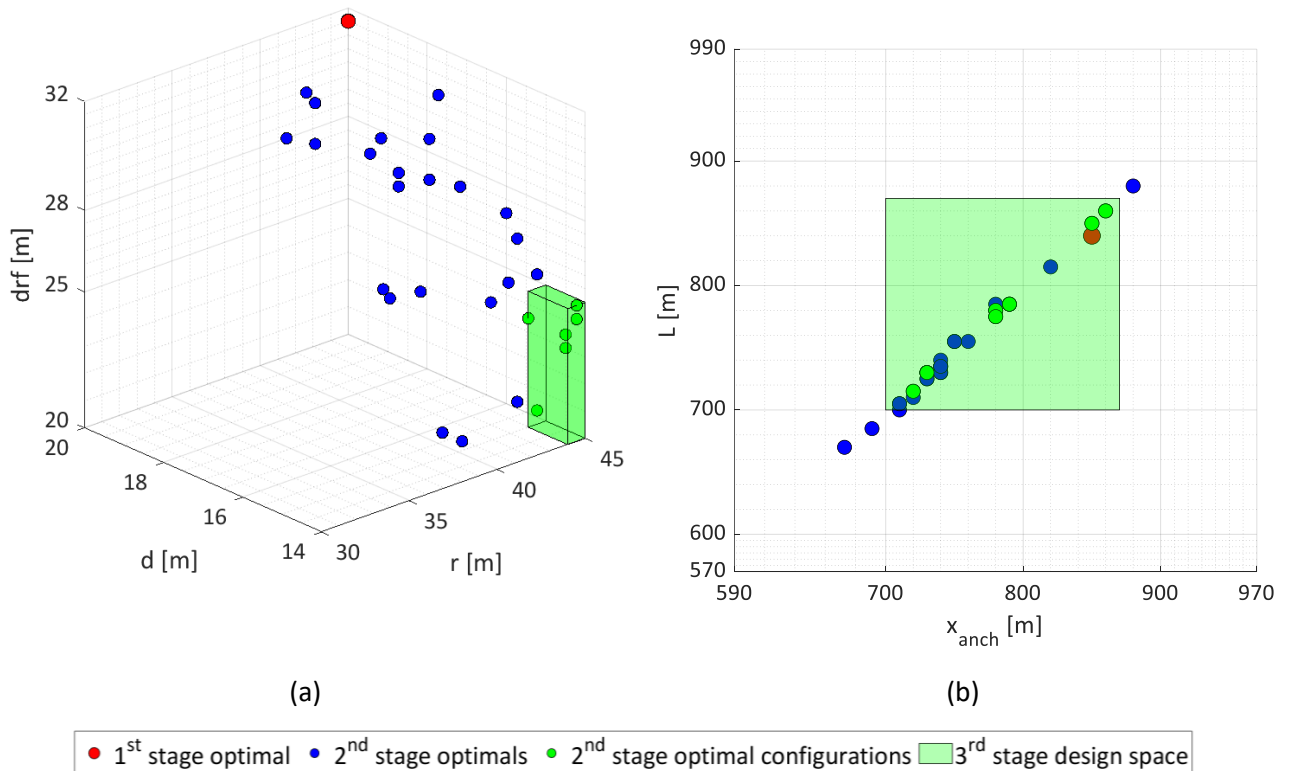
Figure 101: Comparisons of first- and second-stage optimizations results: platform geometry (a) and mooring system layout (b); the new design space, which is adopted in the third stage, is shaded in green.

The new design space is summarized in Table 33.

Table 33: Third-stage SLS fatigue optimization design space.

	Lower bound [m]	Upper bound [m]	Spacing [m]
d	14	15	0.5
r	44	45	0.5
drf	20	25	0.5
x_{anch}	730	860	10
L	x_{anch} -5	x_{anch}	5

Being the fatigue estimation the result of the accumulation of damages occurred under different load conditions, the simulation of a larger number of events is required. Therefore, the reduction of design variables achieved with the 2nd stage optimization was of primary importance for performing an efficient procedure in the 3rd stage. The number of individuals per generations is reduced to 20, while the rest of the setting are kept as in section 8.5.1. Figure 102 shows the cumulative damage (evaluated according to Eq. 8.18) at the tower base scored by the optimum system at each generation. As it is possible to observe, the trend of the objective function is decrescent, which means that, even in a restricted design variable space, there is still room for minimizing the total damage.
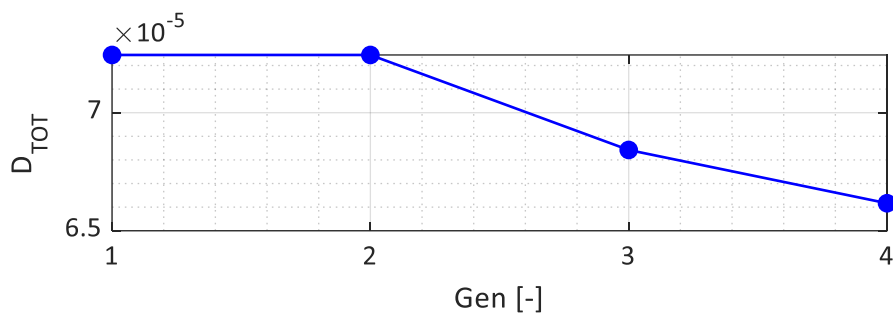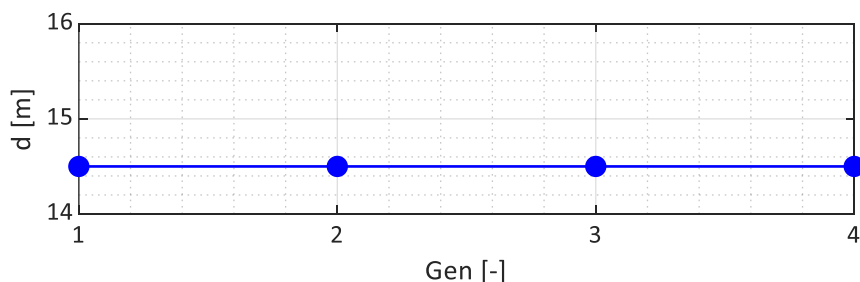

Figure 102: Tuscany site 3rd stage, single-objective SLS Fatigue optimization results: evolution of the cumulative damage during the optimization.

Figure 103 shows the evolution of the platform geometry during the optimization. As it possible to observe, both side column diameter (Figure 103a), d, and platform radius (Figure 103b), r, remain constant for all the four generations. Therefore, the reduction in the fatigue damage for the 3rd and 4th generation (see Figure 102) is not caused by these two variables. In particular, the optimal diameter, equal to 14.5m, is still oriented towards the lower bound of the design space, while the optimal radius is 44.5m, maintaining the average value of the new design space.

As far as it regards the platform draft (Figure 103c), drf, it remains constant at a value of 23.5m for the from 1st to 3rd generation, while it rises to 24m for 4th generation. Overall, larger drafts seem to affect positively the minimization of the fatigue damage since the optimal value is oriented towards the upper bound of the new design space. Moreover, this aspect is in contrast with the results of the 2nd stage optimization (see Table 32), where 4 of the 5 best configurations identified present lower drafts, from 20 m to 20.5 m.
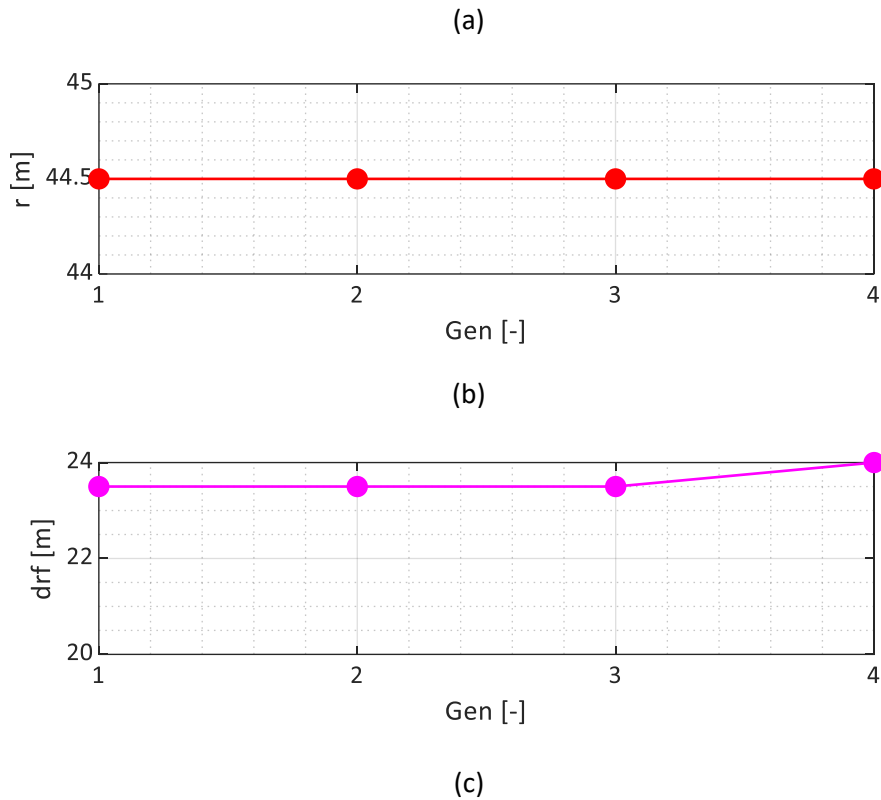
(a)

(b)

(c)

Figure 103: Tuscany site 3rd stage, single-objective SLS Fatigue optimization results: evolution of side column diameter (a), platform radius (b) and draft (c) during the optimization.

Although the increase of the draft at the 4th generation (see Figure 103c) clearly leads to a reduction of the fatigue damage (see 4th generation in Figure 102), platform geometrical variables seem not to have a prevalent effect in this optimization procedure.

Actually, the optimal mooring layout (Figure 104) dominantly affects the minimization of the fatigue loads. As already illustrated in section 8.5.2, results are plotted in terms of L_{HYP} (Figure 104a), L (Figure 104b) and the difference between L and L_{HYP} (Figure 104c). As it is possible to observe comparing Figure 102 to Figures 104a and 104b, both L_{HYP} and L trends during the optimization are similar to the Fatigue damage trends. Thus, the cable geometry significantly affects the reduction of the fatigue damage under the chosen load conditions. Overall, the optimal mooring layout is achieved with a distance from the anchor of 850m and a line length of 845 m, which is relatively larger, therefore more expensive, than the values scored by most of the 2nd stage configurations highlighted in Table 32. Furthermore, 3rd stage optimal mooring layout presents a smaller difference between L and L_{HYP} (see Figure 104c and Figure96c), therefore the cable for the 3rd stage optimization is tauter with respect to the ones of the 2nd stage.
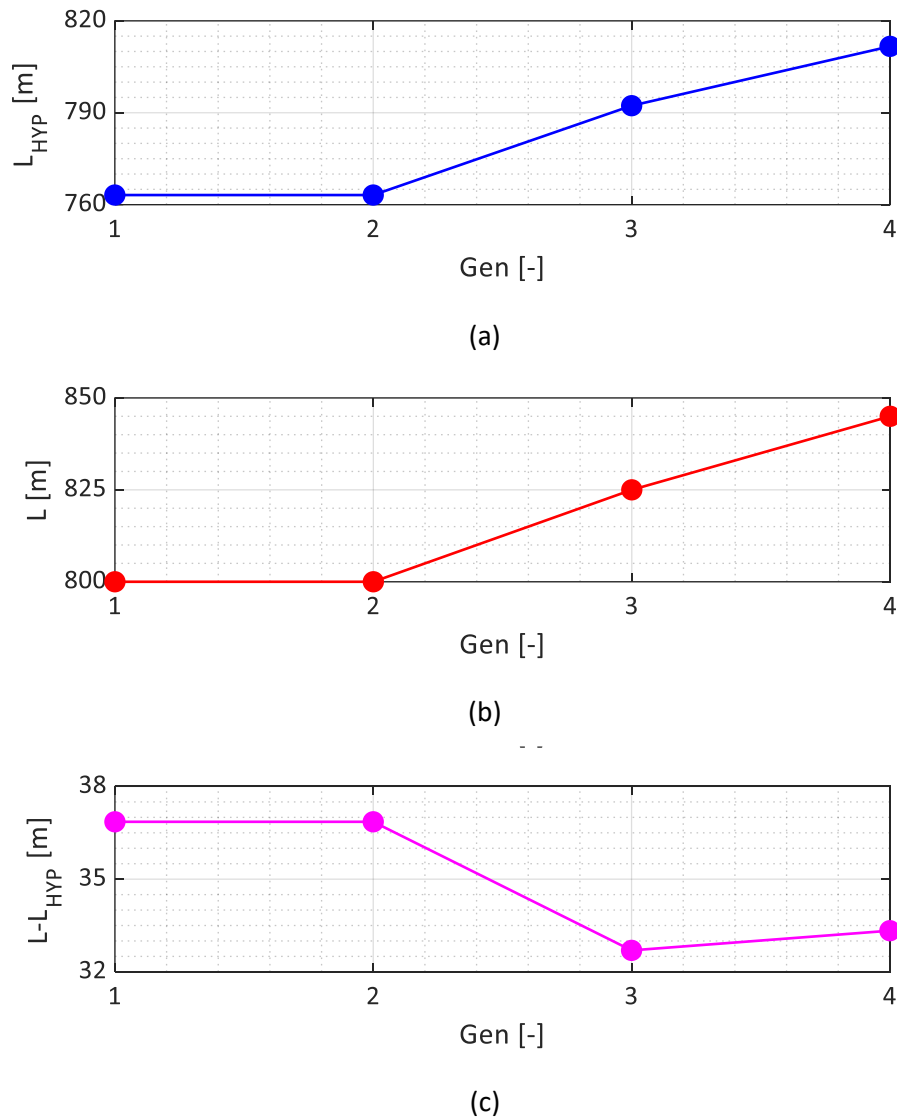
Figure 104: Tuscany site 3rd stage, single-objective SLS Fatigue optimization results, evolution of the mooring layout during the optimization: L_{HYP} (a), L (b) and the difference between L and L_{HYP} (c).

The 3rd stage optimal system is also analysed in terms of maximum tower base bending moment, average displacements at rated wind speed and substructure cost. All of these quantities are calculated under the 50-year return period ULS condition applied both to 1st and 2nd stage optimizations. Moreover, as far as it regards tower base bending moment and substructure costs, the same normalization presented in 2nd stage (see section 8.5.2, Eq. 8.22) is herein adopted.

The evolution of the maximum, normalized, tower base bending moment during the optimization is presented in Figure 105. As already noticed in the previous optimizations, this quantity is direct proportional with the rotation of the system, which, in the case of a FOWT supported by slack catenary moorings, is influenced mostly by the platform geometry. Since the three design variables d, r, and drf are almost constant during the optimization, the normalized bending moment does not vary, and it remains at

around 1.07. Due to the larger draft (equal to 24 m) the 3rd stage optimal system shows better performances than the 2nd stage best configurations (see section 8.5.2, Table 32), in terms of maximum tower base bending moment.
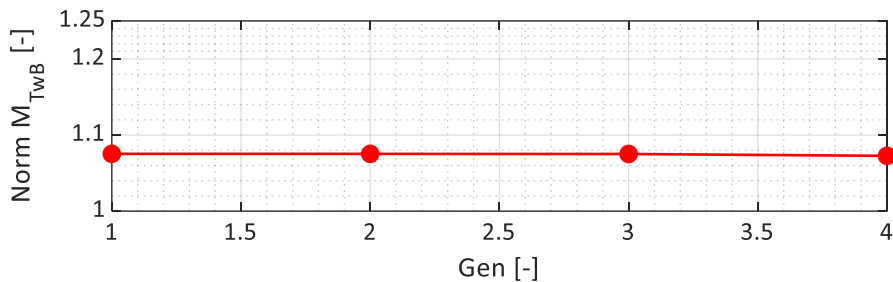

Figure 105: Tuscany site 3rd stage, single-objective SLS Fatigue optimization results: evolution of the normalized tower base bending moment during the optimization.

Normalized substructure cost is presented in Figure 106. A 40% reduction is noticeable with respect to the 1st stage optimized and the upscaled systems. Despite the larger draft and cable length with respect to the 2nd stage optimal configurations (see Figures 103c and 104b, Table 32) the 3rd stage optimized system presents an increase of about the 4% of the cost.
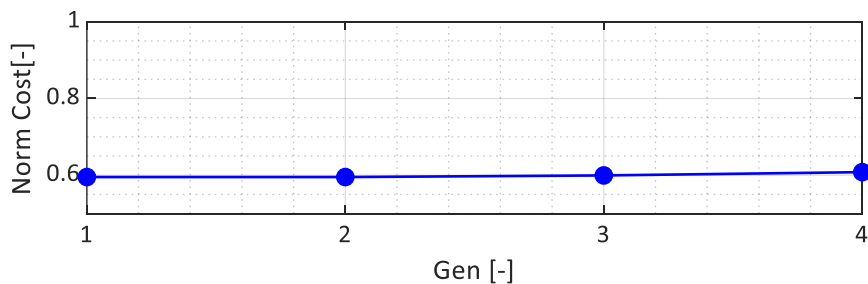

Figure 106: Tuscany site 3rd stage, single-objective SLS Fatigue optimization results: evolution of the normalized tower base bending moment during the optimization.

In the end, static displacements of the system in Surge and Pitch under rated wind speed are presented in Figure 107. As expected, the Surge pattern (see Figure 107a) follows the trends of the mooring-related design variables presented in Figure 105. The optimal systems identified during 1st and 2nd generations are characterized by a displacement of 25.30 m, then, from 3rd generation, the solution evolves towards tauter and longer cables (see Figure 105b and 105c) which increase the horizontal stiffness of the overall mooring system and reduce the static Surge to 21.30 m.

The Pitch rotation is presented in Figure 107b. All the optimal systems identified during the 4 generations shows a constant value of about 1.967°, which is larger than the results scored by the configurations chosen after 2nd stage optimization. Since the mean value of the Pitch rotation is shown to be related with the mean value of the tower base bending moment, the slight reduction of the normalized maximum bending moment, presented in Figure 105 with respect to the optimal configuration of 2nd stage

optimization (Table 32) (1.07 against 1.11), must have been caused by a decreasing of the standard deviation of the load process.
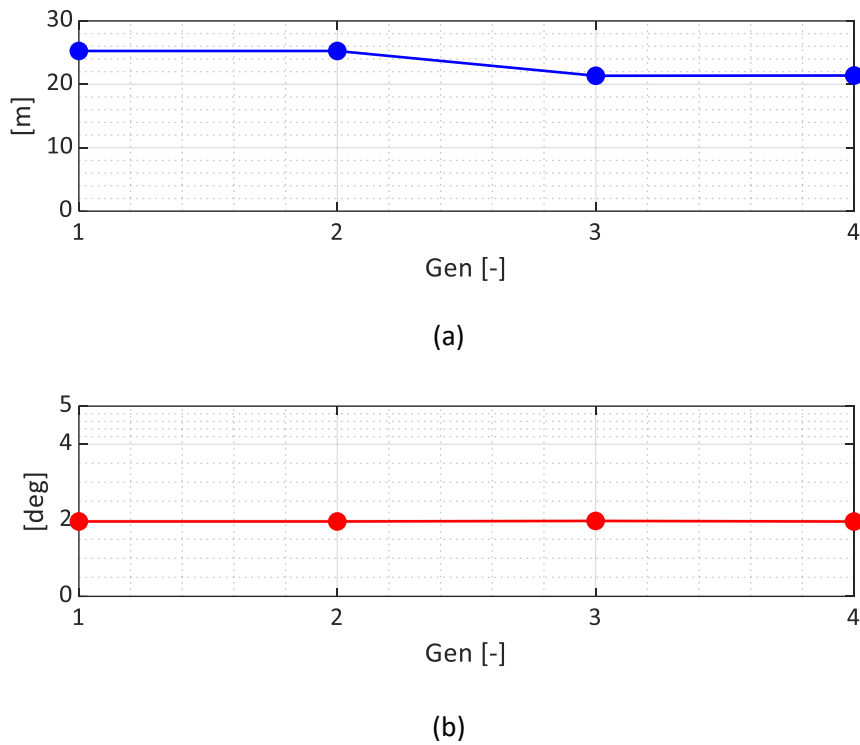

(a)

(b)

Figure 107: Tuscany site 3rd stage, single-objective SLS Fatigue optimization results: evolution of the maximum Surge (a) and Pitch (b) during the optimization

In conclusion, the optimal platform geometry for fatigue damage mitigation is achieved with a side column diameter equal to 14.5m, platform radius and draft of 44.5 m and 24 m, respectively; while the mooring layout is characterized by an anchor distance x_{anch} equal to 850 m and a unstretched cable length, L, of 845 m. 3rd stage optimization results are summarize in Table 34. Figure 108 presents shows the optimal platform geometry (Figure 108a) and the mooring layout (Figure 108b) at rest (dashed line) and under the rated wind speed condition (solid line).

Table 34: Second-stage multi- objective optimization results

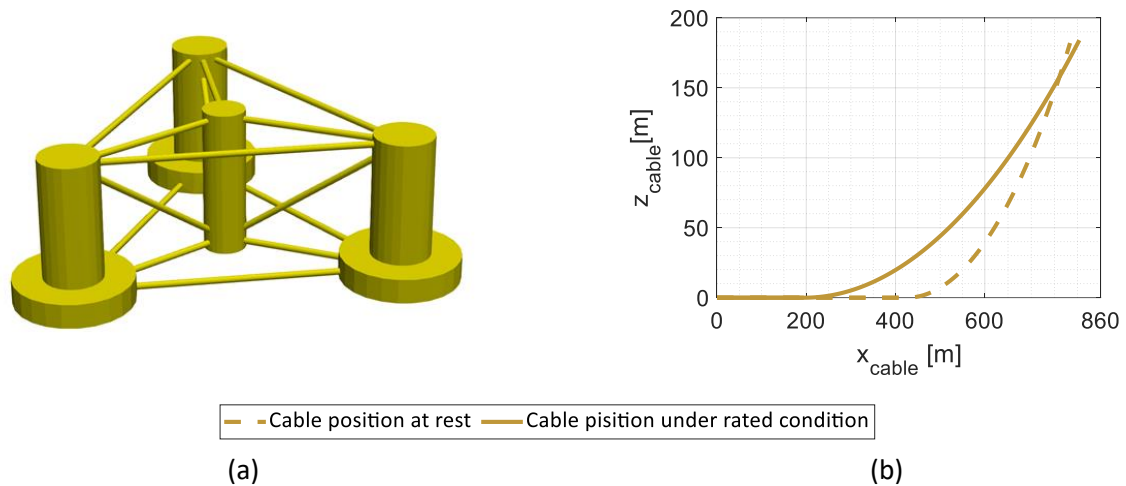| d	r	drf	x_{anch}	L	Norm M_{Twb}	Norm Cost	Surge	Pitch
[m]	[m]	[m]	[m]	[m]	[-]	[-]	[m]	[m]
14.5	44.5	24	850	845	1.073	0.608	21.39	1.967

Figure 108: Optimal system after the 3rd stage optimization: platform geometry (a); cable layout (b) at rest and under rated condition.

8.5.4 Comparison of the results

In this section, the results of the three stages of optimizations are compared and summarized. The First optimization aimed at finding the substructure with a lower cost but better structural performances with respect to the upscaled one. The maximum Tower-base bending moment was chosen as objective function. As expected, the optimal solution was found maximizing the platform dimensions. Such floater was very similar to the one achieved minimizing the Peak of the Pitch RAO (see Chapter 6) in terms of side column diameter and platform radius. These two design variables was found to influence the rotational stiffness of the system and to be very important for the reduction of the mean values of the stresses. However, for the minimization of the dynamic part of the stresses, i.e., the standard deviation of the Tower-base bending moment, a large draft was found to be effective.

Then, the second optimization is targeted to *jointly* minimize the stresses at the turbine base and the costs, normalized with respect to the results scored by the previous stage. The optimal concepts were found to lie in a restricted region of the design space, and to reduces the costs of around the 45% with a controlled increase of the stresses below the 15%. This was achieved reducing the column diameter and the draft, the two design variables which mostly influence the platform costs. Nevertheless, as discussed in section 6.4.1, slender platforms presented better dynamic performances in power production with respect to bluffer solutions. On all considered, the optimized floater for the 2nd stage optimization was the result of contrasting targets: on one hand, the minimization of the costs led to reduced column diameter and drafts, on the other hand the minimization of the tower-base bending moment, led to a larger radius, small columns and drafts between 20m and 24m, balancing the increase of the mean values of the stresses with a reduction of their dynamic part.

Finally, the 3rd stage optimization, aimed at minimizing the fatigue damage under a set of design load conditions, was carried out on a restricted design variable space. The optimal solution, presented in Table 34, shows common features not only with 1st and 2nd stage optimizations but also with the results presented in sections 6.4.1 and 6.4.2:

- Very small column diameter, which reduces the costs but tends to decrease the dynamic part of the stresses;
- Large platform radius, which has a little influence of the costs compared to other design variables but is crucial for the reduction of the mean pitch rotation and mean bending moment at the tower base;
- Intermediate draft, equal to 24 m, which tends to increase costs but plays an important role in controlling both the mean and the standard deviation of the stresses at the tower base.

Nevertheless, it was found that tauter moorings are fundamental in the reduction of the fatigue loads. For this particular case, where a constraint on the portion on the line resting on the seabed is applied, to achieve higher stiffness and therefore tension, the cable evolves towards a solution with small sag and larger footprint. The Tuscany-site optimization procedure workflow is summarized in Figure 109.
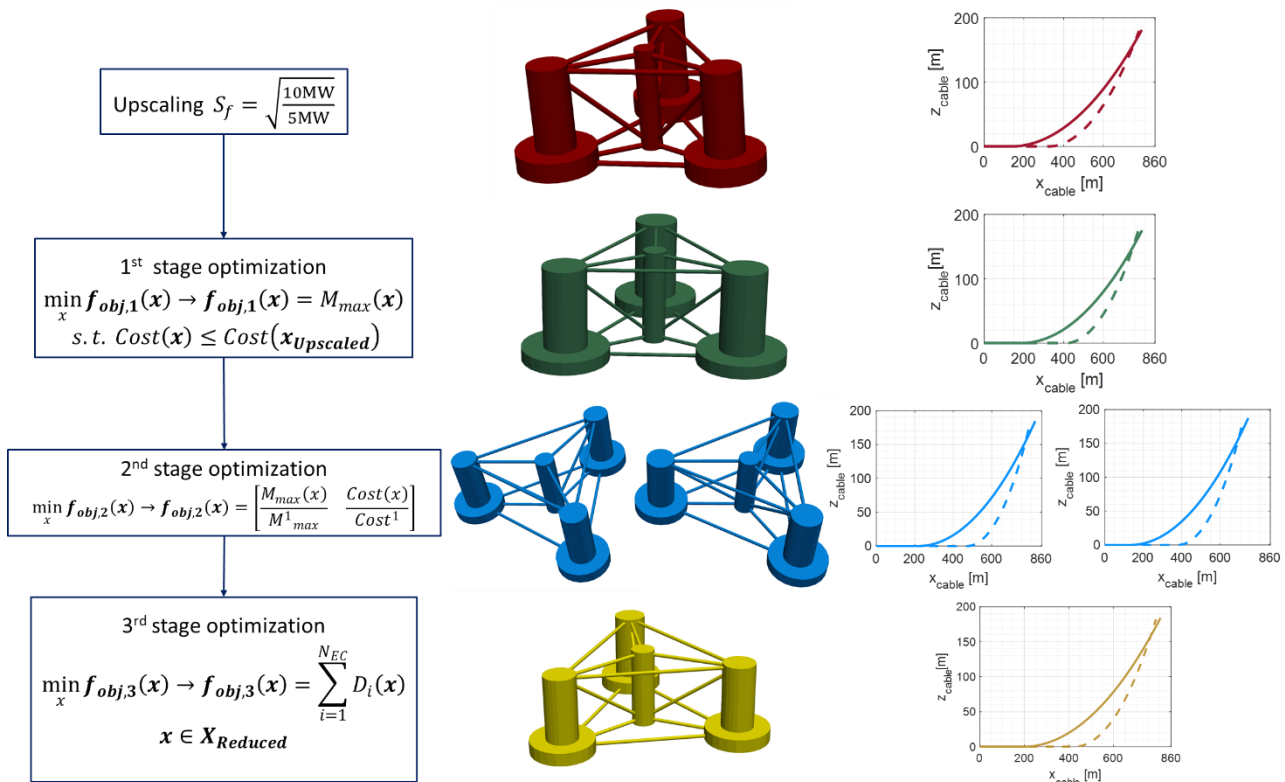

Figure 109: Optimization procedure workflow and results for the Tuscany site.

8.6 Sardinia site optimization

In this section, the 3-stage optimization procedure is applied to the Sardinia site. The upscaled FOWT mooring system is changed due to the change in water depth and anchors. Catenary cables are now made of steel wire (see Table 22), their length is updated to 1205 m, so that the stiffness in the surge direction of the system is kept almost unchanged, while the distance of the anchor from the platform centreline, x_{anch}, to 1180m. The fairlead position is maintained fixed.

8.6.1 First-stage single-objective optimization

The first stage considers ULS conditions presented in Table 28 (see section 8.3.3). For the same reason discussed in Section 8.5.1, the single-objective optimization is performed considering the event $U_{hub} = 11\,m/s$, $H_s = 5.47m$ and $T_p = 9.15m$. The maximum tower-base bending moment, calculated following Eq.8.21, is set as target to be minimized. The same constraints described in section 6.2 and 6.3. desing variables space is changed with respect to section 8.5.1 accoding to Table 29. The same set up of the GA are considered (see Table 30).

GA optimization results are presented form Figure 105 to Figure 91. Figure 110 shows the mean value (blue line) and the maximum value (red line) of the tower base bending moment scored by the optimum system at each generation, while the black solid line refers to the maximum value calculated performing the analysis of the upscaled platform. As it is possible to observe, all the optimized solutions achieve a lower bending moment with respect to the upscaled system, without increase the cost. The distance between the maximum value and the mean value of the bending moment remains almost constant from 1st to 4th generation, denoting that the dynamic behaviour of the optimal solutions is similar.
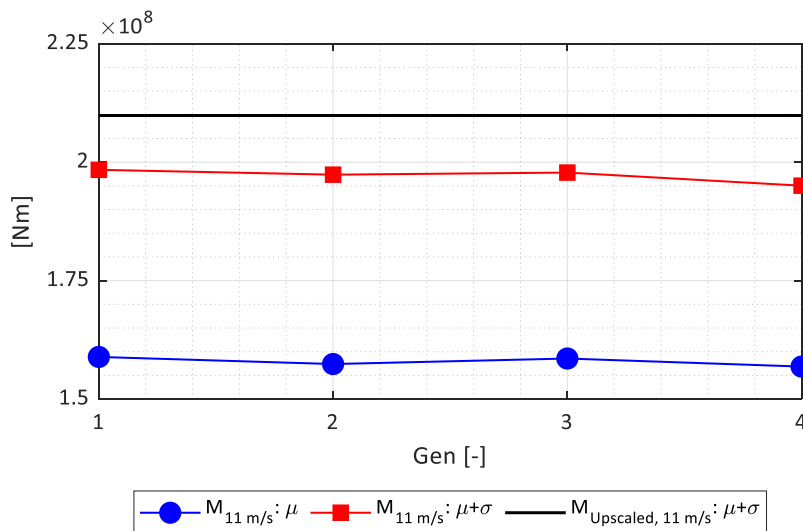

Figure 110: Sardinia site single-objective ULS optimization results: evolution of tower base bending moment during the optimization.

Mean values of the displacements of the optimal systems are presented in Figure 111. Blue line shows the Surge DoF, while red line refers to the Pitch DoF. As can be seen, the optimal solution scores the minimum Pitch rotation among all the generations and a large Surge displacement, equal to 0.79° and 28.94m, respectively.
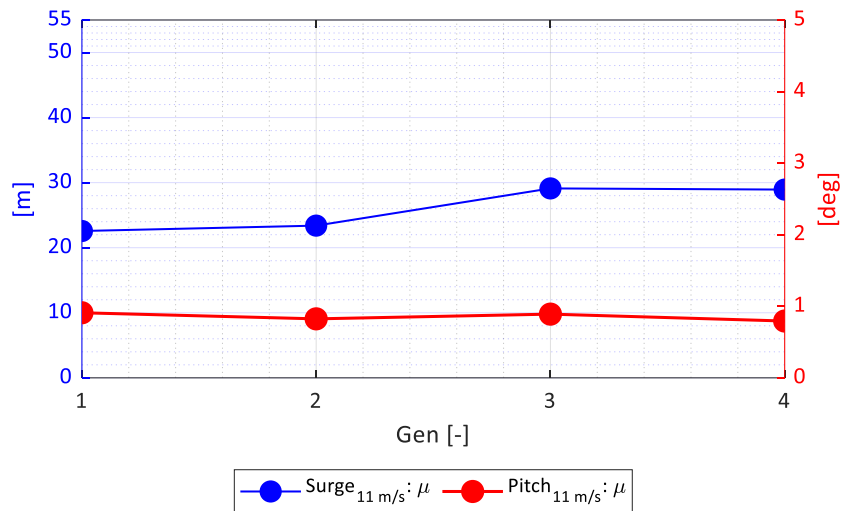

Figure 111: Sardinia site single-objective ULS optimization results: evolution of the mean displacement in Surge (blue line) and Pitch (red line) during the optimization.

As already done for the Tuscany site, the evolution of the design variables is shown to identify the main aspects which lead to the minimization of the tower-base loads for the Sardinia site. Platform and mooring geometry are presented in Figure 112. The optimal after each generation presents the same value of the column diameter (Figure 112a), 20m, which agrees with the results obtained for the Tuscany site. As far as it regards the platform radius (Figure 112b), it exhibits variations, oscillating from 41.5m (1st generation) to 45m (4th generation), which, as discussed in section 8.5.1, are proportional to the changing in the bending moments (blue and red line) shown in Figure 110. The Optimal solution scores also the maximum draft, equal to 32m. Overall the floater which minimizes the tower-base bending moment under extreme load condition is the one which maximizes the three design variables related to the platform geometry.

Focusing the attention on the optimal mooring layout, Figure 112d, and considering the difference between L and L$_{HYP}$, this appears not to be proportional to the mean surge displacement (Figure 111). Actually, the *tauter* cable at rest appears to be the optimal of the 2nd generation, which is not the ones which scores the minimum Surge displacement (Figure 111). In this case, the minimization of the Surge displacement is not only related to the level of tension at rest of the catenaries.

In fact, also their layout plays a primary role, in the sense that a mooring line with a small footprint, i.e., x$_{anch}$, exposed to a motion in the horizontal direction, will tend to become tauter *sooner* that the ones with larger footprints. This results in an increase of the axial deformations and therefore of the tensions, leading to a reduction of the surge displacement.

Such an effect was not noticed in the optimization of the Tuscany site since chains present reduced elastic stiffness and larger weight compared to steel wire ropes. Together with the constraints of the portion of the line resting on the seabed this maintain the geometric part of the cable stiffness always dominant with respect to the elastic stiffness. As can be seen in Figure 112d, 1st generation cables present a smaller footprint and Surge (Figure 111) with respect to the others.

In conclusion, the mooring layout of the optimal system is characterized by a distance from the platform centerline, x_{anch}, of 800m and a cable length, L, of 840m.
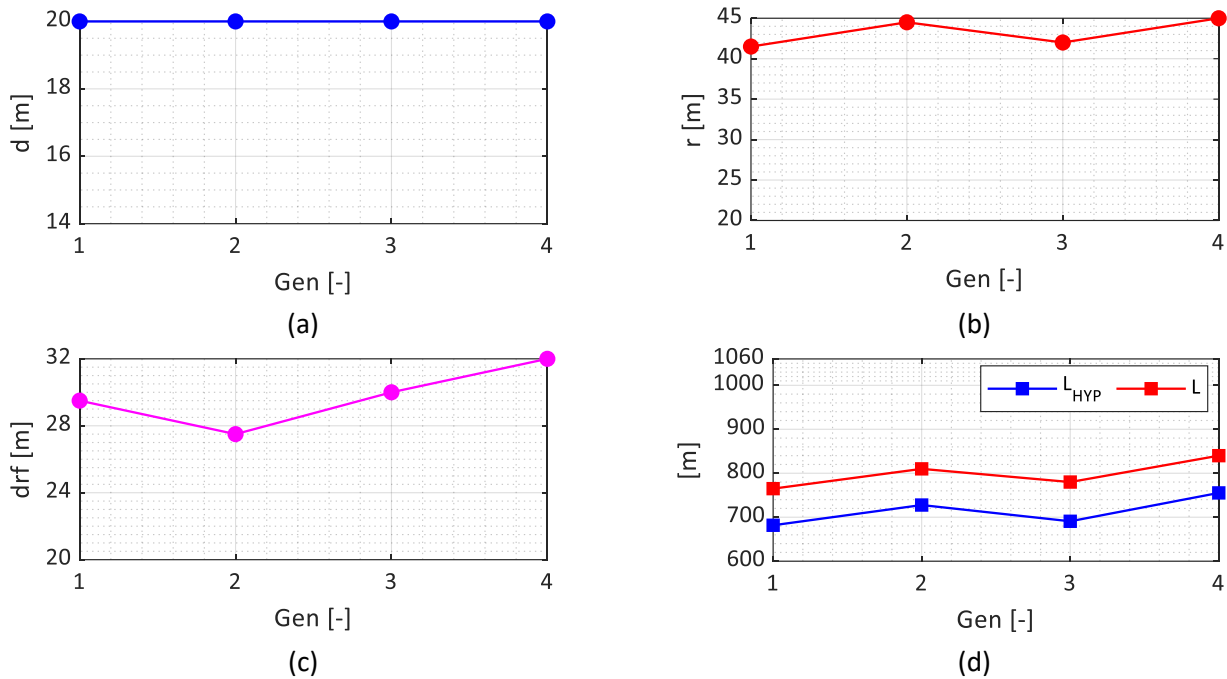

Figure 112: Sardinia site single-objective ULS optimization results: evolution of side column diameter (a), platform radius (b), draft (c) and mooring system layout (d) during the optimization.

Finally, the evolution of the costs is presented in Figure 113. These are evaluated according to Eq. 8.6 considering suction piles anchors. The optimal substructures value (red line) is compared with the one of the upscaled system (black line), which was set as constraint. As can be seen, in agreement with the results for the Tuscany site, the minimization of the tower stresses calls for the increase of the substructure cost, which tends to the constraint value. The optimal concept scores a final cost of 7.879e+06 €, which is 96.73% the upscaled one.
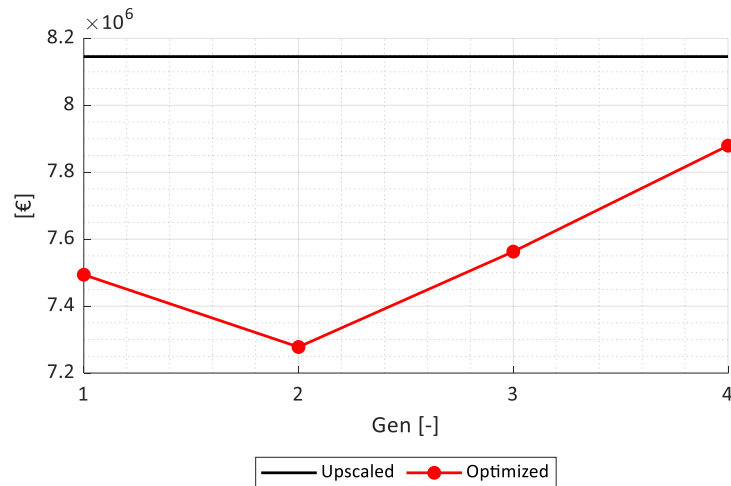
Figure 113: Sardinia site single-objective ULS optimization results: evolution of the substructure during the optimization.

Table 35 summarizes the results of the first stage optimization for the Sardinia site. The comparison between the optimal system (green) and the upscaled one (red) is presented in Figure 114. Top view and lateral views of the two platform concepts are shown in Figure 114a and Figure 114b. Figures 114c and 114d show the layout of the most stressed mooring, with respect to the cable reference frame (the origin is at the anchor point, z-axis positive upwards and x-axis pointing in the direction of the platform), of the optimal and the upscaled solutions, respectively. Dashed lines refer to the position at rest of the catenaries, while solid lines to the shifted position, obtained imposing the mean values of the maximum displacements. In both cases, the portion of the lines resting on the seabed is shown in black, while the suspended portion are plotted accordingly to the colours of Figures 114a and 114b. As can be seen, the mooring lines at rated wind speed are completely suspended, this leads to uplift forces at the suction piles, which are passed to the seabed mostly by friction on the lateral surface of the anchors. The optimal system shows *slacker* moorings at rest (Figure 114c). Moreover, their smaller footprint (x_{anch}) increase the angle of the tension at the fairlead, reducing the horizontal component of the tension and therefore the stiffness in the Surge direction. This results in larger motions but also in a shifted cable with a smaller sag compared to the upscaled one (Figure 114d).

Table 35: ULS single objective optimization results.

d	r	drf	x_{anch}	L	M11m/s: μ+σ	Surge	Pitch	Cost
[m]	[m]	[m]	[m]	[m]	[Nm]	[m]	[m]	[€]
20	45	32	800	840	1.9503e+08	28.94	0.7938	7.8794e+06

(a)   (b)

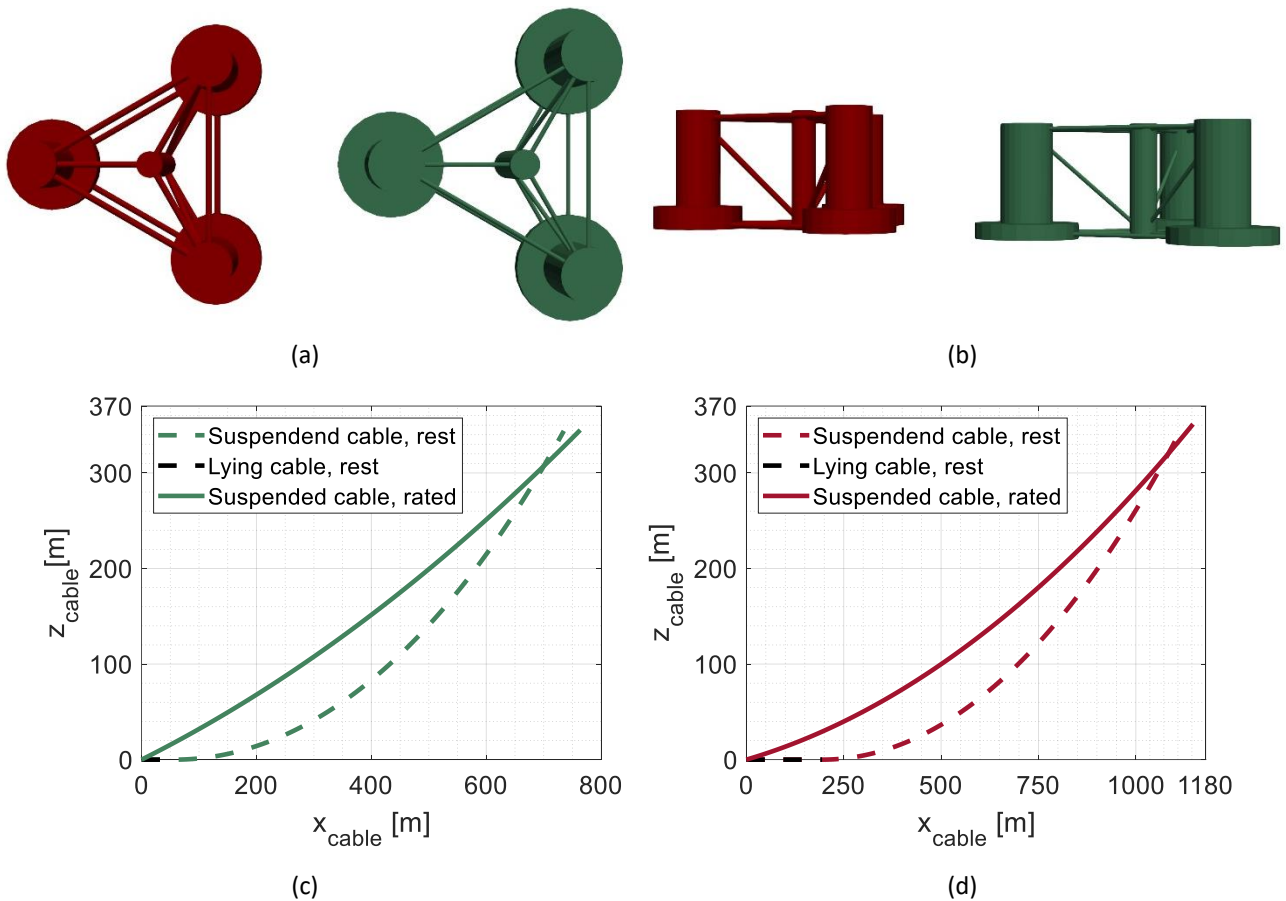(c)   (d)

Figure 114: Sardinia site single-objective ULS optimization results: evolution of the substructure during the optimization.

8.6.2 Second-stage multi-objective optimization

As already discussen in section 8.5.2, the second stage optimization for the Sardinia site is performed considering a multi-objective procedure which involves the tower-base bending moment and the substructure costs as target to be *jointly* minimized. They are normalized as presented in Eq. 8.22, by the results of the first-stage optimization, i.e. 1.9503e+08 Nm and 7.8794e+06€. Being the first objective function normalized by a quantity which have been minimized in the previous optimization, it is expected to be always above 1. This second stage is intended to find a floating configuration which significantly reduces the cost, without increasing excessively the loads on the turbine tower.

The optimization is performed with MATLAB GA algorithm. 3 generations of 200 individuals are considered. Cross over fraction is set to 80%. 41 optimal candidates have been identified. Figure 115 presents the Pareto front, i.e. the results of the multi-objective optimization in the objective function space $\left(f_{obj,1}(x), f_{obj,2}(x) \right)$. X-axis refers to the normalized bending moment, while y-axis refers to the normalized cost of the substructure. As can be seen, the two objective functions are contrasting targets. However, individuals which scores significant cost reductions with a controlled increase of the turbine maximum load are found.
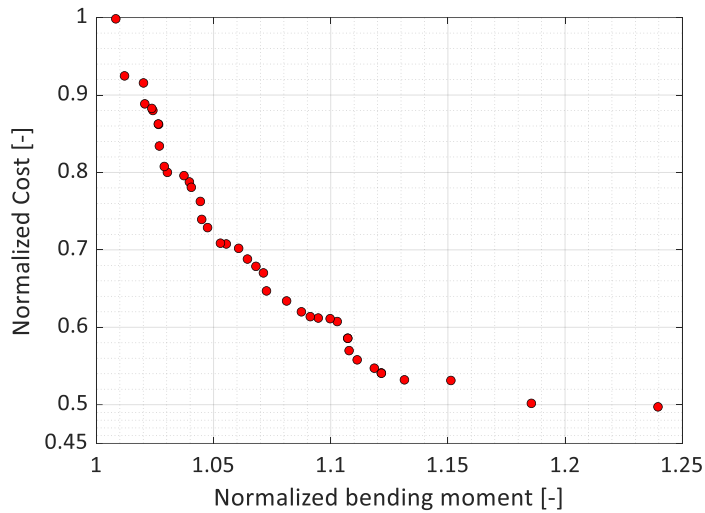
189

Figure 115: Sardinia Second stage multi-objective optimization results: Pareto front.

Figure 116 shows the results progressively from 1 to 41. Eight optimal concepts are found to effectively reduce the substructure costs (Figure 116b) with a reduced increase of the tower loads (Figure 116a). These are highlighted in the following Figures with black lines and circles. The 6th configuration minimizes the costs, consequently, it maximises the bending moment, scoring an increase of 24% with respect to the 1st stage optimized solution (Table 35). Due to such increment, this solution is discarded.
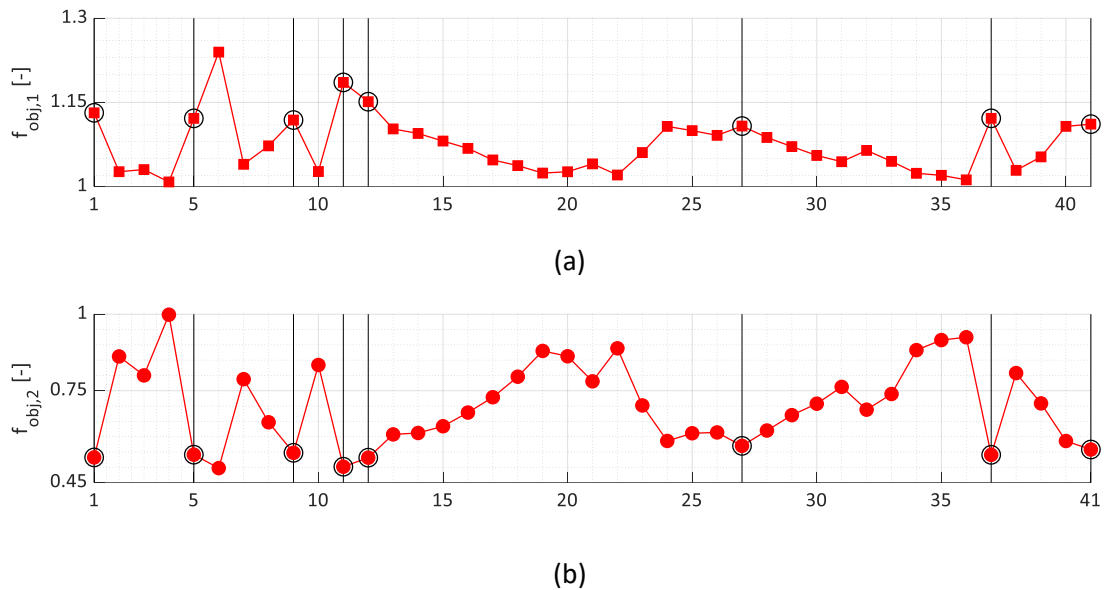

(a)

(b)

Figure 116: Sardinia site, second stage multi-objective optimization results: Normalized bending moment (a) and Normalized cost (b).

The platform dimensions of the 41 optimal systems are presented in Figure 117. As already noticed in section 8.5.2, the side column diameter (Figure 117a) shows a large variation. If the attention is focused on the eight best configurations, they score values which are included between 14m and 15.5m. On the

contrary, the 41 configurations present large platform radius (red line in Figure 117b), r. the group of the eight optimal systems score radii which span from 41.5m to 45m.

Similarly to Figure 114a, platform drafts (Figure 117c) vary from the lower bound, 20m, to the upper bound 32m, but the eight configurations identified present values from 20.5m to 24.5m.

On all considered, the main features which reduces the costs are found to be the side column diameter and the draft, while the platform radius is found to be the variable which balance the increase of the tower base bending moment.
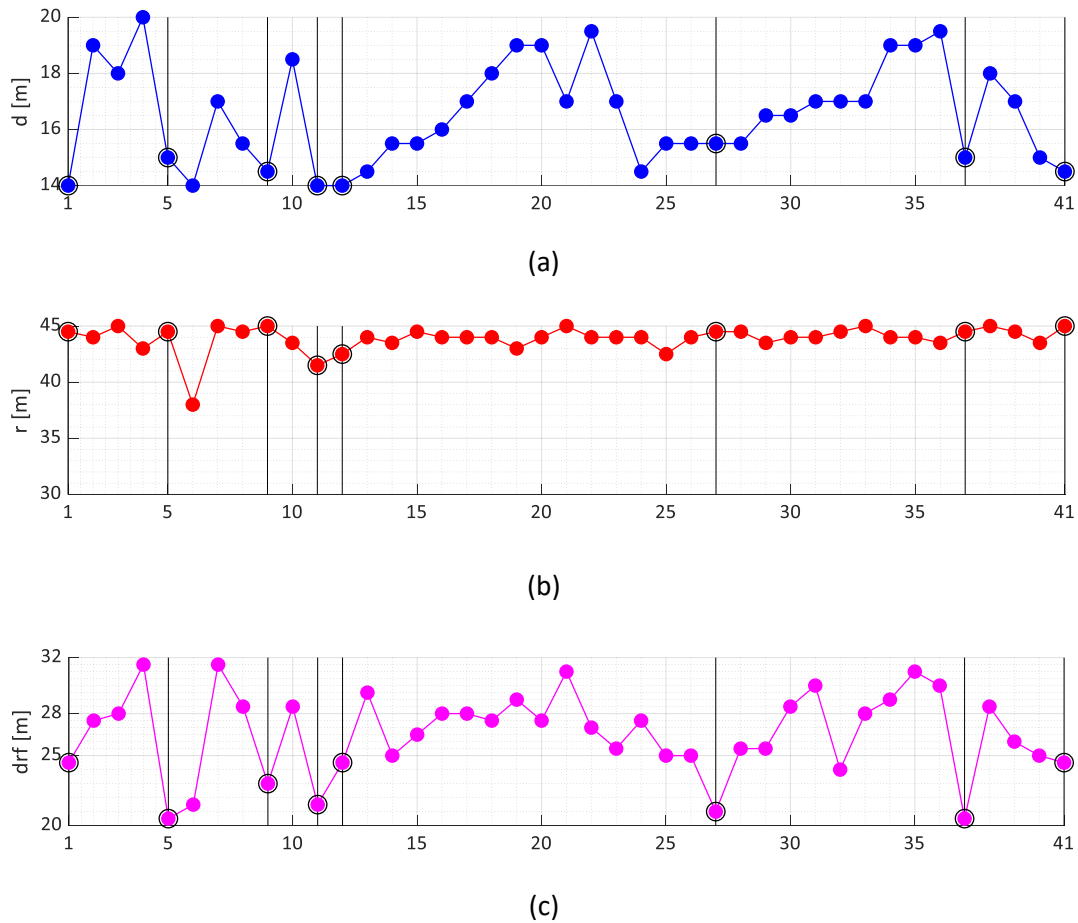

(a)

(b)

(c)

Figure 117: Sardinia site, second stage multi-objective optimization results: optimal side column diameters (a), platform radii (b) and drafts (c).

Mooring lines characteristics of the optimal concepts are presented in Figure 118. L_{HYP} (blue line) is plotted in Figure 115a, while the unstretched cable length (red line), L, is shown in Figure 118b. Overall, these two curves have similar trends. As expected by catenary moorings, L_{HYP} is always smaller than L. Configuration 4 presents the largest L and L_{HYP} values (1010m and 923.63m, respectively), while the lowest ones are achieved by Configuration 8 (745m and 664.15m, respectively). Both concepts do not belong to the eight optimal since they have heavy platforms (see Figure 117), presenting values of the cost function equal to 0.998 and 0.788, respectively. The eight configurations shows intermediate values of L, between 855m and 950m, and L_{HYP}, between 773m to 870m.

To have a better understanding on the mooring system mechanical properties, the difference between L and L_{HYP} is shown in Figure 118c. The maximum and minimum are obtained by Configuration 34 (equal to 104.7m) and Configuration 41 (equal to 78.14m), which is one of the eight best concepts. In conclusion, the optimal configurations score intermediate values which spans from 78m to 89m.
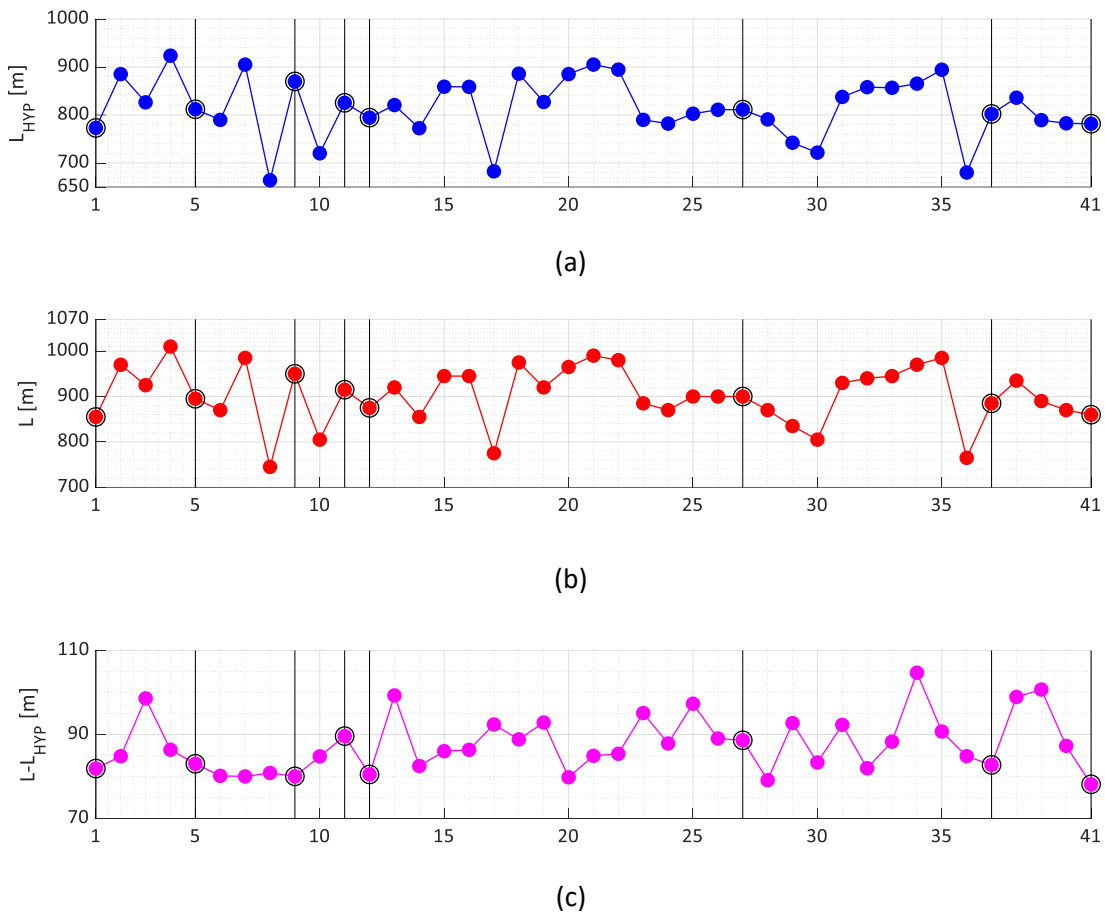

(a)

(b)

(c)

Figure 118: Second stage multi-objective optimization results: L_{HYP} (a), cable unstretched length, L, (b) and difference between L and L_{HYP} (c).

Mean displacement of the optimal systems in Surge and Pitch are presented in Figure 119. Surge DoF results are plotted in Figure 119a. Due to the larger water depth, the displacement of the 41 individuals identified is higher with respect to the ones of the Tuscany site (Figure 97). All the configurations presents large horizontal displacements under rated wind speed, which confirms the results obtained in the first-stage optimization (Figure 111). Also, It presents a very similar trend to L-L_{HYP} curve (Figure 118c) as expected. The maximum value of the Surge motion is scored by Configuration 34 (equal to 54.15m) which is also the one which presents the *slacker* cables, i.e., the maximum value of L-L_{HYP} in Figure 118c). the optimal concepts presents Surge displacements which varies from 22.13m for Configuration 41, to 36.10m for Configuration 11.

The mean value of the Pitch motion is plotted in Figure 116b. By comparing with Figure 117b, the inverse relationship with the platform radius is again noticeable. The 41 individuals presents mean rotations higher

than the optimal system identified in the 1st stage (Table 35). The maximum value is scored by Configuration 6 (equal to 3.16°), which is the one with the largest value of the Bending moment (see Figure 116a); while the minimum is achieved by Configuration 4 (equal to 0.90°), very similar to the optimized concept of the 1st stage. The best configurations show mean Pitch rotation between 1.76° and 2.55°.
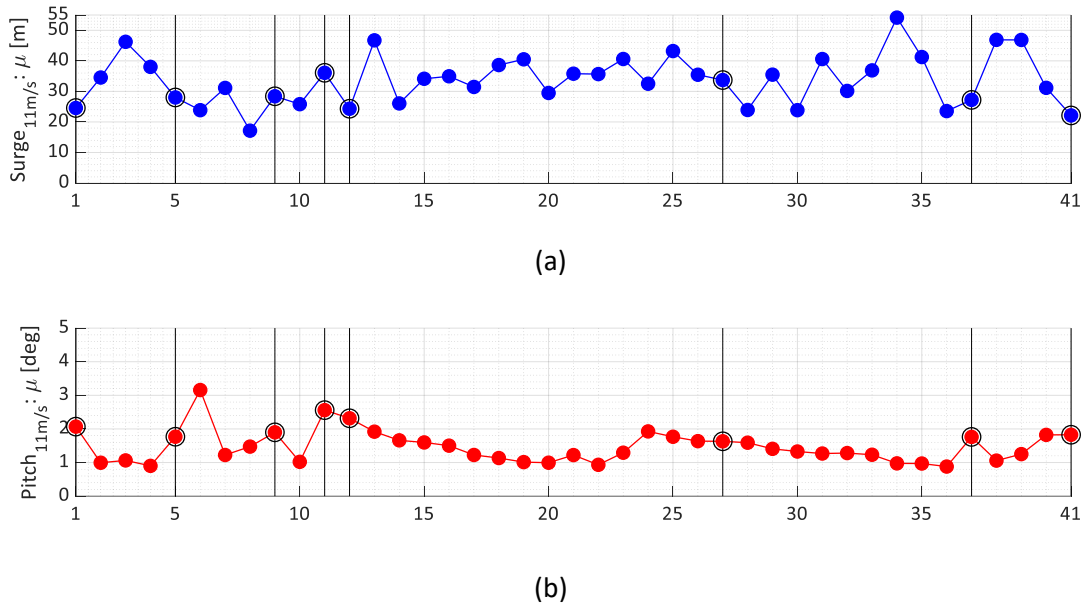

(a)

(b)

Figure 119: Sardinia, second stage multi-objective optimization results: Surge (a) and Pitch (b) mean displacements.

In the end, the cost of the optimal systems are compared in Figure 120 with the costs of the bending moment optimized (section 8.5.1) solution. The best configurations presents very similar results, spanning from 3.96e+06 € to 4.49e+06 €: these limit values are achieved by Configuration 11 and Configuration 27, respectively, which present the lightest and the heaviest platforms in terms of side column diameter and radius among the eight optimal systems. As it is possible to observe, the reduction of the substructure cost can be quantified in more than 3.5 million of euro.
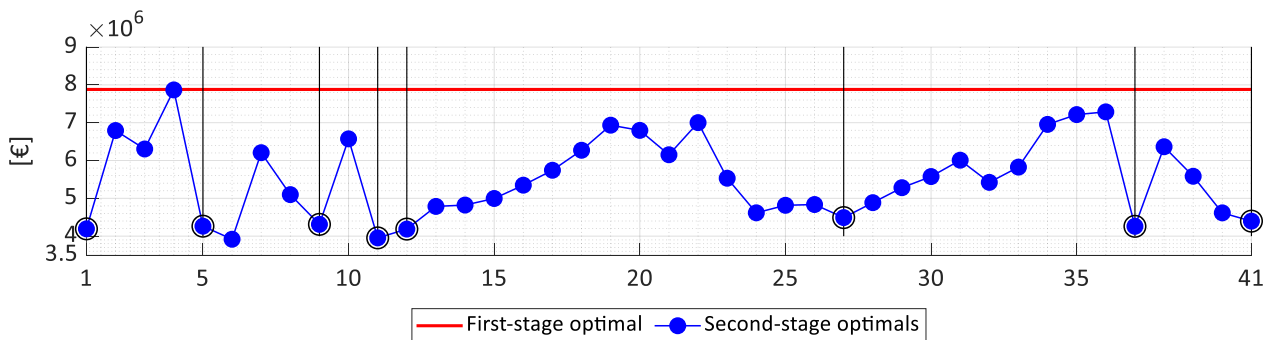

Figure 120: Sardinia, second stage multi-objective optimization results: Substructure cost.

The results related to the eight configurations identified in the 2nd stage multi-objective optimization are summarized in Table 36 and Figure 121. As can be seen, side column diameter and draft of the optimal concepts belong to an interval similar to the one identified for the Tuscany site (see section 8.5.2), while

the platform radius presents a large interval due to Configurations 11 and 12 (4th and 5th row in Table 36). These two have been added for their great reduction of the substructure costs, at the expense of an increase of the bending moment by more than the 15% with respect to the 1st stage optimized system. For this reason, they are not going to be considered in the definition of the new design space for the 3rd stage optimization.

Table 36: Secund-stage multi- objective optimization results.

ID	d	r	drf	x_{anch}	L	$f_{obj,1}$	$f_{obj,2}$	Surge	Pitch	Cost
[-]	[m]	[m]	[m]	[m]	[m]	[-]	[-]	[m]	[deg]	[€]
1	14	44.5	24.5	810	855	1.131	0.532	24.57	2.07	4.193E+06
5	15	44.5	20.5	850	895	1.122	0.541	28.01	1.77	4.263E+06
9	14.5	45	23	910	950	1.119	0.547	28.40	1.90	4.311E+06
11	14	41.5	21.5	860	915	1.186	0.502	36.08	2.56	3.953E+06
12	14	42.5	24.5	830	875	1.151	0.531	24.32	2.32	4.186E+06
27	15.5	44.5	21	850	900	1.108	0.570	33.71	1.63	4.490E+06
37	15	44.5	20.5	840	885	1.122	0.541	27.22	1.76	4.260E+06
41	14.5	45	24.5	820	860	1.111	0.558	22.13	1.83	4.396E+06

Upscaled   1st stage optimized   2nd stage optimized configurations
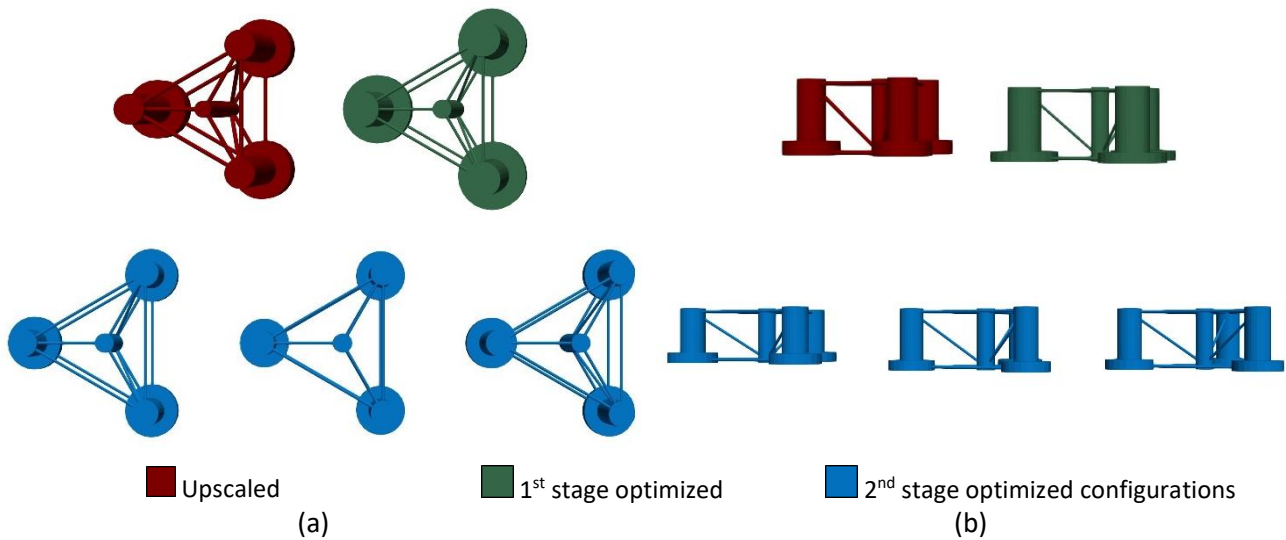
(a)   (b)

Figure 121: Comparison of the most significant optimal configurations after 2nd stage optimization; configuration IDs presented from left to right: n° 5, n° 1 and n° 9.

The mooring lines of the most significant 2nd stage optimized systems are presented in Figure 122. Configuration 5 (Figure 122a) and 1 (Figure 122b) present very similar cable shapes, even if the first one is 40m longer. Configuration 9 (Figure 121c) lines have a larger footprint with respect to the others.
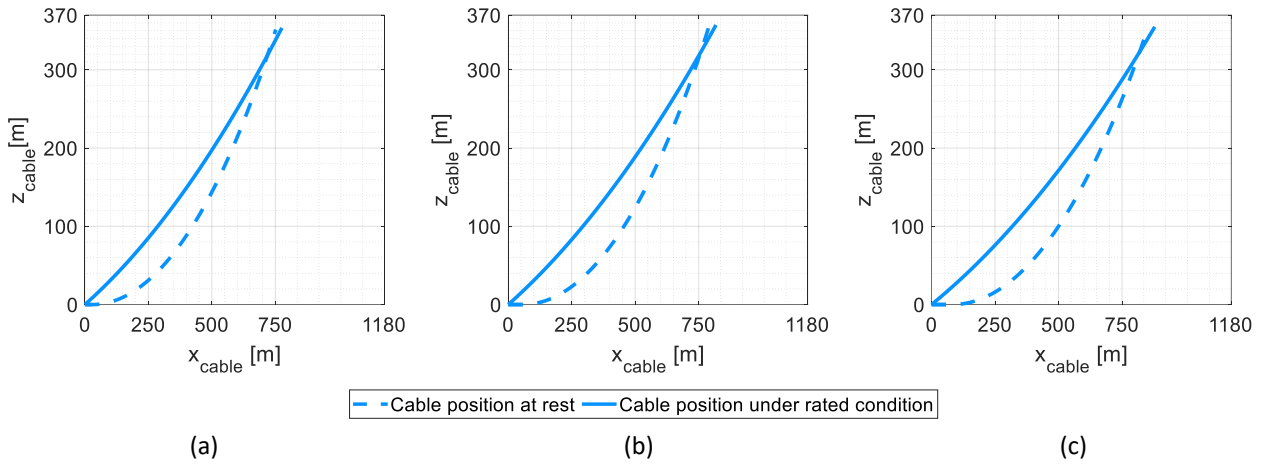
Figure 122: Comparison of the most significant mooring systems after 2nd stage optimization; configuration IDs presented from left to right: n° 5 (a), n° 1 (b) and n° 9 (c).

8.6.3   Third stage SLS Fatigue optimization

As already notice for the Tuscany site (section 8.5.3), the optimal configurations lie in a restricted region of the design space. Figure 123 compares the results obtained from the two optimizations. The optimal configuration obtained from the 1st stage optimization is plotted with a red dot, while all the 41 individuals found from the 2nd stage are represented with blue dots. The eight optimal configurations identified in Table 36, are shown with green dots. Platform geometries are presented in Figure 123a. As it is possible to observe, the seven optimal configurations (green dots) present very similar platform geometries. Side column diameters span from 14 m to 15.5 m, while radii are located in a range even more restricted, from 44 m to 45 m. Drafts variability varies from 20 m to 25 m.

Mooring-related design variables, x_{anch} and L, are presented in Figure 123b. Due to the slack catenary constraints, the optimal systems identified during all the optimizations lie in a diagonal band of the domain of interest, which spans from 810 m to 910 m.

In conclusion, 2nd stage optimization results allow to significantly reduce the design space. 3rd stage SLS optimization is then performed in a restrain domain of variables which is presented by a shaded green region both in Figure 123a and 123b.
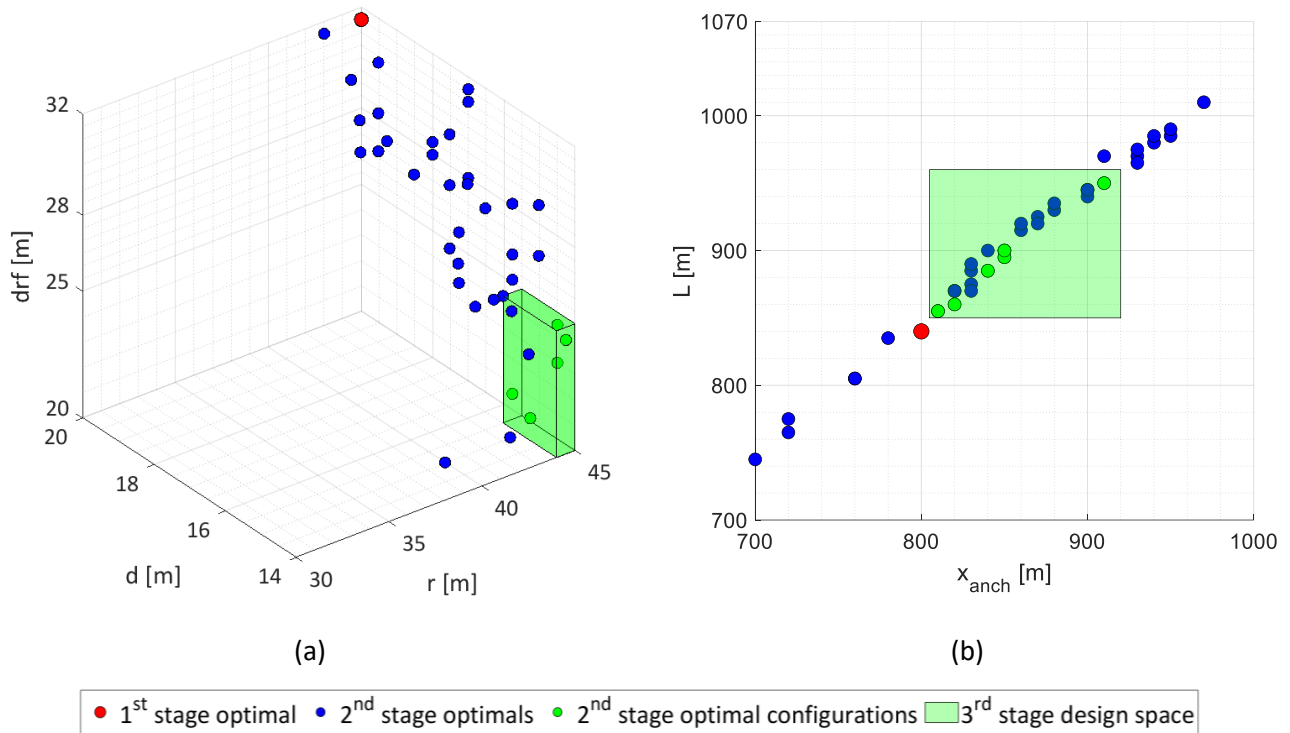
Figure 123: Comparisons of first- and second-stage optimizations results: platform geometry (a) and mooring system layout (b); The new design space, which is adopted in the third stage, is shaded in green.

The new design space is summarized in Table 37.

Table 37: Third-stage SLS fatigue optimization design space.

	Lower bound [m]	Upper bound [m]	Spacing [m]
d	14	15.5	0.5
r	44	45	0.5
drf	20	25	0.5
x_{anch}	810	910	10
L	x_{anch} +40	x_{anch} +55	5

Being the fatigue estimation the result of the accumulation of damages occurred under different load conditions, the simulation of a larger number of events is required. Therefore, the reduction of design variables achieved with the 2nd stage optimization was of primary importance for performing an efficient procedure in the 3rd stage.

The cumulative damage (evaluated according to Eq. 8.18) at the tower base scored by the optimum system at each generation is presented in Figure 124.
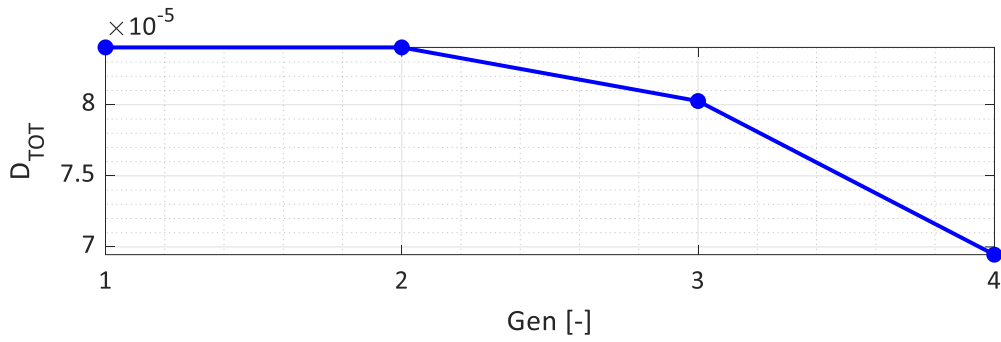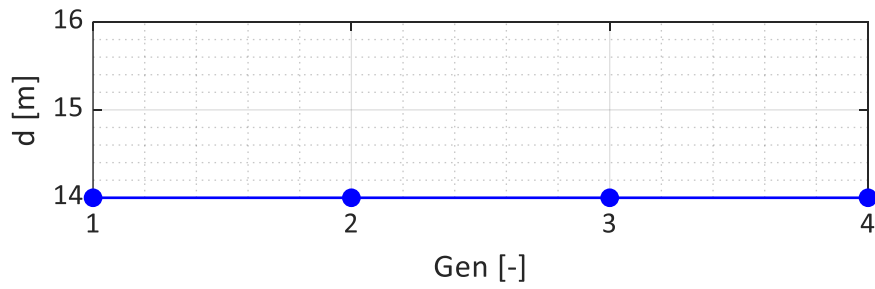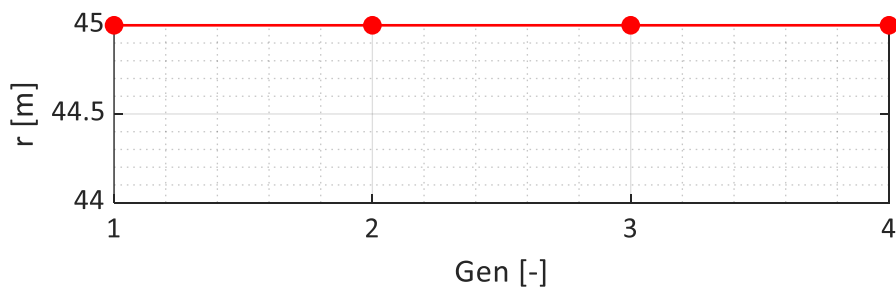
Figure 124: Sardinia site 3rd stage, single-objective SLS Fatigue optimization results: evolution of the cumulative damage during the optimization.

The evolution of platform design variables is presented in Figure 125. The trend of side column diameter (Figure 125a), platform radius (Figure 125b) and draft (Figure 125c) are constant during the optimization, meaning that the reduction of the fatigue damage in Figure 124 is caused by modification in the moorings geometry. The floater presents column diameter equal to 14m, radius of 45m and 24.5m draft, which are similar to the results obtained for the site in Tuscany.
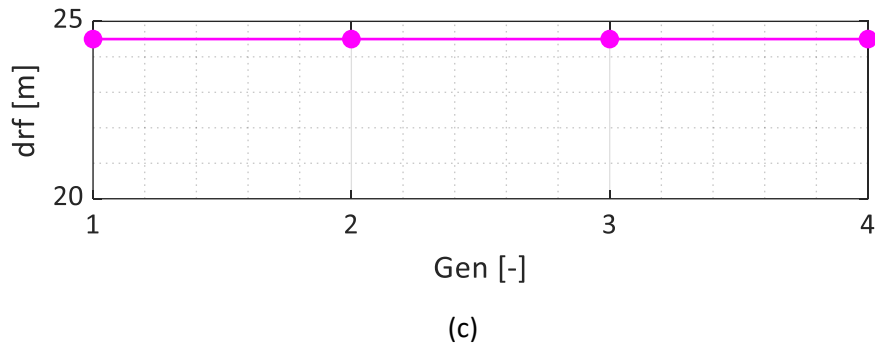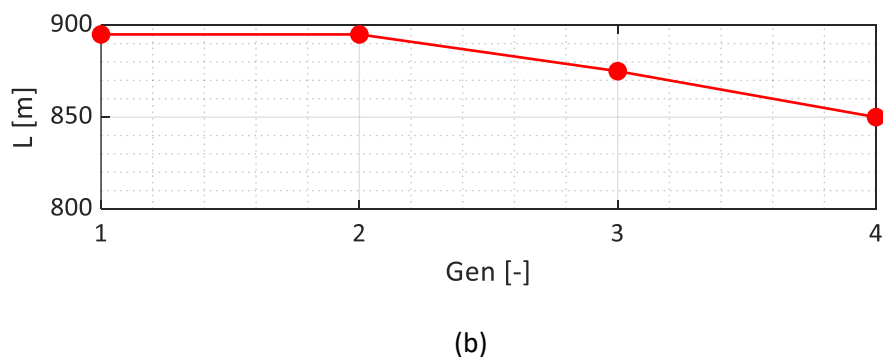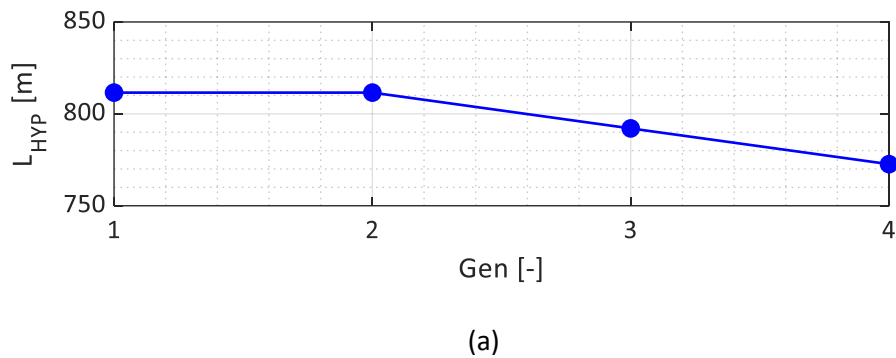

(a)

(b)

(c)

Figure 125: Sardinia site 3rd stage, single-objective SLS Fatigue optimization results: evolution of side column diameter (a), platform radius (b) and draft (c) during the optimization.

The optimal mooring layout is shown in Figure 126, results are plotted in terms of L_{HYP} (Figure 126a), L (Figure 126b) and the difference between L and L_{HYP} (Figure 126c). Both L_{HYP} and L trends during the optimization are similar to the Fatigue damage trends, reducing the mooring footprint until x_{anch}= 810m and L=850m. As discussed in section 8.6.1, this will tend the mooring to become tauter, mitigating the oscillations of the platform and consequently the fatigue loads. Moreover, considering the difference L-L_{HYP} (Figure 126c), the optimal layout tends to evolve towards a tauter solution, which will need larger anchors to withstand higher tensions.
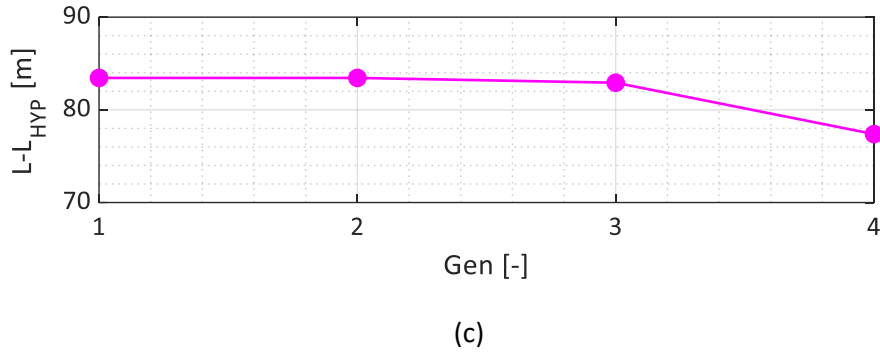

(a)

(b)

(c)

Figure 126: Sardinia site 3rd stage, single-objective SLS Fatigue optimization results, evolution of the mooring layout during the optimization: L_{HYP} (a), L (b) and the difference between L and L_{HYP} (c).

Results of the 3rd stage optimization in terms of maximum bending moment, cost and mean displacements are presented in the following. They are evaluated under the same load condition applied in 1st and 2nd stage optimizations, namely rated wind speed and corresponding wave with the highest H_s.

Figure 127 presents the normalized bending moment, this quantity is proportional with the rotation of the system, which is influenced mostly by the platform geometry. Since the three design variables d, r, and drf are almost constant during the optimization, the normalized bending moment does not vary, and it remains at around 1.12.
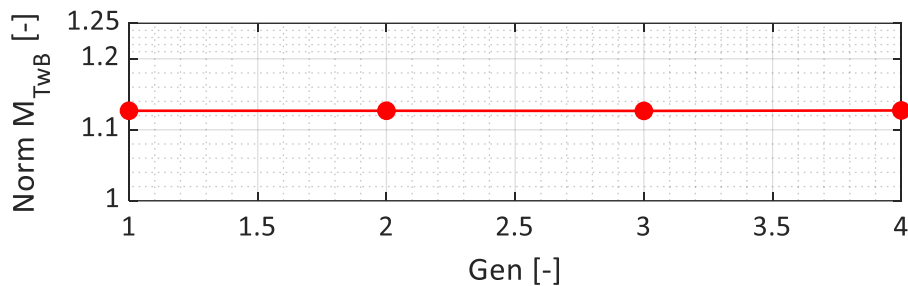

Figure 127: Sardinia site 3rd stage, single-objective SLS Fatigue optimization results: evolution of the normalized tower base bending moment during the optimization.

Normalized substructure cost is presented in Figure 128. A 45% reduction is noticeable with respect to the 1st stage optimal system. This result is also similar to the ones scored in the 2nd stage optimization (see section 8.6.2). being the raw cost of steel wire cables lower with respect to chains, mooring lines have a lower influence on the overall cost with respect to the Tuscany case (see section 8.5.3).
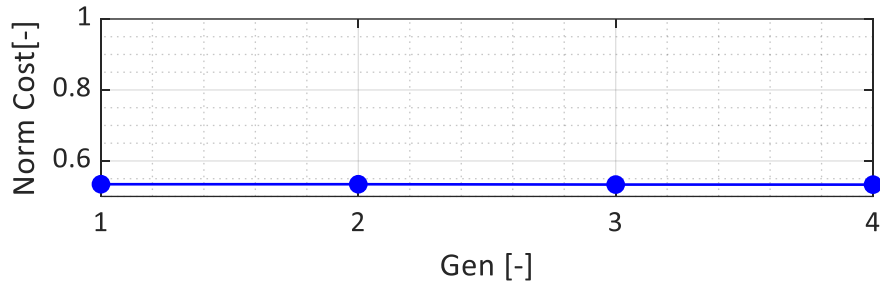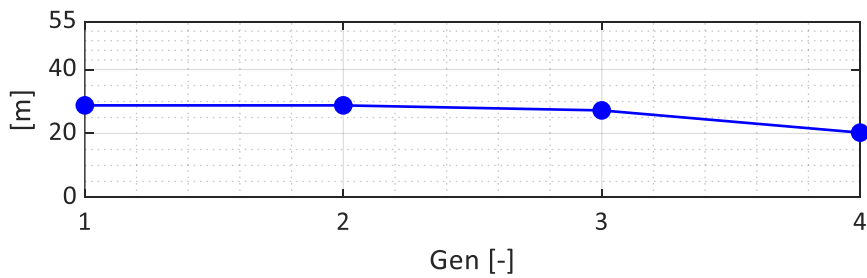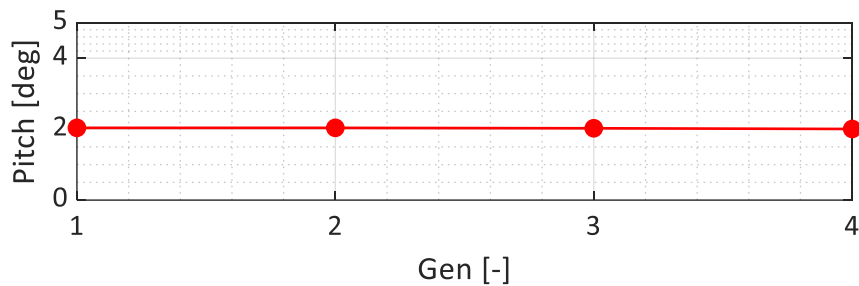
Figure 128: Sardinia site 3rd stage, single-objective SLS Fatigue optimization results: evolution of the normalized tower base bending moment during the optimization.

Finally, the results for the mean displacements are presented in Figure 129. The evolution of the Surge motion (Figure 129a) shows a trend which is similar to the Fatigue damage (Figure 119) and the difference L-L$_{HYP}$ (Figure 129c), denoting the influence of the mooring system. As discussed for Figure 126, the optimal cable is so taut that the horizontal displacement is lower with respect to the upscaled result. On the contrary, the Pitch rotation (Figure 129b) remains almost constant around 2°.

(a)

(b)

Figure 129: Sardinia site 3rd stage, single-objective SLS Fatigue optimization results: evolution of the maximum Surge (a) and Pitch (b) during the optimization

In conclusion, the optimal system for fatigue damage mitigation is presented in Table 38 and Figure 130. The platform geometry (Figure 130a) is very similar to the one obtain for the Tuscany site (Figure 108a), with a small column diameter, large radius and draft in the reduced design space (see Table 37). The mooring layout (Figure 130b) has a similar length with respect to the one of the Tuscany site (Figure 108b)

but, for the larger water depth, it is slightly suspended even at rest. Under rated condition, the sag reduces, and the catenary tends to become a taut line, developing more tension than the previous results of section 8.6.1 and 8.6.2 (see Figures 114 and 122).

Table 38: Second-stage multi- objective optimization results

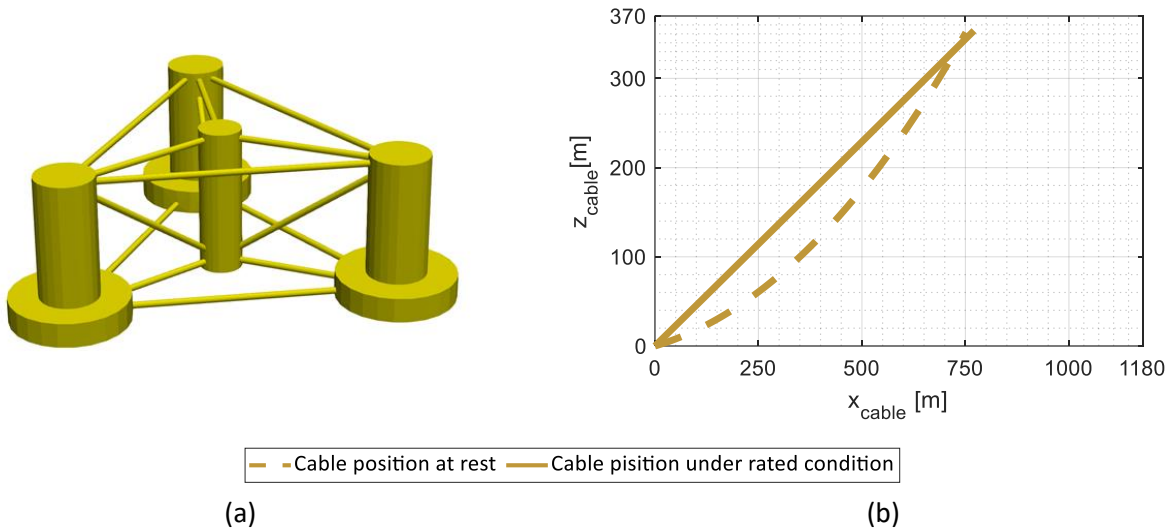| d	r	drf	x_{anch}	L	Norm M_{Twb}	Norm Cost	Surge	Pitch
[m]	[m]	[m]	[m]	[m]	[-]	[-]	[m]	[m]
14	45	24.5	810	840	1.13	0.533	20.26	2.00

Figure 130: Optimal system after the 3rd stage optimization: platform geometry (a); cable layout (b) at rest and under rated condition.

8.6.4   Comparison of the results

In this section, the results of the three stages of optimizations are compared and summarized. The First optimization aimed at finding the substructure with a lower cost but better structural performances with respect to the upscaled one. The maximum Tower-base bending moment was chosen as objective function. As expected, the optimal floater was very similar to the one achieved for the Tuscany site. The slight increase in the draft and the suspended mooring system, together with the different load condition, allowed to obtain better performances with respect to the results of section 8.5.1, scoring a final Tower-base bending moment of 1.9503e+08 Nm against 1.9668e+08 Nm of the Tuscany-site optimized.

Then, the second optimization is targeted to *jointly* minimize the stresses at the turbine base and the costs, normalized with respect to the results scored by the previous stage. As for the Tuscany site, this procedure allowed to identify a restricted design variable space to perform the computationally demanding fatigue damage optimization in the 3rd stage. The configurations identified agreed with the results of section 8.5.2 (2nd stage for the Tuscany site) regarding cost reduction and stress increase. Moreover, similar platform

geometries were identified, characterized by small column diameter, large radius, and variable draft between 20m and 25m. optimal mooring layouts belonged to a smaller range of design variables compared to the 2nd stage results for the Tuscany site. They presented also a larger shape variability (see Table 36), thanks to the removal of the constraints on the line resting on the seabed.

Finally, the 3rd stage optimization, aimed at minimizing the fatigue damage under a set of design load conditions, was carried out on a restricted design variable space. The mooring system was again found critical for this optimization procedure. The optimal solution, presented in Table 38, shows common feature with respect to the Tuscany-site optimized for what regards the platform shape, but opposite for the mooring system. While the cable in section 8.5.3 was characterized by a large footprint, in this case, the optimization evolved towards smaller x_{anch} and cable length. Despite this difference, the results aimed at the same objective: reducing the fatigue loads on the tower base by increasing the mooring system stiffness. On one hand, the constraint on the line resting on the seabed forced the optimization to find stiffer cables by maximizing the footprint. On the other hand, the Sardinia site optimization is free to find stiffer cables even with reduced lengths. This drives the procedure towards shorter lines, which become tauter under wind-wave loadings compared to the Tuscany-site results.

In addition, a comparison between the anchors dimension of the optimized solutions is provided in Table 39.

Table 39: Suction pile dimensions of the optimized systems at the three stages

Pile dimension	1st stage	2nd stage min (Conf. 1)	2nd stage max (Conf. 41)	3rd stage
L [m]	12.319	12.059	12.479	12.536
D [m]	2.129	2.089	2.154	2.162
t [m]	0.014	0.014	0.014	0.014

The Sardinia-site optimization procedure workflow is summarized in Figure 131. As it is possible to observe comparing the mooring line geometries (right side of Figure 131), the final solution presents cable extremely taut if compared with the results of the previous optimization, but also with the results of the Tuscany site procedure (Figure 108). This causes the lower fatigue damage scored by the Sardinia site.
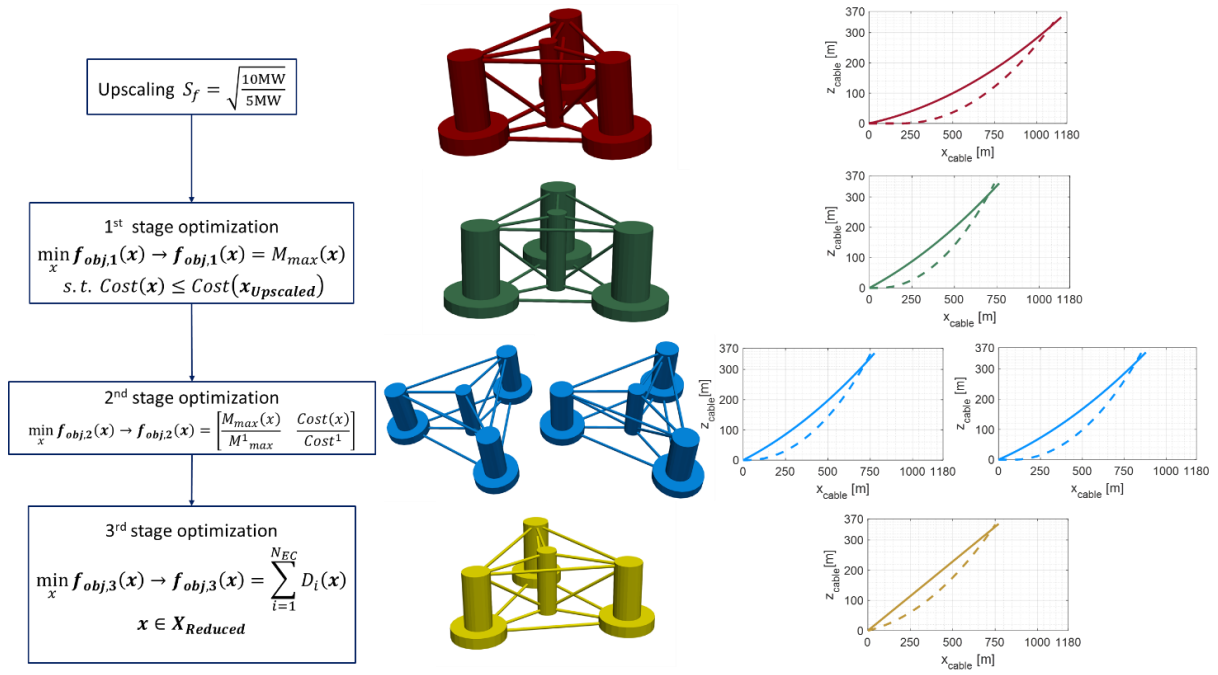
Figure 131: Optimization procedure workflow for the Sardinia site.

Chapter 9.
Conclusion

This concluding Chapter summarizes the principal achievements of this thesis. The work proposes to develop optimization procedures for the design of large FOWTs suitable for specific installations. To do so, fast, and accurate simulation tools need to be adopted. Within this framework, the first part of the research is focused on the development of a coupled FD model capable to estimate the response of the FOWT under the wind-wave loading. The characteristics of the devised tool have been detailed described from Chapter 2 to 4. Firstly, the hydrodynamic modeling of the floating platform is discussed, with particular attention on the potential flow theory and the hydrodynamic forces exerted on slender elements. Then, the modeling of mooring lines adopting a quasi-static formulation is presented. This approach neglects the dynamic behaviour of the cables, considering only their stiffness with respect to the platform DoFs. Examples on both catenary and TLP systems are provided. The wind turbine and aerodynamic modeling is discussed in Chapter 4, with particular attention to the coupling of the rotating rotor and the turbine tower with the floating platform and how to derive such contributions in the FD.

The validation of the assembled coupled FD model is presented in Chapter 5. The NREL 5MW OC4 DeepCwind semisubmersible FOWT [47] is adopted as benchmark case. Results are compared with TD simulations performed in FASTv8. Firstly, RAOs, then the response under turbulent wind and irregular wave are validated. Moreover, important procedures for deriving stresses on the turbine tower and the mooring lines directly in the FD are described.

The second part of the thesis concerns the implementation of the developed FD model in optimization procedures for the design of a semisubmersible platform and catenary mooring lines suitable for a 10MW WT.

Chapter 6 is completely focused on the optimization of the dynamic properties of the substructure, since the Peak of the RAO at platform eigenfrequencies of Surge, Have and Pitch are chosen, one at a time, as target to be minimized. Although these procedures do not consider realistic wind-wave design load conditions, they give useful insight to understand the effect of platform geometry and moorings layout on the response of each component of the system. The optimizations are organized in two, independent, steps. The first one is carried out considering only design variable related to the platform geometry, while

the second one considering both platform and mooring geometry. Constraints related to the maximum displacements of the system, to cable geometry and anchor loads are adopted. The optimized configurations are compared to an upscaled solution obtained from the 5MW NREL semisubmersible FOWT [47]. It was found that optimized concepts shows better performances with a reduced mass of the floating substructure.

On the same 10MW FOWT concept studied, a Site-specific optimization procedure is developed and carried out. Chapter 7 describes the identification of the environmental conditions at three possible sites:

- North Sea installation is characterized by means of data from FINO1 platform, which is in very shallow-water;

- Mediterranean Sea near to the Tuscany cost is characterized by means of DHI and Copernicus databases. It presents a water depth of 200m;

- Mediterranean Sea near to the south-west coast of Sardina is characterized by means of the same databases of the Tuscany site. It presents a water depth of 370m;

Due to the shallow water, the North Sea site is found to be unsuitable for floating installations, therefore it is not considered in the optimizations, but it is studied to compare the results obtained for the Mediterranean site.

To characterize the site-specific wind-wave loadings, the joint distribution of average wind speed, significant wave height and peak spectral period is calculated. These three variables are sufficient for the characterization of the wind-wave design loadings. A FORM is adopted for this purpose, obtaining ECSs for two significant return period: 50-year and 1-year. The first one allows to obtain design loads compatible with a ULS analysis, while the latter with a SLS Fatigue analysis. These two conditions are adopted as load cases for the optimization procedure presented in Chapter 8.

The proposed site-specific optimization is organized in three stages which are connected one to each other. The first one aims at finding the substructure which minimizes the tower-base bending moment under the most critical 50-year return period load condition with rated wind speed (11 m/s at hub height). An additional constraint related to the system cost is set in order to obtain solutions cheaper than the upscaled one. The cost includes raw material and manufacturing price of platform, moorings, and anchors.

Results of the 1st stage optimized system are adopted to perform a multi-objective optimization which considers as objective function the maximum tower-base bending moment (evaluated as in the previous stage) and the cost, these two targets are *jointly* minimized. Results shows that with a controlled increase of the stresses on the turbine, a significant reduction of the costs can be achieved (estimated in 45% the cost of an upscaled solution). Furthermore, this procedure highlights that the optimal solutions lied in a restricted region of the design space. For this reason, the 3rd stage optimization is performed over this new,

smaller, space of variables. The target to be minimized is set to be the fatigue damage under 1-year return period load conditions which span from 9 m/s to 25 m/s of wind speed. The fatigue loads are estimated by the Dirlik spectral method in the FD, directly, from the loads PSDs.

Results show that the mooring system plays a primary role in the mitigation of the fatigue damage. In the end, for both Tuscany and Sardinia sites, the final optimal concept is found to cut the costs of about the 45% with an increase of the stresses around the 10-15%

9.1   Final Remarks

In conclusion, the research proves the capabilities of the developed FD model to simulate the coupled response of a FOWT under the joint action of wind and waves. Moreover, it gives useful insight for the extrapolation of stresses in the mooring lines and the turbine tower, based on simplified structural schemes. Due to the efficiency and versatility, the proposed FD model is suitable for optimizations and early-stage design phases. The first-order hydrodynamic characterization of the platform, which is a very time-consuming part, has been taken outside of the optimization procedure by performing the potential flow simulations in ANSYS AQWA over a fine grid of possible platform geometries. This was found to be a reasonable approximation for the chosen semisubmersible platform, which allows to reduce dramatically the computational time.

The developed optimization procedure shows that there is still room for enhancing the structural performance of large FOWT by means of a focused design of the floating substructure. Moreover, it is shown that upscaling procedure may lead to overdesigned solutions. Concerning that, the site-specific optimizations prove that the possible cost reduction can be of about the 45% with respect to the upscaled cost, without significant losses in the structural performances.

This aspect can be of extremely importance for the exploitation of deep-sea areas where the wind resource is limited. Considering that the average wind speeds in the Mediterranean Sea are generally lower and the wave loads are extremely reduced compared to Northern Europe seas, such a cost reduction may lead to a reduction of the LCOE itself. This may open new possibilities for the exploitation of the wind resources in the Mediterranean Sea.

9.2   Future Works

The exploitation of very deep water (above 400m) gives rise to several critical aspects related to the mooring system and the anchor design. These difficulties will be typical for the installations in the Mediterranean Sea, where the geotechnical properties of the seabed may vary largely, and the higher wind resource is concentrated in very deep-sea areas. For these reasons, efficient cables, and anchors for very deep-water will be studied.

On the opposite, a challenging objective of the technical research is to make floating installations competitive with fixed-bottom solutions in shallow water. In this context, future works will be also focused on the analysis of mooring layouts suitable for supporting multiple turbines, which may cut the costs of the substructures and open new possibilities for FOWTs in shallow water.

As discussed in the previous section, the reduction of the LCOE is a core task for the Floating wind sector, acknowledged by the European Union. In this context, The cost-effectiveness is a core task which must by achieved acting on multiple levels, the substructure cost-optimization can clearly help that, but also the development of multi-purpose floating offshore structures, may set new targets on the reduction of the LCOE.

Given the flexibility of FD simulation model and the site-specific optimization procedures here proposed, future works will be focused on different platform concepts and on multi-objective optimizations pursuing for example targets related to floater's industrialization or to maintenance cost reduction, in order to look for different trade-off solutions between cost and structural performances.

Appendix A

Formulation of the generalized mooring stiffness matrix

In section 3.3, the calculation mooring system stiffness matrix at the equilibrium position, i.e., the reference position, was presented. However, this is a very particular case as the platform would likely undergo large displacements in the majority of the environmental conditions. Thus, the formulation of the stiffness matrix of a single cable is of primary importance for FOWT formulation. Firstly, platform and mooring line kinematic conventions need to be defined.

As already discussed, platform kinematics is expressed according to naval conventions. An inertial reference frame is adopted, referring to six rigid body DoFs. Vector $\boldsymbol{r} = \begin{bmatrix} r_x & r_y & r_z \end{bmatrix}$, defines the translational DoFs of surge, sway, and heave, while the rotations are represented by the Euler angle triad $\begin{bmatrix} \phi & \theta & \psi \end{bmatrix}$ corresponding to roll, pitch, and yaw. Thus, the rotation operator, $\boldsymbol{R}$, can be written as:

$$\boldsymbol{R} = \begin{bmatrix} R_{11} & R_{12} & R_{13} \\ R_{21} & R_{22} & R_{23} \\ R_{31} & R_{32} & R_{33} \end{bmatrix} = \begin{bmatrix} c(\psi)c(\theta) & c(\psi)s(\theta)s(\phi) - s(\psi)c(\phi) & c(\psi)s(\theta)c(\phi) + s(\psi)s(\phi) \\ s(\psi)s(\theta) & s(\psi)s(\theta)s(\phi) + c(\psi)c(\phi) & s(\psi)s(\theta)c(\phi) - c(\psi)s(\phi) \\ -s(\theta) & c(\theta)s(\phi) & c(\theta)c(\phi) \end{bmatrix} \quad \text{(A.1)}$$

where, $c(.)$ and $s(.)$, refer to cosine and sine functions, respectively. The fairlead position can be then expressed in the inertial frame as [60]:

$$\boldsymbol{r}^F = \begin{bmatrix} X^F \\ Y^F \\ Z^F \end{bmatrix} = \boldsymbol{r} + \boldsymbol{R}\boldsymbol{r}^{F,0} = \begin{bmatrix} r_x \\ r_y \\ r_z \end{bmatrix} + \boldsymbol{R}\begin{bmatrix} x^{F,0} \\ y^{F,0} \\ z^{F,0} \end{bmatrix} \quad \text{(A.2)}$$

where, $\boldsymbol{r}$, represents the generalized platform displacement, while $\boldsymbol{r}^{F,0}$ is the fairlead position in the body reference frame. The derivation of the mooring stiffness matrix requires the evaluation of the differential changes of l, h, and beta (see Figure 119), which have been described in section 3.3:

$$\frac{\partial l}{\partial r_x} = \cos(\beta) ; \quad \frac{\partial l}{\partial r_y} = \sin(\beta) ; \quad \frac{\partial l}{\partial r_z} = 0;$$

$$\frac{\partial l}{\partial \zeta} = \cos(\beta)\frac{\partial X^F}{\partial \zeta} + \sin(\beta)\frac{\partial Y^F}{\partial \zeta}, \quad \zeta = \phi, \theta, \psi \quad \text{(A.3)}$$

$$\frac{\partial \beta}{\partial r_x} = \frac{-sin(\beta)}{l}; \quad \frac{\partial \beta}{\partial r_y} = \frac{cos(\beta)}{l}; \quad \frac{\partial \beta}{\partial r_z} = 0;$$

$$\frac{\partial \beta}{\partial \zeta} = \frac{1}{l}\left[cos(\beta)\frac{\partial Y^F}{\partial \zeta} - sin(\beta)\frac{\partial X^F}{\partial \zeta}\right], \quad \zeta = \phi, \theta, \psi \qquad (A.4)$$

$$\frac{\partial h}{\partial r_x} = \frac{\partial Z^F}{\partial r_x} = 0; \quad \frac{\partial h}{\partial r_y} = \frac{\partial Z^F}{\partial r_y} = 0; \quad \frac{\partial h}{\partial r_z} = \frac{\partial Z^F}{\partial r_z} = 1;$$

$$\frac{\partial h}{\partial \zeta} = \frac{\partial Z^F}{\partial \zeta}, \quad \zeta = \phi, \theta, \psi \qquad (A.5)$$

where X^F, Y^F and Z^F represents the fairlead position. The change in position of the fairlead point with respect to the platform orientation can be found by applying the rotation matrix to $r^{F,0}$.
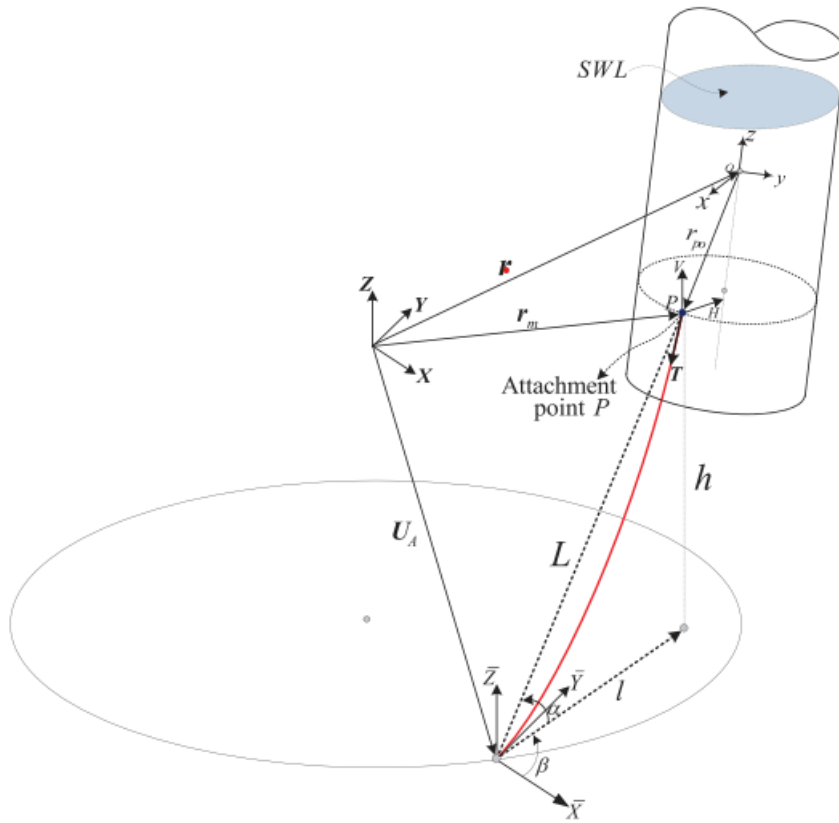
Figure 132: Generic mooring line geometry from [60]

Since the stiffness matrix of a mooring line represent the change of the mooring line forces and moment exerted on the platform with respect to the platform displacement, the generalized 6x6 stiffness matrix form a single line can be derived as c

$$K_m = \frac{\partial F_m}{\partial X} \qquad (A.6)$$

where $\boldsymbol{F_m}$ is the generalized force vector of the single line and $\boldsymbol{X}$ is the generalized displacement. The coefficients of the 6x6 stiffness matrix are function of the in-plane, 2x2 cable stiffness matrix (Eqs. 3.7 and 3.13) [60]:

$$
\boldsymbol{K_m} = -\begin{bmatrix}
\dfrac{\partial T_x}{\partial r_x} & \dfrac{\partial T_x}{\partial r_y} & \dfrac{\partial T_x}{\partial r_z} & \dfrac{\partial T_x}{\partial \phi} & \dfrac{\partial T_x}{\partial \theta} & \dfrac{\partial T_x}{\partial \psi} \\[2mm]
\dfrac{\partial T_y}{\partial r_x} & \dfrac{\partial T_y}{\partial r_y} & \dfrac{\partial T_y}{\partial r_z} & \dfrac{\partial T_y}{\partial \phi} & \dfrac{\partial T_y}{\partial \theta} & \dfrac{\partial T_y}{\partial \psi} \\[2mm]
\dfrac{\partial T_z}{\partial r_x} & \dfrac{\partial T_z}{\partial r_y} & \dfrac{\partial T_z}{\partial r_z} & \dfrac{\partial T_z}{\partial \phi} & \dfrac{\partial T_z}{\partial \theta} & \dfrac{\partial T_z}{\partial \psi} \\[2mm]
\dfrac{\partial M_x}{\partial r_x} & \dfrac{\partial M_x}{\partial r_y} & \dfrac{\partial M_x}{\partial r_z} & \dfrac{\partial M_x}{\partial \phi} & \dfrac{\partial M_x}{\partial \theta} & \dfrac{\partial M_x}{\partial \psi} \\[2mm]
\dfrac{\partial M_y}{\partial r_x} & \dfrac{\partial M_y}{\partial r_y} & \dfrac{\partial M_y}{\partial r_z} & \dfrac{\partial M_y}{\partial \phi} & \dfrac{\partial M_y}{\partial \theta} & \dfrac{\partial M_y}{\partial \psi} \\[2mm]
\dfrac{\partial M_z}{\partial r_x} & \dfrac{\partial M_z}{\partial r_y} & \dfrac{\partial M_z}{\partial r_z} & \dfrac{\partial M_z}{\partial \phi} & \dfrac{\partial M_z}{\partial \theta} & \dfrac{\partial M_z}{\partial \psi}
\end{bmatrix}
\tag{A.7}
$$

$$K_{11} = K_{11}^p \cos^2(\beta) + \frac{H}{l}\sin^2(\beta)$$

$$K_{12} = \sin(\beta)\cos(\beta)\left(K_{11}^p - \frac{H}{l}\right)$$

$$K_{13} = \cos(\beta) K_{12}^p$$

$$K_{14} = \cos(\beta)\left(K_{11}^p \frac{\partial l}{\partial \phi} + K_{12}^p \frac{\partial h}{\partial \phi}\right) - H\sin(\beta)\frac{\partial \beta}{\partial \phi}$$

$$K_{15} = \cos(\beta)\left(K_{11}^p \frac{\partial l}{\partial \theta} + K_{12}^p \frac{\partial h}{\partial \theta}\right) - H\sin(\beta)\frac{\partial \beta}{\partial \theta}$$

$$K_{16} = \cos(\beta)\left(K_{11}^p \frac{\partial l}{\partial \psi} + K_{12}^p \frac{\partial h}{\partial \psi}\right) - H\sin(\beta)\frac{\partial \beta}{\partial \psi}$$

$$K_{21} = K_{12}$$

$$K_{22} = K_{11}^p \sin^2(\beta) + \frac{H}{l}\cos^2(\beta)$$

$$K_{23} = \sin(\beta) K_{12}^p$$

$$K_{24} = \sin(\beta)\left(K_{11}^p \frac{\partial l}{\partial \phi} + K_{12}^p \frac{\partial h}{\partial \phi}\right) - H\cos(\beta)\frac{\partial \beta}{\partial \phi}$$

$$K_{25} = \sin(\beta)\left(K_{11}^p \frac{\partial l}{\partial \theta} + K_{12}^p \frac{\partial h}{\partial \theta}\right) - H\cos(\beta)\frac{\partial \beta}{\partial \theta}$$

$$K_{26} = \sin(\beta)\left(K_{11}^p \frac{\partial l}{\partial \psi} + K_{12}^p \frac{\partial h}{\partial \psi}\right) - H\cos(\beta)\frac{\partial \beta}{\partial \psi}$$

$$K_{31} = K_{13}$$

$$K_{32} = K_{23}$$

$$K_{33} = K_{22}^p$$

$$K_{34} = \left(K_{21}^p \frac{\partial l}{\partial \phi} + K_{22}^p \frac{\partial h}{\partial \phi}\right)$$

$$K_{35} = \left(K_{21}^p \frac{\partial l}{\partial \theta} + K_{22}^p \frac{\partial h}{\partial \theta}\right)$$

$$K_{36} = \left(K_{11}^p \frac{\partial l}{\partial \psi} + K_{12}^p \frac{\partial h}{\partial \psi}\right)$$

$$K_{41} = \left(Y^F - r_y\right)K_{31} - \left(Z^F - r_z\right)K_{21}$$

$$K_{42} = \left(Y^F - r_y\right)K_{32} - \left(Z^F - r_z\right)K_{22}$$

$$K_{43} = \left(Y^F - r_y\right)K_{33} - \left(Z^F - r_z\right)K_{23}$$

$$K_{44} = \left(Y^F - r_y\right)K_{34} - \left(Z^F - r_z\right)K_{24} + V\frac{\partial Y^F}{\partial \phi} - H\sin(\beta)\frac{\partial Z^F}{\partial \phi}$$

$$K_{45} = \left(Y^F - r_y\right)K_{35} - \left(Z^F - r_z\right)K_{25} + V\frac{\partial Y^F}{\partial \theta} - H\sin(\beta)\frac{\partial Z^F}{\partial \theta}$$

$$K_{46} = \left(Y^F - r_y\right)K_{36} - \left(Z^F - r_z\right)K_{26} + V\frac{\partial Y^F}{\partial \psi} - H\sin(\beta)\frac{\partial Z^F}{\partial \psi}$$

$$K_{51} = (Z^F - r_z)K_{11} - (X^F - r_x)K_{31}$$

$$K_{61} = (X^F - r_x)K_{21} - (Y^F - r_y)K_{11} = K_{16}$$

$$K_{52} = (Z^F - r_z)K_{12} - (X^F - r_x)K_{32}$$

$$K_{62} = (X^F - r_x)K_{22} - (Y^F - r_y)K_{12} = K_{26}$$

$$K_{53} = (Z^F - r_z)K_{13} - (X^F - r_x)K_{33}$$

$$K_{63} = (X^F - r_x)K_{23} - (Y^F - r_y)K_{13} = K_{36}$$

$$K_{54} = (Z^F - r_z)K_{14} - (X^F - r_x)K_{34} + H\cos(\beta)\frac{\partial Z^F}{\partial \theta} - V\frac{\partial Y^F}{\partial \theta}$$

$$K_{64} = (X^F - r_x)K_{24} - (Y^F - r_y)K_{14} + H\sin(\beta)\frac{\partial X^F}{\partial \phi} - H\sin(\beta)\frac{\partial Y^F}{\partial \phi}$$

$$K_{55} = (Z^F - r_z)K_{15} - (X^F - r_x)K_{35} + H\cos(\beta)\frac{\partial Z^F}{\partial \theta} - V\frac{\partial Y^F}{\partial \theta}$$

$$K_{65} = (X^F - r_x)K_{25} - (Y^F - r_y)K_{15} + H\sin(\beta)\frac{\partial X^F}{\partial \theta} - H\sin(\beta)\frac{\partial Y^F}{\partial \theta}$$

$$K_{56} = (Z^F - r_z)K_{16} - (X^F - r_x)K_{36} + H\cos(\beta)\frac{\partial Z^F}{\partial \psi} - V\frac{\partial Y^F}{\partial \psi}$$

$$K_{66} = (X^F - r_x)K_{26} - (Y^F - r_y)K_{16} + H\sin(\beta)\frac{\partial X^F}{\partial \psi} - H\sin(\beta)\frac{\partial Y^F}{\partial \psi}$$

Appendix B

Non-Rotating frame Second-Order System Matrices expression

For the sake of completeness, the expression of the mass, damping, stiffness matrices in the system non-rotating frame are reported. Recalling Eqs. 4.7-4.9 and Eq. 4.12 introduced in section 4.2.1, the non-rotating frame second-order System matrices can be written as [62]

$$\boldsymbol{M_{NR}} = \boldsymbol{MT_1},$$

$$\boldsymbol{B_{NR}} = 2\Omega\boldsymbol{MT_2} + \boldsymbol{CT_1},$$

$$\boldsymbol{C_{NR}} = \Omega^2\boldsymbol{MT_3} + \dot{\Omega}\boldsymbol{MT_2} + \Omega\boldsymbol{CT_2} + \boldsymbol{KT_1},$$ $\qquad$ (B.1)

$$\boldsymbol{F_{NR}} = \boldsymbol{FT_{1c}},$$

$$\boldsymbol{u} = \boldsymbol{T_{1c}u_{NR}},$$

where $\boldsymbol{M}$, $\boldsymbol{B}$, $\boldsymbol{C}$, and $\boldsymbol{F}$ have already been introduced in Eq. 4.4. if nF_c and mc are the numbers of control variables in the fixed and rotating frames respectively, then $\boldsymbol{T_{1c}}$ can be defined as [62]:

$$\boldsymbol{T_{1c}} = \begin{bmatrix} \boldsymbol{I_{nF_c \times nF_c}} & & & \\ & \tilde{\boldsymbol{t}} & & \\ & & \ddots & \\ & & & \tilde{\boldsymbol{t}} \\ & & & & \tilde{\boldsymbol{t}} \end{bmatrix}_{(nF_c+3mc)\times(nF_c+3mc)},$$ $\qquad$ (B.2)

Appendix C

Level curves of the ECSs

In this Appendix, ECSs isolines at constant wind speed at hub height are reported, spanning from cut-in to cut-out wind speed (Figure 120 and 121). Blue curves refer to 1-year return period events, while black curves present 50-year return period events at the two designated sites. Fatigue Design events are highlited with red dots.
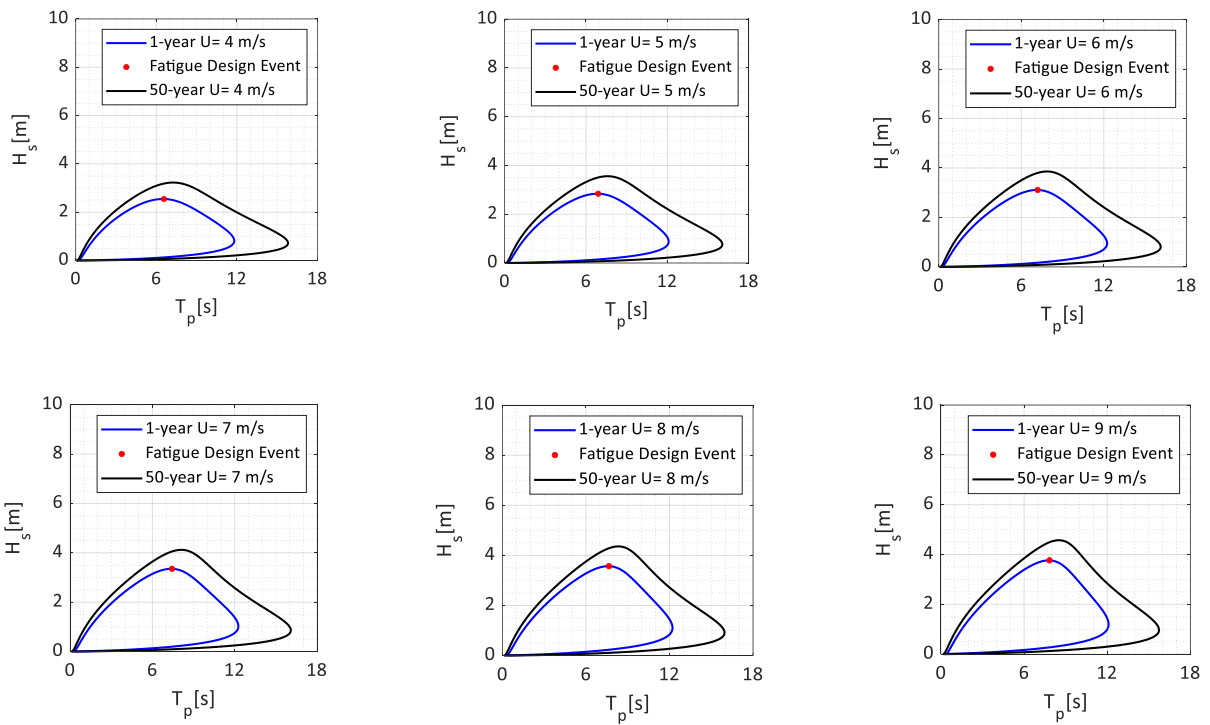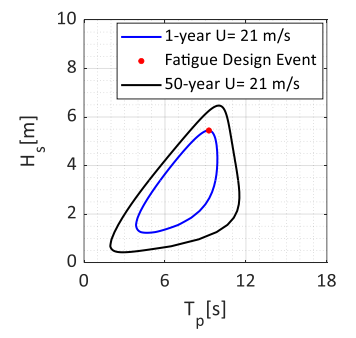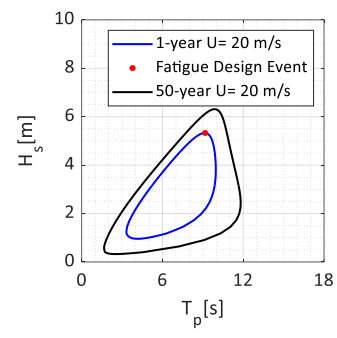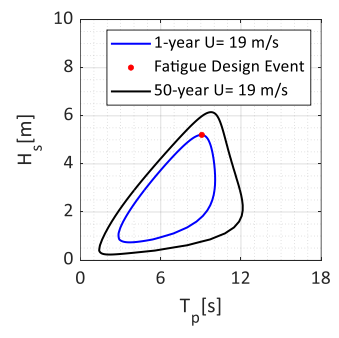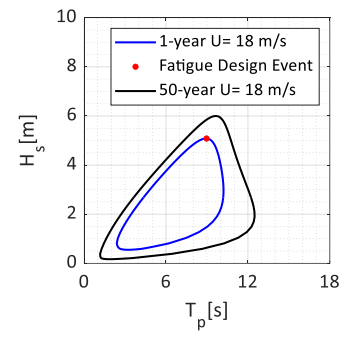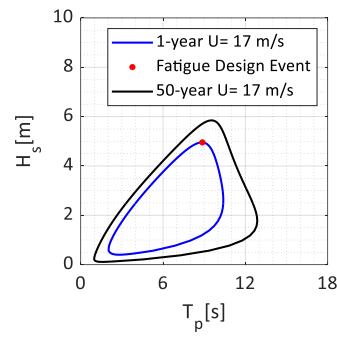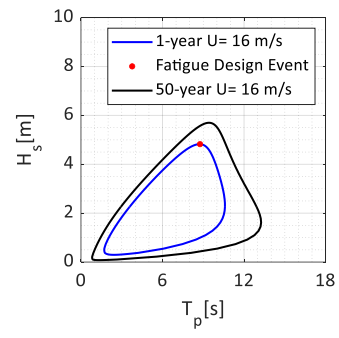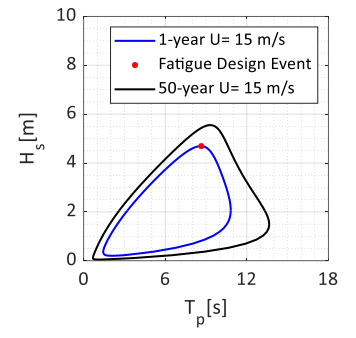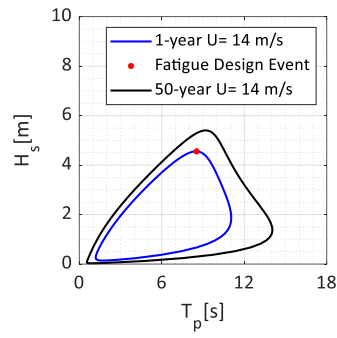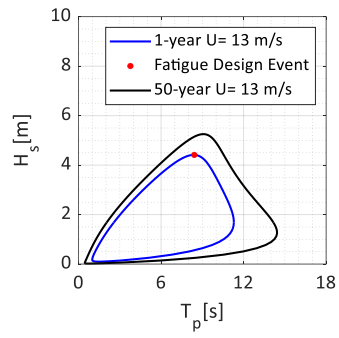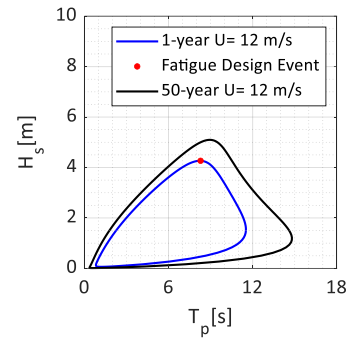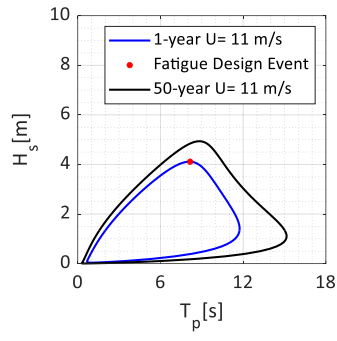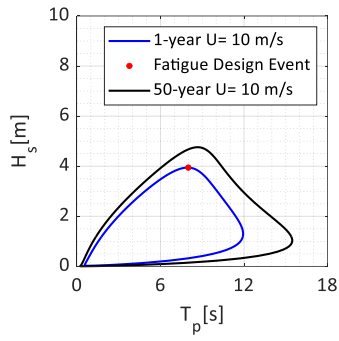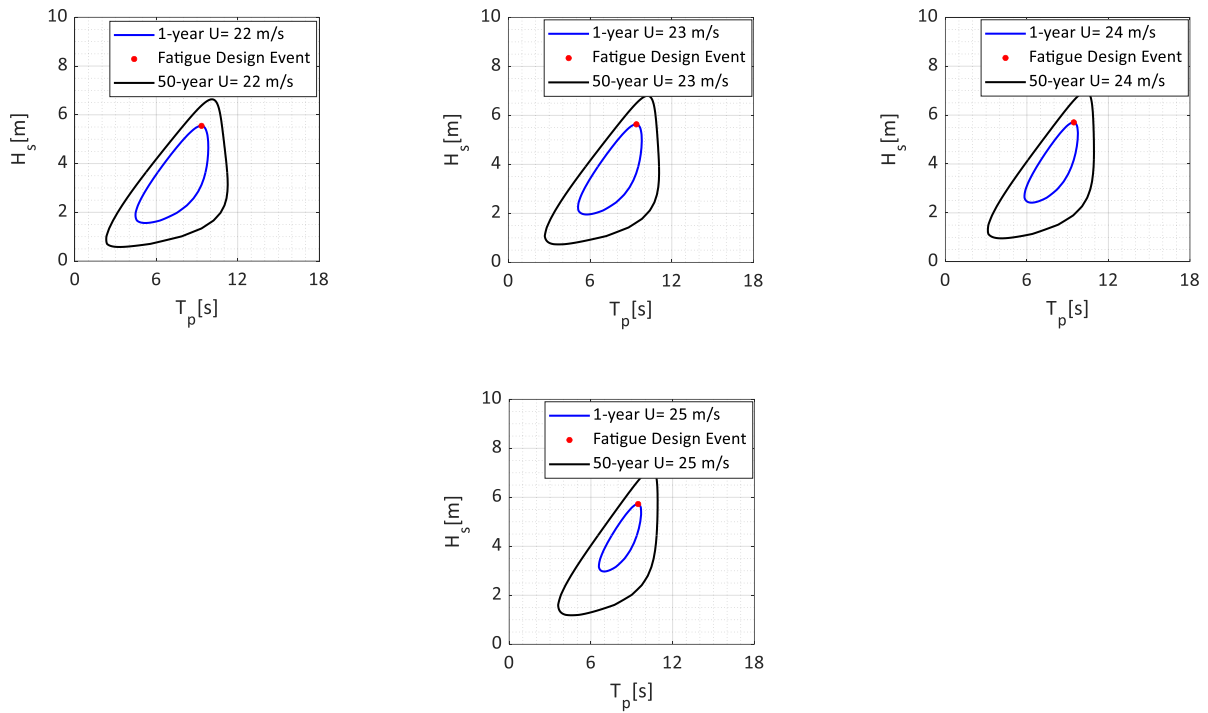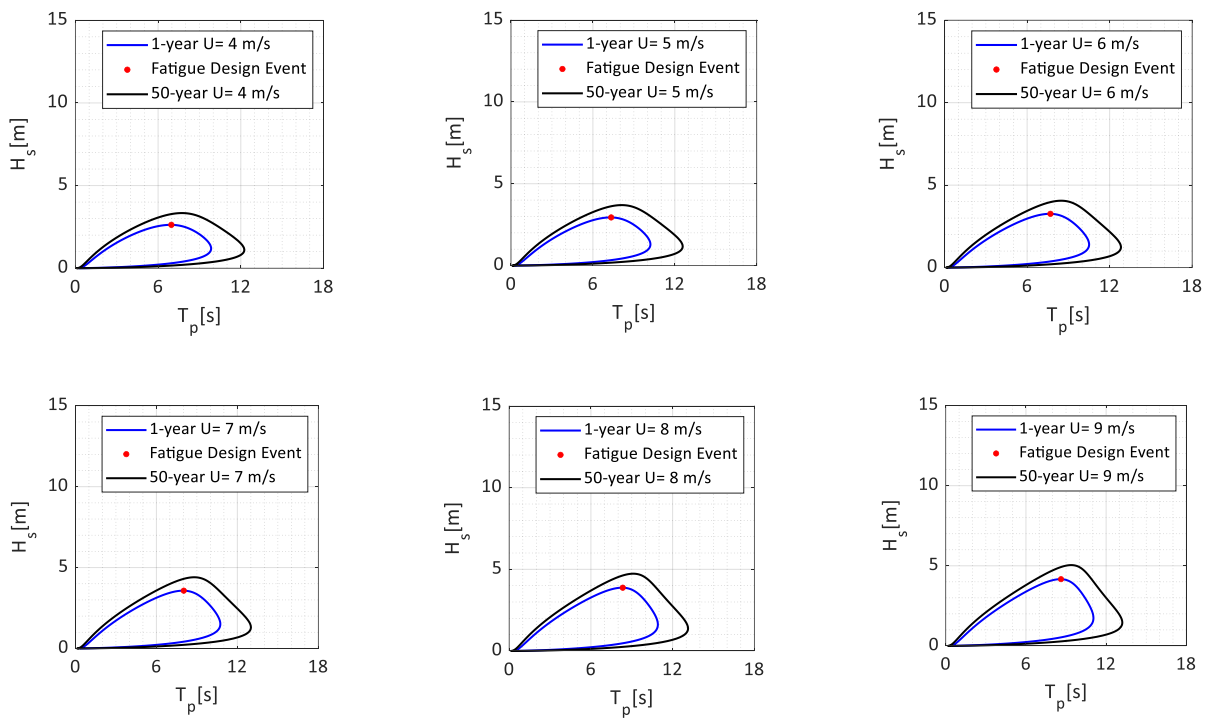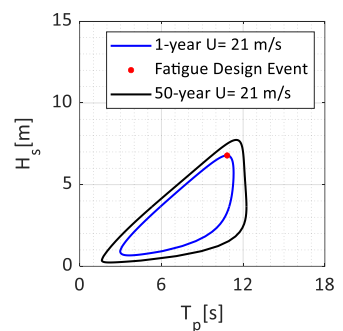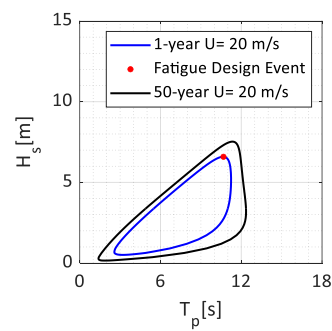
Figure 133: Tuscany site ECS isoline for 1-year and 50-year return periods.
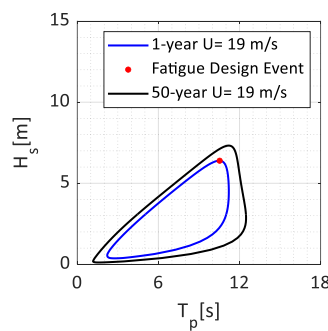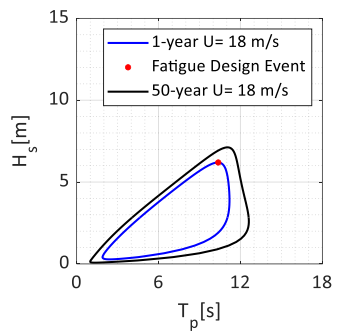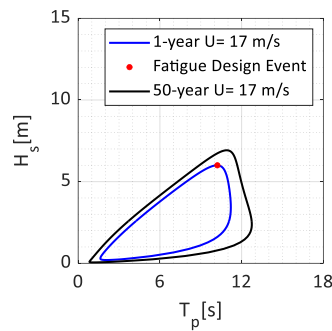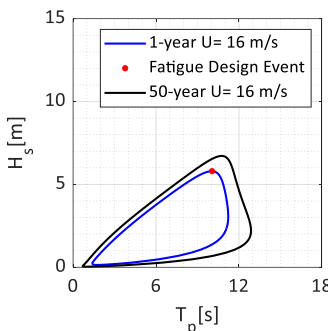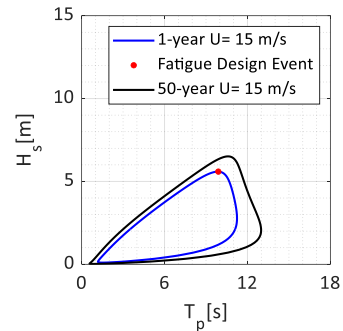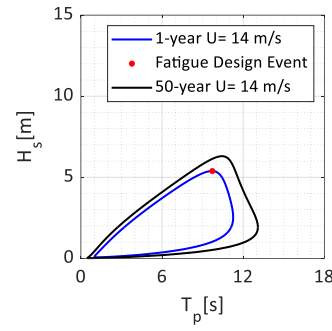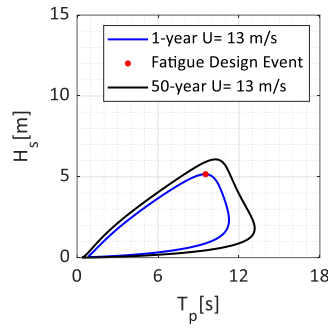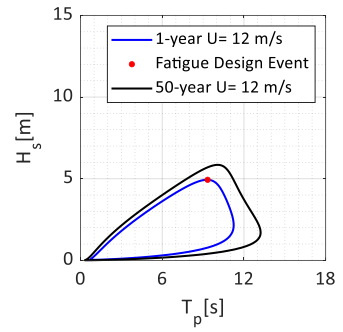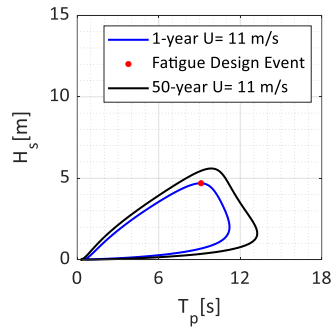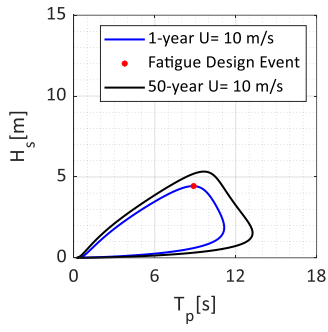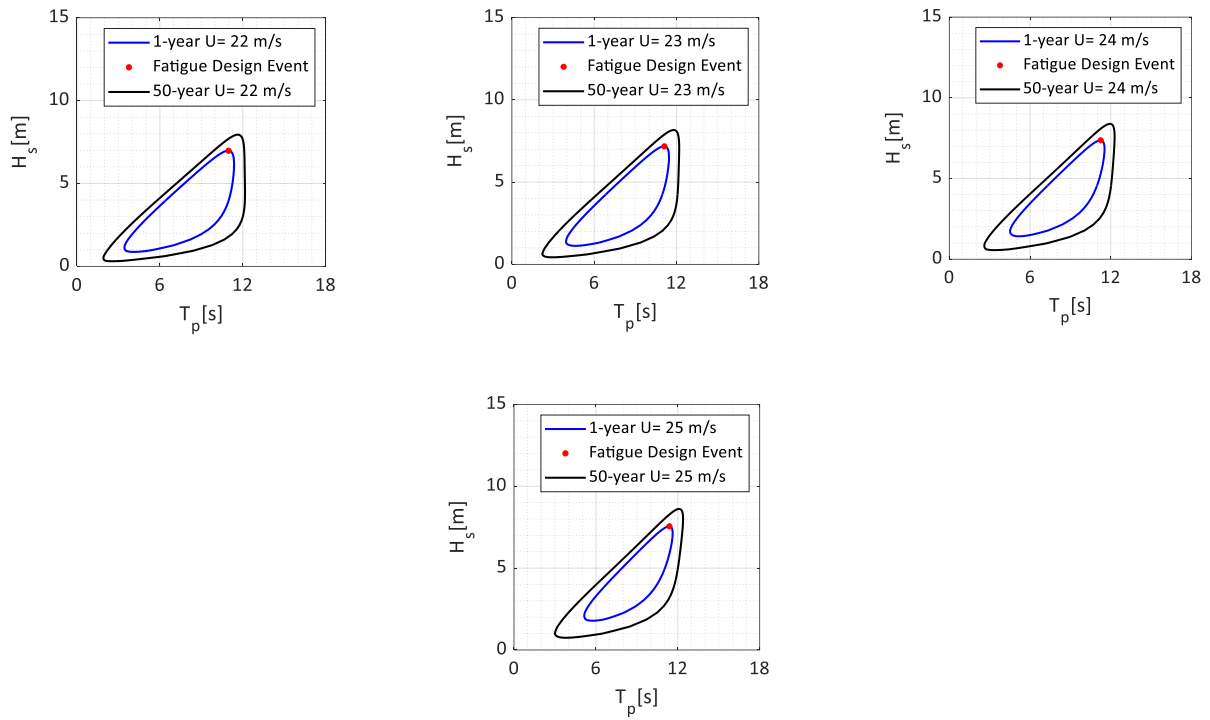
Figure 134: Sardinia site ECS isoline for 1-year and 50-year return periods.

References

[1]   J. Jonkman and M. L. Buhl, "FAST User's Guide," vol. 123, no. 6, pp. 407–8, 2007, doi: 10.2172/15020796.

[2]   A. R. Henderson, "Offshore wind in Europe: Key trends and statistics 2020," *Refocus*, vol. 3, no. 2, pp. 14–17, 2020, doi: 10.1016/s1471-0846(02)80021-x.

[3]   H. Bredmose *et al.*, "The Triple Spar campaign: Model tests of a 10MW floating wind turbine with waves, wind and pitch control," *Energy Procedia*, vol. 137, pp. 58–76, 2017, doi: 10.1016/j.egypro.2017.10.334.

[4]   J. Jonkman, "Definition of the Floating System for Phase IV of OC3," *Contract*, vol. 1, no. May, p. 31, 2010, [Online]. Available: http://scholar.google.com/scholar?hl=en&btnG=Search&q=intitle:Definition+of+the+Floating+System+for+Phase+IV+of+OC3#0.

[5]   A. N. Robertson and J. M. Jonkman, "Loads analysis of several offshore floating wind turbine concepts," *Proc. Int. Offshore Polar Eng. Conf.*, no. October, pp. 443–450, 2011.

[6]   D. Matha, "Model Development and Loads Analysis of a Wind Turbine on a Floating Offshore Tension Leg Platform," *Eur. Offshore Wind Conf.*, no. February, p. 129, 2010, [Online]. Available: http://www.nrel.gov/docs/fy10osti/46725.pdf.

[7]   G. E. Barter, A. Robertson, and W. Musial, "A systems engineering vision for floating offshore wind cost optimization," *Renew. Energy Focus*, vol. 34, no. September, pp. 1–16, 2020, doi: 10.1016/j.ref.2020.03.002.

[8]   T. Larsen and A. Hansen, *How 2 HAWC2, the user's manual*, vol. 2, no. October. 2015.

[9]   E. P. T. Kerja, "Bladed User Manual," *Angew. Chemie Int. Ed. 6(11), 951–952.*, vol. 13, no. April, pp. 15–38, 1967.

[10]   E. Marino, C. Lugni, and C. Borri, "The role of the nonlinear wave kinematics on the global responses of an OWT in parked and operating conditions," *J. Wind Eng. Ind. Aerodyn.*, vol. 123, pp. 363–376, 2013, doi: 10.1016/j.jweia.2013.09.003.

[11]   A. Mockute, E. Marino, C. Lugni, and C. Borri, "Comparison of nonlinear wave-loading models on rigid cylinders in regular waves," *Energies*, vol. 12, no. 21, pp. 1–22, 2019, doi: 10.3390/en12214022.

[12]   E. Marino, A. Giusti, and L. Manuel, "Offshore wind turbine fatigue loads: The influence of alternative wave modeling for different turbulent and mean winds," *Renew. Energy*, vol. 102, pp. 157–169, 2017, doi: 10.1016/j.renene.2016.10.023.

[13]   Z. Chuang, S. Liu, and Y. Lu, "Influence of second order wave excitation loads on coupled response of an offshore floating wind turbine," *Int. J. Nav. Archit. Ocean Eng.*, no. February, pp. 1–9, 2020, doi: 10.1016/j.ijnaoe.2020.01.003.

[14] K. Xu, M. Zhang, Y. Shao, Z. Gao, and T. Moan, "Effect of wave nonlinearity on fatigue damage and extreme responses of a semi-submersible floating wind turbine," *Appl. Ocean Res.*, 2019, doi: 10.1016/j.apor.2019.101879.

[15] K. Xu, Y. Shao, Z. Gao, and T. Moan, "A study on fully nonlinear wave load effects on floating wind turbine," *Journal of Fluids and Structures*. 2019, doi: 10.1016/j.jfluidstructs.2019.05.008.

[16] M. I. Kvittem and T. Moan, "Time domain analysis procedures for fatigue assessment of a semi-submersible wind turbine," *Mar. Struct.*, vol. 40, pp. 38–59, 2015, doi: 10.1016/j.marstruc.2014.10.009.

[17] E. E. Bachynski and T. Moan, "Ringing loads on tension leg platform wind turbines," *Ocean Eng.*, vol. 84, pp. 237–248, 2014, doi: 10.1016/j.oceaneng.2014.04.007.

[18] E. E. Bachynski, M. I. Kvittem, C. Luan, and T. Moan, "Wind-wave misalignment effects on floating wind turbines: Motions and tower load effects," *J. Offshore Mech. Arct. Eng.*, vol. 136, no. 4, pp. 1–12, 2014, doi: 10.1115/1.4028028.

[19] P. Sclavounos, C. Tracy, and S. Lee, "Floating offshore wind turbines: Responses in a seastate Pareto optimal designs and economic assessment," *Proc. Int. Conf. Offshore Mech. Arct. Eng. - OMAE*, vol. 6, pp. 31–41, 2008, doi: 10.1115/OMAE2008-57056.

[20] E. N. Wayman and P. D. Sclavounos, "Coupled Dynamic Modeling of Floating Wind Turbine Systems Preprint," *Offshore Technol. Conf. 1–4 May 2006, Houston, TX*, 2006.

[21] C.-H. Lee, "WAMIT Theory Manual," *WAMIT Theory Man.*, pp. 1–19, 1995.

[22] M. Philippe, A. Babarit, and P. Ferrant, "Comparison of time and frequency domain simulations of an offshore floating wind turbine," *Proc. Int. Conf. Offshore Mech. Arct. Eng. - OMAE*, vol. 5, pp. 589–598, 2011, doi: 10.1115/OMAE2011-49722.

[23] M. Karimi, B. Buckham, and C. Crawford, "A fully coupled frequency domain model for floating offshore wind turbines," *J. Ocean Eng. Mar. Energy*, vol. 5, no. 2, pp. 135–158, 2019, doi: 10.1007/s40722-019-00134-x.

[24] M. Karimi, M. Hall, B. Buckham, and C. Crawford, "A multi-objective design optimization approach for floating offshore wind turbine support structures," *J. Ocean Eng. Mar. Energy*, vol. 3, no. 1, pp. 69–87, 2017, doi: 10.1007/s40722-016-0072-4.

[25] S. Dou, A. Pegalajar-Jurado, S. Wang, H. Bredmose, and M. Stolpe, "Optimization of floating wind turbine support structures using frequency-domain analysis and analytical gradients," *J. Phys. Conf. Ser.*, vol. 1618, no. 4, 2020, doi: 10.1088/1742-6596/1618/4/042028.

[26] A. Pegalajar-Jurado, M. Borg, and H. Bredmose, "An efficient frequency-domain model for quick load analysis of floating offshore wind turbines," *Wind Energy Sci.*, vol. 3, no. 2, pp. 693–712, 2018, doi: 10.5194/wes-3-693-2018.

[27] J. M. Hegseth and E. E. Bachynski, "A semi-analytical frequency domain model for efficient design evaluation of spar floating wind turbines," *Mar. Struct.*, vol. 64, no. November 2018, pp. 186–210, 2019, doi: 10.1016/j.marstruc.2018.10.015.

[28] J. M. Hegseth, E. E. Bachynski, and B. J. Leira, "Effect of environmental modelling and inspection strategy on the optimal design of floating wind turbines," *Reliab. Eng. Syst. Saf.*, vol. 214, no. December 2020, p. 107706, 2021, doi: 10.1016/j.ress.2021.107706.

[29] M. Brommundt, L. Krause, K. Merz, and M. Muskulus, "Mooring system optimization for floating wind turbines using frequency domain analysis," *Energy Procedia*, vol. 24, no. January, pp. 289–296,

2012, doi: 10.1016/j.egypro.2012.06.111.

[30] N. Bruschi, G. Ferri, E. Marino, and B. Claudio, "Influence of Clumps-Weighted Moorings on a Spar Buoy O ff shore Wind Turbine," pp. 15–18, 2020.

[31] G. Barbanti, E. Marino, and C. Borri, "Mooring System Optimization for a Spar-Buoy Wind Turbine in Rough Wind and Sea Conditions," *Lect. Notes Civ. Eng.*, vol. 27, no. 2011, pp. 87–98, 2019, doi: 10.1007/978-3-030-12815-9_7.

[32] J. Liu and L. Manuel, "Alternative mooring systems for a very large offshore wind turbine supported by a semisubmersible floating platform," *J. Sol. Energy Eng. Trans. ASME*, vol. 140, no. 5, pp. 1–9, 2018, doi: 10.1115/1.4039984.

[33] J. Azcona, F. Vittori, U. Schmidt, and F. Savenije, "Design Solutions for 10MW Floating Offshore Wind Turbines Document information," vol. 308974, no. 308974, 2017.

[34] J. Liu, E. Thomas, A. Goyal, and L. Manuel, "Design loads for a large wind turbine supported by a semi-submersible fl oating platform," *Renew. Energy*, vol. 138, pp. 923–936, 2019, doi: 10.1016/j.renene.2019.02.011.

[35] W. ting Hsu, K. P. Thiagarajan, and L. Manuel, "Extreme mooring tensions due to snap loads on a floating offshore wind turbine system," *Mar. Struct.*, vol. 55, pp. 182–199, 2017, doi: 10.1016/j.marstruc.2017.05.005.

[36] M. Leimeister, E. E. Bachynski, M. Muskulus, and P. Thomas, "Rational Upscaling of a Semi-submersible Floating Platform Supporting a Wind Turbine," 2016, doi: 10.1016/j.egypro.2016.09.212.

[37] S. Zhou, K. Müller, C. Li, Y. Xiao, and P. W. Cheng, "Global sensitivity study on the semisubmersible substructure of a floating wind turbine: Manufacturing cost, structural properties and hydrodynamics," *Ocean Eng.*, vol. 221, no. July 2020, p. 108585, 2021, doi: 10.1016/j.oceaneng.2021.108585.

[38] K. A. Shah *et al.*, "A synthesis of feasible control methods for floating offshore wind turbine system dynamics," *Renew. Sustain. Energy Rev.*, vol. 151, no. August, 2021, doi: 10.1016/j.rser.2021.111525.

[39] A. Ghigo, L. Cottura, R. Caradonna, G. Bracco, and G. Mattiazzo, "Platform optimization and cost analysis in a floating offshore wind farm," *J. Mar. Sci. Eng.*, vol. 8, no. 11, pp. 1–26, 2020, doi: 10.3390/jmse8110835.

[40] J. M. Hegseth, E. E. Bachynski, and J. R. R. A. Martins, "Integrated design optimization of spar floating wind turbines," *Mar. Struct.*, vol. 72, no. April, p. 102771, 2020, doi: 10.1016/j.marstruc.2020.102771.

[41] Z. Chen, X. Wang, Y. Guo, and S. Kang, "Numerical analysis of unsteady aerodynamic performance of floating offshore wind turbine under platform surge and pitch motions," *Renew. Energy*, vol. 163, pp. 1849–1870, 2021, doi: 10.1016/j.renene.2020.10.096.

[42] T. Wakui, A. Nagamura, and R. Yokoyama, "Stabilization of power output and platform motion of a floating offshore wind turbine-generator system using model predictive control based on previewed disturbances," *Renew. Energy*, vol. 173, pp. 105–127, 2021, doi: 10.1016/j.renene.2021.03.112.

[43] M. Verma, M. K. Nartu, and A. Subbulakshmi, "Optimal TMD design for floating offshore wind turbines considering model uncertainties and physical constraints," *Ocean Eng.*, vol. 243, no. November 2021, p. 110236, 2022, doi: 10.1016/j.oceaneng.2021.110236.

[44]   W. Yu *et al.*, "Qualification of innovative floating substructures for 10MW wind turbines and water depths greater than 50m," 2017.

[45]   M. Borg, M. W. Jensen, S. Urquhart, M. T. Andersen, J. B. Thomsen, and H. Stiesdal, "Technical definition of the tetraspar demonstrator floating wind turbine foundation," *Energies*, vol. 13, no. 18, pp. 1–11, 2020, doi: 10.3390/en13184911.

[46]   J. B. Thomsen *et al.*, "Modeling the tetraspar floating offshore wind turbine foundation as a flexible structure in orcaflex and openfast," *Energies*, vol. 14, no. 23, pp. 1–14, 2021, doi: 10.3390/en14237866.

[47]   A. Robertson and J. Jonkman, "Definition of the Semisubmersible Floating System for Phase II of OC4," no. September, 2014.

[48]   "AQWA User Manual," vol. 15317, no. October, pp. 724–746, 2012.

[49]   C. Maienza, A. M. Avossa, F. Ricciardelli, D. Coiro, and C. T. Georgakis, "Sensitivity analysis of cost parameters for floating offshore wind farms: An application to Italian waters," *J. Phys. Conf. Ser.*, vol. 1669, no. 1, 2020, doi: 10.1088/1742-6596/1669/1/012019.

[50]   ABS, "Offshore Anchor Data for Preliminary Design of Anchors of Floating Offshore Wind Turbines," *Tech. Stand.*, no. August, 2013, [Online]. Available: www.eagle.org.

[51]   Vryhof, *The guide to anchoring*. 2015.

[52]   Faltinsen O. M, *Sea Loads on Ships and Offshore Structures*. 1990.

[53]   J. M. . Journèe and W. . Massie, "Offshore Hydromechanics," no. January, 2012, doi: 10.1109/ICSENS.2012.6411159.

[54]   J. Jonkman, "Dynamics Modeling and Loads Analysis of an Offshore Floating Wind Turbine," vol. 8, no. 11, pp. 1595–1606, 2012, doi: 10.4161/hv.21225.

[55]   O. M. Faltinsen, F. C. Michelsen, . M Faltinsen, and F. C. Michelsent, "Motions of Large Structures in Waves at Zero Froude Number."

[56]   J. R. Morison, J. W. Johnson, and S. A. Schaaf, "The Force Exerted by Surface Waves on Piles," *J. Pet. Technol.*, vol. 2, no. 05, pp. 149–154, 1950, doi: 10.2118/950149-g.

[57]   F. Savenije and J. Peeringa, "Aero-elastic simulation of offshore wind turbines in the frequency domain," 2009, [Online]. Available: http://www.ecn.nl/docs/library/report/2009/e09060.pdf.

[58]   L. Tao and D. Dray, "Hydrodynamic performance of solid and porous heave plates," *Ocean Eng.*, vol. 35, no. 10, pp. 1006–1014, 2008, doi: 10.1016/j.oceaneng.2008.03.003.

[59]   A. Giusti, "A NONLINEAR MODEL FOR THE DYNAMICS OF MOORED FLOATING PLATFORMS Dottore di Ricerca in Processes, Materials and Constructions in Civil and Environmental Engineering and for the Protection of the Historic-Monumental Heritage *)."

[60]   M. K. Al-Solihat and M. Nahon, "Stiffness of slack and taut moorings," *Ships Offshore Struct.*, vol. 11, no. 8, pp. 890–904, 2016, doi: 10.1080/17445302.2015.1089052.

[61]   Y. B. Yang and J. Y. Tsay, "Geometric nonlinear analysis of cable structures with a two-node cable element by generalized displacement control method," *Int. J. Struct. Stab. Dyn.*, vol. 7, no. 4, pp. 571–588, 2007, doi: 10.1142/S0219455407002435.

[62]   G. Bir, "NWTC Design Codes (MBC)," *Nrel*, vol. 3, no. October, 2008, [Online]. Available: http://wind.nrel.gov/designcodes/postprocessors/mbc.

[63] G. Ferri, E. Marino, N. Bruschi, and C. Borri, "Platform and mooring system optimization of a 10 MW semisubmersible offshore wind turbine," *Renew. Energy*, vol. 182, pp. 1152–1170, 2022, doi: 10.1016/j.renene.2021.10.060.

[64] A. Naess and T. Moan, *Stochastic dynamics of marine structures*, vol. 9780521881. 2010.

[65] J. van der Tempel, *Design of support structures for offshore wind turbines*, no. april. 2006.

[66] E. E. Bachynski, *Design and Dynamic Analysis of Tension Leg Platform Wind Turbines*. 2014.

[67] IEC, "International standard IEC 61400-1, Wind turbines Part 1: Design requirements," *Int. Stand.*, vol. 2005, 2005, [Online]. Available: www.iec.ch.

[68] N. R. E. L. Neil Kelley, Bonnie Jonkman, "TurbSim User' s Guide : Version 1 . 50 TurbSim User' s Guide :," *Wind turbine Numer. Model. FAST Modul. Descr.*, no. September, 2009.

[69] J. M. Jonkman, "Dynamics of offshore floating wind turbines-model development and verification," *Wind Energy*, vol. 12, no. 5, pp. 459–492, 2009, doi: 10.1002/we.347.

[70] G. K. V Ramachandran, A. Robertson, J. M. Jonkman, and M. D. Masciola, "Investigation of Response Amplitude Operators for Floating Offshore Wind Turbines Preprint," no. July, 2013.

[71] J. M. Jonkman, A. N. Robertson, and G. J. Hayman, "HydroDyn User's Guide and Theory Manual."

[72] C. Bak *et al.*, "Design and performance of a 10 MW wind turbine," *J. Wind Energy*, no. July, pp. 1–138, 2013, doi: 10.1017/CBO9781107415324.004.

[73] M. Borg, M. Mirzaei, and H. Bredmose, "LIFES50+ Deliverable D1.2: Wind Turbine Models for the Design," p. 29, 2015.

[74] G. Benassai, A. Campanile, V. Piscopo, and A. Scamardella, "Optimization of Mooring Systems for Floating Offshore Wind Turbines," vol. 57, no. 4, pp. 1–19, 2015, doi: 10.1142/S0578563415500217.

[75] MATLAB, "Optimization Toolbox ᵀᴹ User' s Guide R 2014 b," 2014.

[76] M. Masciola, J. Jonkman, and A. Robertson, "Implementation of a multisegmented, quasi-static cable model," *Proc. Int. Offshore Polar Eng. Conf.*, no. March, pp. 315–322, 2013.

[77] M. Ambiente, "Relazione meteomarina," 2020.

[78] S. R. Winterstein, P. Engineering, and S. Haver, "E NVIRONMENTAL P ARAMETERS FOR E XTREME R ESPONSE : I NVERSE FORM W ITH O MISSION F ACTORS," no. January, 1993.

[79] A. Bang Huseby, E. Vanem, and B. Natvig, "A new approach to environmental contours for ocean engineering applications based on direct Monte Carlo simulations," *Ocean Eng.*, vol. 60, pp. 124–135, 2013, doi: 10.1016/j.oceaneng.2012.12.034.

[80] S. R. Winterstein and S. Haver, "Environmental parameters for extreme response: inverse FORM with omission factors," vol. 2, no. August 1994, pp. 142–148, 2001.

[81] L. Li, Z. Gao, and T. Moan, "Joint environmental data at five European offshore sites for design of combined wind and wave energy devices," *Proc. Int. Conf. Offshore Mech. Arct. Eng. - OMAE*, vol. 8, no. June, 2013, doi: 10.1115/OMAE2013-10156.

[82] D. Al-Sulami, "Exponentiated Exponential Weibull Distribution: Mathematical Properties and Application," *Am. J. Appl. Sci.*, vol. 17, no. 1, pp. 188–195, 2020, doi: 10.3844/ajassp.2020.188.195.

[83] DNV GL AS, "DNVGL-ST-0437: Loads and site conditions for wind turbines," *DNV GL - Stand.*, no. November, p. 108, 2016, [Online]. Available: http://www.dnvgl.com.

[84] I. The MathWorks, "Curve Fitting Toolbox ^{TM} User ' s Guide R 2015 a," p. 754, 2015.

[85] C. B. Hasager *et al.*, "Europe's offshore winds assessed with synthetic aperture radar, ASCAT and WRF," *Wind Energy Sci.*, vol. 5, no. 1, pp. 375–390, 2020, doi: 10.5194/wes-5-375-2020.

[86] A. Myhr, C. Bjerkseter, A. Ågotnes, and T. A. Nygaard, "Levelised cost of energy for offshore floating wind turbines in a lifecycle perspective," *Renew. Energy*, vol. 66, pp. 714–728, 2014, doi: 10.1016/j.renene.2014.01.017.

[87] D. N. Veritas, "FATIGUE DESIGN OF OFFSHORE STEEL STRUCTURES," no. April, 2010.

[88] T. Dirlik, "Application of Computers in Fatigue Analysis," no. February, 1985, [Online]. Available: http://webcat.warwick.ac.uk/record=b1445503~S9.

[89] P. Ragan and L. Manuel, "Comparing estimates of wind turbine fatigue loads using time-domain and spectral methods," *Wind Eng.*, vol. 31, no. 2, pp. 83–99, 2007, doi: 10.1260/030952407781494494.

[90] J. P. Quigley, Y. L. Lee, and L. Wang, "Review and Assessment of Frequency-Based Fatigue Damage Models," *SAE Int. J. Mater. Manuf.*, vol. 9, no. 3, 2016, doi: 10.4271/2016-01-0369.

Curriculum Vitae

Personal Information:

Name	Giulio Ferri
Date of birth	12/05/1992
Nationality	Italian

Work experience:

• January 2022 – Present
DICEA, University of Florence,
Via di Santa Marta 3, Florence
(FI)

Post-Doctoral researcher
Research activity partly funded by the Fondazione CR Firenze entitled: "A new super-fast and accurate isogeometric analysis approach to the simulation of artery stents -ISOStent3D".
Collaboration for the development of an improved isogeometric collocation formulation for spatial shear-deformable beams with arbitrary initial curvature.
Teaching activity in the course Mechanics of Offshore Wind Structures at the University of Florence, Master Degree in Structural Engineering.

Education:

•November 2018 – January 2022
• University of Florence
• Doctor of Philosophy (PhD)
• EQF 8

XXXIV cycle PhD candidate at the University of Florence – International Doctorate in Civil and Environmental Engineering. Research activity focused on platform and moorings modeling and optimization procedures for large semisubmersible floating offshore wind turbines. Title achieved on the 20th of June 2022.

•September 2015 – July 2018
• University of Florence
• Master of Science (M. Sc)
• EQF 7

Master's degree in CIVIL ENGINEERING - STRUCTURES at University of Florence. Title achieved on the 11th of July 2018, master thesis entitled Validated numerical simulation of aerodynamic and aeroelastic behaviour of central box-girder bridge decks (the case of Rhein-crossing bridge in Leverkusen).

•September 2017 – February 2018
• RUB Bochum

Erasmus Traineeship at RUB - Ruhr Universität Bochum, Germany, Department of WINDINGENIEURWESEN UND STRÖMUNGSMECHANIK.

•September 2011 – February 2016
• University of Florence
• Bachelor of Science (B. Sc)
• EQF 6

Bachelor degree in Civil Engineering at University of Florence. Title achieved on the 8th of February 2016, thesis entitled Uses of FRP system in structural reinforce- Design and application on RC frame according to Italian regulations.

• 2006 – 2011
• Scientific lyceum
• Diploma

Scientific lyceum diploma, *Liceo Scientifico Leonardo da Vinci*, Florence, Italy

Publications:

ResearchGate:	https://www.researchgate.net/profile/Giulio-Ferri
ORCID:	https://orcid.org/0000-0002-9127-8547